STELLAR OCCULTATION STUDIES OF SATURN'S RINGS WITH THE HUBBLE SPACE TELESCOPE

by
Amanda Sachie Bosh
S.B. (Earth, Atmospheric, and Planetary Sciences)
S.B. (Materials Science and Engineering)
Massachusetts Institute of Technology (1987)

Submitted in partial fulfillment of the requirements for the degree of

DOCTOR OF PHILOSOPHY
in
EARTH, ATMOSPHERIC, AND PLANETARY SCIENCES

at the
MASSACHUSETTS INSTITUTE OF TECHNOLOGY

February 1994

Author's Signature ______________________
Department of Earth, Atmospheric, and Planetary Sciences
31 December 1993

Certified by ______________________
Professor James L. Elliot
Thesis Supervisor
Department of Earth, Atmospheric, and Planetary Sciences

Accepted by ______________________
Professor Thomas Jordan
Chairman, Department Graduate Committee

ACKNOWLEDGMENTS

I would like to acknowledge the Instrument Definition Team of the Hubble Space Telescope High Speed Photometer for guidance in the understanding of the intricacies of HST data. I also thank Peg Stanley, Andy Lubenow, and Jim Younger, all of whom worked very hard to schedule a very difficult occultation observation on the HST. Alex Storrs has my extreme gratitude for help on every occultation but this first one. Without him in the planetary scheduling department at the Space Telescope Science Institute, we would have gotten much less data than we did. Colleen Townsley has been extremely helpful as our liaison at STScI.

Cathy Olkin did the initial work on the equations for the vector code formulation of the occultation geometry; this has proven very helpful for this work, as have the many discussions we've had. Other past and present graduate students have always been a source of friendship, advice, and good times.

I would also like to thank Dick French, Phil Nicholson, and Bruno Sicardy for the use of non-circular feature data before publication. I extend a special thanks to Phil for a very long, very helpful discussion about the gravitational harmonics problem. Maren Cooke also provided some helpful insight into ringlet kinematics, and measured feature times as part of our Elliot *et al.* (1993) paper in the *Astronomical Journal.*

I thank my thesis advisor, Jim Elliot, for his patient reading of many drafts of this thesis, for his guidance throughout most of my career at MIT, and for letting me spend my last year in graduate school at Lowell Observatory. Last, I thank Matthew Holman, my family, Chicky the cat, and many others for their friendship and support over the years.

This work was supported, in part, by HSP GTO Grant NASG5-1613. The author is partially supported by the NASA Graduate Student Researcher Program.

TABLE OF CONTENTS

Acknowledgments 3
Table of Contents 5
Abstract 7
1. Introduction 9
2. Data 13
3. Model for Geometric Analysis of Occultation Data 21
4. Ring Orbit Models 34
5. Implementation of Models 38
6. Ring-plane Pole Solution 43
7. Comparison with Other Methods of Radius Determination 66
8. Pole precession 68
9. Non-circular Features 71
10. Ringlet Masses 92
11. Gravitational Harmonic Coefficients 99
12. B-Ring Features 111
13. Conclusions 117
Appendix A: Occultation Observations with the Hubble Space Telescope 122
Appendix B: Reprint of Elliot et al. (1993). 126
References 157

STELLAR OCCULTATION STUDIES OF SATURN'S RINGS WITH THE HUBBLE SPACE TELESCOPE

by

Amanda Sachie Bosh

Submitted to the Department of Earth, Atmospheric, and Planetary Sciences on
31 December 1993 in partial fulfillment of the requirements for the Degree of
Doctor of Philosophy in Earth, Atmospheric, and Planetary Sciences

ABSTRACT

Recent determinations of Saturn's ring-plane pole and radius scale incorporated subsets of currently available data (Elliot, *et al.* 1993. *Astron. J.* **106**, 2544-2572; French, *et al.* 1993. *Icarus* **103**, 163-214; Hubbard, *et al.* 1993. *Icarus* **103**, 215-234). We present a solution for Saturn's pole and radius scale using the following occultation data: (i) the 1991 occultation of GSC6323-01396, observed with the Hubble Space Telescope, (ii) the 1989 occultation of 28 Sgr, observed from 11 Earth-based sites, (iii) the 1981 occultation of δ Sco, observed with the photopolarimeter on Voyager 2, and (iv) the 1980 occultation of the Voyager 1 radio science signal, received at Earth. To these data, we fit a solar-system barycentric vector geometric model that includes in-track errors for Voyager (in the form of clock offsets), general relativistic bending by an oblate planet, and pole precession. Since the magnitude of errors in ring-plane radii calculated from this geometric model varies significantly across features, we employ a weighting scheme that assigns higher weights to those features with lower rms residuals. From these model fits, we find a ring plane pole position of $\alpha_p = 40.59287 \pm 0.00470$ degrees, $\delta_p = 83.53833 \pm 0.00022$ degrees at the Voyager 1 epoch, consistent with the results of all above-mentioned works.

We search for inclined rings and find none that are statistically significant. We also find one new feature that is probably non-circular: the inner edge of the C ring, feature 44. This feature appears to be freely precessing (due to Saturn's non-spherical gravity field). In modeling previously determined non-circular features, we find that models for the Titan and Maxwell ringlets agree well with previous models (Porco *et al.* 1984. *Icarus* **60**, 1-16). The center and inner edge of the 1.470 R_S ringlet appear circular, while the outer edge is best fit by a Prometheus 2:1 Lindblad resonant model. The outer edge of the 1.495 R_S ringlet is described by a superposition of Mimas 3:1 Lindblad resonance model and a freely precessing model. These two ringlets were previously thought to be purely freely precessing (Porco & Nicholson, 1987. *Icarus* **72**, 437-467), but now it appears that this is not the case. Despite the proximity of the inner edge of the 1.990 R_S ringlet to the Pandora

9:7 inner Lindblad resonance, this features appears to be freely precessing. The outer edges of the B and A rings were previously shown to be influenced by the Mimas 2:1 and Janus/Epimetheus 7:6 Lindblad resonances, respectively (Porco *et al.*, 1984. *Icarus* **60**, 17-28). We find that both ring edges fit best to a superposition of resonant and freely precessing models. However, residuals are still much larger than for any other ringlet, indicating that there may be other dynamics at work on these features. Finally, the Huygens ringlet is best described by a model that combines freely precessing and Mimas 2:1 Lindblad resonance models. This may be a result of the proximity of this ringlet to the B ring and the strong Mimas 2:1 resonance.

We combine constraints from the location of the Titan ringlet (in an apsidal resonance with Titan) and the measured precession rates of the Maxwell and 1.495 R_S ringlets with previously published constraints from Pioneer tracking data and satellite precession rate measurements (Null *et al.*, 1981. *Astron. J.* **86**, 456-468) to determine new values for Saturn's gravitational harmonics: $J_2 = (16301 \pm 6) \times 10^{-6}$, $J_4 = (-894 \pm 9) \times 10^{-6}$, and $J_6 = (124 \pm 5) \times 10^{-6}$ (for Saturn equatorial radius 60330 km). Values of higher-order harmonics are held fixed: $J_8 = -10 \times 10^{-6}$, $J_{10} = 2 \times 10^{-6}$, $J_{12} = -0.5 \times 10^{-6}$, $J_{14} = J_{16} = \cdots = 0$. The formal errors in these parameters are greatly reduced from those of Nicholson & Porco (1988, *J. Geophys. Res.* **93**, 10209-10224), particularly the error in J_6. J_6 is now determined precisely enough to provide a useful constraint on models of Saturn's interior. The value we find suggests that the interior may be in a state of complex rotation.

Thesis Supervisor: Professor James L. Elliot
Department of Earth, Atmospheric, and Planetary Sciences

1. INTRODUCTION

The study of planetary rings blossomed in the 1970's and 1980's, with the discovery of the Uranian rings (Elliot *et al.* 1977; Millis *et al.* 1977), the Jovian ring (Owen *et al.* 1979), and the Neptunian rings (Covault *et al.* 1986; Hubbard *et al.* 1986; Lane *et al.* 1989; Sicardy *et al.* 1991; Smith *et al.* 1989). Before this time, only one ring system was known, that of Saturn. All the recently-discovered ring systems share features with the Saturnian ring system: the ethereal Jovian ring resembles Saturn's E ring; the isolated Uranian rings resemble the plateaus in Saturn's C ring; and the Neptunian rings (sometimes called "ring arcs"), with their longitudinally variable optical depth, resemble the Encke gap ringlet. Therefore by studying Saturn's rings, we also gain an understanding of all other ring systems.

Through the study of ring kinematics, we hope to learn more about the current processes that produce the pattern of rings we now see, and to resolve the questions of their formation and evolution. There are several competing theories for the formation of rings, centering on the basic unknown: are the rings young or old? Harris (1984) discusses two theories for the formation of the rings: (i) they were formed at the same time as the planet and its satellites were formed, the remains of the circumplanetary disk which did not form a satellite, and (ii) they are the result of the disruption (collisional or tidal) of a previously existing satellite. More recently, Dones (1991) suggested a new explanation for the origin of the rings: they formed during a recent (within the last 10^8 years) tidal disruption of a Saturn-crossing Kuiper belt object or comet. Each of these theories takes into account the current structure of the rings and the forces acting on the rings that would cause them to fall into the planet (gravitational torques, radiation drag, micrometeoroid erosion, etc.) or to spread outward. Since there are many processes that would remove a ring in a short amount of time, the current existence of the rings must be explained by invoking either competing forces or a young age for the rings. Competing forces include shepherd satellites and resonances (Lindblad and vertical) with satellites (French *et al.* 1991). A young age for the rings requires a plentiful source of ring-forming material.

Recent evidence supporting Dones' theory for the formation of Saturn's rings include discoveries of several Kuiper belt candidates (Luu and Jewitt 1993; Luu and Jewitt 1992; Williams *et al.* 1993). A study of the dynamical stability of the Kuiper belt by Holman and Wisdom (1993) finds that perturbations by Neptune can cause objects with initial semimajor axes in the range 32 - 42 AU to have a close encounter with Neptune. Of these, approximately 17% are scattered into the inner solar system, becoming short period comets (Duncan *et al.* 1988). Although Duncan *et al.* do not give a value for the number becoming

Saturn-crossers, the percentage will be greater than 17%. This scattering by Neptune from the Kuiper belt provides a mechanism for the delivery of objects into Saturn-crossing orbits, as required by the Dones theory. The imminent encounter of comet P/Shoemaker-Levy 9 with Jupiter (Horanyi 1993; Shoemaker *et al.* 1993) shows that capture of comets by planets does occur in the solar system.

As attractive as the cometary origin theory for Saturn's rings appears, the true test of this theory will come from studies of ring kinematics. Can we find confinement mechanisms for the rings (evidence that they are old, primordial), or are they slowly creeping planet-ward at a rate of a few centimeters per year (Goldreich and Tremaine 1982) indicating a more recent origin? We cannot answer this question unless we understand the dynamical processes at work in the rings today. To do this, we first need good kinematic models for ring features.

In addition to providing clues about the history of the rings, the study of Saturn's rings also helps determine the interior structure of Saturn. Measurements of rates of apsidal precession for ring features leads to a determination of the values of the gravitational harmonic coefficients for the planet. These values of coefficients are determined by the gravity field of the planet, which is set by the planet's mass distribution. When used with knowledge of the composition and rotation rate of Saturn, these coefficients give us insight into the internal structure of Saturn.

To study the kinematics of ring features, to gain some insight into the dynamics responsible for them, we need high spatial-resolution (<~ 1 km) data of the rings spanning enough time to be able to determine the precession rates of features. These data can either be in the form of pictures from which we can obtain radii at a range of longitudes, or as a scan or cut through the rings at one location. This latter form of data is usually obtained as occultation light curves. By monitoring the intensity of a star as Saturn passes in front of it, we get a map of a line through the rings, at a resolution that may be limited by Fresnel diffraction ($\sqrt{\lambda D/2}$, where λ is the wavelength of the observations, and D is the distance from the receiver to the planet). Other factors that affect the resolution achievable from the ground are the star diameter and the signal-to-noise ratio (S/N) of the data. Ground-based occultation light curves are difficult to obtain because S/N is degraded through atmospheric scintillation (of a bright source—Saturn and its rings are very bright, with visual surface magnitude ~7), and often is the limiting source of noise, over photon noise from the occulted star and the ring background. For these reasons, ground-based observations rely on very bright stars. Unfortunately, bright stars tend to be large stars; if they subtend many tens of kilometers at the distance of Saturn, then the resultant light curve will again have degraded spatial resolution.

Two possible remedies for the paucity of Saturn occultation data are the Hubble Space Telescope (HST) and spacecraft near Saturn. The latter, such as Voyagers 1 and 2, are able to obtain high resolution data because the Fresnel scale (likely to be the limit to resolution for spacecraft) is smaller when nearer the planet. For example, at 2700 Å and 10^6 km from Saturn, the Fresnel scale is only 0.012 kilometers, compared with 0.4 kilometers at Earth. Therefore, occultations observed from spacecraft (or of spacecraft) are especially important. Unfortunately, they are also infrequent, as such missions are very expensive. Voyagers 1 and 2 provided two occultation data sets in 1980 and 1981 with two instruments. The next mission scheduled to visit Saturn, Cassini, will not reach the planet for several more years. The other space-based method, HST, initially held great promise (Elliot *et al.* 1993). Although the HST is not significantly closer to Saturn, it does have the advantages of smaller images than ground-based observations, being free of scintillation, and being able to observe at shorter wavelengths. The smaller images and the lack of scintillation means that the background noise will be lower, allowing the use of smaller apertures to reject more background light. These combine to lessen the amount of background noise and allows for the routine observation of stars many magnitudes fainter than are accessible from the ground. This means that more stars are occulted each year, and the data rate increases. Being able to observe at shorter wavelengths (into the near UV) means that for blue occultation stars, we can reduce the size of the Fresnel scale. For these reasons, the HST was well-suited for observations of occultations by Saturn. However, the main instrument for occultation observations aboard the HST, the High Speed Photometer (HSP) (Bless *et al.* 1992), was removed in December 1993 to make room for COSTAR, the instrument designed to compensate for the HST's spherical aberration (Brown and Ford 1991).

In 1980 and 1981, Voyagers 1 and 2 visited Saturn, the result of which was two excellent occultation light curves. In 1989, Saturn occulted 28 Sgr, an unusually bright (and red) star with V = 5.4 (Harrington *et al.* 1993). This event was observed at many locations on Earth (French *et al.* 1993; Harrington *et al.* 1993; Hubbard *et al.* 1993). And in 1991, Saturn occulted the considerably fainter GSC6323-01396 (V = 11.9) (Bosh and McDonald 1992). This event was observed with the HSP aboard the HST, only one month after the first rigorous Science Verification Test for the instrument (Elliot *et al.* 1993). In the following sections, we will use the data from these four occultations, in geometric and kinematic models Saturn's rings. Each data set has been previously analyzed separately, or with another data set. However, they have not yet been combined. Therefore, in Section 2 we give a brief overview of the data sets, and will mention sources of previous analyses. In Sections 3 and 4 we give the geometric and kinematic models used. We discuss practical issues of implementation in Section 5. We present results from combined data sets for pole position and radius scale in Section 6. In Section 7, we compare ring feature radii determined in this work with radii determined through other methods. We determine the rate of precession of Saturn's pole in Section 8. We search for new non-circular and inclined features in Section 9, and investigate kinematic models for non-circular features. In Section 10 we calculate the masses of two ringlets, the Titan and Maxwell ringlets. We determine values for Saturn's gravitational harmonics and discuss the implications on interior models in Section 11. In Section 12, we investigate the kinematics of features in the B ring. We summarize all results in Section 13. Finally, Appendix A presents a summary of our stellar occultation program using the HSP, and Appendix B is a reprint of a paper detailing the initial analysis of the HST data set.

2. DATA

For the analysis in this work, we used four data sets: (i) "HST", data from the occultation of GSC6323-01396 on 2-3 October 1991 and observed with the HSP on the HST, (ii) "28 Sgr", data from the occultation of the star 28 Sgr on 8 July 1989, observed from 11 fixed telescopes, (iii) "PPS", data from the occultation of δ Sco on 25 August 1981, observed with the Photopolarimeter (PPS) aboard Voyager 2, and (iv) "RSS", data from the occultation of the radio signal from Voyager 1, recorded at DSS-63 in Spain. Often the PPS and RSS data sets together are referred to as simply "Voyager" data. Recent works analyzed combinations of these data sets. Nicholson *et al.* (1990, hereafter referred to as NCP) combined PPS and RSS data to dramatically reduce the errors in the pole position and the ring radii. Hubbard *et al.* (1993, H93) used the 28 Sgr data to fit for the position of Saturn's ring plane pole, with ring radii fixed at the NCP values. French *et al.* (1993, F93) fit for pole position, ring radii, and Voyager trajectory offsets using 28 Sgr, PPS, and RSS data sets. They also report the first detection of the precession of Saturn's pole due mainly to solar torques on Titan transferred to Saturn. Elliot *et al.* (1993, E93, also included as Appendix B) combine HST and 28 Sgr data for the first solution independent of Voyager data. The HST data set is described in detail in E93, and the 28 Sgr data sets are described in F93, H93, and Harrington *et al.* (1993). The Voyager data sets are described in NCP and references therein.

Measured times of feature crossing for all features in the HST data set are listed in Table 3 of E93. Feature times from the Voyager data sets are given in Table II of F93. Times of circular features in the 28 Sgr data sets are listed in Tables III-VI of F93 and in Table III of H93. Times for non-circular features for all 28 Sgr data sets are not given in these sources; they are listed here in Tables 2.1 (immersion times) and 2.2 (emersion times) and in Table II of Harrington *et al.* (1993).

HST Data Set

Twice during October 1991, on 2-3 and again on 7-8, Saturn and its rings occulted the star GSC6323-01396. This unusual event occurred because Saturn was nearing its stationary point; therefore it occulted the same star on two separate occasions. The occultation of this star, cataloged in the HST Guide Star Catalog (STScI 1989), was predicted by Bosh and McDonald (1992) in 1991, shortly before the occultation date. Photometry of the star was reported by Sybert *et al.* (1992): V = 11.9, B–V = 0.7, V–R = 0.5. As this photometry shows, this star is quite faint—6 magnitudes fainter than 28 Sgr, so conventional visual ground-based observational techniques would surely have produced a light curve with vastly insufficient signal-to-noise to be useful. Instead, the first event of this extraordinary pair of occultations was observed using the HSP on the HST. Details of the planning and execution of this observation are given in E93. They also give times of feature crossings for all features identified, circular and non-circular.

Although this star was occulted twice by Saturn, only one of the emersion events was recorded. During this event the sky-plane velocity was very low, ~1 km s^{-1}, so the event velocity was controlled by the orbital velocity of the HST, and as a result the apparent route of the star through the rings was a looping path (see Fig. 4 in E93). Because the path crossed through some ring regions twice, some features were crossed twice during the HSP observations of this occultation. Locations of ring features measured in these data are indicated in Fig. 2.1 (similar to Fig. 8 of E93), which also shows the data obtained during these observations. For this figure, the approximate shape of the ring background was subtracted to highlight ring features. This subtraction was done for presentation only, and is not a rigorous subtraction of background signal.

28 Sgr Data Set

The occultation of 28 Sgr by Saturn in July 1989 was a rare event, because the occulted star was so bright. Because of this, it afforded an unusual opportunity to observe an occultation by Saturn from the ground, even in the visible, and still obtain a light curve of sufficient S/N to be useful for ring kinematic studies. Therefore, this event was observed from many fixed telescopes in North America, South America, and Hawaii. The highest-quality data sets are included in F93 and H93. Both of these works provide feature crossing times for all features presumed circular, but they do not list times for non-circular features. In this work, we incorporate non-circular feature times from five light curves obtained at Mt. Palomar (PAL), McDonald (MCD), the Infrared Telescope Facility (IRTF), and two European Southern Observatory telescopes (ESO1, ESO2).

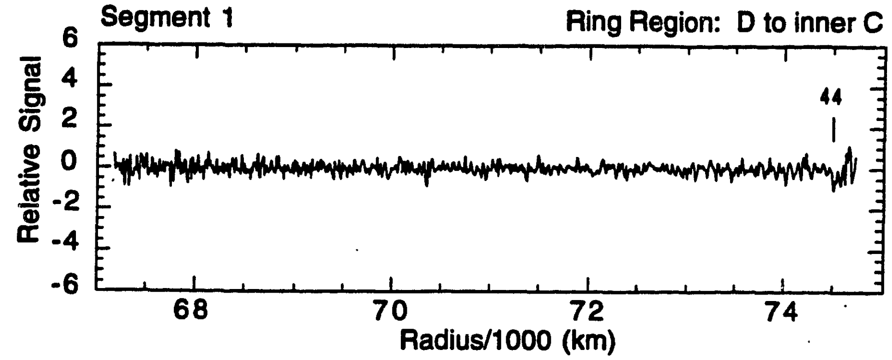
Segment 1
Ring Region: D to inner C
Relative Signal
6
4
2
0
-2
-4
-6
44
68
70
72
74
Radius/1000 (km)

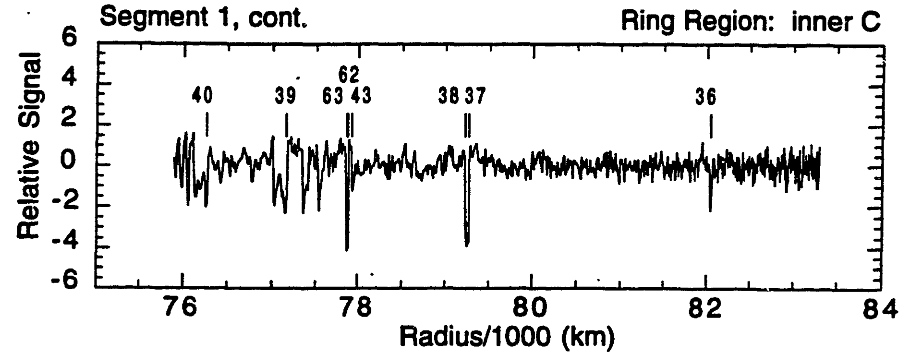
Segment 1, cont.
Ring Region: inner C
Relative Signal
6
4
2
0
-2
-4
-6
40
39
62
63 43
38 37
36
76
78
80
82
84
Radius/1000 (km)

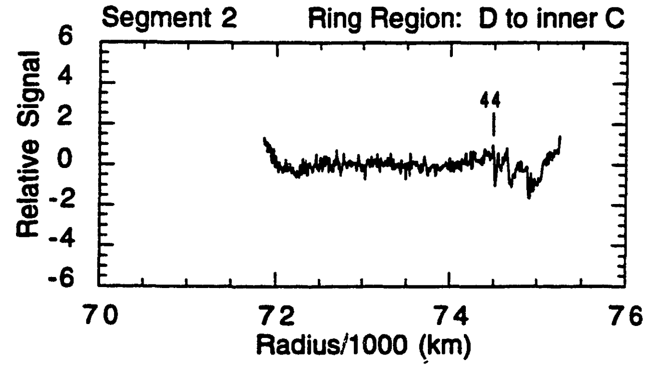
Segment 2
Ring Region: D to inner C
Relative Signal
6
4
2
0
-2
-4
-6
44
70
72
74
76
Radius/1000 (km)

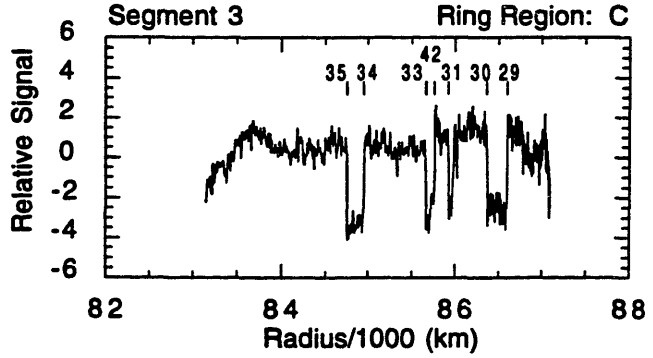
Segment 3
Ring Region: C
Relative Signal
6
4
2
0
-2
-4
-6
35
34
33
42
31
30
29
82
84
86
88
Radius/1000 (km)

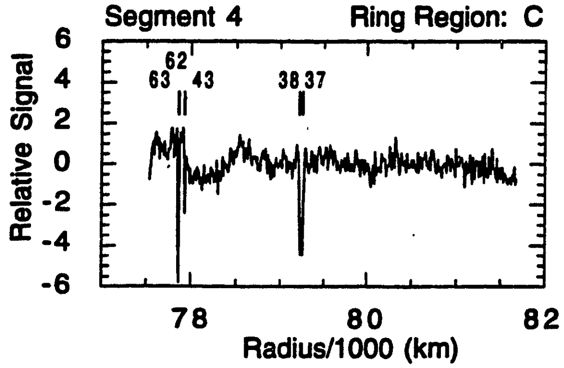
Segment 4
Ring Region: C
Relative Signal
Radius/1000 (km)
6
4
2
0
-2
-4
-6
78
80
82
62
63
43
38
37

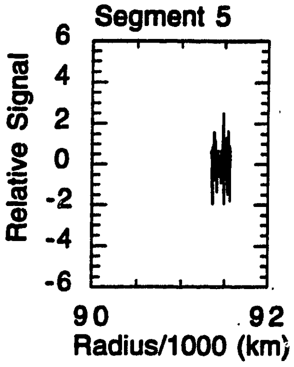
Segment 5
Relative Signal
Radius/1000 (km)
6
4
2
0
-2
-4
-6
90
92

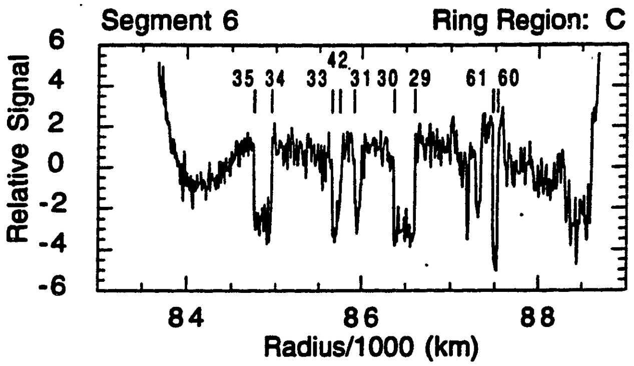
Segment 6
Ring Region: C
Relative Signal
Radius/1000 (km)
6
4
2
0
-2
-4
-6
84
86
88
35
34
33
42
31
30
29
61
60

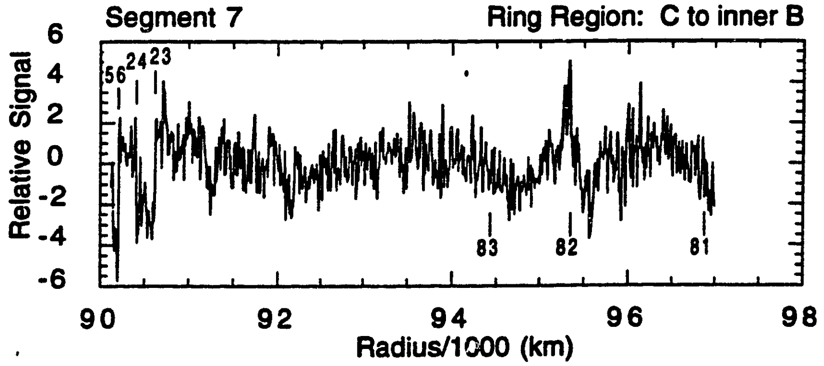
Segment 7
Ring Region: C to inner B
Relative Signal
Radius/1000 (km)
6
4
2
0
-2
-4
-6
90
92
94
96
98
56
24
23
83
82
81

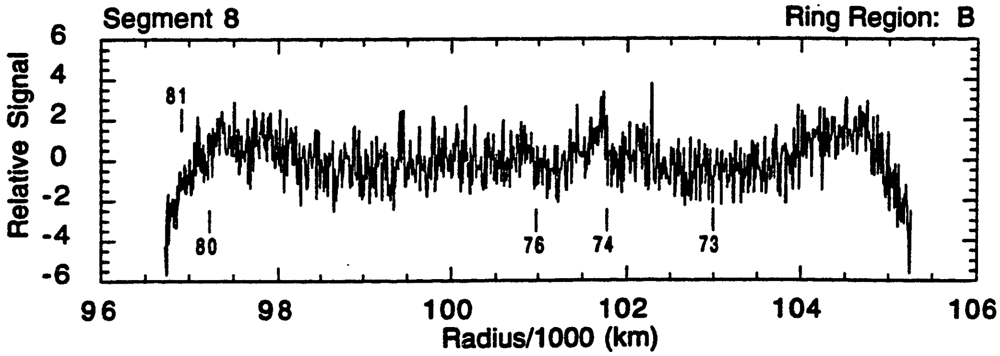
Segment 8
Ring Region: B
Relative Signal
Radius/1000 (km)
6
4
2
0
-2
-4
-6
96
98
100
102
104
106
81
80
76
74
73

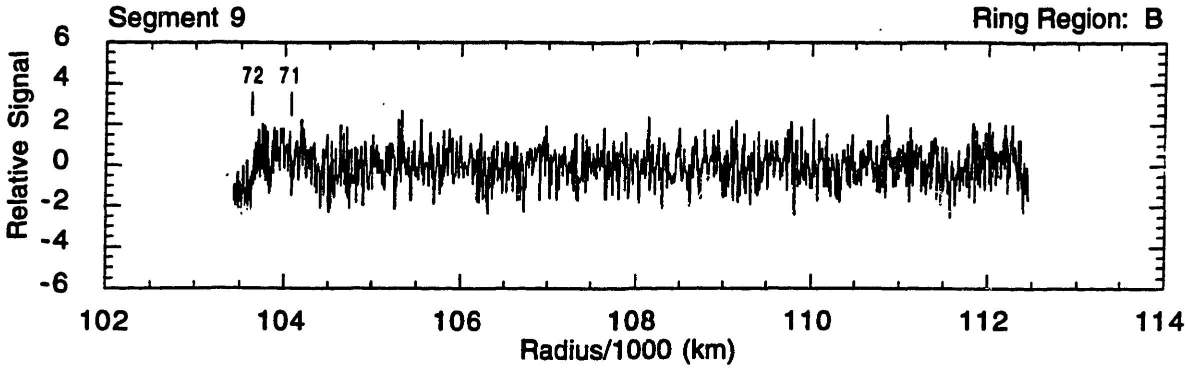
Segment 9 Ring Region: B

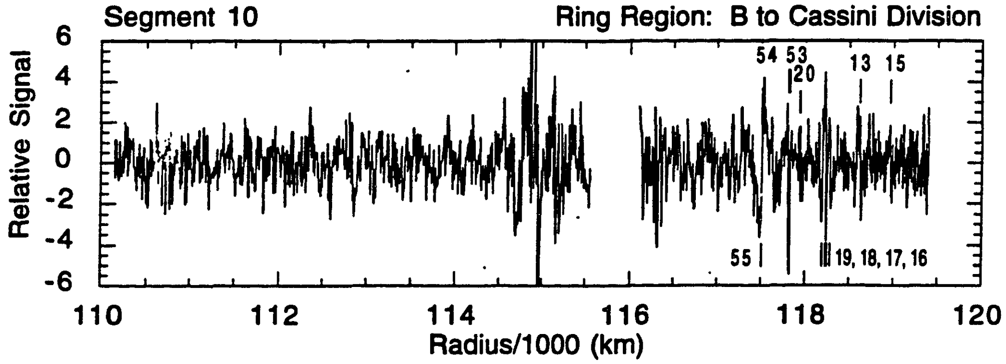
Segment 10 Ring Region: B to Cassini Division

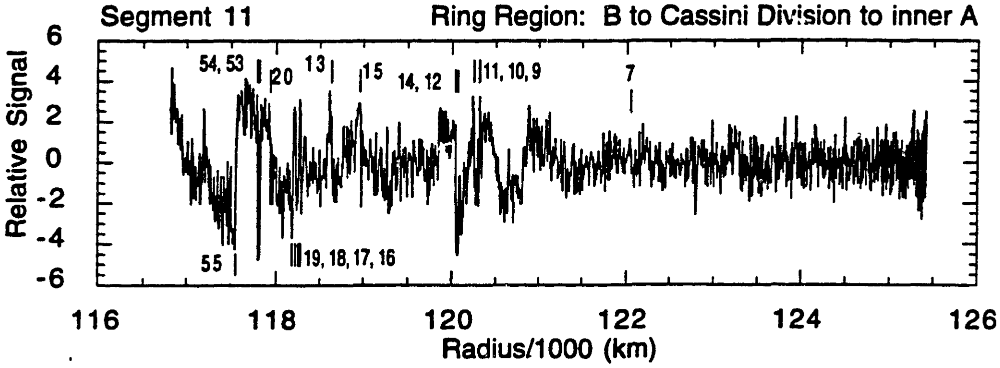
Segment 11 Ring Region: B to Cassini Division to inner A

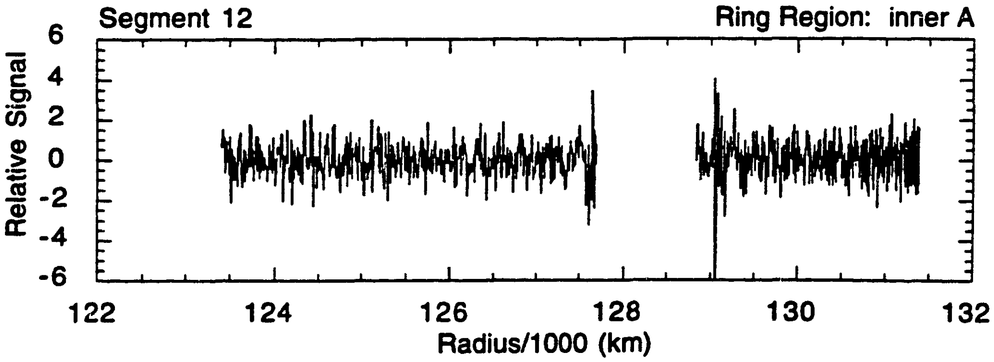
Segment 12 Ring Region: inner A

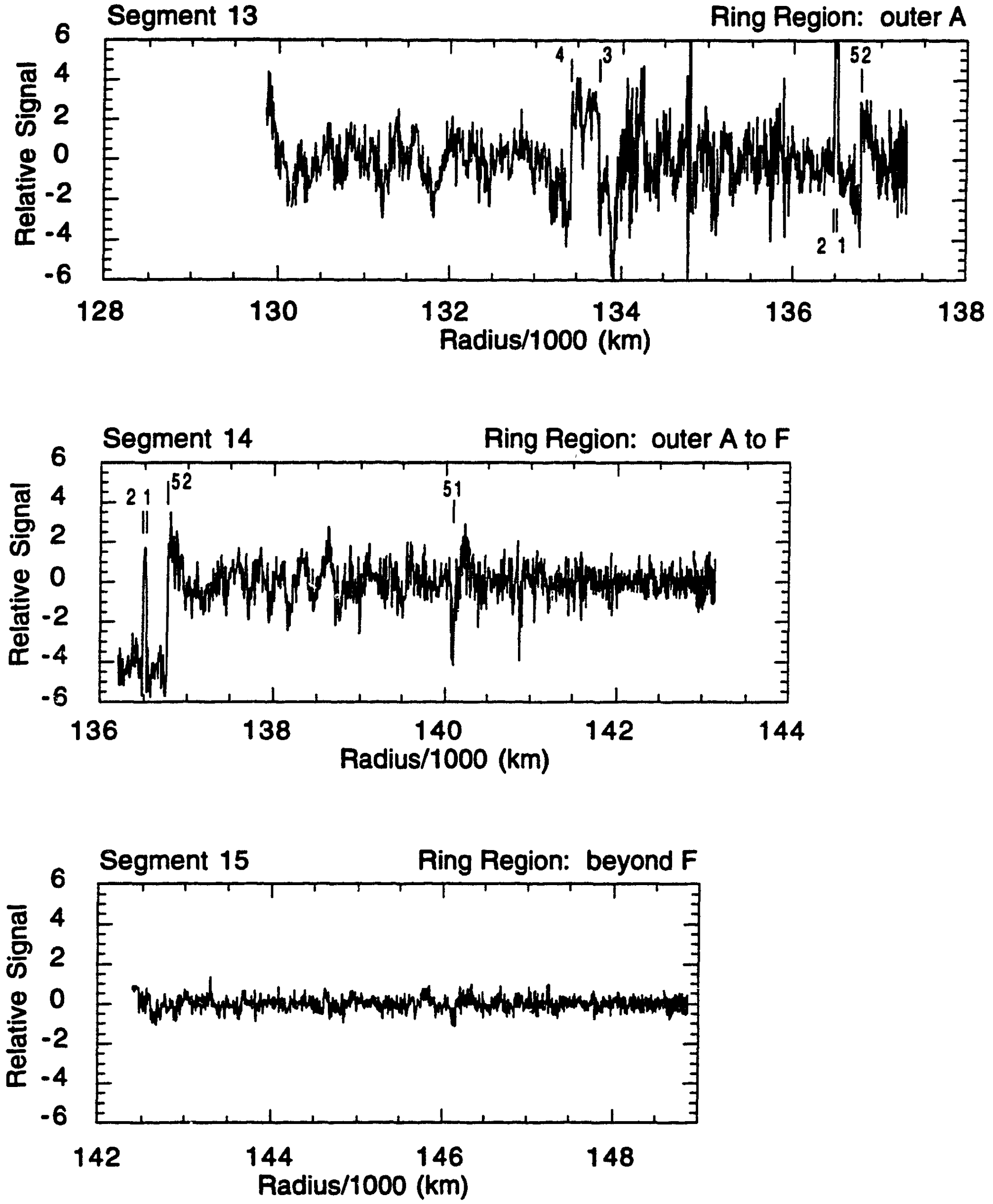

FIG. 2.1. Data from HSP observations at 7500 Å of occultation of GSC6323-01396 on 2-3 October 1991. Adapted from E93. The data were collected in 15 segments, broken by Earth occultations and passage of the HST through the South Atlantic Anomaly. Each plot is labeled with the segment number and the approximate location of the scan, in terms of the classical ring regions. For plotting purposes, the low-frequency component of each profile was filtered out to make the individual ring features more noticeable (see E93 for description of filtering process). This is not a rigorous subtraction of background signal. Unfortunately, this process sometimes makes sharp ring edges and features in high optical depth regions less visible (see segments 7-10).

Table 2.1. Non-Circular Feature Times, Immersion

	Feature times[a] (UTC, h m s), on 1989 7 3			
Feature[b]	ESO1	ESO2	MCD	PAL
52	6 04 13.94	6 04 13.91	6 01 18.59	6 02 05.46
9			6 13 34.47	
10			6 13 35.42	
110			6 13 36.60	
112	6 16 56.75		6 13 46.36	
14	6 16 57.62		6 13 47.24	
17			6 15 06.65	6 15 53.57
117			6 15 07.23	6 15 54.20
18			6 15 07.81	6 15 54.84
53	6 18 39.75	6 18 39.82	6 15 27.12	6 16 14.10
153	6 18 40.30	6 18 40.33	6 15 27.61	6 16 14.59
54	6 18 40.85	6 18 40.84	6 15 28.11	6 16 15.09
55	6 18 52.26	6 18 52.30	6 15 39.70	6 16 26.67
73		6 29 59.84	6 26 29.98	6 27 16.53
74		6 30 58.33	6 27 26.51	6 28 13.39
77			6 28 43.86	6 29 30.49
79	6 34 10.71	6 34 10.36	6 30 33.11	6 31 19.88
80			6 30 49.60	6 31 36.60
56			6 36 04.96	6 36 51.33
156			6 36 06.38	6 36 52.74
57			6 36 07.79	6 36 54.15
58			6 37 11.18	6 37 57.48
158			6 37 11.65	6 37 57.96
59			6 37 12.11	6 37 58.44
60	6 41 57.58	6 41 57.69	6 38 03.23	6 38 49.53
160	6 41 59.43		6 38 04.85	6 38 51.13
61	6 42 01.28		6 38 06.47	6 38 52.73
43				
62	6 49 34.51		6 45 19.43	6 46 05.13
162	6 49 35.04			6 46 05.65
63	6 49 35.56			6 46 06.17

[a] See text for definition of feature time.

[b] Feature number after F93. Features with designations > 100 are the midpoints of broad ring features. The designation is derived by adding 100 to the designation for the outer edge.

Table 2.2. Non-Circular Feature Times, Emersion

	Feature times[a] (UTC, h m s), on 1989 7 3			
Feature[b]	ES1	ES2	MCD	PAL
63	8 40 18.48	8 40 16.82	8 40 11.73	8 40 57.60
162	8 40 19.37		8 40 12.51	8 40 58.37
62	8 40 20.26		8 40 13.29	8 40 59.14
43				
61	8 47 54.51		8 47 25.69	8 48 10.16
160	8 47 55.83		8 47 26.80	8 48 11.23
60	8 47 57.15		8 47 27.90	8 48 12.30
59			8 48 21.01	8 49 05.29
158			8 48 21.42	8 49 05.70
58			8 48 21.82	8 49 06.10
57			8 49 25.87	
156			8 49 27.25	
56			8 49 28.63	
22				
80			8 54 43.89	8 55 28.34
79			8 55 02.44	8 55 45.65
77			8 56 52.23	8 57 34.79
74			8 58 10.09	8 58 52.08
73			8 59 06.69	8 59 49.23
55	9 11 19.00		9 10 02.18	9 10 42.38
54	9 11 33.23		9 10 15.08	9 10 55.23
153	9 11 33.76		9 10 15.59	9 10 55.72
53	9 11 34.28		9 10 16.11	9 10 56.22
18			9 10 33.71	9 11 13.79
117			9 10 34.30	9 11 14.37
17			9 10 34.89	9 11 14.95
14	9 13 16.38		9 11 55.13	9 12 34.90
112	9 13 17.16		9 11 55.86	9 12 35.65
110				
10				
9				
52	9 26 11.16		9 24 29.50	9 25 06.88

[a] See text for definition of feature time.

[b] Feature number after F93. Features with designations > 100 are the midpoints of broad ring features. The designation is derived by adding 100 to the designation for the outer edge.

PPS and RSS Data Sets

The RSS occultation occurred on 13 November 1980, after the close approach of Voyager 1 to Saturn. The PPS occultation occurred on 25 August 1981, before the close approach of Voyager 2 to Saturn. Both data sets are described in NCP; times of feature crossing for both circular and non-circular features are provided in this reference as well.

3. MODEL FOR GEOMETRIC ANALYSIS OF OCCULTATION DATA

Previous Models

In E93, we developed a solar-system barycentric, planet-plane formulation for the geometric analysis of occultation data. The advantage of this method over previous "sky-plane" treatments (Elliot *et al.* 1978) is that the direction of the occulted star remained constant (if proper motion and parallax are small enough to be ignored), thereby freeing us from "perspective" corrections (Elliot *et al.* 1978). Here, we present a solar-system barycentric, vector method for the geometric analysis of stellar occultation data. In addition, we generalize this to apply to occultations where the source is a nearby spacecraft instead of a star. This generalization can also apply to stars with non-negligible proper motions and parallaxes. This formulation is similar to the model of F93. Because these models are comparable but are numerically implemented in different languages, they provide important cross-checks for each other. The vector model described here has the advantage of being able to easily include considerations for spacecraft occultations (where the spacecraft is the source, as well as where it is the receiver) and for non-equatorial rings.

Basic Vector Equations

The goal of the geometric modeling is to calculate the magnitude of the vector from the planet center to the feature, $\mathbf{r}_{\mathrm{pf}}$, from physical ephemerides and the time the occulted signal arrived at the observer. Through this calculation, we convert observed feature occultation times to corresponding ring-plane radii. Much of the development of equations for this quantity are given in E93. However, the relevant equations will be repeated here for the derivation of the vector formulation. The expression for the vector from the planet center, "p", to the feature, "f", at the time the signal intersected the feature, t_{f}, is given by the difference between vectors from the solar system barycenter to the feature, $\mathbf{r}_{\mathrm{f}}$, and from the solar system barycenter to the planet center, $\mathbf{r}_{\mathrm{p}}$:

$$\mathbf{r}_{\mathrm{pf}}(t_{\mathrm{f}}) = \mathbf{r}_{\mathrm{f}}(t_{\mathrm{f}}) - \mathbf{r}_{\mathrm{p}}(t_{\mathrm{f}}) \tag{3.1}$$

Vectors with a single subscript are understood to originate at the solar-system barycenter. The solar-system barycentric position of the occulting body is calculated from appropriate ephemerides. Normally, this is calculated from ephemerides for the planet-system barycenter (with respect to the solar-system barycenter), $\mathbf{r}_{\mathrm{b}}$, and from planet-system barycentric ephemerides for all satellites in the system, $\mathbf{r}_{\mathrm{b}j}$, scaled by the ratio of satellite mass M_j to planet mass M_{p}:

$$\mathbf{r}_\mathrm{p}(t) = \mathbf{r}_\mathrm{b}(t) - \sum_{j}^{\textit{all satellites}} \frac{M_j}{M_\mathrm{p}} \mathbf{r}_{\mathrm{b}j}(t) \tag{3.2}$$

We cannot yet calculate $\mathbf{r}_\mathrm{pf}$ because we do not know the time the light ray intercepted the feature or $\mathbf{r}_\mathrm{f}(t_\mathrm{f})$. Therefore, we rewrite Eq. (3.1) by adding and subtracting the vector from the solar system barycenter to the receiver, $\mathbf{r}_\mathrm{r}$, calculated at the time the signal was received, t_r:

$$\mathbf{r}_\mathrm{pf}(t_\mathrm{f}) = \left[\mathbf{r}_\mathrm{f}(t_\mathrm{f}) - \mathbf{r}_\mathrm{r}(t_\mathrm{r})\right] - \left[\mathbf{r}_\mathrm{p}(t_\mathrm{f}) - \mathbf{r}_\mathrm{r}(t_\mathrm{r})\right] \tag{3.3}$$

The most convenient form for the vector $\mathbf{r}_\mathrm{r}$ depends on the format of the observer ephemeris. In the case of a spacecraft such as Voyager as the observer, $\mathbf{r}_\mathrm{r}$ is the simplest form. However, for the HST and for ground-based observatories, a more convenient form is found by writing it as the sum of the vector from the solar system barycenter to the Earth center, $\mathbf{r}_\mathrm{e}$, and the geocentric vector to the receiver, $\mathbf{r}_\mathrm{er}$:

$$\mathbf{r}_\mathrm{r}(t) = \mathbf{r}_\mathrm{e}(t) + \mathbf{r}_\mathrm{er}(t) \tag{3.4}$$

Next we redefine the right-hand side of Eq. (3.3) in terms of vectors from the receiver to the planet center and from the receiver to the feature:

$$\mathbf{r}_\mathrm{rp}(t_\mathrm{r}, t_\mathrm{f}) = \mathbf{r}_\mathrm{p}(t_\mathrm{f}) - \mathbf{r}_\mathrm{r}(t_\mathrm{r}) \tag{3.5}$$

$$\mathbf{r}_\mathrm{rf}(t_\mathrm{r}, t_\mathrm{f}) = \mathbf{r}_\mathrm{f}(t_\mathrm{f}) - \mathbf{r}_\mathrm{r}(t_\mathrm{r}) \tag{3.6}$$

These vectors are "non-simultaneous" vectors. For example, $\mathbf{r}_\mathrm{rf}(t_\mathrm{r}, t_\mathrm{f})$ is the vector originating at the receiver at time t_r (the time the occulted signal was received by the observer) and terminating at the feature at time t_f. Thus $\mathbf{r}_\mathrm{rf}$ is opposite in sign from the actual direction of signal propagation. Now we form another relation for the receiver-feature vector. This vector is in the apparent direction of the star; it is in the apparent direction and not the true direction because the stellar signal is deflected by the planet's gravitational field as it passed the planet. This is referred to as general relativistic (GR) bending. Therefore, we write $\mathbf{r}_\mathrm{rf}(t_\mathrm{r}, t_\mathrm{f})$ as:

$$\begin{aligned} \mathbf{r}_\mathrm{rf}(t_\mathrm{r}, t_\mathrm{f}) &= \mathbf{r}_\mathrm{f}(t_\mathrm{f}) - \mathbf{r}_\mathrm{r}(t_\mathrm{r}) \\ &= d_\mathrm{rf}(t_\mathrm{r}, t_\mathrm{f})\left(\hat{\mathbf{r}}_\mathrm{s} + \delta\mathbf{r}_\mathrm{s}\right) \end{aligned} \tag{3.7}$$

where $\hat{\mathbf{r}}_\mathrm{s}$ is the true direction to the source, unaffected by GR bending (and viewed from the location the ray would have intersected the observer if there were no GR bending) and $\delta\mathbf{r}_\mathrm{s}$ is the amount of GR deflection. The distance between the receiver and the feature is denoted by d_rf, and is the magnitude of $\mathbf{r}_\mathrm{rf}$. Here, we assume that the source position is constant. Later, we expand this for a moving source. Using Eqs. (3.3, 3.5-3.7), we form a more convenient relation for $\mathbf{r}_{\mathrm{pf}}(t_{\mathrm{f}})$:

$$\mathbf{r}_{\mathrm{pf}}(t_{\mathrm{f}}) = -\mathbf{r}_{\mathrm{rp}}(t_{\mathrm{r}},t_{\mathrm{f}}) + d_{\mathrm{rf}}(t_{\mathrm{r}},t_{\mathrm{f}})\,(\hat{\mathbf{r}}_{\mathrm{s}} + \delta\mathbf{r}_{\mathrm{s}}) \tag{3.8}$$

From the fact that the vector $\mathbf{r}_{\mathrm{pf}}$ is orthogonal to the ring-plane pole we can determine the receiver-feature distance. To do this, we take the dot product of both sides of Eq. (3.8) with the pole of the ring feature, $\hat{\mathbf{n}}_{\mathrm{r}}$. (If the features are not inclined, this becomes the ring plane pole, $\hat{\mathbf{n}}_{\mathrm{p}}$.) Using the fact that $\mathbf{r}_{\mathrm{pf}}$ is orthogonal to the feature pole, and rearranging to solve for $d_{\mathrm{rf}}(t_{\mathrm{r}},t_{\mathrm{f}})$ we find the following equation:

$$d_{\mathrm{rf}}(t_{\mathrm{r}},t_{\mathrm{f}}) = \frac{\mathbf{r}_{\mathrm{rp}}(t_{\mathrm{r}},t_{\mathrm{f}})\cdot\hat{\mathbf{n}}_{\mathrm{r}}}{(\hat{\mathbf{r}}_{\mathrm{s}} + \delta\mathbf{r}_{\mathrm{s}})\cdot\hat{\mathbf{n}}_{\mathrm{r}}} \tag{3.9}$$

One quantity still unknown in these equations is the feature crossing time, t_{f}. This time is equal to the received time backdated for the time it took the signal to travel the distance between the receiver and feature. The equation for t_{f} is as follows, where c is the speed of light:

$$t_{\mathrm{f}} = t_{\mathrm{r}} - \frac{d_{\mathrm{rf}}(t_{\mathrm{r}},t_{\mathrm{f}})}{c} \tag{3.10}$$

Eqs. (3.8-3.10) are used to iterate on a self-consistent light-travel time and receiver-feature vector.

The equations for the amount of GR bending, $\delta\mathbf{r}_{\mathrm{s}}$, are given in H93 but will be repeated here in our notation. The amount that the starlight is deflected depends on the distance of closest approach of the ray to the planet. This closest approach vector, ρ, is the perpendicular distance between the ray and the planet:

$$\begin{aligned}\rho &= D(\hat{\mathbf{r}}_{\mathrm{s}} + \delta\mathbf{r}_{\mathrm{s}}) + \mathbf{r}_{\mathrm{r}}(t_{\mathrm{r}}) - \mathbf{r}_{\mathrm{p}}(t_{\mathrm{f}})\\ &= -\mathbf{r}_{\mathrm{rp}}(t_{\mathrm{r}},t_{\mathrm{f}}) + D(\hat{\mathbf{r}}_{\mathrm{s}} + \delta\mathbf{r}_{\mathrm{s}})\end{aligned} \tag{3.11}$$

The distance D is the projection of the receiver-planet vector onto the bent star direction.

$$D = \mathbf{r}_{\mathrm{rp}}(t_{\mathrm{r}},t_{\mathrm{f}})\cdot(\hat{\mathbf{r}}_{\mathrm{s}} + \delta\mathbf{r}_{\mathrm{s}}) \tag{3.12}$$

Here we make the approximation that $(\hat{\mathbf{r}}_{\mathrm{s}} + \delta\mathbf{r}_{\mathrm{s}})$ is a unit vector. It is easiest to derive the components of the bending in coordinates that are aligned with the planet's pole direction. The bending is broken up into its component perpendicular and parallel to the projection of planet's spin axis on the plane of the sky (u,v—see E93 for the definition of this and other coordinate systems).

We then use the H93 definition of the angular deflection of the light ray:

$$\delta \mathbf{r}_{\mathrm{s}}\Big|_{uvw} = \mathrm{K}\frac{4GM_{\mathrm{p}}}{c^2\rho^2}\begin{bmatrix} u(t_{\mathrm{f}})\left(1 - J_2 R_{\mathrm{p}}^2 \cos^2 B_{\mathrm{s}} \dfrac{3v(t_{\mathrm{f}})^2 - u(t_{\mathrm{f}})^2}{\rho^4}\right) \\ v(t_{\mathrm{f}})\left(1 + J_2 R_{\mathrm{p}}^2 \cos^2 B_{\mathrm{s}} \dfrac{3u(t_{\mathrm{f}})^2 - v(t_{\mathrm{f}})^2}{\rho^4}\right) \\ 0 \end{bmatrix} \tag{3.13}$$

where J_2 is the second-order gravitational harmonic, u and v are the components of ρ, and

$$\rho = \sqrt{u^2 + v^2} \tag{3.14}$$

We rotate this deflection back into whatever coordinate system we are working in to get the resulting equation for $\delta \mathbf{r}_{\mathrm{s}}$.

Coordinate Systems

All quantities in this model are input in the J2000.0 *XYZ* rectangular coordinate system (USNO 1992). To convert between this and the planet-centered *uvw* system needed for the GR bending calculation, we utilize an intermediate "shadow-plane" coordinate system, *fgh*, which was defined in E93. This rectangular coordinate system is in the planet-shadow plane (defined to be perpendicular to the star direction, through the center of the Earth) and is centered on the shadow. E93 define $\mathbf{R}_1$, a matrix for rotating from *XYZ* to *fgh* that uses the right ascension and declination of the occulted star, α_{s} and δ_{s}:

$$\mathbf{R}_1 \equiv \mathbf{R}_{XYZ\to fgh} = \begin{bmatrix} \hat{\mathbf{f}}\cdot\hat{\mathbf{X}} & \hat{\mathbf{f}}\cdot\hat{\mathbf{Y}} & \hat{\mathbf{f}}\cdot\hat{\mathbf{Z}} \\ \hat{\mathbf{g}}\cdot\hat{\mathbf{X}} & \hat{\mathbf{g}}\cdot\hat{\mathbf{Y}} & \hat{\mathbf{g}}\cdot\hat{\mathbf{Z}} \\ \hat{\mathbf{h}}\cdot\hat{\mathbf{X}} & \hat{\mathbf{h}}\cdot\hat{\mathbf{Y}} & \hat{\mathbf{h}}\cdot\hat{\mathbf{Z}} \end{bmatrix} = \begin{bmatrix} -\sin\alpha_{\mathrm{s}} & \cos\alpha_{\mathrm{s}} & 0 \\ -\cos\alpha_{\mathrm{s}}\sin\delta_{\mathrm{s}} & -\sin\alpha_{\mathrm{s}}\sin\delta_{\mathrm{s}} & \cos\delta_{\mathrm{s}} \\ \cos\alpha_{\mathrm{s}}\cos\delta_{\mathrm{s}} & \sin\alpha_{\mathrm{s}}\cos\delta_{\mathrm{s}} & \sin\delta_{\mathrm{s}} \end{bmatrix} \tag{3.15}$$

From here, we convert to the *uvw*, "planet-plane" coordinate system (E93). This system is centered on the planet, with the *u* axis parallel to the major axes of apparent ring ellipses (as seen from the geocenter), the *v* axis parallel to the minor axes, and the *w* axis in the direction of the star. The rotation matrix for this conversion is $\mathbf{R}_2$:

$$\mathbf{R}_2 \equiv \mathbf{R}_{fgh\to uvw} = \begin{bmatrix} \hat{\mathbf{u}}\cdot\hat{\mathbf{f}} & \hat{\mathbf{u}}\cdot\hat{\mathbf{g}} & \hat{\mathbf{u}}\cdot\hat{\mathbf{h}} \\ \hat{\mathbf{v}}\cdot\hat{\mathbf{f}} & \hat{\mathbf{v}}\cdot\hat{\mathbf{g}} & \hat{\mathbf{v}}\cdot\hat{\mathbf{h}} \\ \hat{\mathbf{w}}\cdot\hat{\mathbf{f}} & \hat{\mathbf{w}}\cdot\hat{\mathbf{g}} & \hat{\mathbf{w}}\cdot\hat{\mathbf{h}} \end{bmatrix} = \begin{bmatrix} \cos P_\mathrm{s} & -\sin P_\mathrm{s} & 0 \\ \sin P_\mathrm{s} & \cos P_\mathrm{s} & 0 \\ 0 & 0 & 1 \end{bmatrix} \tag{3.16}$$

Here, we make use of one of three angles commonly used to describe planet pole orientations as well as ring and satellite orbits. These three angles are P_s, the position angle of the minor axis of the apparent ring ellipse; B_s, the planetocentric latitude of the Earth; and U_s, the geocentric longitude of the star, measured in the planet's equatorial plane (Rohde and Sinclair 1992).

$$\sin B_\mathrm{s} = -\sin\delta_\mathrm{n}\sin\delta_\mathrm{s} - \cos\delta_\mathrm{n}\cos\delta_\mathrm{s}\cos(\alpha_\mathrm{s}-\alpha_\mathrm{n}) \tag{3.17}$$

$$\begin{aligned} \cos B_\mathrm{s}\cos P_\mathrm{s} &= +\sin\delta_\mathrm{n}\cos\delta_\mathrm{s} - \cos\delta_\mathrm{n}\sin\delta_\mathrm{s}\cos(\alpha_\mathrm{s}-\alpha_\mathrm{n}) \\ \cos B_\mathrm{s}\sin P_\mathrm{s} &= -\cos\delta_\mathrm{n}\sin(\alpha_\mathrm{s}-\alpha_\mathrm{n}) \end{aligned} \tag{3.18}$$

$$\begin{aligned} \cos B_\mathrm{s}\cos U_\mathrm{s} &= \cos\delta_\mathrm{s}\sin(\alpha_\mathrm{s}-\alpha_\mathrm{n}) \\ \cos B_\mathrm{s}\sin U_\mathrm{s} &= \sin\delta_\mathrm{s}\cos\delta_\mathrm{n} - \cos\delta_\mathrm{s}\sin\delta_\mathrm{n}\cos(\alpha_\mathrm{s}-\alpha_\mathrm{n}) \end{aligned} \tag{3.19}$$

In the above equations, α_s and δ_s are the right ascension and declination of the star (in J2000.0), and α_n and δ_n are the right ascension and declination of the planet pole (also in J2000.0).

The last rotation to be presented here is that from *uvw* to *xyz*, the planet's equatorial coordinate system. This system is centered on the planet, with the *z* axis in the direction of the planet's pole (spin axis), the *x* axis is the intersection of the planet's equatorial plane with the Earth's J2000.0 equatorial plane, and the *y* axis is orthogonal. Note that the *xyz* coordinate system does not describe the ring plane if the ring is inclined. This rotation uses $\mathbf{R}_3$:

$$\mathbf{R}_3 \equiv \mathbf{R}_{uvw\to xyz} = \begin{bmatrix} \hat{\mathbf{x}}\cdot\hat{\mathbf{u}} & \hat{\mathbf{x}}\cdot\hat{\mathbf{v}} & \hat{\mathbf{x}}\cdot\hat{\mathbf{w}} \\ \hat{\mathbf{y}}\cdot\hat{\mathbf{u}} & \hat{\mathbf{y}}\cdot\hat{\mathbf{v}} & \hat{\mathbf{y}}\cdot\hat{\mathbf{w}} \\ \hat{\mathbf{z}}\cdot\hat{\mathbf{u}} & \hat{\mathbf{z}}\cdot\hat{\mathbf{v}} & \hat{\mathbf{z}}\cdot\hat{\mathbf{w}} \end{bmatrix} = \begin{bmatrix} -\sin U_\mathrm{s} & \sin B_\mathrm{s}\cos U_\mathrm{s} & \cos B_\mathrm{s}\cos U_\mathrm{s} \\ \cos U_\mathrm{s} & \sin B_\mathrm{s}\sin U_\mathrm{s} & \cos B_\mathrm{s}\sin U_\mathrm{s} \\ 0 & \cos B_\mathrm{s} & -\sin B_\mathrm{s} \end{bmatrix} \tag{3.20}$$

Offsets & Corrections

The previous sections give the basic vector description of the geometry of occultations, and rotation matrices for converting among coordinate systems. A part of the model not yet included are offsets to the planetary ephemeris, the observer ephemeris, the star position, the receiver clock, and the planet pole direction. The planetary-ephemeris offset from the actual planet center, p, to the ephemeris value for this, p', is given by

$$\mathbf{r}_{\mathrm{pp}'}(t_f)\Big|_{XYZ} = \begin{bmatrix} X_{\mathrm{pp}'} \\ Y_{\mathrm{pp}'} \\ Z_{\mathrm{pp}'} \end{bmatrix} = \mathbf{R}_1^{-1}\mathbf{r}_{\mathrm{pp}'}(t_f)\Big|_{fgh} = \mathbf{R}_1^{-1}\begin{bmatrix} f_o \\ g_o \\ h_o \end{bmatrix} \tag{3.21}$$

The quantities f_o and g_o were used is previous analyses of occultation data for the planetary ephemeris offset. The offset in the direction of the planet, h_o—a range offset, is zero. The observer-ephemeris offset from the actual position of the observer, r, to the ephemeris value, r', is similarly given by:

$$\mathbf{r}_{\mathrm{rr}'}(t_r)\Big|_{XYZ} = \begin{bmatrix} X_{\mathrm{rr}'} \\ Y_{\mathrm{rr}'} \\ Z_{\mathrm{rr}'} \end{bmatrix} \tag{3.22}$$

The star position offset is as follows. The "s" subscript refers to the actual star direction which is the sum of the catalogue star direction (s') and a correction term (o). The correction term is an offset in right ascension and declination of the star position, given in arc seconds.

$$\alpha_s = \alpha_{s'} - \alpha_o \tag{3.23}$$

$$\delta_s = \delta_{s'} - \delta_o \tag{3.24}$$

The true time is expressed as a function of the received clock time, t_c, and an offset, t_o:

$$t = t_c - t_o \tag{3.25}$$

The offset to the planet pole direction arises due to planetary precession. As an approximation (sufficient for these analyses), we express this in terms of a linear pole precession rate, in both right ascension ($\dot{\alpha}_n$) and declination ($\dot{\delta}_n$):

$$\begin{aligned} \alpha_n &= \alpha_n(t) = \alpha_n(t_n) + \dot{\alpha}_n(t - t_n) \\ \delta_n &= \delta_n(t) = \delta_n(t_n) + \dot{\delta}_n(t - t_n) \end{aligned} \tag{3.26}$$

where t_n is the reference epoch for the position of the pole.

Numerical Implementation of Vector Equations: Fitting in Radius

To perform the model calculation, we calculate $\mathbf{r}_{\mathrm{pf}}$ from Eq. (3.8). To do this, we calculate quantities in the *XYZ* coordinate system described above. To make this model calculation faster, we separate it into two parts. First, the term $\mathbf{r}_{\mathrm{rp}}(t_{\mathrm{r}},t_{\pi})$ is calculated for all feature measurements, and these quantities are stored in a file. The time t_{π} is the time the light ray passed through the planet plane. The vector $\mathbf{r}_{\mathrm{rp}}$ is calculated at this time instead of at t_{f} because t_{f} is not known until after the iteration is performed. When the calculation is split in this way, a small approximation is introduced because the value of t_{π} depends on the star position. If the star position is later altered (through fitting for a star position offset), the previous determination of t_{π} is no longer exact. The intermediate file is read in, and then the calculation continues with the iteration for t_{f} and for the second term in Eq. (3.8). Incorporating this break in the calculation and the previously described offsets into the equation for the vector between the feature and the planet center, we get:

$$\mathbf{r}_{\mathrm{rp}}(t_{\mathrm{r}},t_{\mathrm{f}}) = \mathbf{r}_{\mathrm{r'p'}}(t_{\mathrm{r}},t_{\pi}) - \mathbf{r}_{\mathrm{pp'}}(t_{\mathrm{f}}) - \mathbf{r}_{\mathrm{rr'}}(t_{\mathrm{r}}) + t_{\mathrm{o}}\dot{\mathbf{r}}_{\mathrm{rp}}(t_{\mathrm{r}},t_{\mathrm{f}}) + (t_{\mathrm{f}} - t_{\pi})\dot{\mathbf{r}}_{\mathrm{p}}(t_{\pi}) \tag{3.27}$$

Two iteration loops are involved in this calculation: one for the time t_{f}, and one for the amount of GR bending, $\delta\mathbf{r}_{\mathrm{s}}$. After these loops are completed, we have the feature vector, $\mathbf{r}_{\mathrm{pf}}$. From this, we calculate the observed feature radius (scalar) and the observed feature longitude, θ_{f}:

$$\mathbf{r}_{\mathrm{pf}}\Big|_{xyz} = \mathbf{R}_3 \cdot \mathbf{R}_2 \cdot \mathbf{R}_1 \cdot \mathbf{r}_{\mathrm{pf}}\Big|_{XYZ} \tag{3.28}$$

$$r_{\mathrm{pf}}(t_{\mathrm{f}}) = \left|\mathbf{r}_{\mathrm{pf}}(t_{\mathrm{f}})\right| = \sqrt{x_{\mathrm{f}}^2(t_{\mathrm{f}}) + y_{\mathrm{f}}^2(t_{\mathrm{f}}) + z_{\mathrm{f}}^2(t_{\mathrm{f}})} \tag{3.29}$$

$$\begin{aligned} \sin\theta_{\mathrm{f}}(t_{\mathrm{f}}) &= y_{\mathrm{f}}(t_{\mathrm{f}})/r_{\mathrm{pf}}(t_{\mathrm{f}}) \\ \cos\theta_{\mathrm{f}}(t_{\mathrm{f}}) &= x_{\mathrm{f}}(t_{\mathrm{f}})/r_{\mathrm{pf}}(t_{\mathrm{f}}) \end{aligned} \tag{3.30}$$

In the above equations, r_{pf} is the scalar radius of the feature, and $\{x_{\mathrm{f}},y_{\mathrm{f}},z_{\mathrm{f}}\}$ are the coordinates of that feature in the *xyz* coordinate system. Although these coordinates have only a single subscript, their origin is the center of the planet, since that is the origin of the *xyz* coordinate system. The feature longitude, θ_{f}, is measured east from the ascending node of the intersection of the Earth's equatorial plane for J2000.0 with the planet's equatorial plane.

When using this model in a least-squares fit for model parameters, the usual method is to fit in radius. For this method, the observed feature radius given in Eq. (3.29) is compared against the model radius. The other fitting method, fitting in time (described next), is more closely related to the measured quantities: observed times of feature crossings. These are compared against times predicted by the model. As discussed in E93, fitting in time is an appropriate method if the errors in the feature times followed a Gaussian distribution. However, when the models for the features are a non-negligible source of error (as they are here), then fitting in radius may be the better approach. In E93, we tried both methods for several fits. Both methods produced results that differed by less than one formal error. In E93, as here, we use the method of fitting in radius as our standard method. Further tests are not performed in this work.

Numerical Implementation of Vector Equations: Fitting in Time

When fitting in time rather than in radius, we need to calculate a model time, t_{m}, that we compare with the observed time, t_{r}. This quantity is given in E93, and the relation is reproduced here:

$$t_{\mathrm{m}} = t_{\mathrm{f}} - \frac{r_{\mathrm{pf}}(t_{\mathrm{f}}) - a_{\mathrm{f}}}{\dot{r}_{\mathrm{pf}}(t_{\mathrm{f}})} \tag{3.31}$$

Therefore, in order to calculate the model time, we need the time derivative of the feature-radius vector, $\dot{\mathbf{r}}_{\mathrm{pf}}(t_{\mathrm{f}})$. We get this quantity by taking the time derivative of Eq. (3.8), which defines $\mathbf{r}_{\mathrm{pf}}(t_{\mathrm{f}})$.

$$\begin{aligned}\frac{\partial \mathbf{r}_{\mathrm{pf}}}{\partial t} &= -\frac{\partial \mathbf{r}_{\mathrm{rp}}}{\partial t} + \frac{\partial d_{\mathrm{rf}}}{\partial t}(\hat{\mathbf{r}}_{\mathrm{s}} + \delta\mathbf{r}_{\mathrm{s}}) + d_{\mathrm{rf}}\left(\frac{\partial \hat{\mathbf{r}}_{\mathrm{s}}}{\partial t} + \frac{\partial \delta\mathbf{r}_{\mathrm{s}}}{\partial t}\right) \\ &\approx \underbrace{-\frac{\partial \mathbf{r}_{\mathrm{rp}}}{\partial t}}_{\#1} + \underbrace{\frac{\partial d_{\mathrm{rf}}}{\partial t}(\hat{\mathbf{r}}_{\mathrm{s}} + \delta\mathbf{r}_{\mathrm{s}})}_{\#2} + \underbrace{d_{\mathrm{rf}}\frac{\partial \hat{\mathbf{r}}_{\mathrm{s}}}{\partial t}}_{\#3}\end{aligned} \tag{3.32}$$

The one term removed in this approximation, $d_{\mathrm{rf}}\partial\delta\mathbf{r}_{\mathrm{s}}/\partial t$, proves to be negligible and can be ignored for this analysis. Terms #1 and #3 are direct from input quantities (and term #3 is zero if we are dealing with a fixed star); however, term #2 must be calculated from the next equation:

$$
\begin{aligned}
\frac{\partial d_{\mathrm{rf}}}{\partial t} &= \frac{\frac{\partial \mathbf{r}_{\mathrm{rp}}}{\partial t}\cdot\hat{\mathbf{n}}_{\mathrm{p}}}{(\hat{\mathbf{r}}_{\mathrm{s}}+\delta\mathbf{r}_{\mathrm{s}})\cdot\hat{\mathbf{n}}_{\mathrm{p}}} - \frac{\mathbf{r}_{\mathrm{rp}}\cdot\hat{\mathbf{n}}_{\mathrm{p}}}{\left[(\hat{\mathbf{r}}_{\mathrm{s}}+\delta\mathbf{r}_{\mathrm{s}})\cdot\hat{\mathbf{n}}_{\mathrm{p}}\right]^2}\left(\frac{\partial \hat{\mathbf{r}}_{\mathrm{s}}}{\partial t}+\frac{\partial \delta\mathbf{r}_{\mathrm{s}}}{\partial t}\right)\cdot\hat{\mathbf{n}}_{\mathrm{p}} \\
&\approx \frac{\frac{\partial \mathbf{r}_{\mathrm{rp}}}{\partial t}\cdot\hat{\mathbf{n}}_{\mathrm{p}}}{(\hat{\mathbf{r}}_{\mathrm{s}}+\delta\mathbf{r}_{\mathrm{s}})\cdot\hat{\mathbf{n}}_{\mathrm{p}}} - \frac{\mathbf{r}_{\mathrm{rp}}\cdot\hat{\mathbf{n}}_{\mathrm{p}}}{\left[(\hat{\mathbf{r}}_{\mathrm{s}}+\delta\mathbf{r}_{\mathrm{s}})\cdot\hat{\mathbf{n}}_{\mathrm{p}}\right]^2}\left(\frac{\partial \hat{\mathbf{r}}_{\mathrm{s}}}{\partial t}\cdot\hat{\mathbf{n}}_{\mathrm{p}}\right) \\
&= \frac{\left(\frac{\partial \mathbf{r}_{\mathrm{rp}}}{\partial t}-d_{\mathrm{rf}}\frac{\partial \hat{\mathbf{r}}_{\mathrm{s}}}{\partial t}\right)\cdot\hat{\mathbf{n}}_{\mathrm{p}}}{(\hat{\mathbf{r}}_{\mathrm{s}}+\delta\mathbf{r}_{\mathrm{s}})\cdot\hat{\mathbf{n}}_{\mathrm{p}}}
\end{aligned}
\tag{3.33}
$$

Again, the term $\partial\delta\mathbf{r}_{\mathrm{s}}/\partial t$ is negligible and is ignored. In addition, the time derivative of $\hat{\mathbf{n}}_{\mathrm{p}}$, while not strictly zero, is extremely small and is ignored. We substitute this into Eq. (3.32) and thus solve for $\dot{\mathbf{r}}_{\mathrm{pf}}(t_{\mathrm{f}})$. The scalar value of the velocity is found using the following equation:

$$
\dot{r}_{\mathrm{pf}} = \frac{x_{\mathrm{pf}}\dot{x}_{\mathrm{pf}} + y_{\mathrm{pf}}\dot{y}_{\mathrm{pf}} + z_{\mathrm{pf}}\dot{z}_{\mathrm{pf}}}{r_{\mathrm{pf}}} \tag{3.34}
$$

Special case for Voyager 1

The formulation described above works for a fixed star, with negligible proper motion or parallax. For this analysis, however, we will need to be able to use the Voyager spacecraft as the star, or signal source, to analyze the radio occultation data (RSS) (Tyler *et al.* 1981). In addition, this formulation can be used whenever the proper motion of the star is known. The major change is that the star position is no longer a fixed quantity:

$$
\hat{\mathbf{r}}_{\mathrm{s}} \rightarrow \hat{\mathbf{r}}_{\mathrm{s}}(t) \tag{3.35}
$$

We substitute for the fixed star unit vector in Eq. (3.8) to get the following equation for use with radio occultation data:

$$
\mathbf{r}_{\mathrm{pf}}(t_{\mathrm{f}}) = -\mathbf{r}_{\mathrm{rp}}(t_{\mathrm{r}},t_{\mathrm{f}}) + d_{\mathrm{rf}}(t_{\mathrm{r}},t_{\mathrm{f}})\left(\hat{\mathbf{r}}_{\mathrm{s}}(t_{\mathrm{s}}) + \delta\mathbf{r}_{\mathrm{s}}\right) \tag{3.36}
$$

We retain the notation used previously, that of $\hat{\mathbf{r}}_s$ for the direction to the source. When used previously, this notation implied a vector from the solar system barycenter in the direction of the star. For a fixed star at infinite distance, this unit vector points in the same direction from anywhere in the solar system. Now that the source is not at infinite distance, this is no longer true, and the source direction depends on the position of the observer. Thus, the unit vector to the source is formed by dividing the vector from the receiver to the source, $\mathbf{r}_{\mathrm{rs}}$, by its magnitude:

$$\hat{\mathbf{r}}_{\mathrm{s}}(t_{\mathrm{s}}) = \frac{\mathbf{r}_{\mathrm{rs}}(t_{\mathrm{r}},t_{\mathrm{s}})}{|\mathbf{r}_{\mathrm{rs}}(t_{\mathrm{r}},t_{\mathrm{s}})|} \tag{3.37}$$

The time the signal left the source, t_{s}, is found by projecting back from the received time:

$$t_{\mathrm{s}} = t_{\mathrm{r}} - \frac{|\mathbf{r}_{\mathrm{rs}}(t_{\mathrm{r}},t_{\mathrm{s}})|}{c} \tag{3.38}$$

The ephemeris for the source is formed by combining ephemerides for the planet and the source:

$$\mathbf{r}_{\mathrm{rs}}(t_{\mathrm{r}},t_{\mathrm{s}}) = \mathbf{r}_{\mathrm{p}}(t_{\mathrm{s}}) - \mathbf{r}_{\mathrm{r}}(t_{\mathrm{r}}) + \mathbf{r}_{\mathrm{ps}}(t_{\mathrm{s}}) \tag{3.39}$$

For use in Eq. (3.32), we find the time derivative of the source vector:

$$\frac{\partial \hat{\mathbf{r}}_{\mathrm{s}}}{\partial t} = \frac{\dot{\mathbf{r}}_{\mathrm{rs}}(t_{\mathrm{r}},t_{\mathrm{s}})}{|\mathbf{r}_{\mathrm{rs}}(t_{\mathrm{r}},t_{\mathrm{s}})|} \tag{3.40}$$

These equations ignore the difference in distance traveled due to GR bending.

When analyzing the geometry of an occultation of a radio signal, there is an additional iteration step to determine the direction of the source unit vector (illustrated in Fig. 4.1). It is not the vector from the receiver to the source, as this ignores the fact that the ray underwent GR bending. Instead, the source direction is the vector from the point the ray would have crossed the shadow plane if there were no GR bending, to the source (at the appropriate backdated time). In addition, because the ray did not originate at infinity, the actual amount of bending will be somewhat less than the total integrated bending. Including this full formulation results in a change of feature radius by at most 0.007 km over not including GR bending at all. Because this is much larger than the typical feature rms of 0.5 km, we have chosen to ignore GR bending for the analysis of RSS occultation data.

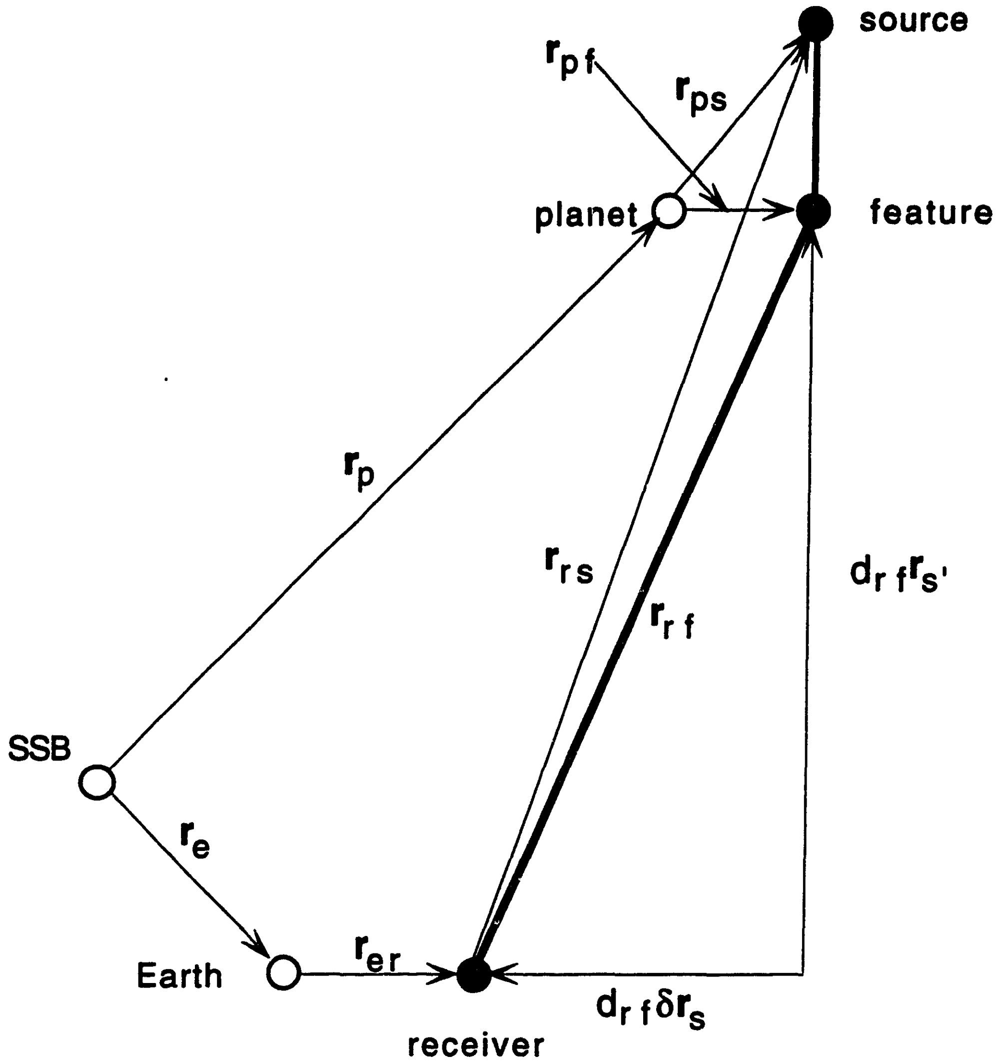

FIG. 4.1. The geometry of an occultation of a Voyager spacecraft signal. See text for definition of vector symbols. Here, $\hat{\mathbf{r}}_{s'}$ is the actual direction of the star as viewed from the location the occulted signal would have intersected the shadow plane if there were no general relativistic bending. This same vector diagram is relevant for both stellar occultations observed by a spacecraft near the planet, and for an occultation of a stellar signal. For an occultation observed from a point near the planet, the vector to the receiver is measured from the solar system barycenter or some other point, instead of from Earth. For an occultation of a stellar signal, star moves out to infinite distance, and the vectors $\mathbf{r}_{rs}$ and $\hat{\mathbf{r}}_{s'}$ become parallel.

Inclined Rings

To include the general case of inclined rings, we use the ring plane pole for each ring instead of the planet pole. The transformation between the ring plane pole and the planet pole is a function of the inclination of the ring, *i*, and the longitude of the ascending node, *Ω*, measured prograde from the intersection of Earth's equator (J2000.0) with that of the mean ring plane.

Because $\hat{\mathbf{n}}_p$ is assumed to be coincident with the mean ring plane, and rings are assumed to be inclined with respect to this plane, we need to transform $\hat{\mathbf{n}}_r$ into the planet equatorial coordinate system by using the ring's inclination (*i*) and longitude of ascending node (*Ω*). Both angles are shown in Fig. 4.2. We first introduce a new coordinate system, $\xi\eta\zeta$, which is centered on the planet with ζ in the direction of the angular momentum vector of the ring plane, ξ in the direction of the ascending node, and η is orthogonal. We need to express $\hat{\mathbf{n}}_r$ in terms of *xyz*. To do this, we first rotate around ξ by -*i*, and then around *z* (normal to the planet equator) by -*Ω*.

$$\mathbf{R}_4 = \mathbf{R}_{\xi\eta\zeta\rightarrow xyz} = \begin{bmatrix} \cos\Omega & -\sin\Omega\cos i & \sin\Omega\sin i \\ \sin\Omega & \cos\Omega\cos i & -\cos\Omega\sin i \\ 0 & \sin i & \cos i \end{bmatrix} \tag{3.41}$$

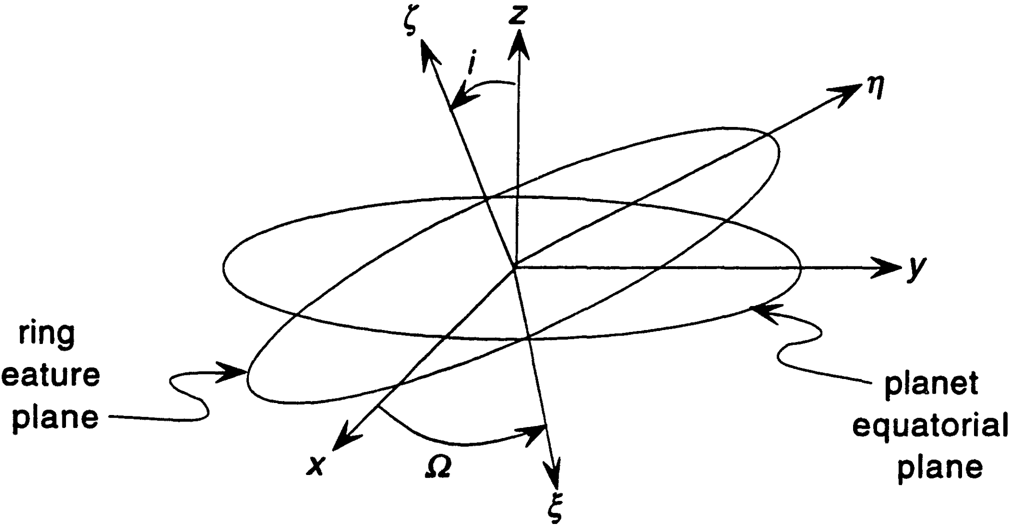

FIG. 4.2. Orientation of inclined ring with respect to planet's equatorial plane, and the two angles which describe this orientation: the longitude of the ascending node, Ω, and the inclination of the ring orbit, *i*.

Using this rotation matrix, we find the ring-plane pole in the planet's equatorial coordinate system:

$$\hat{\mathbf{n}}_{\mathrm{r}}\big|_{xyz} = \mathbf{R}_4 \cdot \hat{\mathbf{n}}_{\mathrm{r}}\big|_{\xi\eta\zeta} = \mathbf{R}_4 \cdot \begin{bmatrix} 0 \\ 0 \\ 1 \end{bmatrix} = \begin{bmatrix} \sin\Omega\sin i \\ -\cos\Omega\sin i \\ \cos i \end{bmatrix} \tag{3.42}$$

This can now be rotated into *XYZ*, using matrices $\mathbf{R}_1$, $\mathbf{R}_2$, and $\mathbf{R}_3$. This ring-plane pole vector is then used in Eq. (3.9). The longitude of the ascending node used above is a function of time, because it regresses due to the planet's gravitational harmonics. The following equation takes this into account:

$$\Omega(t) = \Omega_0(t_n) + \dot{\Omega}(t - t_n) \tag{3.43}$$

4. RING ORBIT MODELS

Circular

Three different models for ring orbits are used in this work: circular, simple eccentric, and multi-lobed eccentric. A circular orbit model is used for those rings which are assumed to be circular. This model was used exclusively in recent works (E93, F93, H93, NCP); it is also used here in test cases and some fits. The sole parameter in this case is a, the semimajor axis of the ring feature.

$$r(\theta,t)=a \tag{4.1}$$

Simple Eccentric

The logical extension of this simple model is to expand it to include simple ellipses. This introduces as parameters eccentricity (e), longitude of periapse (ϖ_0), apsidal precession rate ($\dot{\varpi}$), and reference epoch (t_0). The longitude of periapse is defined from the intersection of the Earth's equator (J2000.0) with the planet's equator ($\theta = 0$ in the xyz coordinate system). The approximation in Eq. 4.2 for small eccentricities is introduced to make the equations for simple and multi-lobed ellipses parallel.

$$r(\theta,t)=\frac{a\left(1-e^2\right)}{1+e\cos\left[\theta-\varpi_0-\dot{\varpi}\left(t-t_0\right)\right]}\approx a\left\{1-e\cos\left[\theta-\varpi_0-\dot{\varpi}\left(t-t_0\right)\right]\right\} \tag{4.2}$$

Multi-lobed Eccentric

The final kinematic model considered here is that of a non-circular ring with self-excited normal modes, or of a non-circular ring at an inner Lindblad resonance (French *et al.* 1991). The additional parameters in this model are Ω_p, the pattern speed of the feature distortion, and m, a positive integer that describes the number of lobes in the multi-lobed ellipse. An ellipse with m=1 is a simple ellipse (Eq. 4.2). An ellipse with m=2 is a body-centered ellipse.

$$r(\theta,t)=a\left\{1-e\cos m\left[\theta-\varpi_0-\Omega_p\left(t-t_0\right)\right]\right\} \tag{4.3}$$

Apsidal Precession Rate, Nodal Regression Rate

To calculate the pattern speed, we first need expressions for the mean motion and the apsidal precession rate. These depend on the gravitational potential of the planet, which is generally non-spherical. Contributions to the potential from external satellites and nearby ring material are small and are not considered here. For an equatorial test particle, the mean motion n, radial frequency κ, and vertical frequency μ are given by the following equations (Shu 1984):

$$rn^2(r,z) = \left.\frac{\partial \varphi_\mathrm{p}}{\partial r}\right|_{z=0} \tag{4.4}$$

$$\kappa^2(r) = \frac{1}{r^3}\frac{d}{dr}\left[\left(r^2 n\right)^2\right] \tag{4.5}$$

$$\mu^2(r) = \left[\frac{\partial^2 \varphi_\mathrm{p}}{\partial z^2}\right]_{z=0} \tag{4.6}$$

where z is the cylindrical coordinate expressing height above the equatorial plane, and φ_p is the planetary potential. By invoking Laplace's equation, we find the following relation among these three frequencies:

$$\mu^2 + \kappa^2 = 2n^2 \tag{4.7}$$

The non-spherical gravitational potential can be expressed in terms of the mass and equatorial radius of the planet, M_p and R_p, and the gravitational harmonic coefficients J_2, J_4, and J_6:

$$\begin{aligned}\varphi_\mathrm{p}(r,z=0) &= -\frac{GM_\mathrm{p}}{r}\left[1-\sum_{\mathrm{n=1}}^{\infty} J_{2\mathrm{n}}\left(\frac{R_\mathrm{p}}{r}\right)^2 P_{2\mathrm{n}}(0)\right] \\ &\cong -\frac{GM_\mathrm{p}}{r}\left[1+\frac{1}{2}J_2\left(\frac{R_\mathrm{p}}{r}\right)^2-\frac{3}{8}J_4\left(\frac{R_\mathrm{p}}{r}\right)^4+\frac{5}{16}J_6\left(\frac{R_\mathrm{p}}{r}\right)^6\right]\end{aligned} \tag{4.8}$$

$P_{2n}(z)$ is the Legendre polynomial at z. These are calculated at z=0 because we make the approximation that all rings are close to equatorial. We also assume that the gravitational potential is rotationally and north-south symmetric.

The rates of apsidal precession, $\dot{\varpi}$, and of nodal regression (used for inclined rings), $\dot{\Omega}$ are found from the radial and vertical frequencies in the following manner:

$$\dot{\varpi} = n - \kappa \tag{4.9}$$

$$\dot{\Omega} = n - \mu \tag{4.10}$$

From the above Eqs. (4.4-4.10), we can calculate these rates (with an approximation for small inclinations) in terms of the gravitational harmonic coefficients (Nicholson and Porco 1988):

$$\dot{\varpi} = \sqrt{\frac{GM}{r^3}}\left[\frac{3}{2}J_2\left(\frac{R_p}{r}\right)^2 - \frac{15}{4}J_4\left(\frac{R_p}{r}\right)^4 + \frac{27}{64}J_2^3\left(\frac{R_p}{r}\right)^6 - \frac{45}{32}J_2J_4\left(\frac{R_p}{r}\right)^6 + \frac{105}{16}J_6\left(\frac{R_p}{r}\right)^6\right] \tag{4.11}$$

$$\dot{\Omega} = \sqrt{\frac{GM_p}{r^3}}\left[-\frac{3}{2}J_2\left(\frac{R_p}{r}\right)^2 + \frac{15}{4}J_4\left(\frac{R_p}{r}\right)^4 + \frac{9}{4}J_2^2\left(\frac{R_p}{r}\right)^4 - \frac{105}{16}J_6\left(\frac{R_p}{r}\right)^6 - \frac{315}{32}J_2J_4\left(\frac{R_p}{r}\right)^6 - \frac{351}{64}J_2^3\left(\frac{R_p}{r}\right)^6\right] \tag{4.12}$$

We refer to $\dot{\varpi}$ as the rate of "free precession," meaning a precession due to only the non-spherical gravity field of the planet.

Resonance Pattern Speeds

The pattern speed of a ring feature is its rate of forced precession due to torque from the forcing satellite. As given by Eqs. (20) and (22) in Porco and Nicholson (1987), the pattern speed is related to the apsidal precession rate by:

$$m\Omega_p = (m-1)n + \dot{\varpi} \tag{4.13}$$

where n is the Keplerian mean motion of the ring particle. Thus for $m = 1$, the pattern speed is simply the apsidal precession rate, and Eq. (4.3) reduces to Eq. (4.2). In terms of frequencies of the forcing satellite, the pattern speed is given by:

$$m\Omega_p = (m+k+p)n' - k\dot{\varpi}' - p\dot{\Omega}' \tag{4.14}$$

where n', $\dot{\varpi}'$, and $\dot{\Omega}'$ are the mean motion, apsidal precession rate, and nodal regression rate of the satellite. The resonance label, as in the example "Mimas 3:1", is given by $(m+k+p)/(m-1)$.

Resonance Locations

With the above expression for pattern speed, we can calculate the locations of inner Lindblad resonances with satellites (vertical resonances are not considered here). Inner Lindblad resonances (ILRs) are resonances in which the perturbation frequency differs from the mean motion of the ring particle at the resonance location by an integer multiple of the radial frequency κ (Eq. 4.5) (Shu 1984). We calculate locations of ILRs using the method of Lissauer & Cuzzi (1982). The resonance locations presented here incorporate new determinations of Saturn's gravitational harmonics (Nicholson and Porco 1988, hereafter referred to as NP88), and of the mean motions of satellites (Harper and Taylor 1993). Listed in Table 4.1 are resonances located near numbered ring features (including those not considered in this analysis). The resonance locations are found in the same manner as Lissauer & Cuzzi (1982): by first finding the radius of the satellite based on its mean motion, then calculating the satellite precession rate if necessary to find the right-hand side of Eq. (4.14). Then Eq. (4.13) is solved for the resonance location.

Table 4.1. Locations of Inner Lindblad Resonances

Resonance	Location (km)	Feature	Feature Description[a]
Prometheus 2:1	88712.89	158	CR 1.470 R_S ringlet
Pandora 2:1	90168.97	156	CR 1.495 R_S ringlet
Mimas 3:1	90197.56	56	OER 1.495 R_S ringlet
Mimas 2:1	117553.42	55	OER B Ring
		153	CR Huygens ringlet
Pandora 9:7	120039.37	14	IER 1.990 R_S ringlet
Prometheus 10:8	120278.81	112	CR 1.994 R_S ringlet
Prometheus 5:4	120304.64	10	OER 1.994 R_S ringlet
Atlas 6:5	122074.21	7	IER A Ring
Prometheus 11:9	122074.47	7	IER A Ring
Epimetheus 7:6	136740.55	52	OER A Ring
Janus 7:6	136785.03	52	OER A Ring

[a] IER, inner edge of ring feature; CR, centerline of ring feature; OER, outer edge of ring feature.

5. IMPLEMENTATION OF MODELS

Specifics of Fits

To fit the previously-described models to the data, we used the fitting process described in E93: a non-linear least-squares fitting process, implemented in *Mathematica* (Wolfram 1991). Since the data are observed times of ring features, the most straight-forward fit would be to fit in time, minimizing the sum of squared residuals in time. The other option is to convert the observed times into "observed radii", and compare these against model radii, and thus to perform the fit in radius. In E93, we find that there is no significant difference between fitting in time and fitting in radius; also, we argue that this is the more correct method, since it is more likely that there are errors in the models for the rings presumed to be circular. Therefore we adopt the method of fitting in radius. Using the occultation geometry parameters the observed time is converted into observed radius and observed longitude. The model radius is then calculated from the ring orbit model using this observed longitude.

Because the magnitude of errors in the data sets used vary, we investigate weighting of data. Until now, all data were considered equally in the fits. This was not a bad approximation, but we suspected that lower rms data sets should be given higher weight in the fits than were given lower weight data sets. Since the differences in rms for observatories can be as great as a factor of 2.5, we implement a weighting scheme to more accurately reflect the weight of the various data sets. Weighting is crucial when including non-circular features, as they typically have high rms residuals than circular features. We adopt a scheme that sets the weight for a feature to be the number of degrees of freedom (d) for that feature divided by the rms for that feature (weights for all data points for a feature were the same), normalized such that the sum of all weights equals the number of data points:

$$w_i = \frac{1}{\sigma_i^2} = \frac{d}{\sum_j \left(y_{obs,j} - y_{model}\right)^2} \tag{5.1}$$

$$N_i = \frac{n}{\sum_i^n w_i} \tag{5.2}$$

$$q_i = N_i w_i \tag{5.3}$$

The number of degrees of freedom, d, was defined to be the number of data points minus the number of ring orbit parameters being fit. The weights thus calculated are re-calculated after every iteration with the new residuals. Additionally, we find it necessary to limit the maximum weight a feature could have to be

$$q_{maximum} = \frac{1}{\sigma_{measured}^{2}} \tag{5.4}$$

or approximately $1/(1 \text{ km})^2$. This is necessary because a runaway situation can develop, in which a feature with a low residual can control the fit thereby minimizing its residual and further increasing its weight. In the end the entire geometry can be controlled by one ring feature.

Model Inputs & Initial Parameters

The ephemeris for the Voyager 1 spacecraft used in this analysis was supplied by M. R. Showalter from the Rings Node of the Planetary Data System. The ephemeris identifier is given in Table 6.1. This version of the ephemeris is the same as that used in the NCP analyses, and differs by less than 0.5 km from the ephemeris of the same name provided by NAIF. This difference exists because the ephemeris used here is a reconstructed ephemeris, and all original information is no longer available. The Showalter ephemeris provided rectangular, geometric, B1950.0 offsets of Voyager 1, Earth center, and sun center, all with respect to the center of Saturn (not the Saturn-system barycenter).

Because our model requires solar-system barycentric ephemerides, we attempted several methods for creating such an ephemeris from the information given. These were to combine the Voyager position given relative to the center of Saturn with the saturnicentric position of the sun or Earth, to create a heliocentric, geocentric, or saturnicentric Voyager position. To this, we add the solar-system barycentric position of the sun, Earth, or Saturn. These added portions were the same as were used in the creation of other ephemerides used in the analyses. Surprisingly, not all methods achieved the same results. The resulting solar-system barycentric position of Voyager differed by 1 to 1000 km among these methods. When used as input ephemerides for the occultation geometric model, the resulting ring radii differed by 1 to 1000 km. To decide among these methods for the one to use in this analysis, we use Fig. 12 of F93 as a test case. In this figure are plotted the differences between F93 adopted solution radii and those calculated from the Voyager 1 RSS data using the ephemerides constructed as described above and the F93 adopted solution final parameters. From this test case, we find that using the saturnicentric position of Voyager added to the solar-system barycentric position of the Saturn center gave the closest agreement--the largest difference was 0.15 km.

The Voyager 2 spacecraft ephemeris was easier to obtain than that of Voyager 1. The Navigation Ancillary Information Facility (NAIF) at the Jet Propulsion Laboratory (Acton 1990) supplied the requested file, which was the same as that indicated by NCP. Again using Fig. 12 of F93 as a test case, we find the agreement to be very good, with differences always less than 0.06 km. These differences in ring-plane radii (using F93 adopted solution) due to ephemerides for Voyagers 1 and 2 are shown in Fig. 5.1.

Other ephemerides used in these analyses include solar-system barycentric ephemerides for the Earth center, Saturn-system barycenter, and Saturn barycentric ephemerides for eight Saturn satellites. These last ephemerides are used to convert from Saturn barycenter coordinates Saturn center coordinates. Ephemerides for the Earth and the Saturn-system barycenter are rectangular, geometric positions from the DE-130 (precessed to J2000.0), tabulated against barycentric dynamical time (TDB). Ephemerides for the Saturn satellites are also rectangular, geometric coordinates tabulated against TDB, calculated from special files provided by NAIF. See Table 6.1 for filenames.

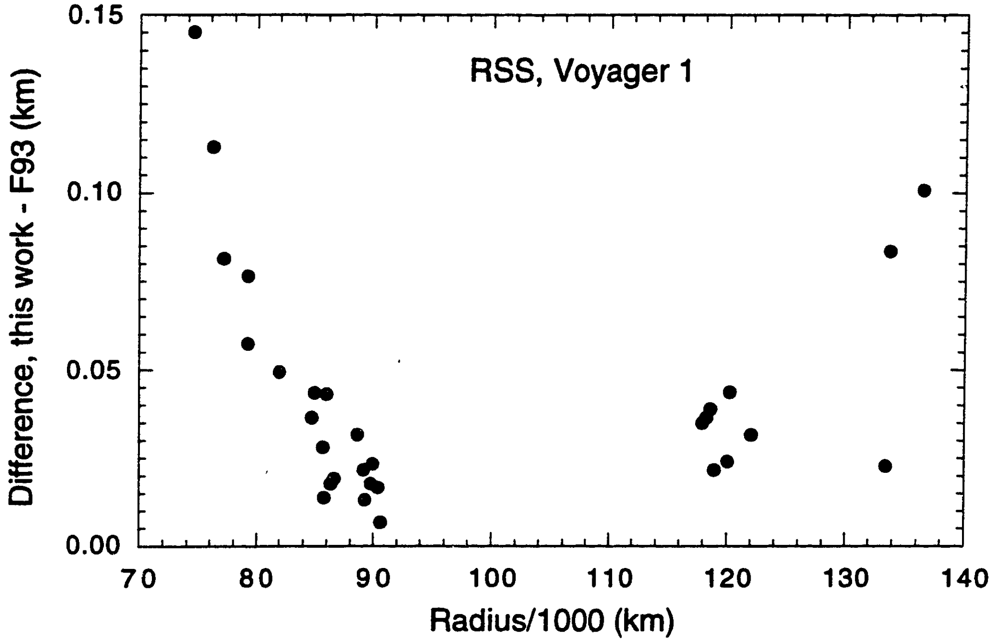

FIG. 5.1. Differences in radius residuals between this work and those presented in Fig. 9 of F93. (a) Residuals from Voyager 1 data are always less than 0.15 km (less than feature rms residuals). The differences are probably due to different ephemerides for the Voyager 1 spacecraft.

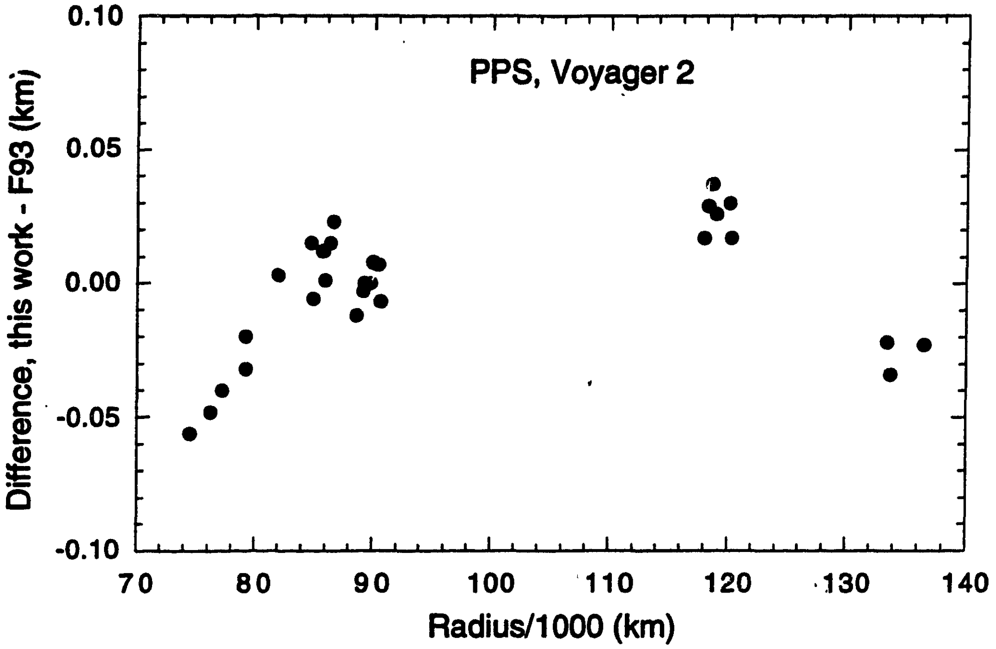

FIG. 5.1. (b) Residuals from Voyager 2 data are always less than 0.06 km (less than feature rms residuals). The differences are probably due to errors in determining values from Fig. 9 of F93.

Test Cases

As described in E93, extensive tests were performed, comparing our occultation geometry modeling code to that used in F93, who in turn compared with H93. In E93, we tested that input quantities, intermediate results, and final model results were equal to within a few meters. We consider this a good test of all parts of the problem, because we used ephemerides from different sources, used two different models ("planet-plane" vs. "vector"), coded in different languages (Mathematica vs. FORTRAN) by different people, and ran the fits on different computers (Sun SPARC-10 vs. DEC-5000). We compared our values with those given by F93 in Tables B-I, B-II, and B-III. We then prepared our own, more comprehensive, table of sample values (Table 5.1), for use in future test cases.

Table 5.1. Numerical Values for Certain Cases

Quantity	Symbol	28 Sgr MCD Test Case	GSC6323-01396 HST Test Case
Pole position[a], J2000 (deg)	α_n, δ_n	40.587582 83.534223	40.586206 83.534078
Star position, J2000 (deg)	$\alpha_{s'}, \delta_{s'}$	281.5858161129 –22.3922368088	302.6267812500 –20.6132222222
Planet ephemeris offset (km)	f_o, g_o	0.0 0.0	0.0 0.0
Star position offset (arcsec)	α_o, δ_o	0.164221 –0.125531	0.956999 –0.107345
Clock offset (s)	t_o	–0.077274	0.0
Feature name		38	23
Clock time (UTC)	t_c	1989 7 3 8 41 12.4041	1991 10 3 2 2 21.5950
Received time (UTC)	t_r	1989 7 3 8 41 12.4814	1991 10 3 2 2 21.5950
Earth center (km)	$\mathbf{r}_e(t_r)\big\|_{fgh}$	2135192.637357 –1477916.428756 151969338.341209	136973906.170086 30580115.083202 53116337.204003
Receiver relative to Earth center (km)	$\mathbf{r}_{er}(t_r)\big\|_{fgh}$	2420.217832 4872.313198 3322.601021	–4422.527537 3504.074565 4106.602768
Time at planet plane (UTC)	t_π	1989 7 3 7 26 10.7821	1991 10 3 0 42 55.2547
Planet system barycenter (km)	$\mathbf{r}_b(t_\pi)\big\|_{fgh}$	2061844.806959 –1475252.842513 1501525132.692888	136880668.806791 30586930.561072 1482033121.315271
Planet center relative to system barycenter (km)	$\mathbf{r}_{bp}(t_\pi)\big\|_{fgh}$	–222.297581 –52.003695 –155.623141	210.465321 57.771464 209.921215
Velocity of planet center relative to solar system barycenter (km s^{-1})	$\dot{\mathbf{r}}_p(t_\pi)\big\|_{fgh}$	9.142927 0.345519 –0.085487	9.027025 1.572242 –1.151416
Planet center relative to receiver (km)	$\mathbf{r}_{rp}(t_r, t_\pi)\big\|_{fgh}$	–75990.345811 –2260.730651 1349552316.127516	–88604.370437 3369.174768 1428912887.429715
Time at feature (UTC)	t_f	1989 7 3 7 26 10.7081	1991 10 3 0 42 55.1927
Feature coordinates in shadow plane (km)	$f_f(t_r), g_f(t_r)$	75991.022451 2260.756222	88604.929771 –3369.077348
Shadow plane radius (km)	$\sqrt{f_f^2 + g_f^2}$	76024.644109	88668.958841
Magnitude of GR bending (km)	$f_s(t_\pi), g_s(t_\pi)$	30.181760 0.966758	27.353807 –1.011010
Feature coordinates at planet plane (km)	$\mathbf{r}_{pf}(t_f)\big\|_{uvw}$	75321.384070 10536.981657 22186.586579	88397.969103 7268.992113 18575.480669
Planet plane radius (km)	$\sqrt{u_f^2 + v_f^2}$	76054.841270	88696.331310
Feature coordinates in ring plane (km)	$\mathbf{r}_{pf}(t_f)\big\|_{xyz}$	–55552.811223 –56484.233817 0.000001	–28317.191366 –86082.659944 0.000005
Ring plane radius (km)	$\left\|\mathbf{r}_{pf}(t_f)\right\|$	79224.891951	90620.569795
Feature longitude (deg)	$\theta_{pf}(t_f)$	225.476318830	251.791199066

6. RING-PLANE POLE SOLUTION

Using the models for occultation geometry and ring orbits described in Sections 3 and 4, we can fit for ring parameters using times of ring features measured in the GSC6323-01396, 28 Sgr, δ Sco, and RSS occultations. Some previous solutions for the ring-plane pole are listed in Table 6.2. Recent determinations of the pole position, such as F93 and NCP, have very small errors for the position and lead to ring radii that are in very good agreement with those determined from other methods (see Section 7). The solution of E93 provides the first solution independent of Voyager data, for an important check of the validity solution incorporating Voyager data. Older solutions, such as Simpson *et al.* (1983, listed in Table 6.2 as STH) and Kozai (1957), are listed in this Table because they are referred to later in Section 11.

Standard Parameters

Our standard set of parameters included in fits will be as follows, unless otherwise noted. Our data include measured times of features presumed circular (and equatorial) from the four available occultation data sets: GSC6323-01396, 28 Sgr, δ Sco, and RSS. Free parameters in the model fits are the pole right ascension and declination (J2000.0, at the Voyager 1 epoch, UTC 1980 November 12 23:46:32), star position offsets in right ascension and declination for GSC6323-01396 and 28 Sgr, clock offsets for all 28 Sgr stations except the IRTF, Voyager 1 and 2 in-track trajectory offsets in the form of clock offsets, and semimajor axes of included features. Fixed parameters are the masses of Saturn and its satellites, the magnitude and direction of pole precession, the gravitational harmonic J_2, clock offsets for the HST and IRTF data sets, and the star position offsets for δ Sco. Values for most of these fixed parameters are given in Table 6.1. The rate of pole precession is fixed at the value given in F93, precessed to J2000.0. The gravitational harmonic J_2 is used to calculate the amount that the path of electromagnetic radiation is bent as it passes Saturn (Eq. 3.13). The value of this parameter is determined in Section 11; however, the pole solution is insensitive to this parameter so we use our initial value for it, that given by NP88.

We fix the clock offset of the HST data set at 0. This is justified in E93, as fits including the HST clock offset as a free parameter all result in a value for this parameter that is consistent with 0. In addition, analysis of Crab pulsar data indicates that the HST clock is accurate to within 6 ms (Percival 1992). See E93 for additional details on the calibration of the HST clock. We choose to fix the IRTF clock at 0 as well, because of all the 28 Sgr clocks whose calibrations indicate there should be no offset, we are most familiar with that of the IRTF. We note that there are lingering discrepancies in the 28 Sgr data set, because when fit by itself it does not produce a solution consistent with other data sets (see Fig. 13 in E93, Fig. 8a in F93). One possible source of error in this data set could be erroneous observatory locations. Allowing clock offsets for most 28 Sgr stations is an attempt to partially compensate for any errors in observatory locations.

Table 6.1. Values of Parameters Usually Fixed in Fits (adapted from E93).

Parameter	Value	Reference
Physical Constants		
speed of light, c (km s^{-1})	299792.458	Seidelmann (1992)
Receiver Coordinates		
Ground-based observatories		Table I of F93
HST ephemeris	file "PBA20000R.ORX"	Space Telescope Science Institute
Voyager 1 ephemeris	trajectory ID t810308	NAIF (Acton 1990)
Voyager 2 ephemeris	trajectory ID t811001	NAIF (Acton 1990)
DSS-63 (Voyager 1)	E. Long.: 4^h 14^m $52^s.9021$ Lat.: 40° $14'$ $28''.8429$	(C. H. Acton, private communication)
Earth and Moon		
Barycenter ephemeris	DE-130	Standish (1990)
Mass ratio, M_e/M_m	81.300587	DE-130 (Standish 1990)
Earth equatorial radius (km)	6378.137	MERIT 1983 (Archinal 1992)
Earth flattening	1/298.257	MERIT 1983 (Archinal 1992)
Saturn system		
Barycenter ephemeris	DE-130	Standish (1990)
Satellite ephemerides	file "SAT018H.BSP"	NAIF (Acton 1990)
$J_2R_p^2$ (km^2)	59316335.9433	Table VII of F93
GM_{system} (km^3 s^{-2})	37940626.075	(W. M. Owen, private communication)
GM_{p} (km^3 s^{-2})	37931246.375	derived from system and satellite masses
GM_{Mimas} (km^3 s^{-2})	2.5	(W. M. Owen, private communication)
$GM_{\mathrm{Enceladus}}$ (km^3 s^{-2})	5.6	(W. M. Owen, private communication)
GM_{Tethys} (km^3 s^{-2})	44.1	(W. M. Owen, private communication)
GM_{Dione} (km^3 s^{-2})	77.3	(W. M. Owen, private communication)
GM_{Rhea} (km^3 s^{-2})	154.1	(W. M. Owen, private communication)
GM_{Titan} (km^3 s^{-2})	8977.7	(W. M. Owen, private communication)
GM_{Hyperion} (km^3 s^{-2})	1.	(W. M. Owen, private communication)
GM_{Iapetus} (km^3 s^{-2})	117.4	(W. M. Owen, private communication)

Table 6.1, continued.

Parameter		Value	Reference
Stars			
28 Sgr			
	FK4/B1950.0	$\alpha_s' = 18^h\,43^m\,19^s.7946475$	F93
		$\delta_s' = -22^\circ\,26'\,46''.88424$	
	FK5/J2000.0	$\alpha_s' = 18^h\,46^m\,20^s.5958671$	derived from the B1950.0 position
		$\delta_s' = -22^\circ\,23'\,32''.0525118$	
	proper motion	0	approximation for this reduction
	parallax	0	approximation for this reduction
GSC6323-01396			
	FK4/J2000.0	$\alpha_s' = 20^h\,10^m\,30^s.35$	Bosh and McDonald (1992)
		$\delta_s' = -20^\circ\,36'\,47''.6$	
	FK5/J2000.0	$\alpha_s' = 20^h\,10^m\,30^s.4275$	derived from the FK4 position
		$\delta_s' = -20^\circ\,36'\,47''.6$	
	proper motion	0	assumption
	parallax	0	assumption
δ Sco			
	FK4/B1950.0	$\alpha_s' = 15^h\,57^m\,22^s.2979$	Nicholson *et al.* (1990)
		$\delta_s' = -22^\circ\,28'\,52''.172$	
	FK5/J2000.0	$\alpha_s' = 16^h\,00^m\,20^s.0182$	derived from the FK4 position
		$\delta_s' = -22^\circ\,37'\,17''.642$	
	proper motion	0	assumption
	parallax	0	assumption
Transformations[a]			
B1950.0->J2000.0		rotation with X(0)	Eq. (5.711-4) of Standish *et al.* (1992)
TDB -> UTC		function library "SPICELIB"	Acton (1990)
Precession of receiver		procedure on p. B18	USNO (1992)
Nutation of receiver		procedure on p. B20	USNO (1992)
geodetic->geocentric		Eq. (4.22-7)	Archinal (1992)

[a] This table is an adaptation of Table 4 of E93. The table in E93 includes a transformation from "SOGS seconds" to UTC for converting HST ephemerides. We have since learned that time argument of the HST ephemerides are given in UTC, so no such conversion is necessary.

Table 6.2. Results of Model Fits

Fit	Coordinates of Pole (deg, J2000) α_n	δ_n	Epoch of Pole[a]	Radius of Feature 23 (km)	RMS (km)	Comments
Previous Solutions						
E93	40.5929 ± 0.0151	83.53478 ± 0.00531	Voyager 1	90618.53 ± 4.61	1.328	Includes HST & 28 Sgr data sets
F93	40.5955 ± 0.0036	83.5381 ± 0.0002	Voyager 1	90614.87 ± 0.50	1.295	Includes 28 Sgr & both Voyager data sets
NCP[b]	40.5892 ± 0.0102	83.5384 ± 0.0003	Voyager	90613.7 ± 2.0	0.69	Includes both Voyager data sets
STH[b]	40.588 ± 0.016	83.539 ± 0.002	Voyager			Includes lower resolution Voyager data sets
Kozai[b]	40.608 ± 0.023	83.5219 ± 0.0036	Voyager			Includes satellite position data
GSC6323-01396						
1[b]	40.6260 ± 0.4780	83.52660 ± 0.05206	HST	90610 ± 566	1.682	
28 Sgr						
2[b]	40.4446 ± 0.0470	83.61402 ± 0.02362	28 Sgr	90557.24 ± 17.70	1.272	
PPS and RSS						
3[b]	40.3812 ± 0.0766	83.54894 ± 0.00398	Voyager	90556.13 ± 24.19	0.631	
28 Sgr, PPS, and RSS						
4	40.5955 ± 0.0036	83.53812 ± 0.00018	Voyager 1	90614.88 ± 0.50	1.295	
GSC6323-01396, 28 Sgr, PPS, and RSS						
5	40.5929 ± 0.0047	83.53833 ± 0.00022	Voyager 1	90614.98 ± 0.54	1.333	All 28 Sgr clock offsets free except IRTF
6	50.5930 ± 0.0031	83.53832 ± 0.00016	Voyager 1	90614.98 ± 0.44	1.326	28 Sgr clock offsets fixed or free as in F93
7[c]	40.5929 ± 0.0047	83.53833 ± 0.00022	Voyager 1	90614.97 ± 0.54	1.306	Remove feature 44 (possibly non-circular)
8	40.5957 ± 0.0046	83.53826 ± 0.00027	Voyager 1	90614.43 ± 2.78	1.302	Includes only MCD data from 28 Sgr set
GSC6323-01396, PPS, and RSS						
9	40.6033 ± 0.0061	83.53738 ± 0.00047	Voyager 1	90625.12 ± 5.30	1.573	

[a] The epoch "28 Sgr" is defined as the mean epoch of the 28 Sgr occultation, approximately 1989 Jul. 3 8:0:0. The epoch "HST" is the mean epoch of the occultation of GSC6323-01396, approximately 1991 Oct. 3 7:0:0. The epoch "Voyager" is the mean epoch of the RSS (Voyager 1) and PPS (Voyager 2) occultations, approximately 1981 Apr. 5. The epoch "Voyager 1" is defined as UTC 1980 Nov. 12 23:46:32. Unless otherwise noted, all precession rates are fixed at the rate predicted by F93.

[b] The precession rates for the indicated fits are fixed at 0.

[c] Adopted solution

Fits with Features Presumed Circular

As the simplest extension of the E93 and F93 solutions, we fit for ring-plane pole positions and ring radii combining all data sets used in these two analyses. The results of this fit are listed as Fit 5 in Table 6.2. This fit utilizes the standard set of fixed and free parameters described above. The features presumed circular in this fit are those adopted as circular in F93, without the B-Ring features. While this solution is very close to that of F93, note that the formal errors on the pole are larger than those of F93. This is because we choose to allow all time offsets of the 28 Sgr data sets except IRTF to be free, as we did in E93. This increases the number of free parameters of the fit, and thus the resulting formal errors are slightly larger. As a test of the magnitude of the formal errors, we perform Fit 6, which differs from Fit 5 in that the time offsets of the 28 Sgr data sets are fixed or free as they were in the F93 analysis. This solution is indistinguishable from Fit 5, while the formal errors of the pole position are slightly smaller than they were in F93; this is due to the additional data set included here and the fact that this fit is weighted. The formal errors do not decrease by a large amount because the rms errors of the GSC6323-01396 data set are larger than those of the 28 Sgr data sets: 1.9 km vs. an average value of 1.2 km.

As a test of the amount of influence the 28 Sgr data set has on the result, we run Fit 9 in Table 6.2. We do this because as Fit 2 shows, the 28 Sgr data set when fit by itself, does not produce a result consistent with that of the combined fit. If all assumptions about the data set are correct (that there are no systematic errors in feature time measurements, observatory coordinates, etc.), then the result of a fit to these data should differ from the true solution by no more than (approximately) its formal error. Since Fit 2 differs from the true solution, approximated by the F93 solution, we conclude that all assumptions are not correct, and that the 28 Sgr data set must have inconsistencies that may affect the solution of any fit in which it is included. We test the effect this data set has on the pole solution by combining three data sets that give consistent solutions on their own: GSC6323-01396, δ Sco (Voyager 2), and RSS (Voyager 1). We see from this fit that the pole is consistent with neither F93 nor NCP. For this fit, the HST clock offset is held constant at 0; however, allowing it to be fit does not change the result significantly. One problem with this particular fit is the geometric coverage of the three data sets involved. All of the GSC6323-01396, δ Sco, and RSS data sets are one-sided; that is, they sampled only immersion or emersion, not both. This means that the ring feature radii are not well constrained by these data sets. Because they are not well constrained, the solution is free to adjust the radii by a large amount (as happens here) while searching for the lowest residuals. This results in radii that are inconsistent with radii determined from other, non-occultation methods (Section 7). We attempt to overcome this problem by including one 28 Sgr data set, MCD. We allow the clock offset for this to be free. With a free clock offset and only one 28 Sgr data set, this has very little effect on the location of the pole; however, it acts to better constrain the ring-plane radii, as this is a two-sided occultation observation. This results of this fit are listed as Fit 8 in Table 6.2. We find a slightly different pole position than is found when including the full 28 Sgr data set. Even with our weighting scheme, because the 28 Sgr data set includes many observatories, these data are weighted more heavily. When we remove this 28 Sgr bias, we find a pole position which is not very different from that we find when including the entire 28 Sgr data set. This indicates that although there may be unresolved discrepancies in the 28 Sgr data set, they are not affecting the pole solution greatly.

Search for Ellipticity in Features Assumed Circular

The accuracy of the above-determined solutions depends on the validity of the assumption that the included features are circular. We now explicitly check this assumption. With the additional longitudinal coverage provided by the GSC6323-01396 occultation data set, we attempt to fit the occultation times in our full data set to an eccentric ring orbit model (Eq. 4.2). This fit can be performed with one of two methods: "partial" or "full". In the first "partial" method, we fit a non-circular ring orbit model to the radii calculated from a full geometric model. The parameters of this ring orbit model are the ring parameters: semimajor axis, eccentricity, longitude of periapse, apsidal precession rate (or pattern speed) and the symmetry parameter *m* (describes the number of lobes in a multi-lobed ellipse). In the second "full" method, the ring parameters are included as part of the overall fit using the occultation geometry and the ring orbit models. The parameters here are the ring parameters listed above as well as the geometric occultation parameters: ring-plane pole position, magnitude of pole precession, clock offsets, and star position offsets. The partial method is faster, as it does not include parameters not directly related to the feature under study; however, it does not allow the geometric parameters to change in response to changes in the fitted ring parameters. The two methods will yield similar results if the particular feature under study has little influence on the geometric parameters. Therefore, the difference between results of the two methods is a measure of the amount of influence a ring feature has on the pole solution as a whole. Until this work, all previous investigations of non-circular features in Saturn's rings have used the partial method.

Partial fits were performed to radii determined from the full, circular-features-only fit (Fit 5, Table 6.2). In these fits, we searched for signs of significant non-circularity in all features presumed circular. The results of these partial fits are given in Table 6.3. We note that the results of this fit show an interesting lack of features with $0 < e/\sigma_e < 1$ (see histogram in Fig. 6.1). The most likely explanation for this behavior is incomplete coverage in true anomaly (longitude in a frame co-rotating at the apsidal precession rate or pattern speed) coupled with large scatter of measured points. If the coverage in true anomaly is very incomplete—at worst, the 28 Sgr data sets define two angles separated by approximately 180°—the formal result of the fit can include a non-zero eccentricity with apoapse and periapse completely unconstrained by any data points. The fitted eccentricity will be determined by the small differences in true anomaly of the 28 Sgr data points and any scatter in these points. Therefore, interpretation of the results of these fits must always include investigation into the coverage of the data points, and the formal value of the eccentricity may be unrealistic. See Fig. 12.1 (c, d) for an extreme example of this case. Figure 6.2 shows sample plots of partial fit results for various values of e/σ_e.

Table 6.3. Partial Fits to Features Presumed Circular, to Check for Non-Circularity.

Feature	a (km)	$e \times 10^4$	e/σ_e	ϖ_0 (deg)	$\dot{\varpi}$ (deg day^{-1})	rms (km)	# pts
44	74492.33 ± 0.59	0.88 ± 0.29	3.1	254.2 ± 17.1	26.5582 ± 0.0037	1.48	10
40	76262.99 ± 0.68	0.75 ± 0.38	2.0	253.7 ± 23.0	24.3485 ± 0.0051	1.96	10
39	77164.57 ± 0.29	0.17 ± 0.11	1.6	161.1 ± 68.0	23.2867 ± 0.0141	0.86	10
38	79220.37 ± 0.26	0.09 ± 0.10	0.9	56.8 ± 89.9	21.1519 ± 0.0195	0.86	13
37	79263.87 ± 1.11	0.90 ± 0.61	1.5	349.2 ± 22.7	21.0892 ± 0.0051	1.78	12
36	82040.51 ± 0.16	0.05 ± 0.03	1.9	263.2 ±192.4	18.5943 ± 0.0479	0.43	9
35	84749.01 ± 0.54	0.20 ± 0.24	0.8	51.2 ± 66.3	16.5095 ± 0.0140	1.36	20
34	84949.20 ± 0.37	0.19 ± 0.10	1.8	116.4 ± 83.2	16.3392 ± 0.0206	1.59	19
33	85660.48 ± 0.29	0.09 ± 0.06	1.4	44.7 ± 80.9	15.8830 ± 0.0177	0.73	10
42	85758.42 ± 0.47	0.21 ± 0.18	1.2	40.3 ± 84.1	15.8413 ± 0.0193	1.65	17
31	85921.38 ± 0.47	0.48 ± 0.26	1.9	81.8 ± 22.6	15.6203 ± 0.0051	1.44	10
30	86370.17 ± 0.38	0.22 ± 0.24	0.9	62.3 ± 23.4	15.3830 ± 0.0060	0.73	16
29	86600.86 ± 0.37	0.13 ± 0.11	1.1	339.7 ± 71.2	15.2658 ± 0.0171	1.12	20
28	88594.55 ± 0.38	0.14 ± 0.13	1.1	261.0 ± 70.9	13.8861 ± 0.0167	0.97	14
27	89188.56 ± 0.25	0.15 ± 0.14	1.1	275.8 ±128.9	13.6980 ± 0.0317	0.75	16
41	89294.88 ± 0.31	0.16 ± 0.16	1.0	43.5 ± 56.0	14.0619 ± 0.0132	1.14	17
26	89786.76 ± 0.16	0.13 ± 0.06	2.3	19.0 ± 52.8	13.3469 ± 0.0123	0.62	17
25	89939.80 ± 0.26	0.29 ± 0.10	2.8	155.3 ± 23.6	13.2907 ± 0.0056	0.74	19
24	90403.90 ± 0.39	0.13 ± 0.11	1.2	77.6 ±109.4	12.8612 ± 0.0212	1.47	15
23	90615.06 ± 0.36	0.11 ± 0.20	0.6	180.4 ±104.7	12.9277 ± 0.0212	1.34	19
20	117932.25 ± 0.25	0.08 ± 0.06	1.3	68.2 ± 70.5	5.0557 ± 0.0168	0.69	11
16	118283.26 ± 0.38	0.08 ± 0.06	1.4	113.8 ± 76.7	4.9355 ± 0.0162	1.02	10
15	118965.06 ± 0.87	0.42 ± 0.49	0.9	321.5 ± 28.3	4.8402 ± 0.0082	1.59	17
13	118628.55 ± 0.36	0.27 ± 0.13	2.0	321.9 ± 25.9	4.8887 ± 0.0063	1.32	19
12	120072.80 ± 0.46	0.33 ± 0.08	4.2	267.6 ± 46.6	4.6849 ± 0.0118	1.42	10
11	120246.57 ± 0.34	0.18 ± 0.07	2.8	32.6 ± 42.4	4.5717 ± 0.0102	1.01	10
7	122049.78 ± 0.30	0.34 ± 0.08	4.1	181.9 ± 25.1	4.4759 ± 0.0062	1.02	13
4	133423.55 ± 0.32	0.12 ± 0.07	1.6	110.7 ± 64.5	3.1829 ± 0.0153	1.33	18
3	133745.13 ± 0.36	0.08 ± 0.07	1.3	8.9 ±141.9	3.1613 ± 0.0360	1.37	17
1	136522.47 ± 0.17	0.05 ± 0.04	1.3	27.8 ± 61.7	2.9377 ± 0.0132	0.57	19

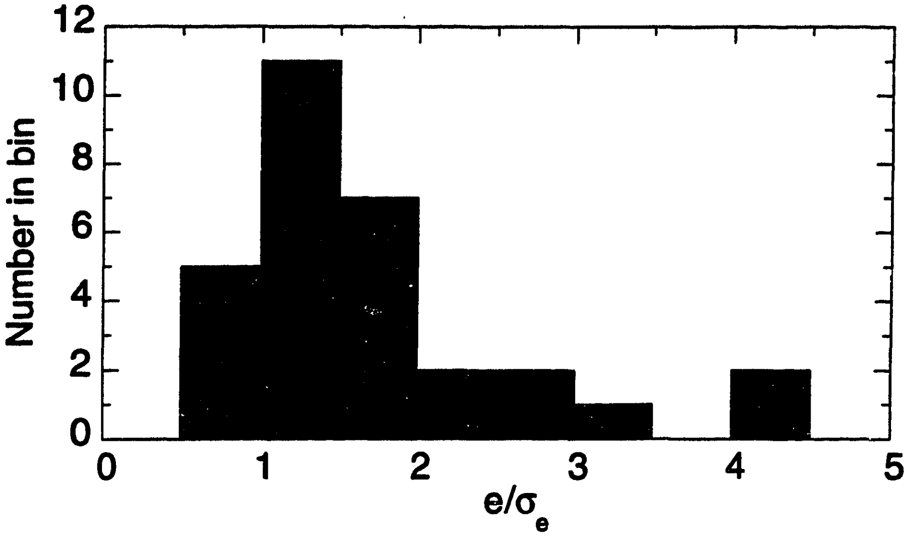

FIG. 6.1. Distribution of ratio of fitted eccentricity to formal error in eccentricity for partial fits to features presumed circular (Table 6.3). Note the surprising lack of values with e/σ_e between 0 and 0.5. For circular features, as most of these are presumed to be, one would expect this area to be more highly populated. However, the limited longitudinal coverage and large radial scatter of data points results in spurious incidents of non-circularity. See text for further discussion.

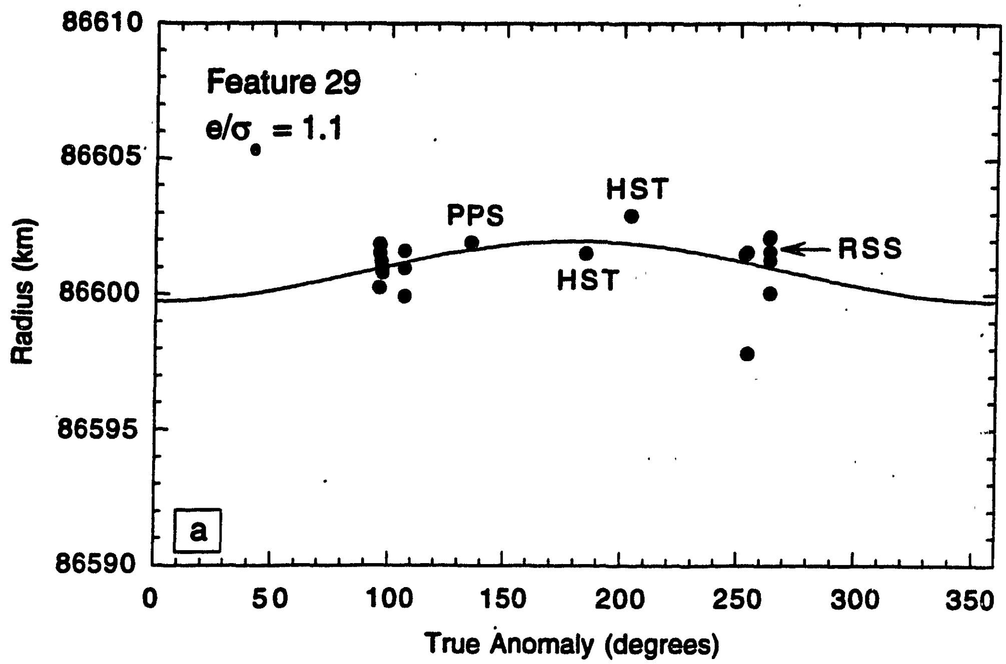

FIG. 6.2. True anomaly vs. radius for 4 features presumed circular. In these plots, all points from the GSC6323-01396 (HST), δ Sco (PPS), and RSS occultations are labeled. All other points are from many observations of the 28 Sgr occultations. Note the relatively large scatter of these points, which may contribute to the frequent non-zero eccentricities. (a) Feature 29.

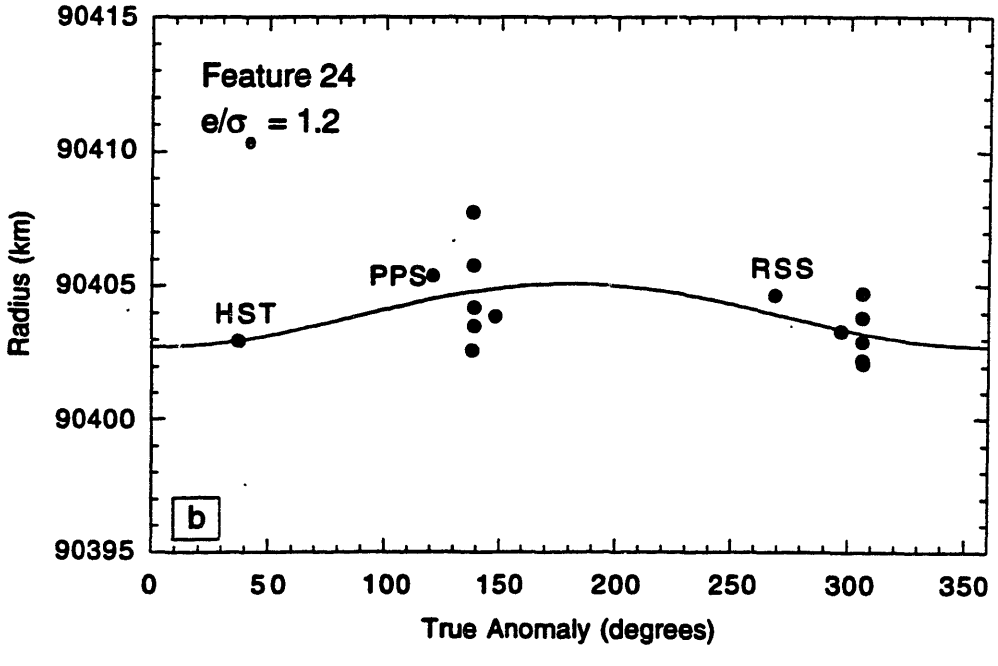

FIG. 6.2 (b). Feature 24.

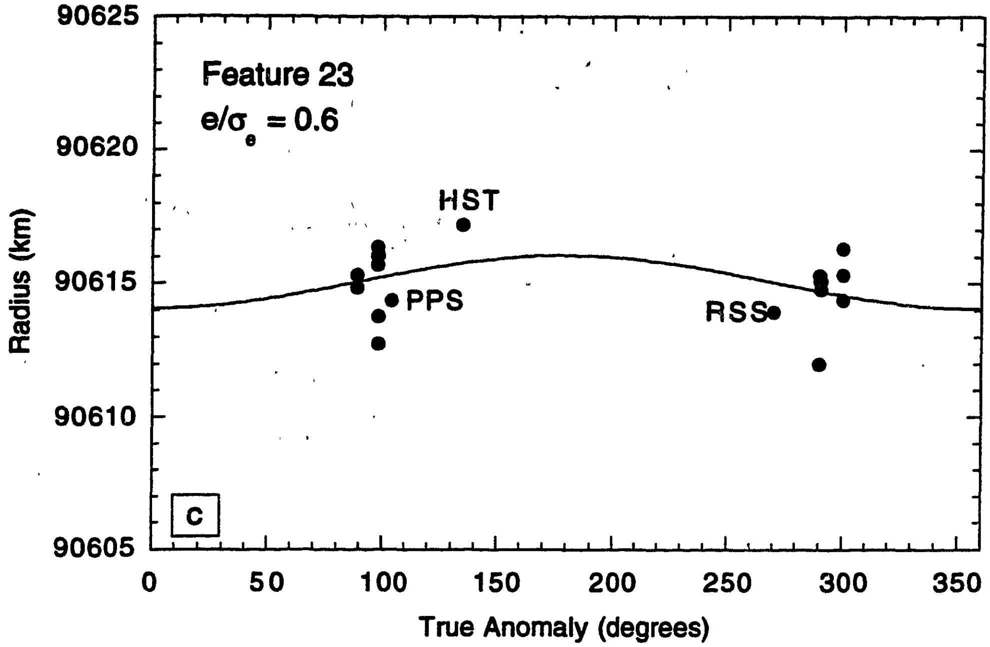

FIG. 6.2 (c). Feature 23.

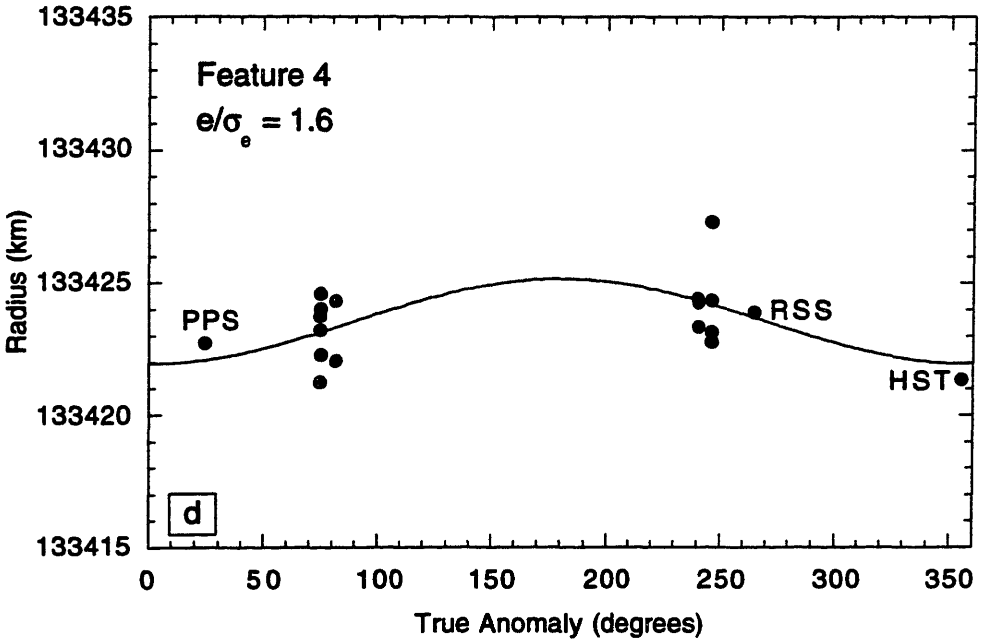

FIG. 6.2 (d). Feature 4.

For now, we select as the criterion for non-circularity an eccentricity that is 1.5 times the error in the eccentricity. All features conforming to this criterion were then subjected to a full fit, in which we fit for semimajor axis, eccentricity, longitude of periapse, and apsidal precession rate, along with the usual geometric parameters of pole position, clock offsets, star position offsets, and circular feature radii. We included the apsidal precession rate as a fitted parameter (with an initial value that found in the partial fits). We found that the fitted values of these (from the partial fits, Table 6.3) were often significantly different from those predicted by the NP88 values of gravitational harmonics; there are perturbations to these rates which need to be accounted for when dealing with our current level of accuracy (see Section 11). The non-circular features results of this full fit are given in Table 6.4. At this point, we reject any features with eccentricity less than twice its formal error. This leaves eight features of those previously presumed circular that have possibly significant eccentricities: 44 (inner edge of C Ring), 40, 34, 25 (outer edges of C-Ring plateaus), 13 (outer edge of a Cassini Division gap), 12 (outer edge of the 1.990 R_S ringlet), 11 (inner edge of the 1.994 R_S ringlet), and 7 (inner edge of A Ring). Fig. 6.3 shows plots of the true anomaly (J2000.0, Voyager 1 epoch) against ring-plane radius from the full fit for each of these features.

Table 6.4. Full Fit to Features with $e > 1.5\sigma_e$

Feature	a (km)	$e \times 10^4$	e/σ_e	ϖ_0 (deg)	$\dot{\varpi}$ (deg day^{-1})	$\dot{\varpi}_{\rm pred}$
44*	74492.16 ± 0.68	0.90 ± 0.27	3.3	252.2 ± 16.0	26.5578 ± 0.0035	26.5527
40*	76262.79 ± 0.82	0.78 ± 0.39	2.0	254.1 ± 22.7	24.3484 ± 0.0050	24.3385
39	77164.42 ± 0.53	0.23 ± 0.12	1.9	153.5 ± 55.8	23.2853 ± 0.0118	23.3031
37	79263.86 ± 1.14	0.88 ± 0.58	1.5	355.4 ± 25.1	21.0906 ± 0.0057	21.1053
36	82040.40 ± 0.57	0.06 ± 0.05	1.2	261.0 ±225.6	18.6029 ± 0.0391	18.5950
34*	84949.08 ± 0.57	0.20 ± 0.10	2.0	89.5 ± 80.8	16.3315 ± 0.0206	16.3661
31	85921.36 ± 0.65	0.44 ± 0.25	1.8	79.7 ± 23.3	15.6200 ± 0.0053	15.6990
26	89786.63 ± 0.54	0.11 ± 0.09	1.2	18.2 ±107.0	13.3456 ± 0.0241	13.3711
25*	89939.78 ± 0.57	0.34 ± 0.14	2.4	153.7 ± 26.6	13.2906 ± 0.0064	13.2884
13*	118628.47 ± 0.68	0.30 ± 0.13	2.3	321.4 ± 22.0	4.8886 ± 0.0053	4.8975
12*	120072.80 ± 0.77	0.35 ± 0.09	3.9	287.6 ± 38.5	4.6907 ± 0.0097	4.6901
11*	120246.47 ± 0.68	0.17 ± 0.06	2.8	32.5 ± 43.1	4.5707 ± 0.0103	4.6659
7*	122049.66 ± 0.67	0.36 ± 0.08	4.5	178.9 ± 23.8	4.4752 ± 0.0059	4.4242
4	133423.41 ± 0.73	0.10 ± 0.06	1.7	75.9 ± 93.3	3.1728 ± 0.0233	3.2198

* Indicated features are likely to be eccentric. Others are presumed circular.

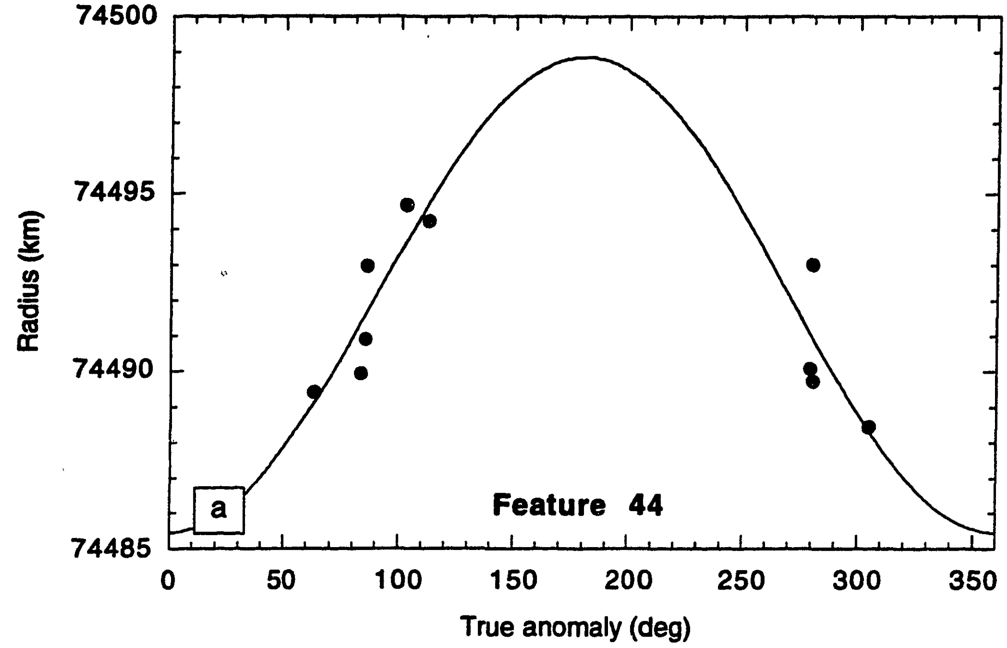

FIG. 6.3. Radius vs. true anomaly (J2000.0) for suspected non-circular features: (a) Feature 44, inner edge of C Ring.

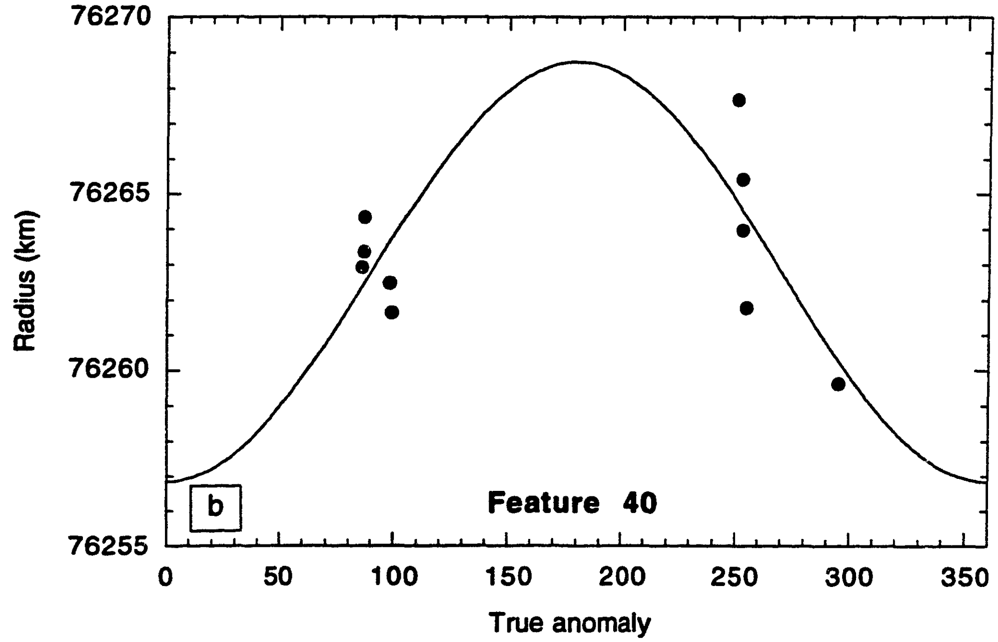

FIG. 6.3 (b). Feature 40, outer edge of a C-Ring plateau.

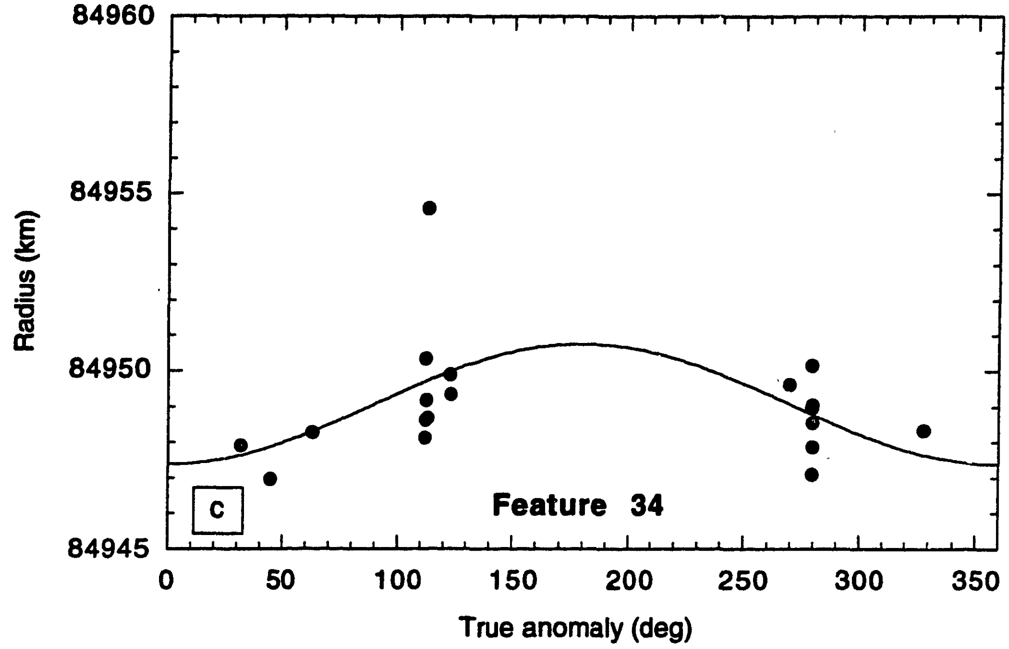

FIG. 6.3 (c). Feature 34, outer edge of a C-Ring plateau.

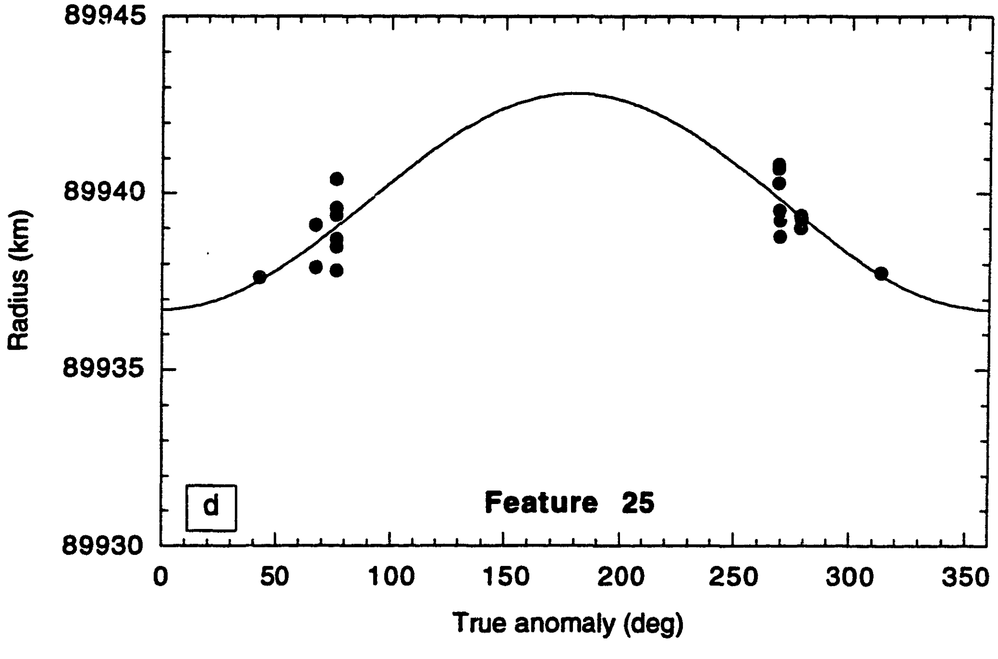

FIG. 6.3 (d). Feature 25, outer edge of a C-Ring plateau.

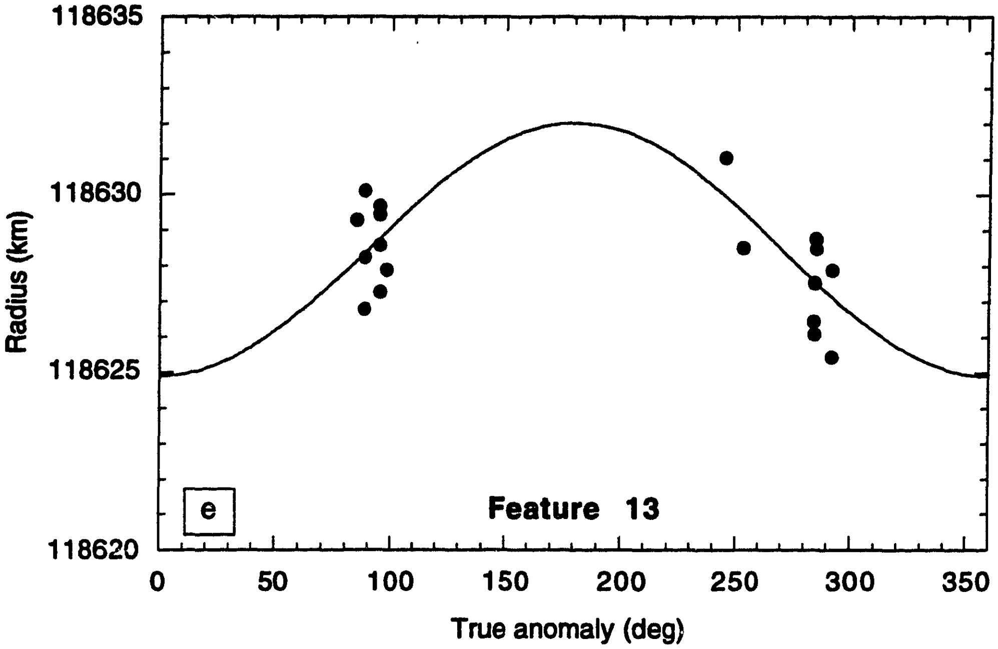

FIG. 6.3 (e). Feature 13, outer edge of a gap in the Cassini Division.

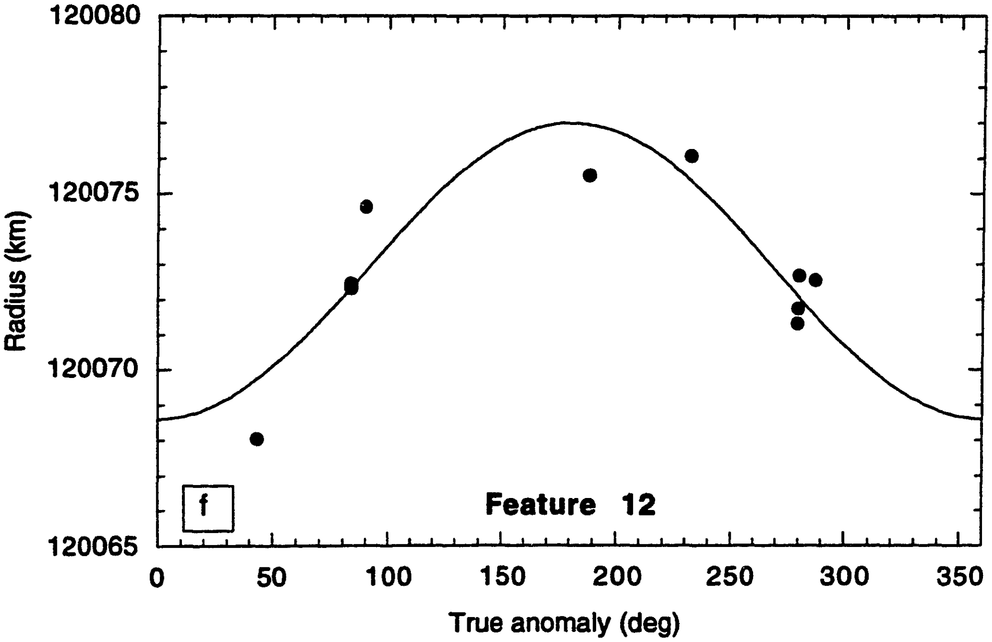

FIG. 6.3 (f). Feature 12, outer edge of 1.990 R_S ringlet.

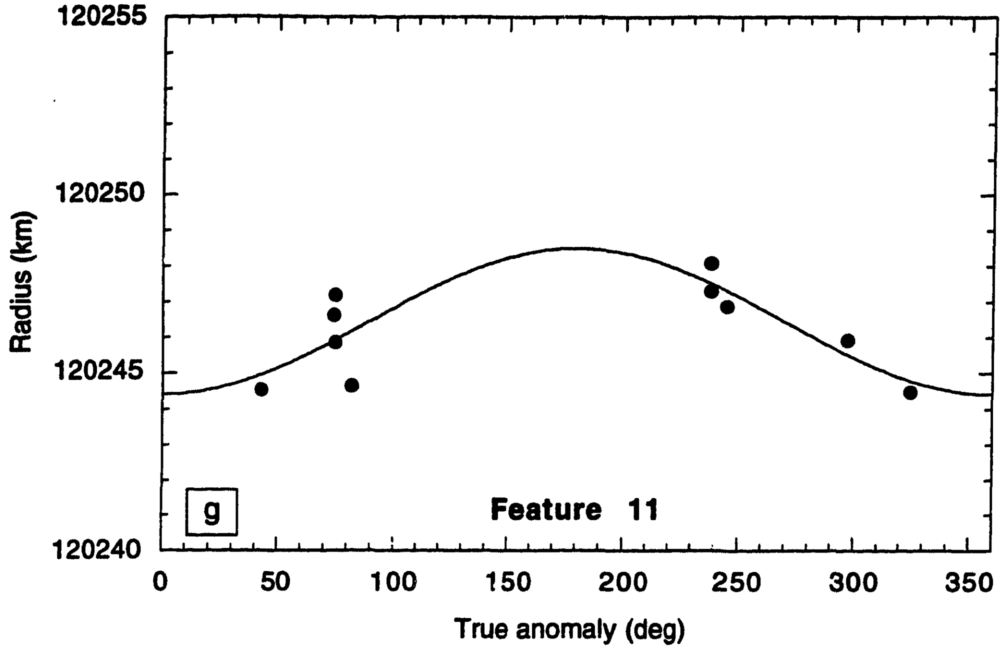

FIG. 6.3 (g). Feature 11, inner edge of 1.994 R_S ringlet.

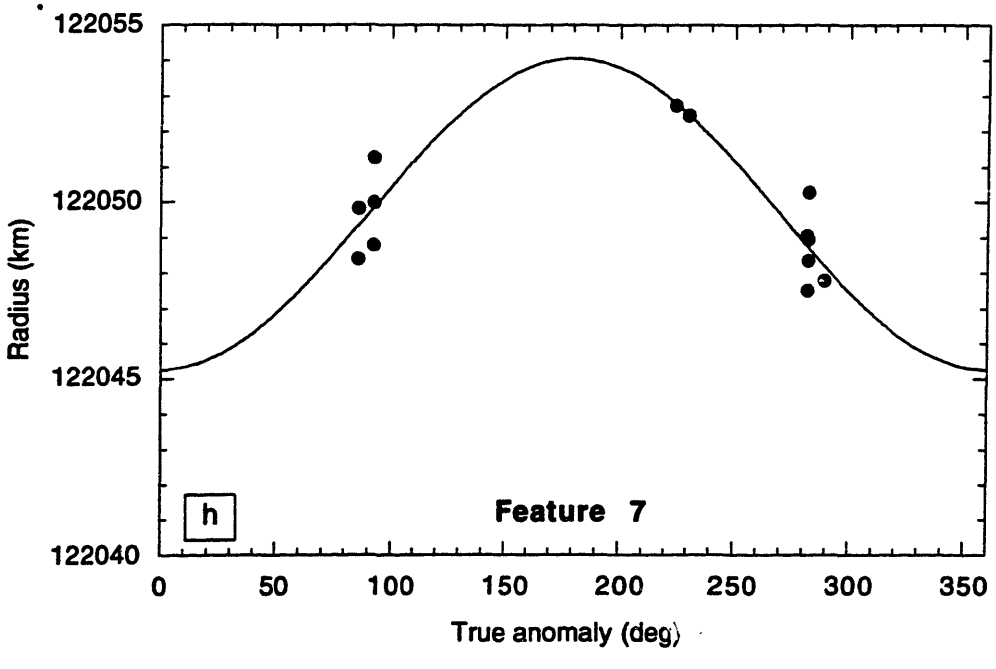

FIG. 6.3 (h). Feature 7, inner edge of A Ring.

Examination of Fig. 6.3 shows that some of the features with statistically significant eccentricities in fact appear ill-constrained because data exist only at the nodes, not near periapse or apoapse. These are all features except 44. This is a highly subjective step, and one could argue for including or rejecting almost any of the above features as eccentric. Additional data, filling in some gaps in longitude, will help to determine which of these features are eccentric. For now, we adopt feature 44 as the only new eccentric feature. This feature has an amplitude of 7 ± 2 km. As noted in Section 4, Table 4.1, there are no Lindblad resonances near this feature.

Inclinations

In addition to undiscovered non-circular features, the accuracy of the pole solutions also depends on the inclinations of those features assumed to be equatorial (all features). To find initial parameters for fits to ring inclinations and longitudes of ascending nodes, we first perform a full fit, holding the pole of the mean ring plane, ring radii, clock offsets, and gravitational harmonics fixed, and fitting for inclinations and longitudes of ascending nodes for all rings. The nodal regression rate is determined from the values of the gravitational harmonics (here we use the NP88 values). The results of this restricted full fit are given in Table 6.5. Using the same criterion as employed when searching for ring eccentricities, we find three features which warrant further investigation: feature 4 (inner edge of the Encke Gap), feature 11 (inner edge of the 1.994 R_S ringlet), and feature 15 (outer edge of a gap in the Cassini Division). The inclinations and longitudes of ascending nodes for these three features are then included as fitted parameters in a full fit, results for which are given in Table 6.6. None of these features have significant inclinations; therefore we conclude that our assumption that all rings are equatorial is adequate for our current level of accuracy.

Table 6.5. Investigation of Features for Inclinations.

Feature	i	$\lvert i \rvert/\sigma_i$	Ω_0[a]
44	–0.000252 ± 0.000378	0.7	55.4 ± 50.3
40	–0.001558 ± 0.002062	0.8	76.8 ± 24.8
39	–0.000418 ± 0.000637	0.7	2.9 ± 71.1
162	0.000753 ± 0.000324	2.3	11.9 ± 13.6
38	0.000419 ± 0.000694	0.6	294.6 ± 180.
37	–0.000281 ± 0.000320	0.9	350.3 ± 180.
36	–0.000093 ± 0.000333	0.3	73.0 ± 180.
35	–0.000107 ± 0.000402	0.3	34.0 ± 163.3
34	0.000592 ± 0.000615	1.0	307.9 ± 17.5
33	–0.000345 ± 0.000330	1.0	314.1 ± 20.2
42	–0.000467 ± 0.000652	0.7	37.8 ± 22.0
31	0.000408 ± 0.000472	0.9	47.0 ± 41.0
30	–0.000140 ± 0.000491	0.3	327.4 ± 39.8
29	–0.000116 ± 0.000176	0.7	83.5 ± 37.9
160	0.000414 ± 0.000309	1.3	55.4 ± 23.9
28	0.000211 ± 0.000176	1.2	65.2 ± 30.8
158	–0.000294 ± 0.000332	0.9	331.5 ± 18.7
27	0.000287 ± 0.000295	1.0	206.4 ± 180.
41	0.000124 ± 0.000166	0.7	42.6 ± 70.6
26	–0.000244 ± 0.000464	0.5	350.7 ± 34.6
25	–0.000032 ± 0.000210	0.2	86.4 ± 179.5
156	0.000128 ± 0.000286	0.4	325.8 ± 62.4
24	0.000118 ± 0.000463	0.3	316.8 ± 180.
23	–0.000179 ± 0.000250	0.7	3.1 ± 58.5
153	–0.000161 ± 0.000445	0.4	317.9 ± 180.
20	–0.000110 ± 0.000158	0.7	321.8 ± 31.3
16	–0.000185 ± 0.000191	1.0	303.0 ± 31.2
15	–0.001828 ± 0.000721	2.5	311.4 ± 2.9
13	–0.000178 ± 0.000255	0.7	299.8 ± 37.9
112	–0.000165 ± 0.000235	0.7	314.3 ± 22.2
11	0.000522 ± 0.000354	1.5	296.9 ± 10.5
7	0.000238 ± 0.000175	1.4	318.4 ± 37.7
4	0.000263 ± 0.000170	1.5	60.5 ± 14.4
3	0.000141 ± 0.000229	0.6	313.1 ± 154.6
1	0.000068 ± 0.000123	0.6	40.7 ± 46.5

[a] Some values of the longitude of the ascending node were unconstrained because the feature inclination was low. The formal error for these was greater than 180°, but for the table were set to 180°.

Table 6.6. Results of Full Fit for Possibly Inclined Features.

Feature	i	$\lvert i \rvert / \sigma_i$	Ω_0
11	0.001748 ± 0.002698	0.6	305.3 ± 17.1
15	−0.001939 ± 0.001827	1.1	307.2 ± 15.3
4	0.000916 ± 0.012000	0.1	57.3 ± 15.4
162	0.000668 ± 0.003790	0.2	18.1 ± 180.

Adopted Solution

Because we discovered one new eccentric feature (feature 44), we perform Fit 7 (Table 6.2). As expected, the results are indistinguishable from those of Fit 5. This is because we alter only one feature. Feature 44 does not have much control over the position of the pole, as evidenced by the similarity of Fits 5 and 7, and also by the similarity of the parameters found in the partial fit (Table 6.3) and the full fit (Table 6.4). We found no inclined features. We could add to the number of data points fit by our model by including all non-circular features with well-known orbit models. These include feature 44 and those features studied in detail in Section 9. This adds at most 9 features to the 29 features already included in Fit 7. Test fits of this type have shown that inclusion of these non-circular features does not affect the position of the pole or the radius scale significantly. In fact, the change in pole position is much less than one formal error. While the geometric parameter values do not change very much, the formal errors increase because many of the non-circular features we add have higher rms values than the circular ones in Fit 7. Although we do not present a fit of this type here, this is a desirable direction for future fits, as performing a fit in this manner produces a geometric solution that is takes into account as many ring features as possible, and gives a globally consistent solution.

Fit 7 (Table 6.2) is the most comprehensive solution for Saturn ring geometry to date. It includes data from the RSS, PPS, 28 Sgr, and GSC6323-01396 occultations (spanning almost 11 years). It does not include feature 44, which was previously included as a circular feature but was found in this work to have significant eccentricity. No features were found to be inclined. It fits for star position offsets for 28 Sgr and GSC6323-01396, and clock offsets for all 28 Sgr stations except IRTF. It includes in-track errors for the Voyager 1 and 2 ephemerides (in the form of clock offsets). Full results of this adopted fit are presented in Table 6.7. This table also lists rms residuals per degree of freedom by feature and by station. The radius residuals per observing station are displayed in Fig. 6.4.

We note that a previous fit for α_0 and δ_0 offsets to δ Sco was attempted (to compensate for E-terms which were not accounted for in the position of this star). The fitted value was statistically indistinguishable from zero, so we fixed the value at zero.

Table 6.7. Adopted Solution[a]

Saturn Ring-Plane Pole, Voyager 1 epoch	Adopted Solution[a], Present Work
α_n (deg, J2000.0)	40.59287 ± 0.00470
δ_n (deg, J2000.0)	83.53833 ± 0.00022
$d\alpha_n/dt$ (deg yr^{-1}, J2000.0)	−0.00061172
$d\delta_n/dt$ (deg yr^{-1}, J2000.0)	−0.00006420
Gravitational Harmonic Coefficient	
J_2	0.016301 (fixed)

Star	$\alpha_0 \cos\delta_s$ (arcsec)	δ_0 (arcsec)
GSC6323-01396	0.896121 ± 0.000064	−0.108080 ± 0.000052
28 Sgr	0.152137 ± 0.000074	−0.125815 ± 0.000072
δ Sco	0.0	0.0
RSS	0.0	0.0

Station Code[b]	Clock Offset, t_0 (s)	RMS (km)	Station Code[b]	Clock Offset, t_0 (s)	RMS (km)
HST	0.000	1.78	MCD	−0.077 ± 0.011	0.76
CAT	−0.077 ± 0.016	1.31	MMT	−0.110 ± 0.018	1.68
CTIO	−0.060 ± 0.017	0.81	PAL	−0.033 ± 0.012	0.99
ESO1	0.166 ± 0.018	1.30	SPM	−0.020 ± 0.013	1.26
ESO2	0.146 ± 0.018	1.57	UKIRT	−0.043 ± 0.015	1.92
IRTF	0.000	0.96	PPS	0.094 ± 0.072	1.23
KPi	−0.110 ± 0.017	1.62	RSS	−0.011 ± 0.046	1.15
KPe	−0.102 ± 0.018	0.79			

Circular Features

Feature[b]	Semimajor Axis (km)	RMS (km)	Feature[b]	Semimajor Axis (km)	RMS (km)
40	76263.51 ± 0.74	2.07	26	89786.77 ± 0.51	0.73
39	77164.44 ± 0.51	0.95	25	89939.26 ± 0.51	0.92
38	79220.38 ± 0.50	0.81	24	90403.97 ± 0.59	1.51
37	79264.83 ± 0.65	1.79	23	90614.97 ± 0.54	1.27
36	82040.61 ± 0.54	0.49	20	117932.16 ± 0.62	0.66
35	84749.39 ± 0.52	1.34	16	118283.33 ± 0.62	0.98
34	84949.17 ± 0.56	1.63	13	118628.33 ± 0.63	1.40
33	85660.66 ± 0.53	0.74	15	118965.93 ± 0.67	1.60
42	85758.45 ± 0.58	1.63	12	120072.84 ± 0.89	2.32
31	85921.22 ± 0.62	1.48	11	120246.25 ± 0.68	1.30
30	86370.52 ± 0.50	0.71	7	122049.75 ± 0.72	1.60
29	86601.17 ± 0.50	1.08	4	133423.49 ± 0.69	1.41
28	88594.25 ± 0.52	0.91	3	133745.16 ± 0.69	1.32
27	89188.55 ± 0.51	0.81	1	136522.35 ± 0.67	0.58
41	89295.01 ± 0.51	1.08			

[a] Fit 7 of Table 6.2.

[b] Station codes and feature names are after F93. "HST" is the Hubble Space Telescope, used for observations of the occultation of GSC6323-01396.

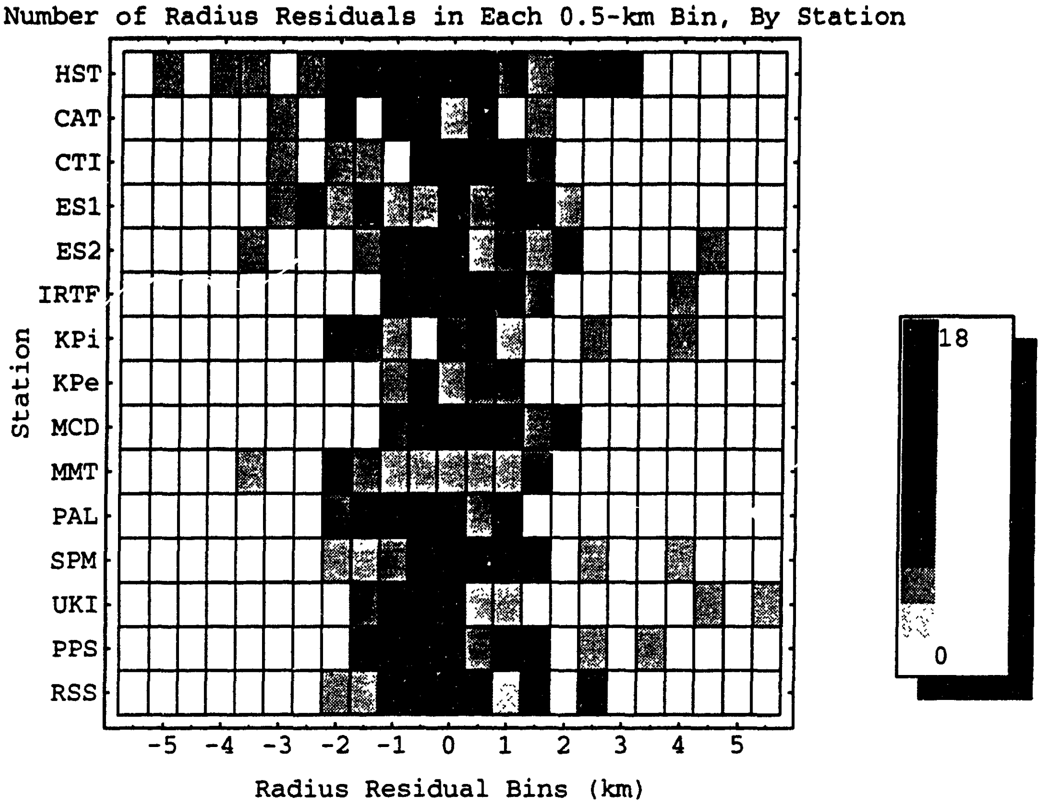

FIG. 6.4. Radius residuals by station. The number of radius residuals in each 0.5-km bin are displayed in this figure. The grey-scale key on the right provides the mapping from grey level to number of points in a bin. All residuals are included in this figure; that is, there are no radius residuals that fall outside of the range plotted here.

Comparison with Other Solutions

The ring-plane pole determined from Fit 7 differs from that of F93 by approximately 1 formal error: differences in pole right ascension and declination are –0.0016 ± 0.0059 and 0.0002 ± 0.0003 degrees, respectively. The differences between this analysis and that of F93 are that we include an additional data set (HST), more clock offsets as fitted parameters, and offsets to the star position rather than to the planet ephemeris. In addition, we do not include feature 44 nor any feature in the B ring as circular. Pole positions from this adopted solution, F93, and NCP are plotted in Fig. 6.5. Because there is little difference in pole position, feature radii are also similar. Differences in feature radii are plotted in Fig. 6.6.

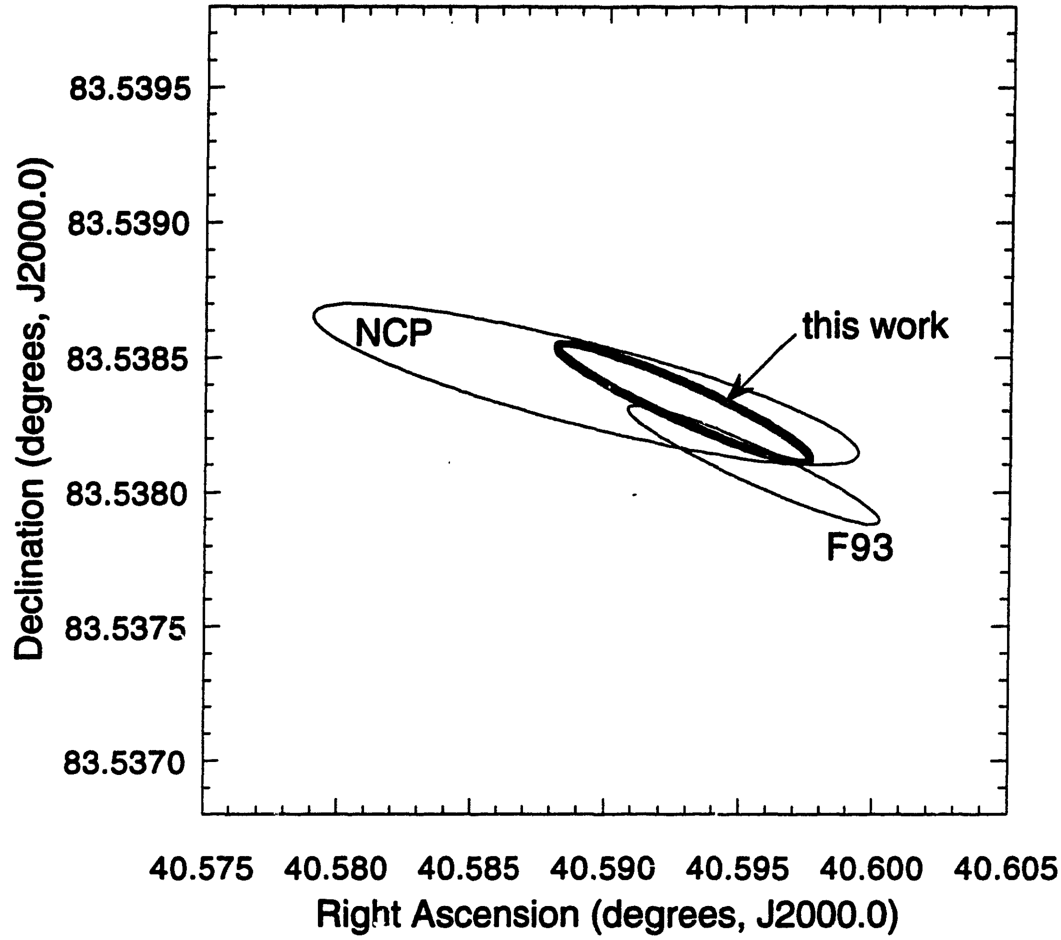

FIG. 6.5. Plot of pole solutions, all in J2000.0 at the Voyager 1 epoch. Included are the adopted solution from this work (including data from GSC6323-01396, 28 Sgr, δ Sco, and RSS occultations), F93 (28 Sgr, δ Sco, and RSS), and NCP (δ Sco and RSS). Because the pole locations of the adopted solution and of F93 differ by about 1 formal error, their error ellipses overlap only slightly.

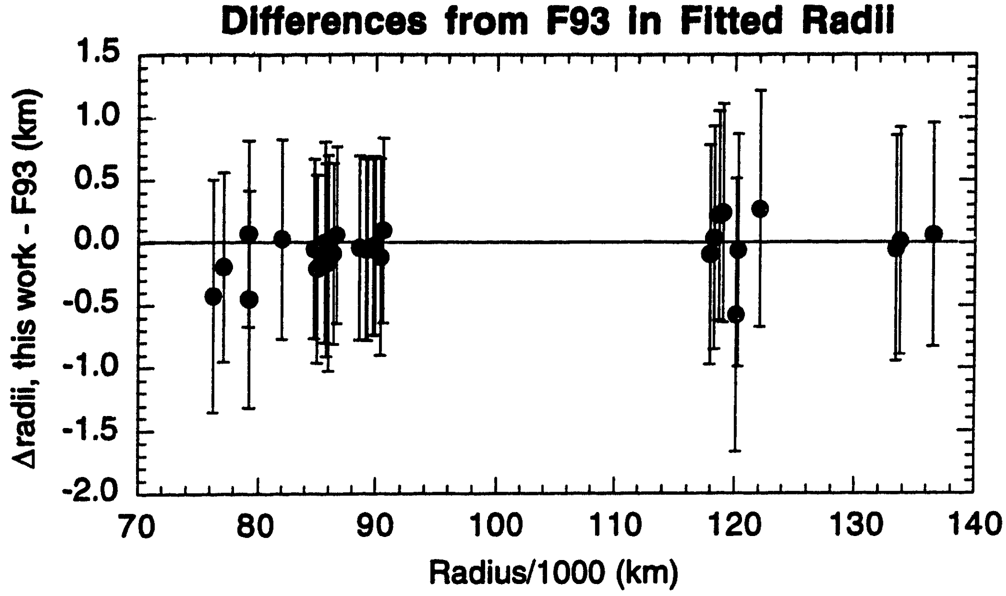

FIG. 6.6. Feature radius differences between the adopted solution of this work and that of F93. The radii are expected to be approximately equal because the ring-plane poles of the two solutions are similar. In fact the radii are very similar, with no systematic differences apparent.

The clock offsets for Voyagers 1 and 2 are found to be –0.01 ± 0.05 and 0.09 ± 0.07—within the upper limits of 0.10 and 0.17 sec respectively (NCP). We see similar behavior of 28 Sgr clock offsets as was noted in E93. As in E93, we assume this indicates discrepancies in station coordinates and/or some real clock offsets.

7. COMPARISON WITH OTHER METHODS OF RADIUS DETERMINATION

Because the radii determined from Fit 7 differ so little from those of F93, the discussion therein concerning other methods of radius determination also applies here. Alternate methods for determining radii of ring features include: determination of density wave radius by fitting amplitude and wavelength to a model that determines location and surface density (Brophy and Rosen 1992, and references therein; Rosen *et al.* 1991a; Rosen *et al.* 1991b); and through modeling the wake produced on the Encke Gap edges by the satellite Pan (Showalter 1991; Showalter *et al.* 1986). A summary of radii determined from these methods and in this work is presented in Table 7.1.

Table 7.1. Methods of Radius Determination

Method	Radius Difference (km): adopted soln - alt method	Reference
Density wave linear model	-5	Rosen *et al.* (1991b)
Density wave dispersion model	<-1	Rosen *et al.* (1991b)
Pan wake analysis	2.9	Showalter (1991)

As F93 state, the density wave-determined radii are consistent with those of F93, and are therefore consistent with the radii found in this work. Density waves arise at Lindblad resonances (inner and outer) with satellites; bending waves can form at vertical resonances (Shu 1984). These waves arise because of the self-gravity of the ring material. Therefore, one can fit the observed structure to a model whose parameters include satellite mass and location, location in the rings, and local surface density. Current density and bending wave models do not take into account the local surface density enhancements that have been observed in both density waves and bending waves (Bosh 1990; Gresh *et al.* 1986; Rosen *et al.* 1991b). This unmodeled effect can change the radius determined through density and bending wave modeling by up to 3 km (NCP).

The other method of radius determination considered here applies to only two ring features: the inner and outer edges of the Encke Gap, features numbers 4 and 3 respectively. The satellite Pan orbits near the center of the Encke Gap. The presence of this satellite was predicted in 1986 based on waves observed on both edges of the Encke Gap (Cuzzi and Scargle 1985). The satellite was later found in Voyager images of the Encke Gap, very near the predicted location (Showalter 1991). In addition to causing waves on the edges of the gap, this satellite also produces a "wake" (similar to a water wake produced by a boat) that propagates inward from the inner edge and outward from the outer edge. As a water wake is stationary with respect to the boat, this wake is also stationary in the frame corotating with the satellite. The physics describing the formation of this wake are different from those of density and bending waves, as the self-gravity of the ring particles does not play a role (and thus the local surface density does not affect the shape of the wake). Instead, this wake is formed when ring particles receive a small gravitational "kick" when passing the satellite, resulting in a small radial velocity and thus an eccentricity. Because the ring particles at different radii move at different orbital speeds (Keplerian shear), differences in density develop and become observable as a wake. This regular pattern of densities is modeled with parameters describing the number of wavelengths from the satellite and the orbital velocities of the satellite and the ring material in the wake. Using this model, Showalter (1991) finds locations for these two features. These radii are 2.9 km smaller than those found in this work. The accuracy of the radii determined by Showalter depends on the measurement accuracy of the mean motion of Pan (~0.006 deg day^{-1}) and knowledge of Saturn's mass and gravity field.

8. POLE PRECESSION

The combination of recent high-resolution data sets has allowed pole solutions with formal errors small enough to be able to detect the precession of Saturn's pole over the 11 years between the Voyager 1 RSS data set and the GSC6323-01396 HST data set. As summarized in F93, the pole precession resulting solely from solar torques is expected to have a period of 7×10^6 years, for a pole displacement of 0.7 arcsec in 9 years, or 0.9 arcsec in 11 years. In contrast, the formal error in the pole position is approximately 1.7 arcsec, larger than the predicted motion. However, F93 argue that greater contributors to pole precession than direct solar torques are solar torques on satellites transferred to Saturn through the strong planet-satellite torques (primarily Titan). This decreases the precession period by about a factor of 4, making the predicted displacement 3.4 arcsec in 11 years. This displacement is larger than the formal error in the pole position, and therefore we should be able to measure it.

The largest source of error in this theoretical determination of Saturn's precession rate is the uncertainty in the value of Saturn's moment of inertia (F93). This amounts to an uncertainty of approximately 10% of the rate. This is small compared with our fitted errors in this rate. Another source of uncertainty in the precession rate is its dependence on the instantaneous obliquity of Saturn vs. the orbit-averaged value. Currently, the instantaneous value is less than half the average value. Depending on the response of the system to the changing torque, the instantaneous value of the precession rate could be less than that presented by F93 (Nicholson, 1993, private communication).

In all fits including pole precession in this Section, we fix the in-track offsets for Voyagers 1 and 2 (equivalent to clock offsets) at 0. This is necessary because the ring feature radii, and hence the pole position, are very strongly correlated with the Voyager in-track offsets. This strong correlation exists because both Voyager data sets are one-sided and therefore constrain the ring radii very little (see Section 6 for more discussion). Because both fitted in-track offsets (see Table 6.7) are close to 0, this is not an unreasonable approximation.

In Table 8.1 and Figure 8.1 we present a set of fits to various subsets of the occultation data sets used here. The numbering of these fits continues from Table 6.2. Fit 10 in Table 8.1 uses only the 28 Sgr, δ Sco, and RSS data sets. We fit for the ratio of the magnitude of pole precession consistent with the data sets to that predicted in F93 (value listed in Table 6.1). We refer to this as a fit for a common ratio. Note that this fixes the *direction* of pole precession at the predicted direction, and fits only for its magnitude. Fit 10 approximately reproduces F93's value of 0.86 ± 0.31 for this same ratio. This confirms the fidelity of our fitting method and numerical implementation. The value found in Fit 10 is consistent with a ratio of 1, which corresponds to a precession rate equal to the predicted value.

Fit 11 of Table 8.1 includes all four data sets in a fit for the common pole precession ratio. For this fit we find a common ratio of 1.30 ± 0.33, also consistent with a ratio of 1. Because there is some concern about the internal consistency of the 28 Sgr data set (Section 6) we perform Fit 12. This fit includes only the GSC6323-01396, δ Sco, and RSS data sets. We find a common ratio of –0.06 ± 0.97 for this fit, consistent with both no pole precession and the calculated precession rate (F93). As we did in Section 6, we attempt to place a further constraint on the radii by including data from one 28 Sgr station (MCD). We allow the clock offset for this station to be a fitted parameter, as are the star position offsets. In this way, we use the MCD data set to constrain the ring-plane radii, but not the pole. From this fit (Fit 13), we find a common ratio of 0.34 ± 0.78, consistent with ratios of both 0 and 1. The last fit in this table, Fit 14, is similar to Fit 13. It differs in that the star position offsets are held fixed at the value determined in Fit 7 (Table 6.2). The pole and radii are relatively insensitive to these parameters, so holding them fixed should not bias the result. In this fit, we find a common ratio of 0.55 ± 0.26. This fit provides the best solution for pole precession rate possible at this time. It is unaffected by any lingering inconsistencies in the 28 Sgr data set.

These fits provide evidence that the true pole precession rate is close to the rate calculated by F93. Observations of the crossing of the Earth through Saturn's ring plane in 1995 may help resolve this issue, if times of crossing can be determined accurately enough. The accuracy of these measurements will depend on the complexities of the photometric model for Saturn's rings as they near the edge-on configuration. If the time of ring-plane crossing can be determined, this will aid in the determination of the rate of pole precession because the time of crossing differs by as much as an hour depending on the magnitude of the precession (Nicholson and French 1993).

Table 8.1. Geometric Fits Including Pole Precession

Fit Code	Data Sets[a]	Coordinates of Pole[b] (deg) α_n	δ_n	Precession Rate Ratio[c]	Radius of Feature 23 (km)	RMS (km)
10	SV	40.5893 ± 0.0013	83.53836 ± 0.00004	0.90 ± 0.31	90615.42 ± 0.37	1.30
11	GSV	40.5896 ± 0.0013	83.53838 ± 0.00004	1.30 ± 0.33	90615.63 ± 0.38	1.33
12	GV	40.5889 ± 0.0017	83.53837 ± 0.00006	–0.06 ± 0.97	90616.17 ± 0.70	1.15
13	GMV	40.5893 ± 0.0015	83.53838 ± 0.00005	0.34 ± 0.78	90616.14 ± 0.49	1.01
14	GMV	40.5887 ± 0.0013	83.53833 ± 0.00004	0.55 ± 0.26	90615.73 ± 0.57	1.24

[a] Data set codes are: (G) GSC6323-01396, (S) all 28 Sgr stations, (M) MCD station of 28 Sgr, and (V) Voyager δ Sco and RSS.

[b] The pole position are given at the Voyager 1 epoch.

[c] The precession rate ratio is the ratio of the precession rate consistent with the data to that predicted by F93.

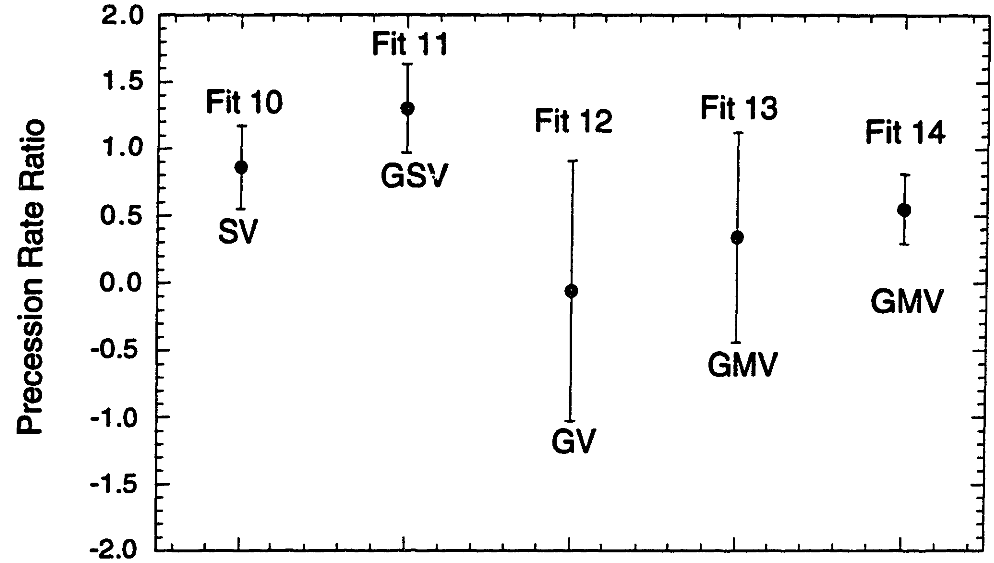

FIG. 8.1. Fitted values of the ratio of measured pole precession rate to the rate predicted by F93. A fitted value for precession rate equal to the predicted value would have a ratio of 1. A fit consistent with no polar precession would have a ratio of 0. In general the errors of these parameters are too large to conclude anything other than that the value of pole precession consistent with the available data is close to the predicted rate. The fit to GSC6323-01396, MCD/28 Sgr, δ Sco, and RSS data yields the smallest formal errors, and suggests a value for the precession rate that is half the predicted value. Data set codes are described in the footnote to Table 8.1.

9. NON-CIRCULAR FEATURES

In the previous sections, we presented a geometric solution incorporating all high-resolution occultation data sets currently available. We now use this solution and all data sets to investigate the kinematics of non-circular ring features. We study nine features: the outer edges of the A and B rings, the Titan, Maxwell, 1.470 R_S, 1.495 R_S, Huygens, and 1.990 R_S ringlets, and the inner edge of the C ring. For each of these ring features, we look at resonances that could be influencing their kinematics (see Table 4.1). We then investigate whichever portion of the ring feature is relevant: the outer edge of the 1.495 R_S ringlet, the center of the Huygens ringlet, etc. In this section, we study the kinematics of these ring features and compare the results with previous studies of this kind. In the next section, we investigate properties of ringlets.

Note that there are other features in Saturn's rings that have been identified as non-circular but are not included in this analysis: the F ring, the inner edge of the Encke gap, both edges of the Keeler gap, and several density and bending waves, to name a few. These features were not included in this analysis for one or more of several reasons: (i) they were not part of the set of measured features or there were too few data points (density and bending waves); (ii) the models are still being developed (Encke and Keeler gaps); or (iii) the features have not been modeled in the detail needed (F ring).

C Ring, Inner Edge (Feature 44)

The inner edge of the C ring, feature 44 (see Fig. 2.1), was previously thought to be circular. In Section 6, we found that this features has a significant eccentricity. The best-fitting model is an $m = 1$ ellipse with an amplitude of almost 7 km. There are no Lindblad resonances with known satellites located near this ring feature (Table 4.1), so we assume it is precessing freely under Saturn's non-spherical gravity field. In Table 9.1 we present results of fits to circular and elliptical models. Figure 9.1 shows the best-fit ellipse model and the data points. Because this feature is the closest freely-precessing feature to Saturn, it will be very sensitive to the higher-order gravitational harmonics (see Section 11).

Table 9.1. Model Fits for Inner Edge of C Ring (Feature 44)

Model[a]	m	a (km)	$e \times 10^4$	ϖ_0[b] (deg)	$\dot{\varpi}$ (deg day^{-1})	RMS (km)
this work						
circular	—	74491.52 ± 0.68	—	—	—	2.152
fp	1	74492.33 ± 0.59	0.88 ± 0.29	55.9 ± 10.9	26.5582 ± 0.0037	1.478

[a] "fp" indicates a freely-precessing, simple elliptical model.

[b] Epoch UTC 1980 11 13 03 17 40.

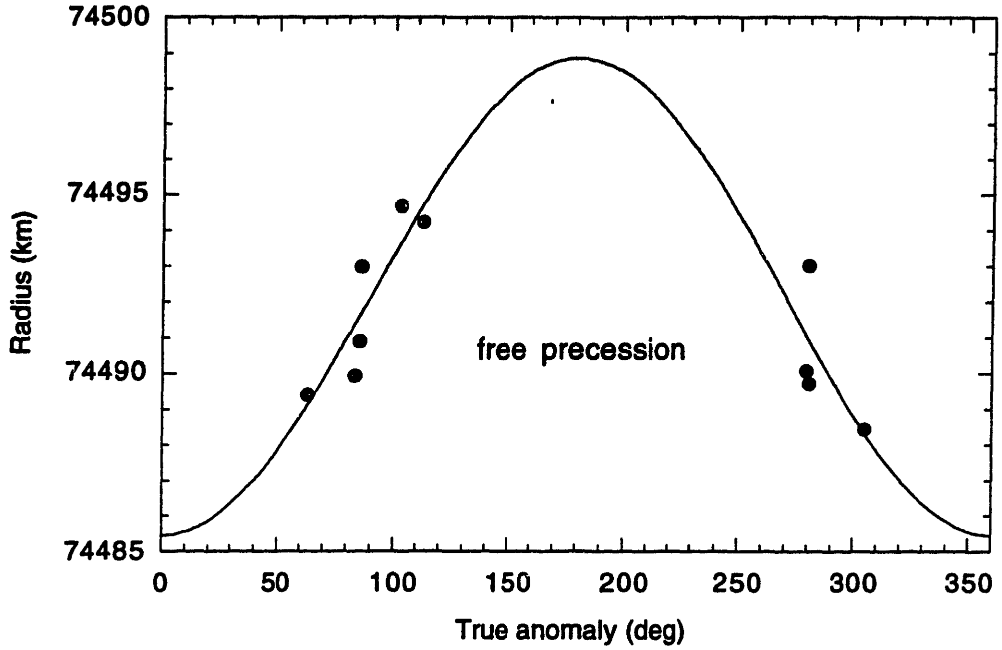

FIG. 9.1. Freely-precessing ellipse model for inner edge of C ring, feature 44. True anomaly is calculated at the epoch UTC 1980 11 13 03 17 40. This feature was discovered in this work to be non-circular. However, as apoapse and periapse were not sampled, this identification is still tentative.

Titan Ringlet, Center (Feature 162)

The Titan ringlet was previously shown to be in a 1:0 (apsidal) resonance with Titan (Porco *et al.* 1984, hereafter referred to as P84a). This means that the longitude of periapse of this ringlet precesses at a rate equal to the mean motion of Titan. The association of this ringlet with this resonance provides a very strong constraint on the values of gravitational harmonics for Saturn (see Section 11). We present results of kinematic model fits in Table 9.2. Notice that the rms residual per degree of freedom is smallest for the model in which the pattern speed is fixed at the value for the mean motion of Titan (Harper and Taylor 1993). The model with this pattern speed free has an only slightly higher rms value, and the parameter values are nearly identical. The higher rms value is explained by the different number of free parameters. In Table 9.2 we also include results from P84a. Upon examination of the current and previous results, we find excellent agreement. The 1σ discrepancy in semimajor axis values is due mainly to the different pole positions used (P84a used the STH pole). Use of the pole derived in this work instead of the STH pole would decrease radii by approximately 4-10 km. Therefore the agreement in these two quantities is quite good.

The agreement between P84a values of eccentricity and apsidal reference angle and values determined in this work are similarly good. At the epoch of these parameters, the longitude of Titan (J2000.0) is 276.9° (Rosen *et al.* 1991a). Thus we find that the periapse of the Titan ringlet is 172.9 ± 3.5 degrees away from Titan. For an eccentric ringlet outside the resonance location, we expect these longitudes to differ by 180°. Therefore we find that the periapse of the Titan ringlet is leading the apoapse of Titan's orbit by 7.1 ± 3.5 degrees. This is similar to the value found by NP88 for this same quantity: 13 ± 5. It is not clear at this point if this is an indication for libration. NP88 estimate a libration period of ~49 years, so it may be that this ringlet is librating around the apoapse of Titan. Additional temporal coverage is necessary to resolve this question.

Table 9.2. Model Fits for Center of Titan Ringlet (Feature 162)

Model[a]	m	a (km)	$e \times 10^4$	ϖ_0[b] (deg)	$\dot{\varpi}$ (deg day^{-1})	RMS (km)
this work						
circular	—	77874.19 ± 5.60	—	—	—	18.570
fp	1	77878.09 ± 0.53	2.53 ± 0.07	102.9 ± 7.5	22.5773 ± 0.0024	1.657
Titan 1:0	1	77878.06 ± 0.48	2.54 ± 0.07	104.0 ± 3.5	22.57697682	1.552
P84a[c]						
fp	1	77871 ± 8	2.6 ± 0.2	110 ± 16	22.57 ± 0.06	
Titan 1:0	1	77871 ± 7	2.6 ± 0.2	109 ± 5	22.577	

[a] "fp" indicates a freely-precessing, simple elliptical model. "Titan1:0" indicates the Titan 1:0 apsidal resonance model.

[b] Epoch UTC 1980 11 13 03 17 40.

[c] Values for longitude of periapse from this work are converted to our longitude system, precessed to J2000.0, and adjusted for the difference in epoch.

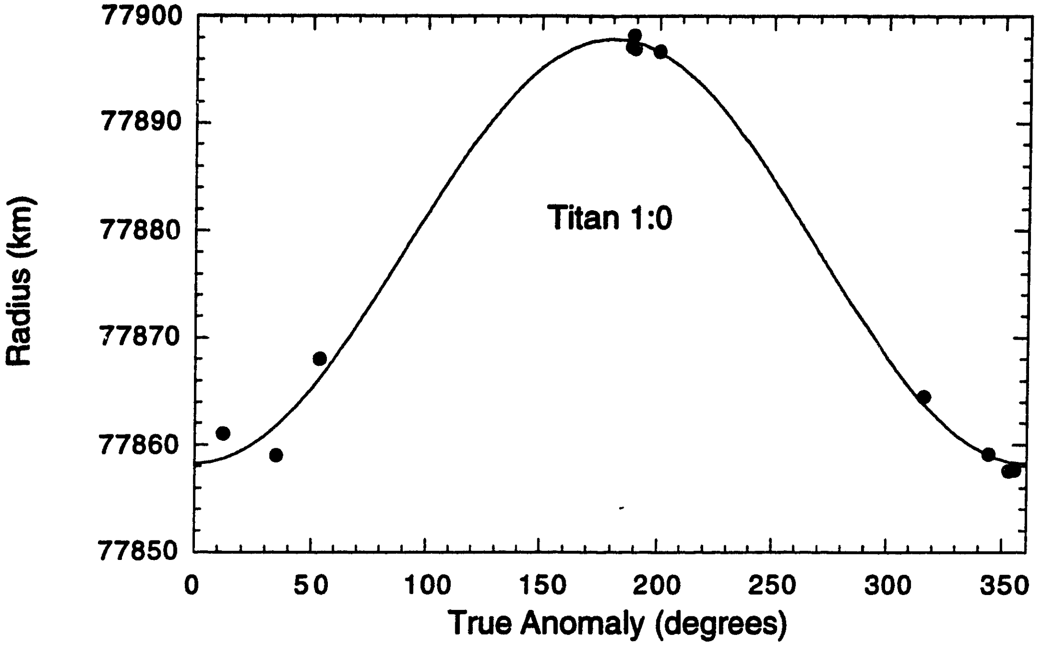

FIG. 9.2. Titan 1:0 apsidal precession model for the center of the Titan ringlet, feature 162. True anomaly is calculated at the epoch UTC 1980 11 13 03 17 40. The periapse of the model ellipse leads the apoapse of Titan's orbit by approximately 7°. This feature provides a tight constraint on Saturn's gravitational harmonics.

Maxwell Ringlet, Center (Feature 160)

A freely-precessing simple ellipse model for the Maxwell ringlet was proposed by P84a. Model parameters from this work are compared with P84a values in Table 9.3. As with the Titan ringlet, we again find good agreement in parameter values. An exception is in the value of eccentricity. In this work, we find an eccentricity that is more than 2σ different from the P84a value. While the P84a data did not sample apoapse, they do have data points at periapse. However, the data used here include neither periapse nor apoapse. Although the formal error on the parameter value should be large enough to include the true value, any errors in any of the data points may act to produce the wrong result, especially when apoapse and periapse are not sampled. Therefore, the value determined in this work may not be correct. The P84a value may also be incorrect: feature radii were determined by offsets from fiducials presumed circular. The P84a fiducials may not be circular (they were not tested in this work). It is impossible to determine the correct value of eccentricity at this time. Additional data sets are needed to resolve this discrepancy. This uncertainty in the true value of eccentricity has a minimal effect on the free precession rate or the longitude of periapse. The precession rate determined here will be used in Section 11 as a constraint on the gravitational harmonics.

Table 9.3. Model Fits for Center of Maxwell Ringlet (Feature 160)

Model[a]	m	a (km)	$e \times 10^4$	ϖ_0[b] (deg)	$\dot{\varpi}$ (deg day^{-1})	RMS (km)
this work						
circular	—	87514.82 ± 4.68	—	—	—	14.802
fp	1	87510.05 ± 0.57	4.64 ± 0.23	240.4 ± 2.2	14.6937 ± 0.0007	1.606
P84a[c]						
fp	1	87491 ± 8	3.4 ± 0.4	255 ± 9	14.69 ± 0.03	

[a] "fp" indicates a freely-precessing, simple elliptical model.

[b] Epoch UTC 1980 11 13 03 17 40.

[c] Values for longitude of periapse from this work are converted to our longitude system, precessed to J2000.0, and adjusted for the difference in epoch.

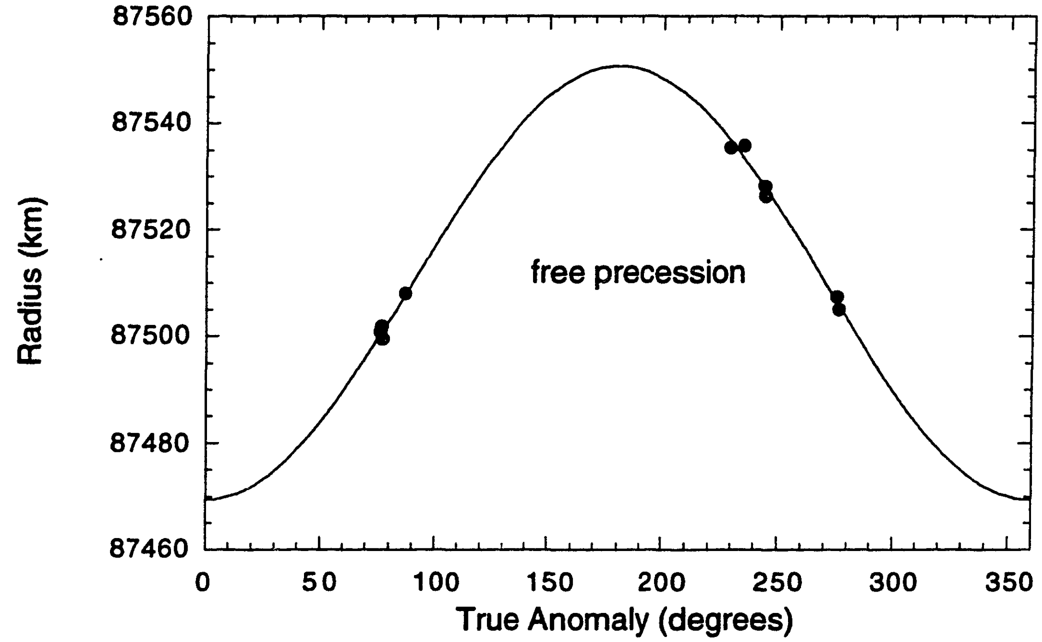

FIG. 9.3. Freely-precessing, simple elliptical model for the center of the Maxwell ringlet, feature 160. True anomaly is calculated at the epoch UTC 1980 11 13 03 17 40. The precession rate of this feature provides a tight constraint on Saturn's gravitational harmonics.

1.470 R_S Ringlet, Center (Feature 158)

Porco and Nicholson (1987, hereafter referred to as PN87) suspected that the ringlet at 1.470 R_S is non-circular, based on large residuals from Voyager occultation and imaging data. They found that the center of this ringlet was best described by a freely precessing Keplerian ellipse, while the inner and outer edges of the ringlet appeared to be forced by the

Prometheus 2:1 inner Lindblad resonance (ILR). However, none of the models attempted provided a conclusive result. The center of the ringlet is near the location of the Prometheus 2:1 ILR (Table 4.1), while the inner edge of the ringlet is near the Mimas 3:1 inner vertical resonance (IVR).

For studies of this ringlet, we begin by examining the center of the ringlet. Results of model fits are presented in Table 9.4. We attempted circular, free-precession, and resonantly forced models, as well as a model composed of the superposition of freely precessing and resonantly forced models. Data and these models are shown in Fig. 9.4. The model that fit the occultation data best (with the lowest rms residual per degree of freedom) is the circular model. The rms residual from this circular fit is quite low, 0.6 km, and is approximately equal to the rms residuals of other features presumed circular. Thus, there is no evidence from these occultation data that the centerline of the 1.470 R_S ringlet is non-circular.

While PN87 found that the best model for the center of the 1.470 R_S ringlet was that of a freely precessing Keplerian ellipse, that model is indeed very close to being circular. The amplitude of their best-fit ellipse is only 1.4 ± 0.8 km. The results of PN87 for this ringlet (center, inner and outer edges) are shown in Fig. 9.5.

Table 9.4. Model Fits for Center of 1.470 R_S Ringlet (Feature 158)

Model[a]	m	a (km)	$e \times 10^4$	ϖ_0[b] (deg)	$\dot{\varpi}$ (deg day^{-1})	RMS (km)
this work						
circular	—	88710.66 ± 0.23	—	—	—	0.599
fp	1	88711.02 ± 0.37	0.15 ± 0.13	66.3 ± 27.1	13.9965 ± 0.0115	0.615
Prom2:1	2	88710.36 ± 1.24	0.10 ± 0.14	39.6 ± 52.1	587.2536 ± 0.0085	0.610
comb.	1	88691.75 ± 23.77	4.17 ± 5.27	237.3 ± 1.6	13.8914 ± 0.0007	0.651
	2		2.31 ± 2.85	290.366	587.280129	
PN87[c]						
fp	1	88715.5 ± 6.2	0.16 ± 0.09	213 ± 8	13.9623	
Prom2:1	2	88715.7 ± 6.4	0.02 ± 0.07	172 ± 73	587.28	

[a] "fp" indicates a freely-precessing, simple elliptical model. "Prom2:1" indicates a model forced by the Prometheus 2:1 inner Lindblad resonance. "comb." indicates the superposition of the Prometheus 2:1 ILR and freely precessing models.

[b] Epoch UTC 1980 11 13 03 17 40.

[c] Values for longitude of periapse from this work are converted to our longitude system, processed to J2000.0, and adjusted for the difference in epoch.

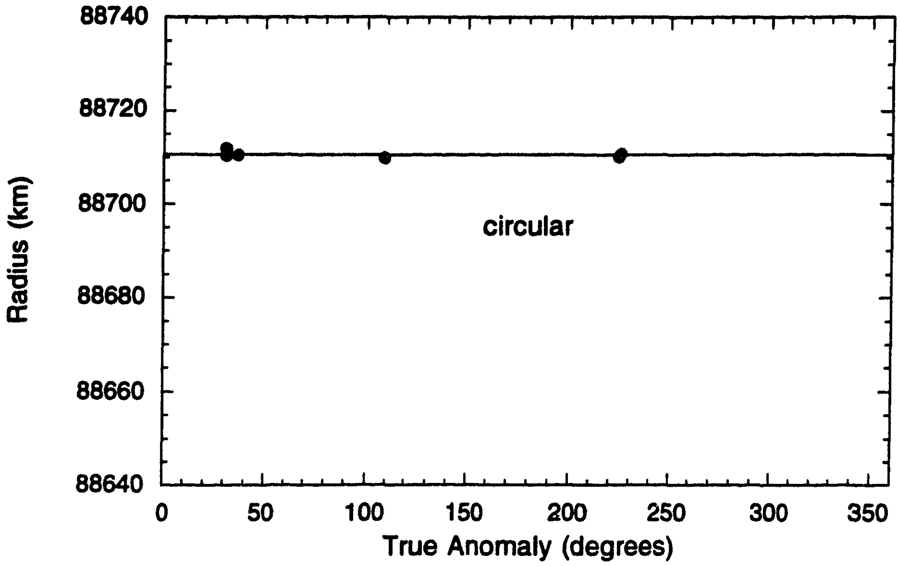

FIG. 9.4. Models for the center of the 1.470 R_S ringlet, feature 158. True anomaly is calculated at the epoch UTC 1980 11 13 03 17 40. (a) Circular model and data points. This model has the lowest rms residual of all the models attempted.

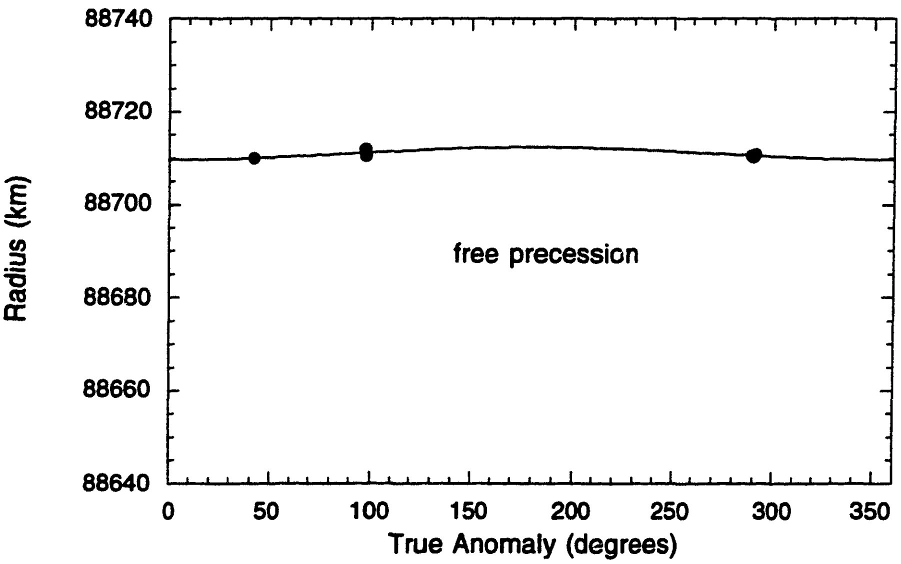

FIG. 9.4. (b) Freely-precessing simple ellipse model.

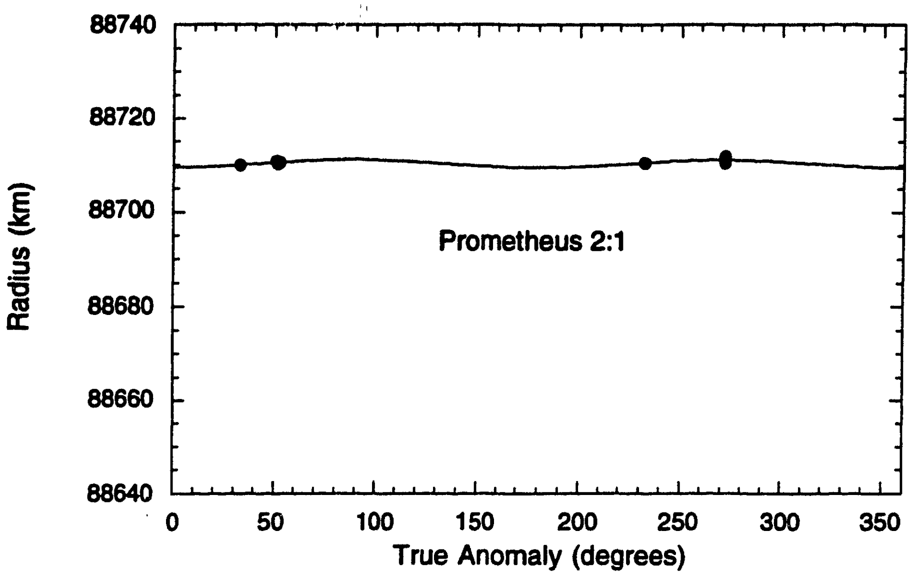

FIG. 9.4. (c) Prometheus 2:1 ILR model.

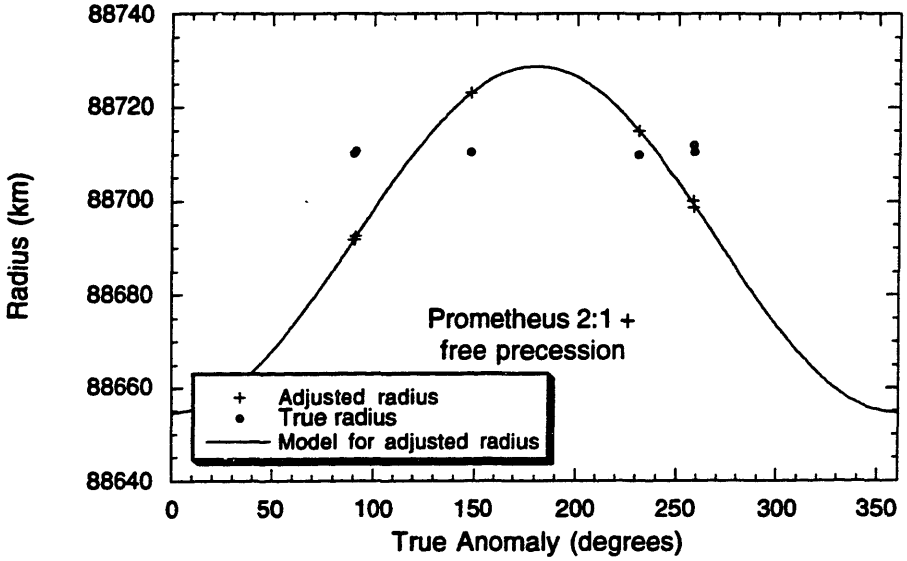

FIG. 9.4. (d) Combination of freely-precessing and Prometheus 2:1 models. The line plotted here is the contribution of the freely precessing portion to the ring kinematics. The data points plotted here have been adjusted to remove the contribution of the Prometheus 2:1 forcing.

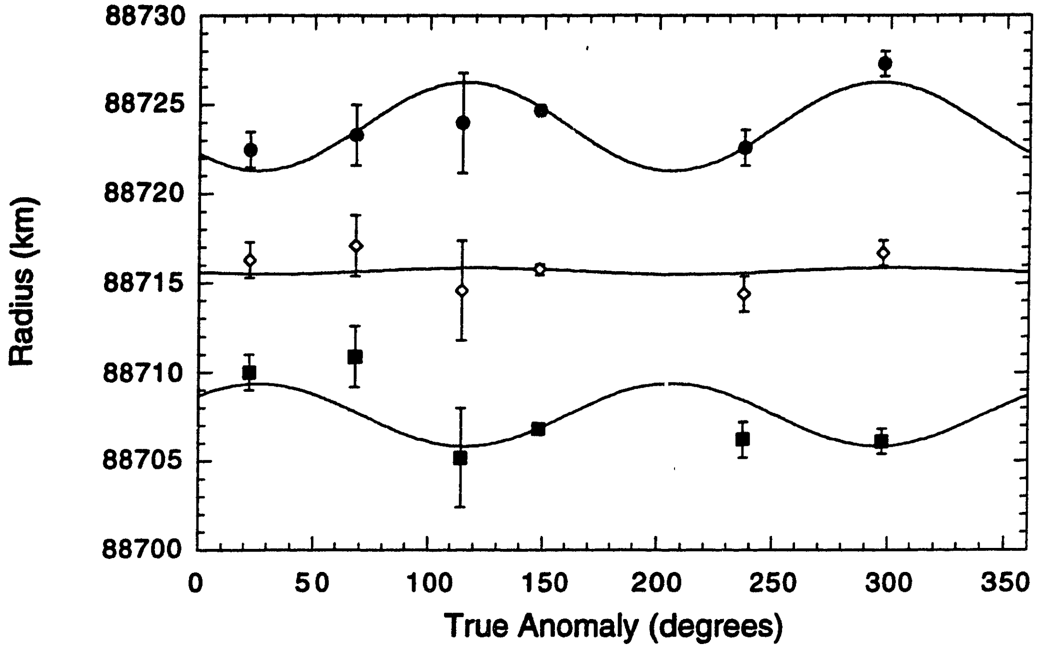

FIG. 9.5. After PN87, Fig. 6(a). Note that PN87 found no evidence for non-circularity of the center of the 1.470 R_S ringlet. The outer and inner edges of this ringlet (filled circles and squares, respectively) are phased such that the perturbations destructively interfere at the ringlet's center.

While the center of the 1.470 R_S ringlet appears to be circular, PN87 found that the inner and outer edges are potentially non-circular (Fig. 9.5). Therefore, we investigate these edges in our data set. The results of model fits to these edges are presented in Table 9.5. From these fits, we find that the inner edge of the 1.470 R_S ringlet fits best to a circular model (the Mimas 3:1 IVR model was not attempted here), while the outer edge of this ringlet fits best to a resonantly forced model (pure Prometheus 2:1 ILR). This contrasts the results of PN87, who found that both edges fit best to the Prometheus 2:1 ILR model. The differing results could be due to errors in the imaging data used by PN87. Or they could be the result of insufficient sampling in our modeling (there are only 7 data points available to us for use in these model fits). Clearly the role of the Mimas 3:1 IVR in determining the shape of the inner edge of this ringlets needs to be determined. It is curious that the Prometheus 2:1 ILR lies within the ringlet, very close to the center (within ~2 km), yet the ringlet appears to be circular.

Table 9.5. Model Fits for Inner and Outer Edges of 1.470 R_S Ringlet (Features 59 and 58)

Model[a]	m	a (km)	$e \times 10^4$	ϖ_0[b] (deg)	$\dot{\varpi}$ (deg day^{-1})	RMS (km)
Inner Edge of 1.470 R_S Ringlet (Feature 59)						
this work						
circular	—	88701.16 ± 0.28	—	—	—	0.728
fp	1	88701.11 ± 0.32	0.07 ± 0.07	350.6 ± 91.7	13.9507 ± 0.0428	0.750
Prom2:1	2	88702.94 ± 3.09	0.28 ± 0.42	97.4 ± 14.8	587.2606 ± 0.0046	0.751
comb.	1	88715.28 ± 18.11	4.42 ± 5.58	49.1 ± 1.6	13.9472 ± 0.0004	0.808
	2		−2.80 ± 3.58	290.366	587.280129	
PN87[c]						
fp	1	88707.7 ± 7.1	0.12 ± 0.17	90 ± 65	13.9623	
Prom2:1	2	88707.6 ± 6.6	0.20 ± 0.12	257 ± 13	587.28	
Outer Edge of 1.470 R_S Ringlet (Feature 58)						
this work						
circular	—	88720.17 ± 0.47	—	—	—	1.244
fp	1	88720.84 ± 0.28	0.27 ± 0.10	81.9 ± 14.6	13.9873 ± 0.0073	0.480
Prom2:1	2	88726.70 ± 1.88	0.92 ± 0.26	77.4 ± 2.9	587.3765 ± 0.0012	0.463
comb.	1	88731.04 ± 10.43	3.39 ± 3.21	52.6 ± 2.7	13.9470 ± 0.0003	0.465
	2		−2.09 ± 2.06	290.366	587.280129	
PN87[c]						
fp	1	88723.4 ± 6.9	0.38 ± 0.17	228 ± 10	13.9623	
Prom2:1	2	88723.8 ± 6.5	0.28 ± 0.11	167 ± 8	587.28	

[a] "fp" indicates a freely-precessing, simple elliptical model. "Prom2:1" indicates a model forced by the Prometheus 2:1 inner Lindblad resonance. "comb." indicates the superposition of the Prometheus 2:1 ILR and freely precessing models.

[b] Epoch UTC 1980 11 13 03 17 40.

[c] Values for longitude of periapse from this work are converted to our longitude system, precessed to J2000.0, and adjusted for the difference in epoch.

1.495 R_S Ringlet, Outer Edge (Feature 56)

The kinematics of the 1.495 R_S ringlet, like those of the 1.470 R_S ringlet, were discussed in PN87. They found that a freely precessing model was a marginally better fit than either the Pandora 2:1 ILR or the Mimas 3:1 ILR for the center of this ringlet. Similarly, the freely precessing model fit the outer edge of this ringlet best, while the Pandora 2:1 ILR provided the best fit for the inner edge. PN87 state that neither of their edge models produced an acceptable χ^2 per degree of freedom.

Because the outer edge of the 1.495 R_S ringlet is coincident with the Mimas 3:1 ILR, we concentrate on that edge. We find that the best fit model consists of a superposition of the Mimas 3:1 ILR and a freely precessing component. Results of this fit and others are shown in Fig. 9.6. For the superposition model, we fix the longitude of periapse at the longitude of Mimas (this angle is either the longitude of the forcing body or 180° away from it, depending on the location of the ringlet with respect to the resonance location; the angle can lead or lag these by a fraction of a degree, but this is small compared with our current errors), and the pattern speed at that predicted by the mean motion and apsidal precession rate of Mimas. Although the value of semimajor axis for this superposition model is large (~10 km greater than for other models), the resonantly forced component acts to decrease the ring radius. Thus, the radius of this ring does not make large excursions, but rather remains close to 90198 km.

Table 9.6. Model Fits for Outer Edge of 1.495 R_S Ringlet (Feature 56)

Model[a]	m	a (km)	$e \times 10^4$	ϖ_0[b] (deg)	$\dot{\varpi}$ (deg day^{-1})	RMS (km)
this work						
circular	—	90197.87 ± 1.26	—	—	—	3.327
fp	1	90197.11 ± 0.54	0.64 ± 0.14	210.5 ± 13.2	13.0943 ± 0.0053	1.373
Mimas3:1	2	90199.03 ± 0.95	0.47 ± 0.17	13.4 ± 14.3	572.5094 ± 0.0052	2.262
comb.	1	90210.20 ± 1.82	4.35 ± 0.61	207.0 ± 1.7	13.1539 ± 0.0007	0.753
	2		2.01 ± 0.29	79.253	572.491293	
PN87[c]						
fp	1	90202.0 ± 7.0	0.45 ± 0.10	256 ± 18	13.1591	
Mimas3:1	2	90210.0 ± 8.7	1.66 ± 0.52	334 ± 3	572.491	

[a] "fp" indicates a freely-precessing, simple elliptical model. "Mimas3:1" indicates a Mimas 3:1 ILR model. "comb." indicates a model composed of a superposition of the Mimas 3:1 ILR and the freely precessing models.

[b] Epoch UTC 1980 11 13 03 17 40.

[c] Values for longitude of periapse from this work are converted to our longitude system, precessed to J2000.0, and adjusted for the difference in epoch.

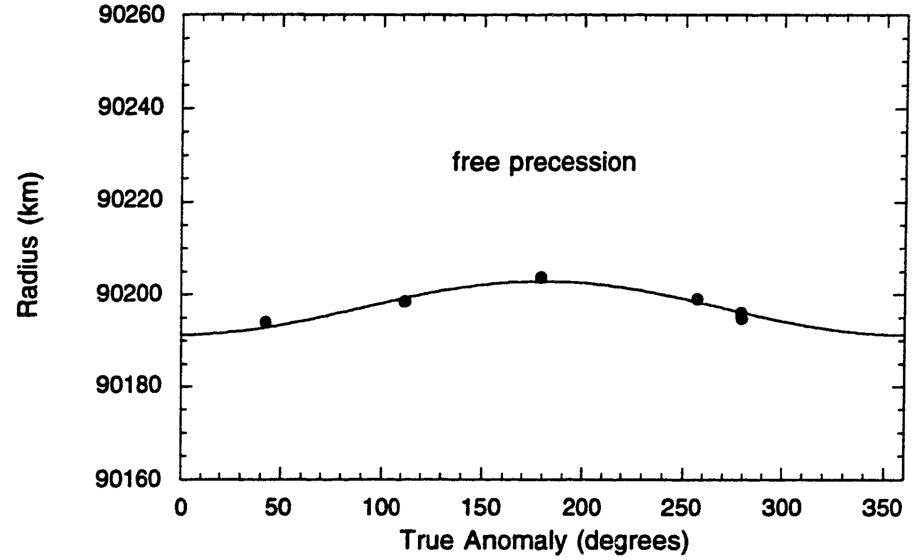

FIG. 9.6. Models for the outer edge of the 1.495 R_S ringlet, feature 56. True anomaly is calculated at the epoch UTC 1980 11 13 03 17 40. (a) Freely-precessing simple ellipse model.

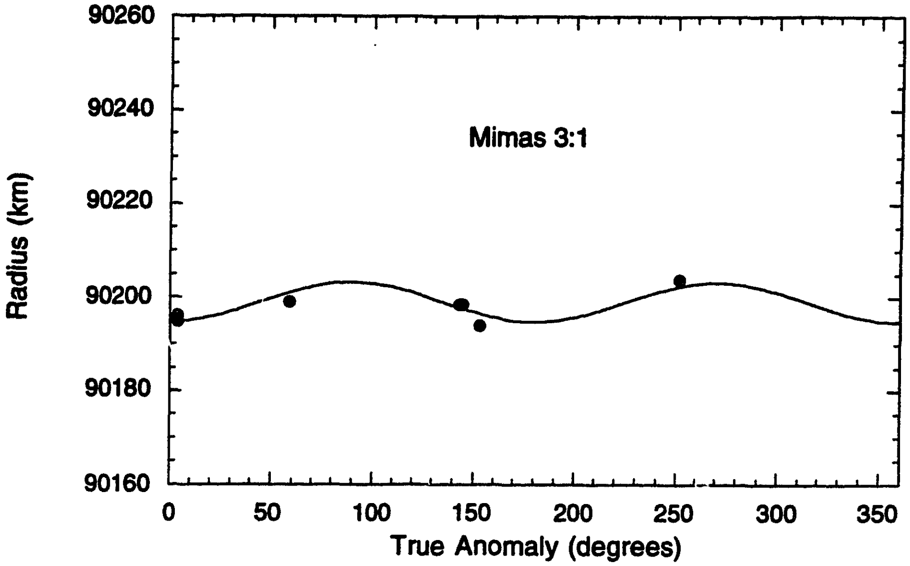

FIG. 9.6. (b) Mimas 3:1 ILR model.

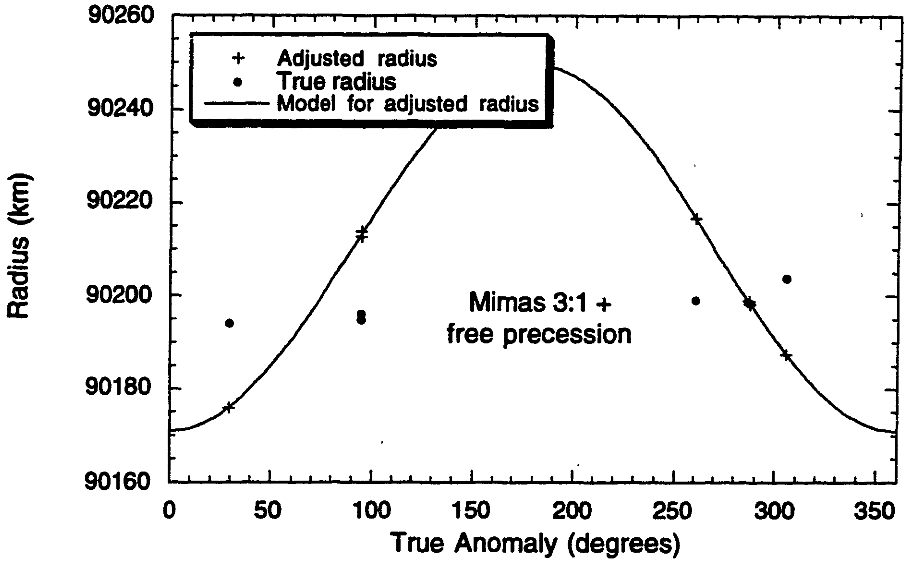

FIG. 9.6. (c) Combination of freely precessing and Mimas 3:1 models. The line plotted here is the contribution of the freely precessing portion to the ring kinematics. The data points plotted here have been adjusted to remove the contribution of the Mimas 3:1 forcing.

B Ring, Outer Edge (Feature 55)

To first order, the outer edge of the B ring is a body-centered, $m = 2$ ellipse with a pattern speed equal to the mean motion of Mimas, and periapse aligned with Mimas. This is the kinematic model developed by (Porco *et al.* 1984a, hereafter P84b). In our modeling, we find that a kinematic model for the resonant forcing of the Mimas 2:1 ILR resonance does not provide an adequate fit (Table 9.7, Fig. 9.7). Instead, a model combining the Mimas 2:1 ILR model and a freely precessing model provides a better fit (lower rms residuals). This is the first "comb." fit listed in Table 9.7. In this fit, we fix the longitude of periapse at the longitude of Mimas at the appropriate epoch, and we fix the pattern speed at the mean motion of Mimas (Harper and Taylor 1993). In fact, a fit with lower rms residuals is achieved when we allow the pattern speed to vary. The pattern speed found in this fit (the second "comb." fit in Table 9.7) is more than 2σ different from the predicted value.

While the superposition model provides the best fit, the rms residuals are still quite large. They are ~11 km for this feature, while other features have rms residuals 0.5 - 1.5 km. This indicates that the superposition model for this ring feature is not adequate. There must be other forces influencing the kinematics of this ring edge. Another sign of this is the difference of the fitted value of pattern speed from the predicted value. Because the optical thickness of this ring is so large, and hence the surface density is large, it is reasonable to assume that the self-gravity of ring particles may play a role in the kinematics of this edge.

The semimajor axis and eccentricity values found in this work are significantly lower than those found in P84b. Our data set includes none of the large-radius points included in the P84b analysis; this may account for the discrepancy. The addition of imaging data to these models will aid greatly in determining more about the kinematics of the outer edge of the B ring.

Table 9.7. Model Fits for Outer Edge of B Ring (Feature 55)

Model[a]	m	a (km)	$e \times 10^4$	ϖ_0[b] (deg)	$\dot{\varpi}$ (deg day^{-1})	RMS (km)
this work						
circular	—	117526.02 ± 3.82	—	—	—	13.219
fp	1	117533.66 ± 6.76	2.22 ± 1.20	356.9 ± 28.2	5.0617 ± 0.0096	13.207
Mimas2:1	2	117537.89 ± 10.39	1.41 ± 1.15	92.7 ± 33.9	381.9866 ± 0.0107	13.924
comb.	1	117533.66 ± 6.76	2.22 ± 1.20	356.9 ± 28.2	5.0617 ± 0.0096	12.190
	2		0.99 ± 0.64	79.253	381.994509	
comb.	1	117550.10 ± 14.53	1.97 ± 1.20	344.9 ± 31.8	5.0597 ± 0.0120	11.514
	2		2.77 ± 1.61	79.253	381.9893 ± 0.0019	
P84b[c]						
Mimas2:1	2	117577 ± 18	6.3 ± 0.8	76 ± 6	381.997	

[a] "fp" indicates a freely-precessing, simple elliptical model. "Mimas2:1" indicates a Mimas 2:1 ILR model. "comb." indicates a superposition of the Mimas 2:1 ILR and freely precessing models.

[b] Epoch UTC 1980 11 13 03 17 40.

[c] Values for longitude of periapse from this work are converted to our longitude system, precessed to J2000.0, and adjusted for the difference in epoch.

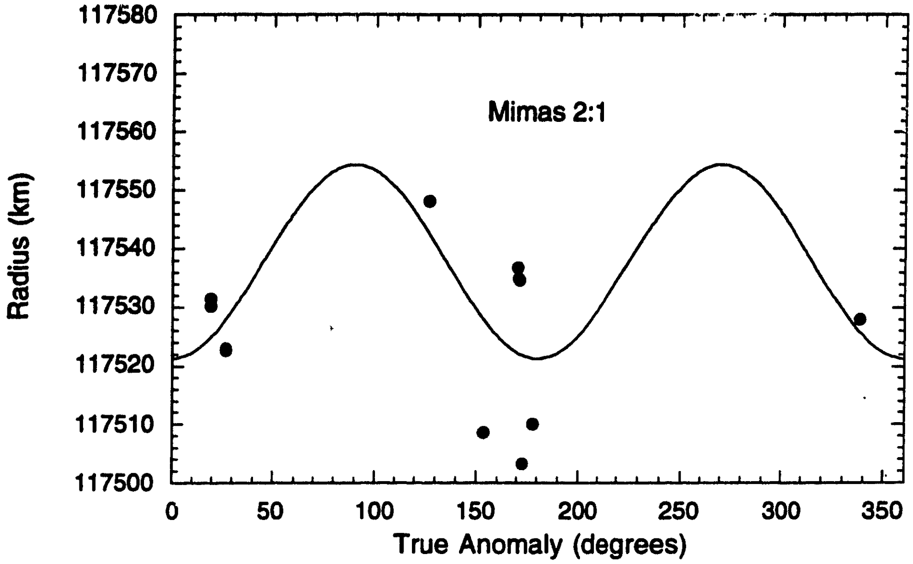

FIG. 9.7. Models for the outer edge of the B ring, feature 55. True anomaly is calculated at the epoch UTC 1980 11 13 03 17 40. (a) Mimas 2:1 ILR model.

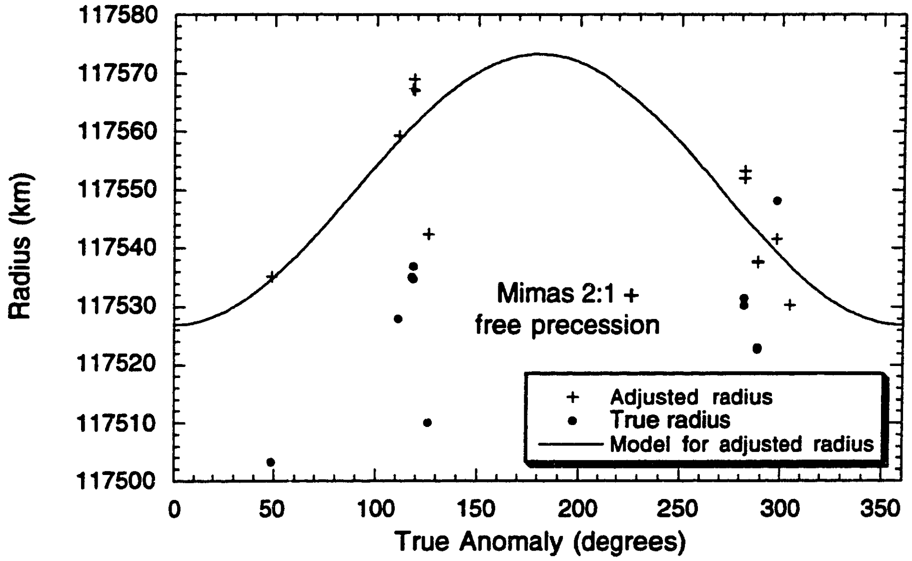

FIG. 9.7. (b) Combination of freely precessing simple and Mimas 2:1 models. The line plotted here is the contribution of the freely precessing portion to the ring kinematics. The data points plotted here have been adjusted to remove the contribution of the Mimas 2:1 forcing.

Huygens Ringlet, Center (Feature 153)

The Huygens ringlet was previously found to be consistent with a freely precessing model (Porco 1983), and more recently was found to fit a superposition of freely precessing and Mimas 2:1 ILR models (Turtle *et al.* 1990). Model parameters from these previous works are unavailable at this time.

A freely precessing model provides an adequate fit to the data available on the center of the Huygens ringlet (Table 9.8, Fig. 9.8). However, the proximity of the B ring and the Mimas 2:1 ILR was thought to also have an affect on the kinematics of the ringlet. A model consisting of the superposition of these two models produces the fit with the lowest rms residuals. The eccentricity of the Mimas 2:1 ILR component is negative in Table 9.8 because the longitude of periapse is fixed at the longitude of Mimas; however, for features outside the resonance location, the longitude of periapse should be 180° away from Mimas. The negative value of the eccentricity indicates that this is the case.

Table 9.8. Model Fits for Center of Huygens Ringlet (Feature 153)

Model[a]	m	a (km)	$e \times 10^4$	ϖ_0 [b] (deg)	$\dot{\varpi}$ (deg day^{-1})	RMS (km)
this work						
circular	—	117813.52 ± 5.35	—	—	—	18.532
fp	1	117814.78 ± 0.47	2.64 ± 0.10	320.6 ± 2.5	5.0302 ± 0.0009	1.498
Mimas2:1	2	117790.98 ± 5.78	3.51 ± 0.60	147.1 ± 8.7	381.9915 ± 0.0025	8.837
comb.	1	117812.20 ± 0.78	2.91 ± 0.10	325.1 ± 1.8	5.0274 ± 0.0009	0.952
	2		–0.33 ± 0.09	79.253	381.994509	

[a] "fp" indicates a freely-precessing, simple elliptical model. "Mimas2:1" indicates the Mimas 2:1 ILR. "comb." indicates a superposition of the Mimas 2:1 ILR and freely precessing models.

[b] Epoch UTC 1980 11 13 03 17 40.

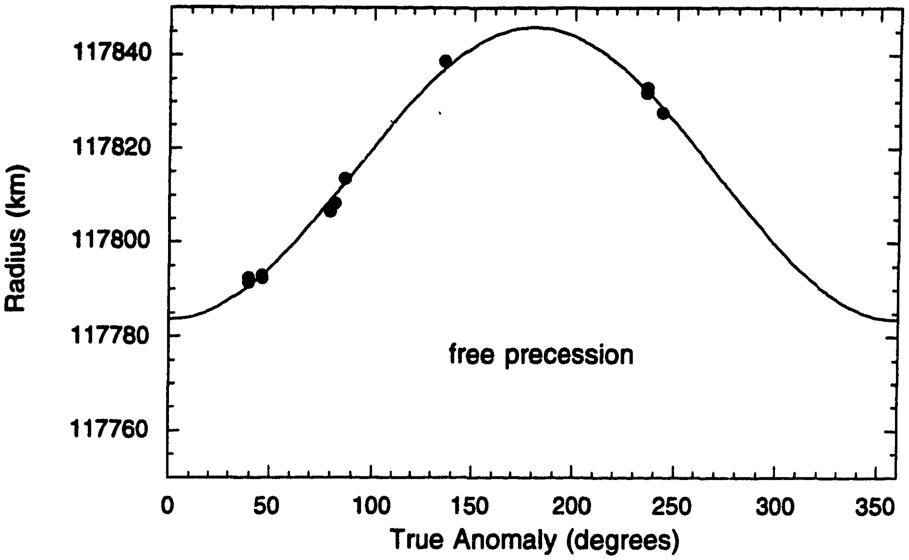

FIG. 9.8. Models for the center of the Huygens ringlet, feature 153. True anomaly is calculated at the epoch UTC 1980 11 13 03 17 40. (a) Freely-precessing simple ellipse model.

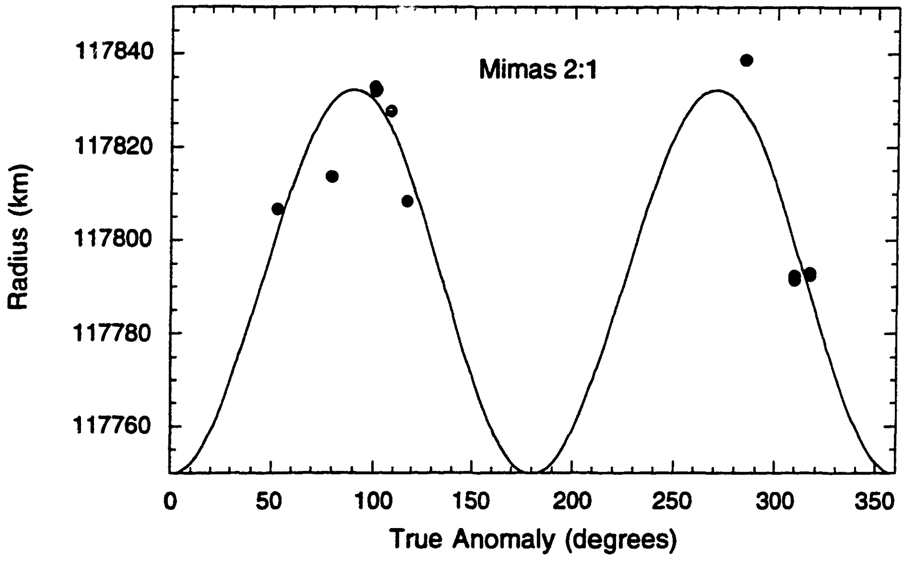

FIG. 9.8. (b) Mimas 2:1 ILR model.

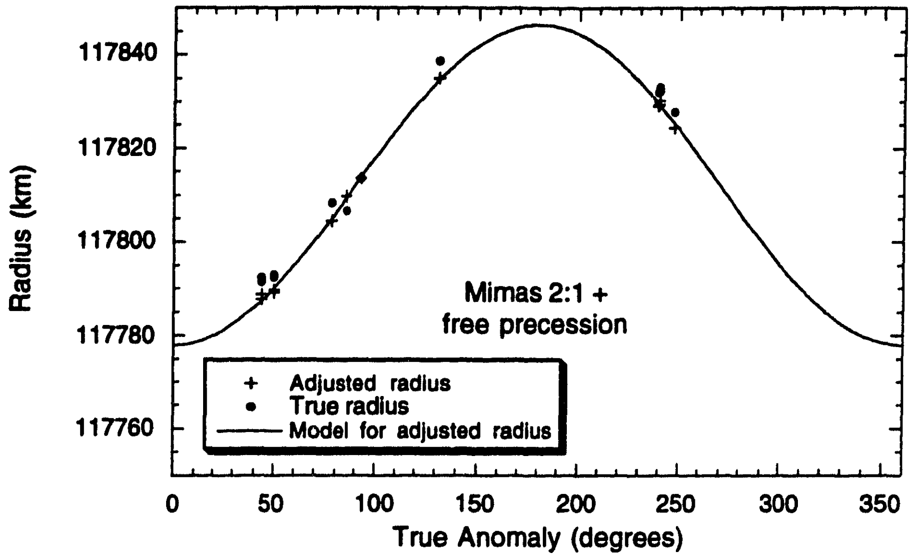

FIG. 9.8. (c) Combination of freely precessing and Mimas 2:1 ILR models. The line plotted here is the contribution of the freely precessing portion to the ring kinematics. The data points plotted here have been adjusted to remove the contribution of the Mimas 2:1 forcing.

1.990 R_S Ringlet, Inner Edge (Feature 14)

The 1.990 R_S ringlet was previously recognized as non-circular (NCP), but no models have been published. Because the inner edge of this ringlet lies near the Pandora 9:7 ILR, we investigate the applicability of this model to this ringlet. Results of model fits are given in Table 9.9 and Fig. 9.9. The model fit with the lowest rms residual is that for the freely precessing model, not the resonantly forced model. The actual resonance location is approximately 3 km interior to the inner edge of this feature; apparently the resonance is not strong enough to influence this nearby ring feature.

We use this to place an upper limit on the mass of Pandora. Given that the forced eccentricity arising from the Pandora 9:7 resonance is less than 0.22×10^{-4}, we use Eq. 30 of NP88 to find an upper limit to Pandora's mass of 9.2×10^{22} g. Rosen *et al.* (1991b) found Pandora's mass to be $(1.31 \pm 0.66) \times 10^{20}$ g by modeling the actual vs. predicted amplitudes of the Pandora 6:5, 7:6, and 8:7 density waves. Thus this constraint is consistent with the Rosen result, but does not improve our knowledge of Pandora's mass.

Table 9.9. Model Fits for Inner Edge of 1.990 R_S Ringlet (Feature 14)

Model[a]	m	a (km)	$e \times 10^4$	ϖ_0[b] (deg)	$\dot{\varpi}$ (deg day^{-1})	RMS (km)
this work						
circular	—	120037.40 ± 0.77	—	—	—	2.315
fp	1	120035.73 ± 1.04	0.32 ± 0.18	248.6 ± 43.0	4.7484 ± 0.0160	2.059
Pand9:7	8	120036.23 ± 1.04	0.22 ± 0.14	294.9 ± 5.8	644.0468 ± 0.0023	2.287
comb.	1	120035.74 ± 1.17	0.32 ± 0.22	248.4 ± 53.9	4.7484 ± 0.0178	2.303
	8		0.01 ± 0.19	327.245	644.014729	

[a] "fp" indicates a freely-precessing, simple elliptical model. "Pand9:7" indicates the Pandora 9:7 ILR model. "comb." indicates a superposition of the Pandora 9:7 and freely precessing models.

[b] Epoch UTC 1980 11 13 03 17 40.

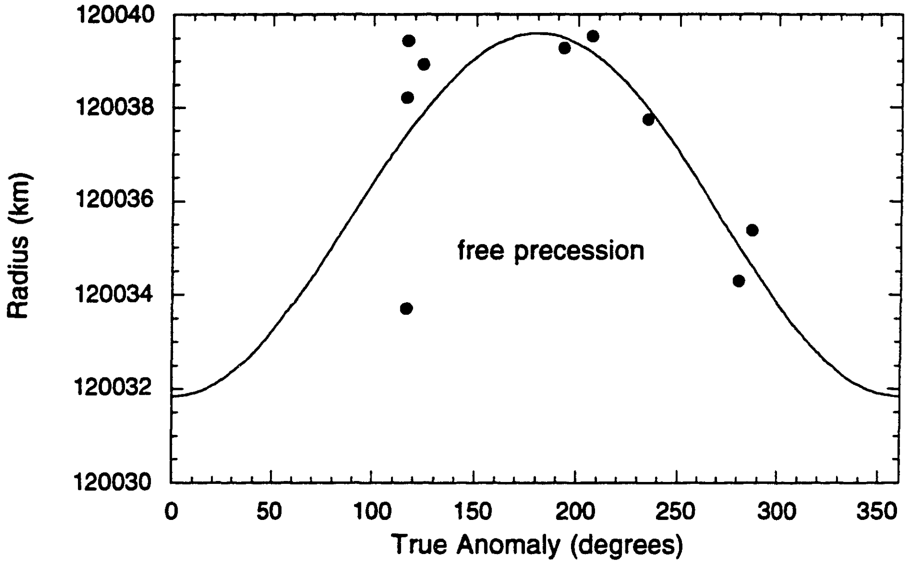

FIG. 9.9. Models for the inner edge of the 1.990 R_S ringlet, feature 14. True anomaly is calculated at the epoch UTC 1980 11 13 03 17 40. (a) Freely-precessing simple ellipse model.

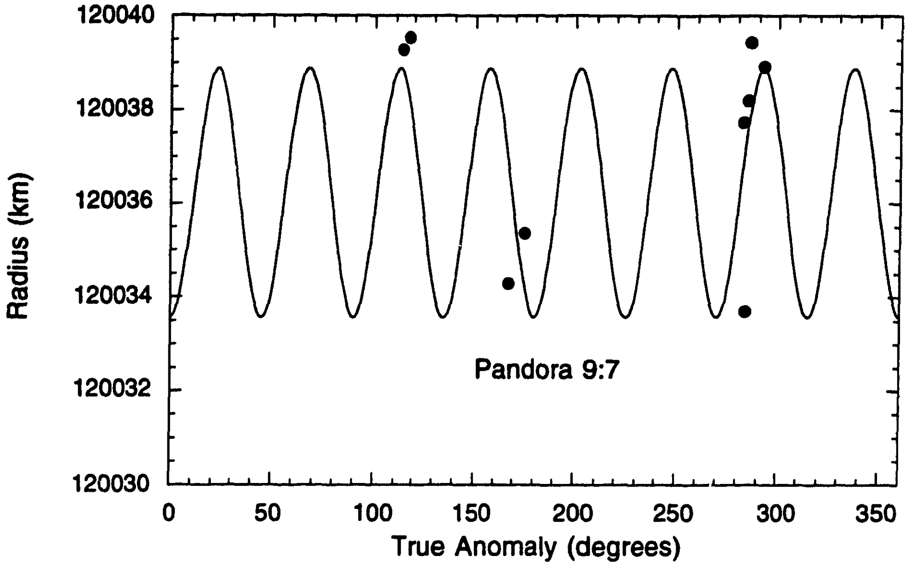

FIG. 9.9. (b) Pandora 9:7 ILR model.

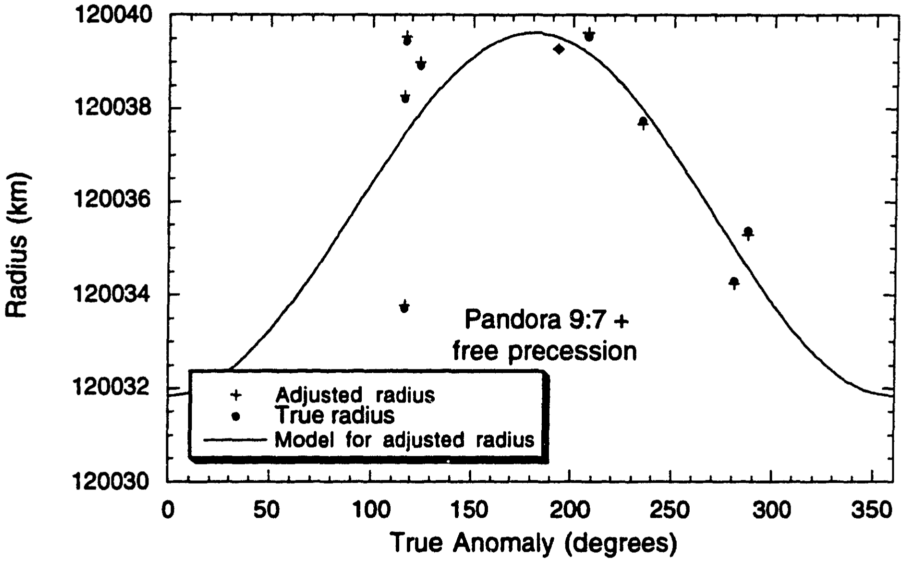

FIG. 9.9. (c) Combination of freely precessing and Pandora 9:7 ILR models. The line plotted here is the contribution of the freely precessing portion to the ring kinematics. The data points plotted here have been adjusted to remove the contribution of the Pandora 9:7 forcing.

A Ring, Outer Edge (Feature 52)

The outer edge of the A ring is located nearby the 7:6 ILR with the coorbital satellites Janus and Epimetheus. To construct a simple kinematic model, we choose to fit this ring feature with the Janus resonance and to ignore any contributions from resonance with Epimetheus. The results of these fits are shown in Table 9.10. Here we find that the rms residual from the Janus 7:6 ILR model is 3.5 km, larger than usual rms residuals of 0.5 - 1.5 km. A superposition model combining the Janus 7:6 ILR and freely precessing models, with longitude of periapse fixed at the longitude of Janus and pattern speed fixed at the mean motion of Janus (Harper and Taylor 1993) yields a larger rms residual, 5.0 km. However, if we allow the pattern speed to vary, we find the lowest rms residual of all models attempted, 1.1 km. The pattern speed then differs from the predicted value by more than 6σ. As with the outer edge of the B ring, this indicates that this model may not be correct, or that there may be other facets to the correct model for this ring feature. While the surface density of the A ring is not as great as that of the B ring, particle self-gravity may still play an important role. Another factor is certainly the presence of Epimetheus in an orbit nearly identical to that of Janus. Although Janus is much more massive than Epimetheus, the latter will still effect the ring kinematics, especially when it is closer to the rings than is the former. These two satellites are in a 7:6 resonance with the outer edge of the A ring, the torques exerted on the satellites by the ring are causing the difference in semimajor axis between these two bodies to decrease, and are also causing a secular drift of the satellites away from the ring (Lissauer *et al.* 1985). Thus a simple model including only Janus may be sufficient for data spanning a short time, but for longer time spans such as we have here, we will need to include the effects of both satellites.

Table 9.10. Model Fits for Outer Edge of A Ring (Feature 52)

Model[a]	m	a (km)	$e \times 10^4$	ϖ_0[b] (deg)	$\dot{\varpi}$ (deg day^{-1})	RMS (km)
this work						
circular	—	136770.95 ± 1.34	—	—	—	4.448
fp	1	136769.68 ± 1.96	0.44 ± 0.36	203.3 ± 56.1	2.9427 ± 0.0183	4.790
Janus7:6	7	136772.69 ± 1.28	0.43 ± 0.16	242.1 ± 6.1	518.2289 ± 0.0020	3.488
comb.	1	136771.53 ± 4.56	0.14 ± 0.62	265.2 ± 180.	2.9309 ± 0.2960	5.016
	7		0.26 ± 0.53	220.645	518.235892	
comb.	1	136769.93 ± 0.93	0.82 ± 0.12	343.5 ± 7.9	3.0239 ± 0.0035	1.144
	7		0.62 ± 0.07	220.645	518.2332 ± 0.0004	
P84b[c]						
Janus7:6	7	136773 ± 8	0.49 ± 0.11	114 ± 10	518.31	

[a] "fp" indicates a freely-precessing, simple elliptical model. "Janus7:6" indicates the Janus 7:6 ILR model. "comb." indicates the superposition of the Janus 7:6 ILR and freely precessing models.

[b] Epoch UTC 1980 11 13 03 17 40.

[c] Values for longitude of periapse from this work are converted to our longitude system, precessed to J2000.0, and adjusted for the difference in epoch.

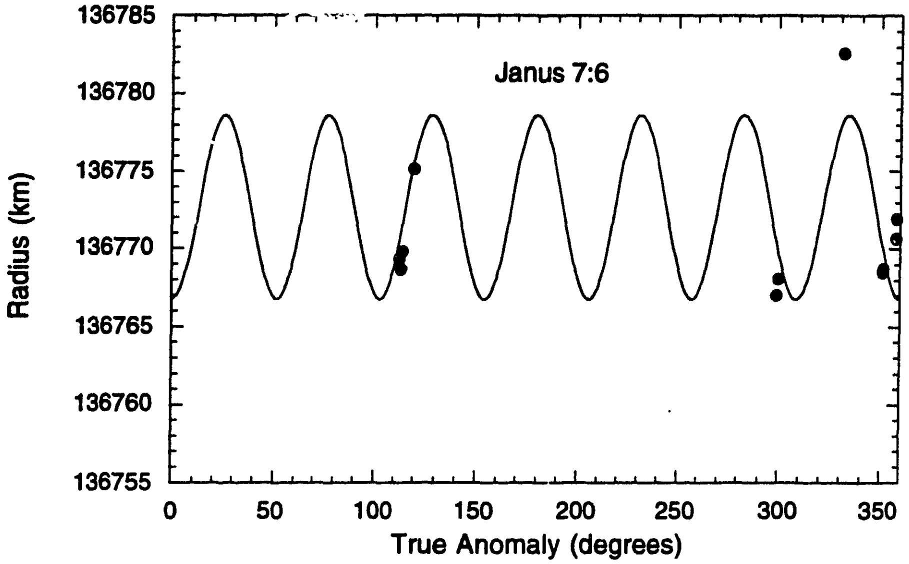

FIG. 9.10. Models for the outer edge of the A ring, feature 52. True anomaly is calculated at the epoch UTC 1980 11 13 03 17 40. (a) Janus 7:6 ILR model.

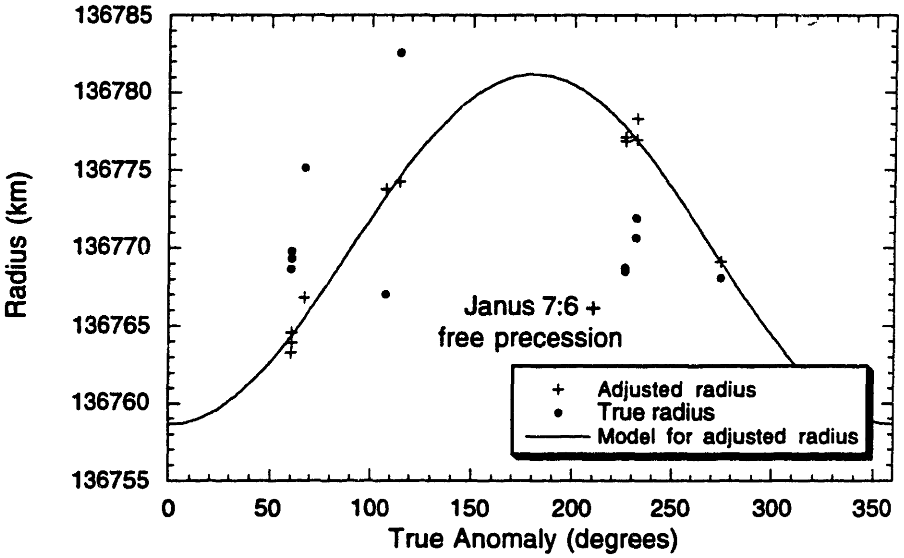

FIG. 9.10. (b) Combination of freely precessing and Janus 7:6 ILR models. The line plotted here is the contribution of the freely precessing portion to the ring kinematics. The data points plotted here have been adjusted to remove the contribution of the Janus 7:6 forcing.

10. RINGLET MASSES

One of the important diagnostics in ringlet study is the determination of whether the ringlet is in locked apsidal precession. If there is no resisting force, we would expect there to be differential precession across the width of the ringlet. However, this is observed to not be the case for several Uranian rings (French *et al.* 1986), and also for the Titan and Maxwell ringlets of Saturn (P84a). These ringlets are in locked-apsidal precession, in which the entire ringlet precesses as a whole rather than differentially precessing. One model for locked-apsidal precession uses an induced precession term that stems from the self-gravity of the ringlet (Goldreich and Tremaine 1979) to counteract the tendency toward differential precession. The indication of this state of locked-apsidal precession is a positive linear width-radius relation (hereafter referred to as simply the with-radius relation), indicating a positive gradient in eccentricity and an alignment of the longitudes of periapse. We search for such a relation in the ringlets fit here. If a ringlet is in locked-apsidal precession, we can then determine the mass of the ringlet.

In Fig. 10.1 we plot the width-radius relations of the ringlets studied here: the Titan, Maxwell, 1.470 R_S, 1.495 R_S, Huygens, and 1.990 R_S ringlets. In these plots the width of the ringlet (difference between radii at outer and inner edges) is plotted against the radius of the ringlet's centerline. There is one outlying point in the width-radius plot of the Titan ringlet (Fig 10.1 (a)); inspection of these data shows that the outlier is a point from the MCD data set of the 28 Sgr occultation. The radius for the inner edge of the ringlet (feature 63) is greater than that for the outer edge (feature 62), indicating that these features were likely swapped when measured. If we change the sign of the width for this point (Fig. 10.1 (b)), it then agrees well with other widths. The data times in Table 2.2 have been corrected to reflect this finding.

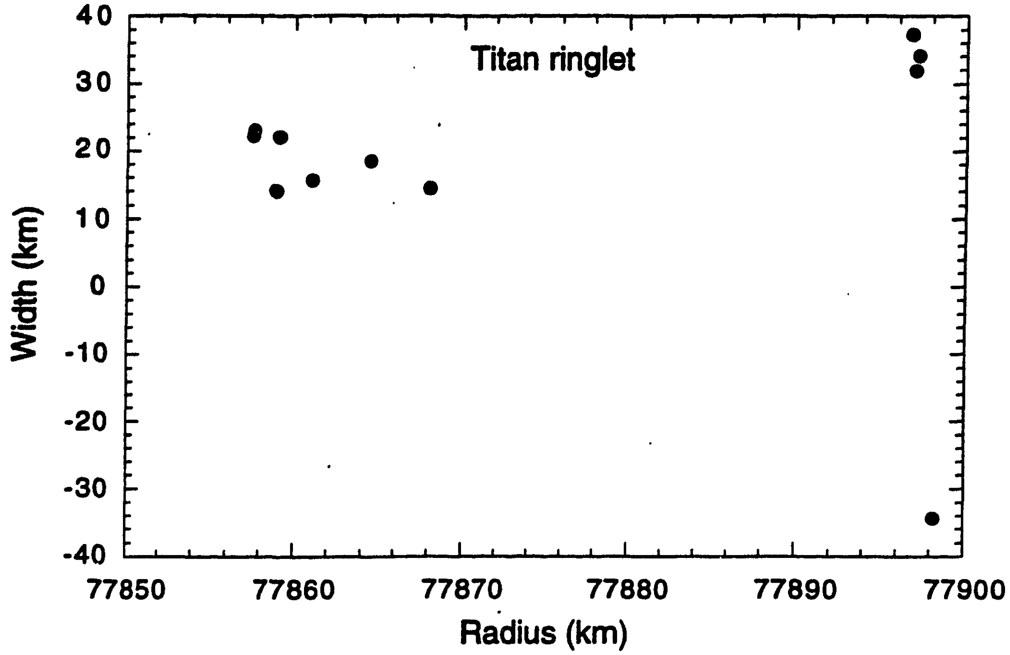

FIG. 10.1. Width-radius relation plots for narrow Saturnian ringlets studied in this work. (a) Titan ringlet. The one outlying point is probably due to a misidentification of the ringlet edges. This is corrected in (b).

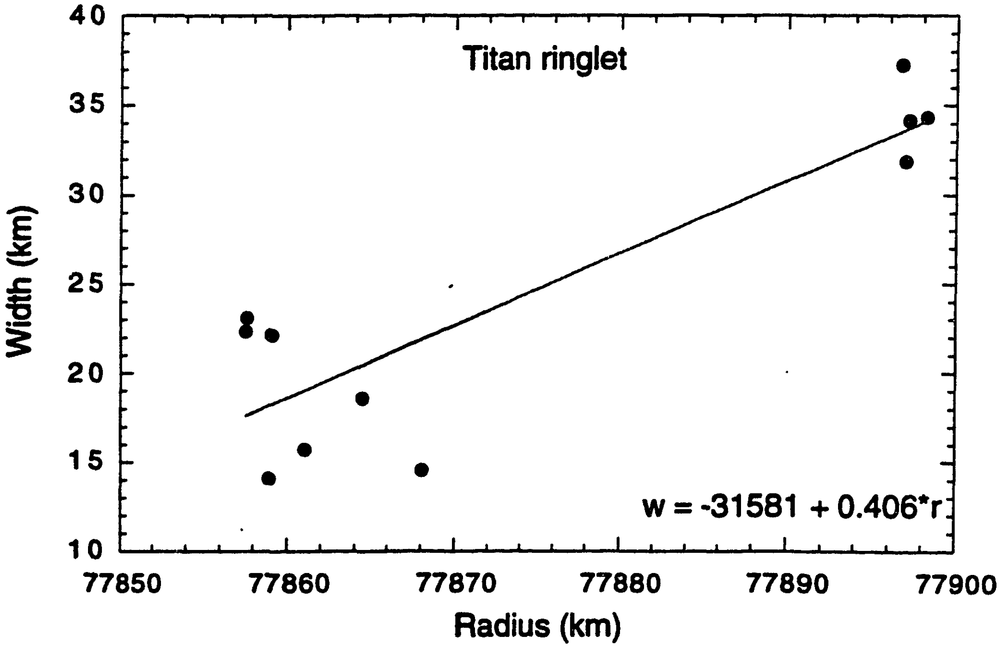

FIG. 10.1. (b) Titan ringlet, with one outlying point corrected. This ringlet shows a fairly strong correlation between width and radius.

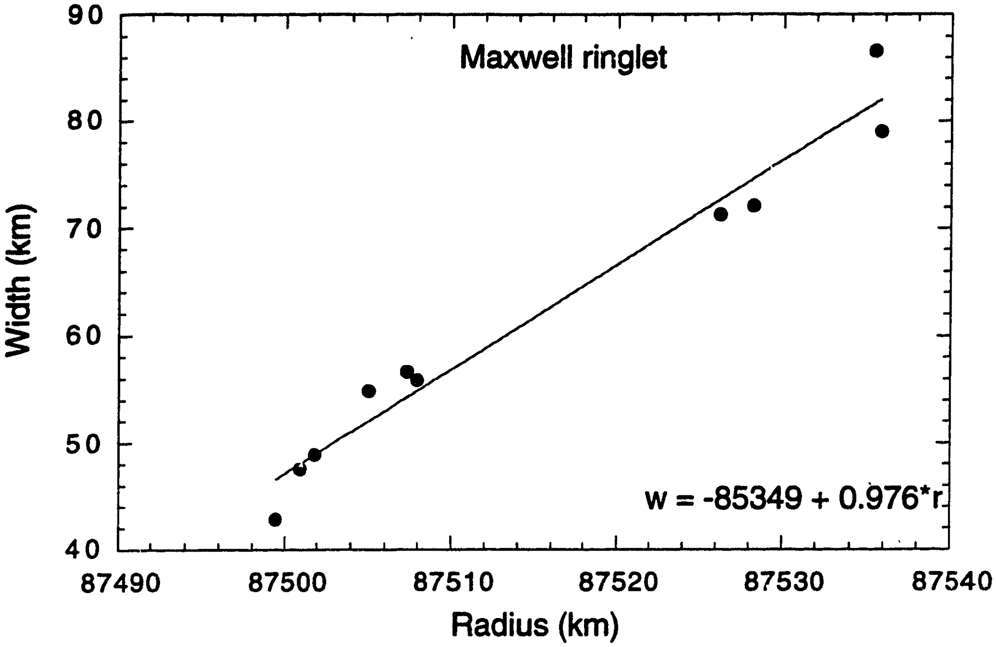

FIG. 10.1. (c) Maxwell ringlet. This ringlet shows a strong correlation between width and radius.

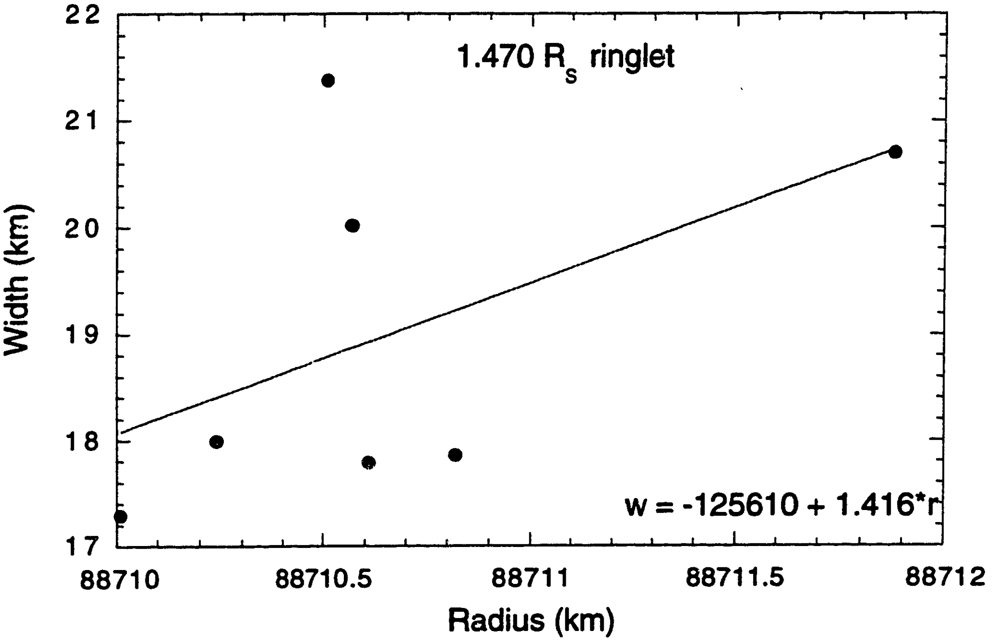

FIG. 10.1. (d) 1.470 R_S ringlet. This ringlet shows a weak correlation between width and radius.

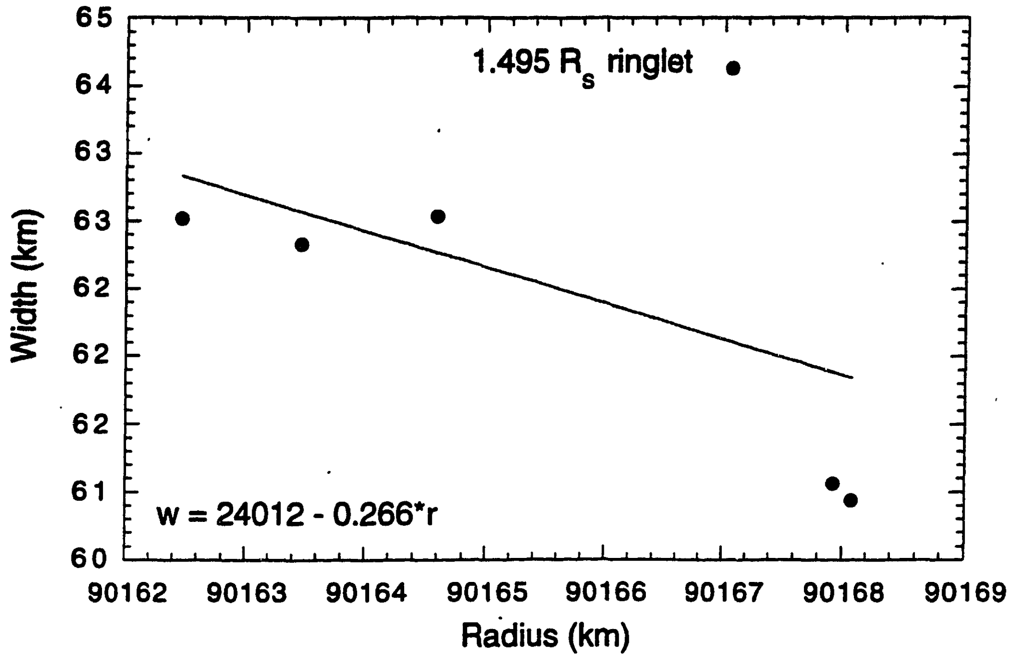

FIG. 10.1. (e) 1.495 R_S ringlet. This ringlet shows a weak correlation between width and radius, with a negative gradient.

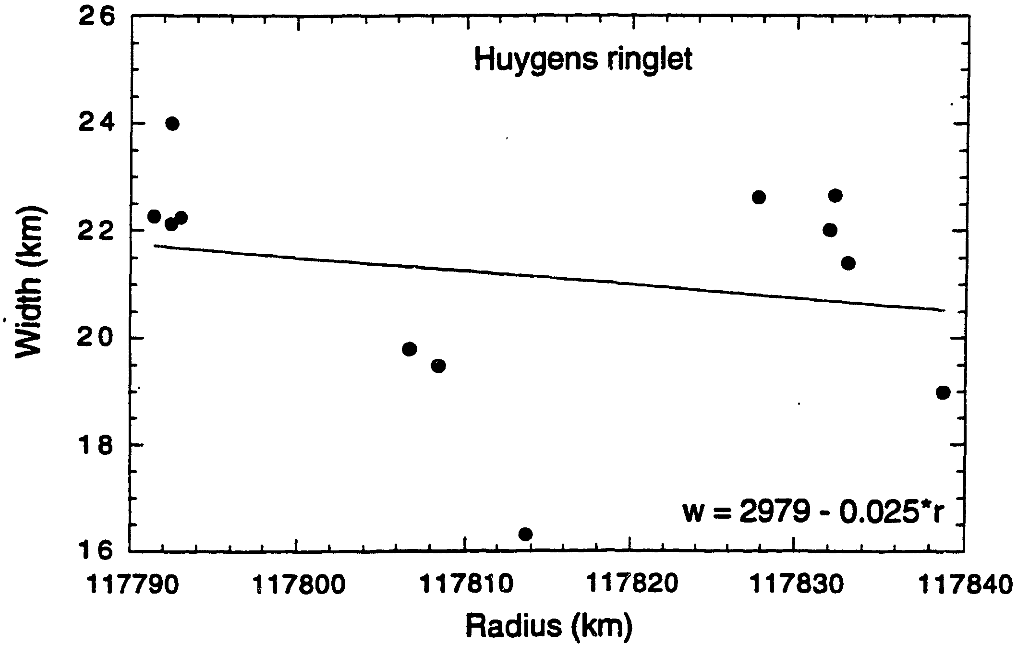

FIG. 10.1. (f) Huygens ringlet. This ringlet shows a very weak correlation between width and radius, with a negative gradient.

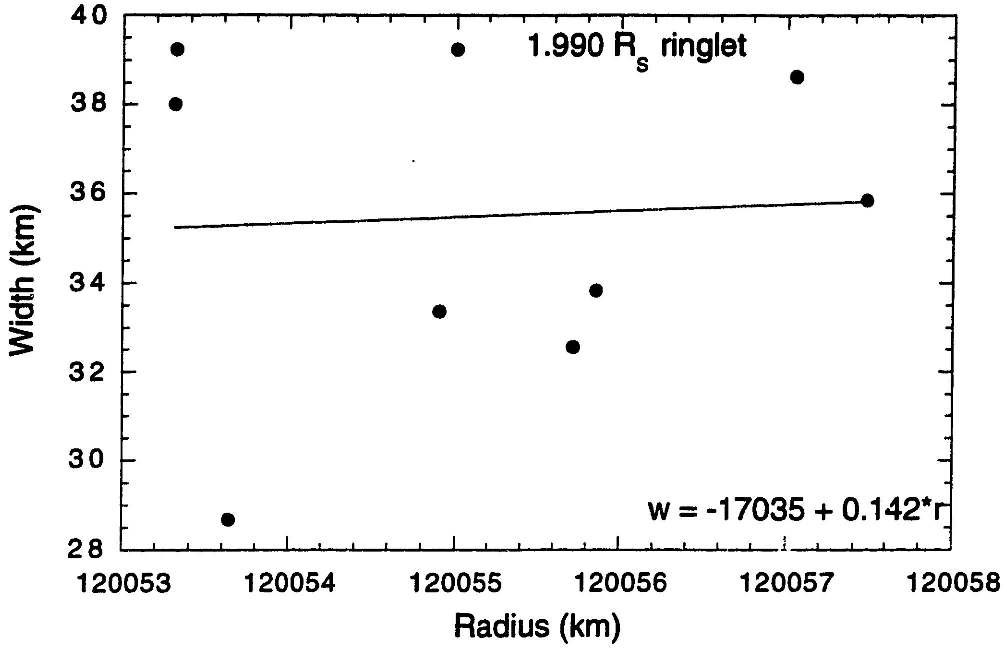

FIG. 10.1. (g) 1.990 R$_S$ ringlet. This ringlet shows no correlation between width and radius.

Of the rings studied, we find only two for which there is a definite width-radius relation: the Titan and Maxwell ringlets. For these ringlets, we determine the difference in semimajor axis and eccentricity between the two edges using Eq. (9) of French *et al.* (1986), and from these determine ring masses using Eq. (28b) of Borderies *et al.* (1983; 1984). These equations describe how to calculate the width (W) and mass of the ringlet (M_r) through their dependence on the half-amplitude of the variation in eccentricity across the ringlet (Δe) and the difference in semimajor axis between the inner and outer edges (Δa); they are reproduced below in our notation:

$$W = r(a+\Delta a, e+\Delta e, \varpi_0 - \Delta\varpi_0) - r(a-\Delta a, e-\Delta e, \varpi_0 + \Delta\varpi_0) \tag{10.1}$$

$$\Delta e = \frac{21\pi e}{4}\frac{M_p}{M_r}J_2\left(\frac{R_p}{a}\right)^2\left(\frac{\Delta a}{a}\right)^3\frac{1}{H(q^2)} \tag{10.2}$$

where $r(a,e,\varpi_0)$ is given by Eq. (46). $H(q^2)$ and q^2 are given by the following equations:

$$H(q^2) = \frac{1-\sqrt{1-q^2}}{q^2\sqrt{1-q^2}} \tag{10.3}$$

$$q^2 \cong \left(\frac{a\Delta e}{\Delta a}\right)^2 + \left(\frac{ae\Delta\varpi_0}{\Delta a}\right)^2 \tag{10.4}$$

We first use Eq. (10.1) to fit for Δa, Δe, and $\Delta\varpi_0$. The values found are then used in Eq. (10.2) to determine the mass of the ringlet. This analysis assumes the ringlet is in equilibrium, for which $\Delta\varpi_0$ would be zero. This analysis is also a simple, two-streamline approximation. Borderies *et al.* state that in a full streamline analysis, the ringlet masses are smaller by a factor of two.

From the ring masses calculated from these equations, we can then determine the ring surface densities, σ. These quantities are listed in Table 10.1, along with values for the same parameters previously determined by P84b. The masses found here for the Titan and Maxwell ringlets total approximately 1% of the mass of the C Ring, as estimated by Harrington *et al.* (1993). The values of σ found here are similar to those found by P84b, approximately 20-25 g cm^{-2}. Note that this method is valid for $\delta e/e \ll 1$, which is not true for the Maxwell Ringlet.

Table 10.1. Physical parameters of Titan and Maxwell Ringlets

	Titan Ringlet (162)		Maxwell Ringlet (160)	
	this work	P84b	this work	P84b
a, km	77878.1 ± 0.5	77871 ± 7	87510.1 ± 0.6	87491 ± 8
$e \times 10^4$	2.53 ± 0.08	2.6 ± 0.2	4.64 ± 0.23	3.4 ± 0.4
$2\Delta a$, km	25.6 ± 1.0	25 ± 3	57.0 ± 1.0	64 ± 3
$2\Delta e \times 10^4$	0.96 ± 0.15	1.4 ± 0.4	4.30 ± 0.42	3.4 ± 0.6
$2\Delta\varpi_0$, deg	19.2 ± 7.6	—	1.2 ± 2.0	—
$M_r \times 10^{18}$, g	3.1 ± 0.9	2.1 ± 1.4[a]	7.1 ± 1.6	6.1 ± 3.8[a]
σ, g cm^{-2}	24.8 ± 7.2	17 ± 11[a]	22.6 ± 5.1	17 ± 11[a]

[a] Errors in these quantities have been altered to reflect the contributions from all sources of error. The errors in the original reference are underestimated because they only account for the error in Δe, and do not propagate this through $H(q^2)$.

As stated above, in equilibrium the apsidal shift, $\Delta\varpi_0$, should be approximately zero. While this is true of the Maxwell ringlet, we find that the Titan ringlet has a significant non-zero apsidal shift. This could be an indication that the ringlet is librating. However, for a librating ringlet with undergoing viscous damping, Borderies *et al.* find a value of -0.05 degrees for the apsidal shift (see their Table I). Not only is this two orders of magnitude smaller than the value found here, but it is also of opposite sign. Clearly something else is acting here, but at this point we do not know what.

If we can ignore the inconsistencies with the Titan ringlet for now (Borderies *et al.* find that libration of a ringlet has little effect on the derived mass of the ring), we see how the calculated masses and surface densities fit in with other measurements of surface density.

Table 10.2 below provides a summary of surface densities throughout the rings calculated by various methods. Of the measurements in the C Ring, we notice that the surface density is about 20 times the background density. This is expected, because the ringlets are more optically thick than the background material. The values presented here imply that the material in the ringlet does not come only from the surrounding gap. If this were the case, the surface density in the ringlets would be about 3 g cm^{-2}, an order of magnitude too small. The surface density estimates of the background may be over-estimates, because the surface density of the background material is often calculated from density and bending wave locations and amplitudes; there tends to be an optical depth enhancement surrounding these waves (Bosh 1990; Gresh *et al.* 1986; Rosen *et al.* 1991a).

Table 10.2. Measurements of Surface Density in Saturn's Rings

Ring Area	Radius (km)	σ, g cm^{-2}	Method	Reference
C	74892	1	Mimas 4:1 DW	(Rosen *et al.* 1991b)
C	77878	25	eccentricity gradient	this work
C	78429-84462	3	radio signal scattering	(Zebker *et al.* 1985)
C	87510	23	eccentricity gradient	this work
C	87654	1	Atlas 2:1 DW	(Rosen *et al.* 1991b)
C	90640-91967	4	radio signal scattering	(Zebker *et al.* 1985)
B	116720	54	Mimas 4:2 BW	(Lissauer 1985)
A	125647	50	Pandora 6:5 DW	(Rosen *et al.* 1991b)
A	125893	59	Prometheus 7:6 DW	(Rosen *et al.* 1991b)
A	127615	68	Prometheus 8:7 DW	(Rosen *et al.* 1991b)
A	127768	30	Mimas 7:4 BW	(Rosen *et al.* 1991b)
A	128001	45	Pandora 7:6 DW	(Rosen *et al.* 1991b)
A	128947	39	Prometheus 9:8 DW	(Rosen *et al.* 1991b)
A	129753	43	Pandora 8:7 DW	(Rosen *et al.* 1991b)
A	130008	53	Prometheus 10:9 DW	(Rosen *et al.* 1991b)
A	130873	40	Prometheus 11:10 DW	(Rosen *et al.* 1991b)
A	131107	36	Pandora 9:8 DW	(Rosen *et al.* 1991b)
A	131592	53	Prometheus 12:11 DW	(Rosen *et al.* 1991b)
A	131898	33	Mimas 5:3 BW	(Rosen *et al.* 1991b)
A	132187	26	Pandora 10:9 DW	(Rosen *et al.* 1991b)
A	132198	40	Prometheus 13:12 DW	(Rosen *et al.* 1991b)
A	132717	50	Prometheus 14:13 DW	(Rosen *et al.* 1991b)
A	132297	30-40	Mimas 5:3 DW	(Rosen *et al.* 1991a)
A	133066	45	Pandora 11:10 DW	(Rosen *et al.* 1991b)
A	135640	24	Mimas 8:5 BW	(Lissauer 1985)

11. GRAVITATIONAL HARMONIC COEFFICIENTS

Gravitational harmonic coefficients are used to describe the departure of a planet's gravity field from spherical symmetry—typically due to rotation, external perturbing potentials, and/or departure from hydrostatic equilibrium (Hubbard 1984). These coefficients, commonly called J_{2n}, can be determined through several methods: (i) observations of their effect on the precession of satellites and rings, (ii) measurements of the motions of spacecraft near the planet, and (iii) calculations from interior models. All three of these methods have been used in the past. Initial determinations of the gravitational harmonic coefficients for Saturn were performed by observing the apsidal precession rates and nodal regression rates of Mimas and Enceladus (Jeffreys 1954; Kozai 1976). However, this allowed only the determination of J_2 and J_4 because the effects of the higher-order harmonics are more difficult to detect with increasing distance from the planet (see Eqs. 4.11 and 4.12). Null *et al.* (1981, hereafter referred to as N81) performed an analysis of the tracking data from Pioneer 11. These data, along with previously published satellite precession and regression rates led to revised values for J_2 and J_4. These values are listed in Table 11.1. More recently, NP88 used the location and eccentricity of the Titan ringlet (1.29 R_S) and the fact that it is in an apsidal resonance with Titan to determine a constraint on J_2, J_4, and J_6 to a high degree of accuracy. Although this is the primary method for the determination of the coefficients for Uranus (French *et al.* 1991), no attempt has been made to determine the values of the gravitational harmonics by incorporating the measured precession rates of the rings.

Table 11.1: Determinations of Gravitational Harmonic Coefficients, for R_p = 60330 km

Method	$J_2 \times 10^6$	$J_4 \times 10^6$	$J_6 \times 10^6$	Reference
Polytrope, index = 1	27680			Eqs. 11.17, 11.18
Satellite motions	16267 ± 9	-1024 ± 5		Kozai, 1976
Spacecraft tracking[a,b]	16296 ± 18	-922 ± 38	81 (fixed)	N81
Titan ringlet apsidal resonance[a,c]	16297 ± 18	-906 ± 61	114 ± 50	NP88

[a] The values for these entries were scaled to our reference radius of 60330 km (if necessary) and adjusted for differences in pole position and radius scale.

[b] For assumed $J_8 = J_{10} = \cdots = 0$.

[c] For $J_8 = -10 \times 10^{-6}$, $J_{10} = 2 \times 10^{-6}$, $J_{12} = -0.5 \times 10^{-6}$, $J_{14} = J_{16} = \cdots = 0$.

The three independent constraints for J_2, J_4, and J_6 used by NP88 were the location of the Titan ringlet and two additional constraints from Pioneer tracking and satellite precession rates incorporated from N81. The formal error in the adopted solution of NP88 most depends mainly on the second of these N81 constraints, a relation between J_4 and J_6 (Eq. 11.3). By replacing this rather weak constraint with a stronger one, we are able to reduce the formal error of the coefficients. To do this, we substitute a constraint from the measured precession rate of a non-circular ring. As NP88 state, the error in the precession rate must be reduced to less than 0.008 deg day^{-1} to be of comparable accuracy to the Titan ringlet constraint. The errors in precession rates present in Tables 9.1-9.10 are as much as 10 times smaller than this. The two ringlets with the smallest errors are the Maxwell and Huygens ringlets.

Pioneer Constraint

To use the Pioneer constraint we must first adjust it for the ring-plane pole, radius scale, and Saturn equatorial radius in use here. We do this by utilizing the partial derivatives given by N81 in Table XI and by scaling the coefficients by $(60000/60330)^{2n}$. The constraint as given in N81, and as modified are given in Eqs. 11.1 and 11.2, respectively. Further analysis has been performed by Campbell and Anderson (1989), incorporating tracking data from Voyager. They get similar results to N81. Their constraints include Voyager tracking, Pioneer tracking, satellite precession rates, and Titan ringlet constraints together, and thus is difficult to use in these analyses because the constraints are not separate. We therefore use the N81 constraints.

Original N81 "Pioneer" constraint:

$$\begin{aligned}&\left(J_2 - 16479\times10^{-6}\right) - 0.4386\left(J_4 + 937\times10^{-6}\right)\\&\qquad +0.1947\left(J_6 - 84\times10^{-6}\right) = (0\pm3)\times10^{-6}\end{aligned} \tag{11.1}$$

Adjusted N81 "Pioneer" constraint:

$$\begin{aligned}&\left(J_2 - 16296.1\times10^{-6}\right) - 0.4434\left(J_4 + 922.3\times10^{-6}\right)\\&\qquad +0.1990\left(J_6 - 81.3\times10^{-6}\right) = (0\pm3)\times10^{-6}\end{aligned} \tag{11.2}$$

We also present the weaker Pioneer constraint given in N81. This constraint will be discussed later.

Original N81 "Pioneer-2" constraint:

$$\left(J_4 + 937\times10^{-6}\right) + 0.49\left(J_6 - 84\times10^{-6}\right) = (0\pm38)\times10^{-6} \tag{11.3}$$

Adjusted N81 "Pioneer-2" constraint:

$$\left(J_4+922.3\times10^{-6}\right)+0.495\left(J_6-81.3\times10^{-6}\right)=(0\pm37)\times10^{-6} \tag{11.4}$$

Titan Ringlet Constraint

For the Titan constraint, we modify the radius scale and adjust for the difference in distance from resonance that arises due to a slightly different value of ringlet eccentricity. We make these changes by re-calculating the coefficients and the partial derivatives using the Titan ringlet and both Pioneer constraints, in the same manner as that in which they were originally derived. Because the errors in the eccentricity and radius scale are much smaller than in NP88, the error for this constraint also decreases. The original and modified constraints are given in Eqs. 11.5 and 11.6 (we drop the relation to resonance location, surface density, J_8, J_{10}, J_{12}, J_{14}, and J_{16} that were in the original constraint as given in NP88).

Original NP88 Titan constraint:

$$\begin{aligned}\left(J_2-16297\times10^{-6}\right)-1.507\left(J_4+910\times10^{-6}\right)&\\ +1.586\left(J_6-107\times10^{-6}\right)=(0\pm12)\times10^{-6}&\end{aligned} \tag{11.5}$$

Adjusted NP88 Titan constraint:

$$\begin{aligned}\left(J_2-16296.8\times10^{-6}\right)-1.5071\left(J_4+905.9\times10^{-6}\right)&\\ +1.5856\left(J_6-114.4\times10^{-6}\right)=(0\pm2.6)\times10^{-6}&\end{aligned} \tag{11.6}$$

Equation 11.6 gives the Titan ringlet constraint in a linear form; however, we shall find it more convenient to use the non-linearized equation:

$$\dot{\varpi}=\dot{\varpi}_{\text{Saturn}}+\dot{\varpi}_{\text{satellites}}+\dot{\varpi}_{\text{rings}}=22.576\,976\,82\pm0.000\,000\,09\text{ deg day}^{-1} \tag{11.7}$$

where the right-hand side of the equation is the mean motion of Titan, from Harper & Taylor (1993). The first term in the sum, $\dot{\varpi}_{\text{Saturn}}$, is the contribution to the total apsidal precession rate induced by the oblate Saturn, given by Eq. 4.11. This equation is an approximation for a gravitational potential with rotational and north-south symmetry. If the potential does not possess north-south symmetry, then odd-numbered gravitational harmonics will appear. However, because all features are equatorial and the multiplicative Legendre polynomials for odd harmonics are all 0 at the equator, these terms will have no effect on the precession rates. The other terms in Eq. 11.7, $\dot{\varpi}_{\text{satellites}}$ and $\dot{\varpi}_{\text{rings}}$, are contributions from perturbations by the satellites and by the rings (NP88). For the Titan ringlet, these two sources amount to approximately 0.002 deg day^{-1}. As we see by comparing against the errors in measured precession rates of non-circular features given in

Tables 9.1-9.10, this is about the same order of magnitude, or greater, than the errors in the measured precession rates. Thus it is important to include these terms in the analysis.

Other perturbations to the gravity-induced precession include general relativity and solar torques. These amount to approximately 23×10^{-6} and 0.6×10^{-6} deg day^{-1}, respectively; therefore they are much smaller than the measurement errors and can be ignored at this time. However, as the time baseline increases and precession rate errors decrease in the future, we will eventually need to include these terms.

To first order in e and i, the satellite contribution to the ringlet at semimajor axis a and mean motion n, as a function of satellite mass m_j, mass of Saturn M_S, and semimajor axis a_j is (NP88):

$$\dot{\varpi}_{\text{satellite}}(a) = \frac{1}{4} n \sum_j \frac{m_j}{M_S} \alpha_j^2 \, b_{3/2}^{(1)}(\alpha_j) \tag{11.8}$$

where α_j is the ratio of the semimajor axis of the ringlet to that of the satellite, and $b_{3/2}^{(1)}$ is the Laplace coefficient with $s = 3/2$ and $k = 1$. The Laplace coefficient is represented by the following series (Brouwer and Clemence 1961):

$$\begin{aligned} b_s^{(k)}(\alpha) = {} & \frac{s(s+1)(s+2)\cdots(s+k-1)}{1 \cdot 2 \cdot 3 \cdots k} \alpha^k \\ & \times \left[1 + \frac{s(s+k)}{1(k+1)} \alpha^2 + \frac{s(s+1)(s+k)(s+k+1)}{1 \cdot 2(k+1)(k+2)} \alpha^4 + \cdots \right] \end{aligned} \tag{11.9}$$

For satellites, $\alpha \ll 1$, and then $b_{3/2}^{(1)}(\alpha)$ can be approximated as

$$b_{3/2}^{(1)}(\alpha) \approx 3\alpha + \frac{45}{8} \alpha^3 \qquad (\alpha \ll 1) \tag{11.10}$$

The calculation for the ring contribution to the precession rate is more complicated. Following the method of NP88, we separate it into three components: the contributions from rings interior and exterior to the ringlet in question, $\dot{\varpi}_{\text{r,int}}$ and $\dot{\varpi}_{\text{r,ext}}$, and the contribution from ring material very near the ringlet, $\dot{\varpi}_{\text{r,near}}$, for which the small e approximation of Eq. 11.8 does not hold. Then,

$$\dot{\varpi}_{\text{rings}} = \dot{\varpi}_{\text{r,int}} + \dot{\varpi}_{\text{r,ext}} + \dot{\varpi}_{\text{r,near}} \tag{11.11}$$

The $\dot{\varpi}_{\text{r,int}}$ and $\dot{\varpi}_{\text{r,ext}}$ contributions are found by approximating the rings as a set of narrow ringlets. We use the parameters given by NP88 in their Table 3. Then, $\dot{\varpi}_{\text{r,ext}}$ for each constructed "ringlet" is found using the same equation as for satellites (Eq. 11.8). The contribution from $\dot{\varpi}_{\text{r,int}}$ is (NP88):

$$\dot{\varpi}_{\mathrm{r,int}}(a) = \frac{1}{4} n \sum_j \frac{m_j}{M_S} \alpha_j \, b_{3/2}^{(1)}(\alpha_j) \tag{11.12}$$

Note that for rings, we generally cannot use the convenient approximation for the Laplace coefficient given in Eq. 11.10, because $\alpha \approx 1$, and must incorporate more terms than the first two (we use the first 400, resulting in an error of less than 0.5% for $\alpha = 0.99$). The equation for $\dot{\varpi}_{\mathrm{r,near}}$ is developed in the Appendix of NP88. Their final equation is a function of local surface density σ, and distances to the nearest ring material on either side of the center of the ringlet $\delta a_{\mathrm{in,out}}$:

$$\dot{\varpi}_{\mathrm{r,near}} = \frac{2na^3}{M_S} \sigma \left[\frac{G(q_{\mathrm{in}})}{|\delta a_{\mathrm{in}}|} + \frac{G(q_{\mathrm{out}})}{|\delta a_{\mathrm{out}}|} \right] \tag{11.13}$$

The functions q and G are given by the following equations:

$$q_{\mathrm{in,out}} \equiv \frac{ae}{\delta a_{\mathrm{in,out}}}, \tag{11.14}$$

$$G(q) \equiv \frac{1 - \sqrt{1 - q^2}}{q^2} \tag{11.15}$$

Values for σ and $\delta a_{\mathrm{in,out}}$ are given in Table 3 of NP88.

The values of $\dot{\varpi}_{\mathrm{satellites}}$ and $\dot{\varpi}_{\mathrm{rings}}$ are insensitive to the small changes we will be making in the gravitational harmonics. They are more sensitive to the change in radius scale between this work and NP88. Therefore, we calculate the value of this quantity at the new radii, using the adjusted NP88 coefficients, and then fix it at this value. These values are given in Table 11.2.

Table 11.2. Contributions to Precession Rate from Satellites and Rings.

Ringlet	$e \times 10^4$	$\lvert\delta a_{\mathrm{in}}\rvert$ (km)	$\lvert\delta a_{\mathrm{out}}\rvert$ (km)	$\dot{\varpi}_{\mathrm{contributions}}$ (deg day^{-1})			
				satellites	rings, int + ext	rings, near	satellites + rings
Feature 44	0.88	50	50	0.0001308	0.0001290	0.0022084	0.0024681
Maxwell	4.64	150	75	0.0001708	0.0016592	0.0014860	0.0033160
1.470 R_S	0.15	100	50	0.0001748	0.0035819	0.0021381	0.0058948
1.495 R_S	0.50	50	50	0.0001799	0.0008114	0.0029284	0.0039197
Huygens	2.73	450	150	0.0002940	0.0009014	0.0009758	0.0021712
1.990 R_S	2.91	300	50	0.0003054	0.0007827	0.0029825	0.0040706

Constraints from Other Ringlets

To incorporate a constraint from another non-circular ringlet, we use an equation of the form of Eq. 11.7. Instead of the setting the right-hand side of this equation to the mean motion of Titan, we set it to the measured free precession rate of the feature (Eq. 11.16). This feature can be either freely precessing (as the Maxwell ringlet is), or it can be a superposition of free and forced modes (as the 1.495 R_S ringlet appears to be). In this latter case, the right-hand side of Eq. 11.16 is the measured free precession rate only.

$$\dot{\varpi} = \dot{\varpi}_{\text{Saturn}} + \dot{\varpi}_{\text{satellites}} + \dot{\varpi}_{\text{rings}} = \dot{\varpi}_{\text{measured}} \pm \sigma_{\dot{\varpi}} \tag{11.16}$$

One conceptual advantage to giving the linearized form of the Titan ringlet constraint (Eq. 11.7) is that it shows the sensitivity of the constraint to the various gravitational harmonic coefficients. This is shown by the multiplicative factor before each coefficient. Thus, we see that the Titan ringlet constraint is most sensitive to the J_6 term, while the Pioneer/satellites constraint is most sensitive to J_2. When adding a third constraint, we wish to choose one that provides as orthogonal a constraint as possible, and one that does not have any unmodeled effects that could skew the result. To check for orthogonality, we present the sensitivities of the constraints posed by the other narrow ringlets studied in this work in Table 11.3. The Maxwell, 1.470 R_S, and 1.495 R_S ringlets are most sensitive to J_4, while the Huygens and 1.990 R_S ringlets are most sensitive to J_2. Thus the Maxwell, 1.470 R_S, or 1.495 R_S ringlets would provide the best constraint.

Table 11.3. Sensitivities of Ringlet Constraints to Gravitational Harmonics.

Ringlet	Location	$\partial\dot{\varpi}/\partial J_2$	$\partial\dot{\varpi}/\partial J_4$	$\partial\dot{\varpi}/\partial J_6$
Feature 44	74492.33	1476	-2431	2795
Titan	77878.06	1263	-1903	2001
Maxwell	87510.07	840	-1001	833
1.470 R_S	88710.36	801	-929	752
1.495 R_S	90210.20	755	-847	663
Huygens	117812.20	297	-195	89
1.990 R_S	120035.73	278	-176	78

We next calculate the precession rate from the adjusted NP88 coefficients, including the effects of satellites and rings (Table 11.2). In Table 11.4, the results are compared with the measured rates. The precession rate residual of the Huygens ringlet is 2.5 times that of the Maxwell ringlet. Additionally, the residual of the 1.495 R_S ringlet is 2.6 times smaller than that of the Maxwell ringlet. It appears that the Maxwell and 1.495 R_S ringlets are the most likely to be adequately modeled and thus used in the determination of gravitational harmonics. The Huygens, 1.470 R_S, and 1.990 R_S ringlets and the inner edge of the C ring (feature 44) all have uncomfortably large residuals, and thus are likely to have additional perturbations beyond those included in their models. The measured precession rates of these features cannot be taken as adequately representing the true precession rate of the ringlet. Therefore, the Maxwell and 1.495 R_S ringlets are the best candidates for an additional constraint on the gravitational harmonics.

Table 11.4. Calculated vs. Measured Precession Rates.

Ringlet	Model[a]	a (km)	$\dot{\varpi}_{\rm pred}$ (deg day^{-1})	$\dot{\varpi}_{\rm meas}$ (deg day^{-1})	$\dot{\varpi}_{\rm meas} - \dot{\varpi}_{\rm pred}$ (deg day^{-1})
Feature 44	fp	74492.33	26.6018	26.5582 ± 0.0037	0.0436 ± 0.0037
Maxwell CR	fp	87510.07	14.6957	14.6937 ± 0.0007	–0.0020 ± 0.0007
1.470 R_S CR	fp	88711.02	13.9851	13.9965 ± 0.0115	0.0114 ± 0.0115
1.495 R_S OER	fp with Mimas 3:1	90210.20	13.1547	13.1539 ± 0.0007	–0.0008 ± 0.0007
Huygens CR	fp with Mimas 2:1	117812.20	5.0224	5.0274 ± 0.0009	0.0051 ± 0.0009
1.990 R_S IER	fp	120035.73	4.6994	4.7484 ± 0.0160	0.0489 ± 0.0160

[a] fp = freely precessing

Solving for Gravitational Harmonics

To solve for the values of gravitational harmonics using the Pioneer (Eq. 11.2), Titan (Eq. 11.7), and other ringlet constraints (Eq. 11.16), we perform a simultaneous solution of three equations with three variables (J_2, J_4, and J_6). We try solutions using the Maxwell ringlet and the 1.495 R_S ringlet and compare them (Table 11.5). For all solutions, we fix the values of J_8, J_{10}, and J_{12} at those adopted by NP88.

Table 11.5. Solutions for Gravitational Harmonics for R_S = 60330 km.

Case	Constraints Used	$J_2 \times 10^6$	$J_4 \times 10^6$	$J_6 \times 10^6$
s1	Pioneer, Titan, Maxwell	16301.6 ± 6.5	-889.1 ± 12.5	127.3 ± 8.4
s2	Pioneer, Titan, 1.495 R_S	16298.6 ± 6.7	-899.5 ± 12.3	119.3 ± 8.1
s3	Titan, Maxwell, 1.495 R_S	16409.8 ± 94.2	-726.4 ± 145.7	213.8 ± 79.4

The errors in coefficients in each case are calculated by adjusting each constraint by one formal error and then again solving for the coefficients. The main source of errors in cases s1 and s2 are from the Pioneer constraint, followed closely by the Maxwell constraint. The

Titan constraint contributes small errors because the errors in the position and eccentricity of this ringlet have been significantly reduced over those used in NP88. Given that the Pioneer constraint is the major source of error, we attempted case s3, replacing the Pioneer constraint with an additional ringlet constraint. We find that the values of gravitational harmonics deviate by about 1 formal error from those necessary to satisfy the Pioneer constraint. This happens because the constraints imposed by the Maxwell and 1.495 R_S ringlets are not sufficiently orthogonal. Any small error in the determination of either of these constraints will therefore cause the solution to deviate significantly from reality; the formal error of such a solution will not necessarily be large enough to encompass the "true" solution. We find this same behavior when we attempt to fit for the gravitational harmonics using only the precession rates of the ringlets studied here. Besides harboring possible errors, these ringlets present almost parallel constraints and thus do not yield a believable result. Therefore, we conclude that we cannot discard the Pioneer constraint. Solutions s1 and s2 provide the best results at this stage.

Table 11.6. Fits for Gravitational Harmonics for $R_S = 60330$ km

Fit	Constraints Used	$J_2 \times 10^6$	$J_4 \times 10^6$	$J_6 \times 10^6$	$J_8 \times 10^6$
f1[a]	Pioneer, Titan, Maxwell, 1.495 R_S	16409.5 ± 6.7	−726.8 ± 10.3	213.6 ± 5.5	−10.0 (fixed)
f2[b]	Pioneer, Titan, Maxwell, 1.495 R_S	16300.7 ± 7.8	−893.4 ± 12.8	123.8 ± 7.5	−10.0 (fixed)
f3[b]	Pioneer, Pioneer-2, Titan, Maxwell, 1.495 R_S	16300.5 ± 5.5	−893.8 ± 9.0	123.6 ± 5.2	−10.0 (fixed)
f4[b]	Pioneer, Pioneer-2, Titan, Maxwell, 1.495 R_S	16298.3 ± 2.3	−990 ± 29	−82 ± 61	−138 ± 38
f5[b]	Pioneer, Pioneer-2, Titan, Maxwell, 1.495 R_S	16300.7 ± 5.4	−893.5 ± 6.6	123.6 (fixed)	−10.2 ± 3.3

[a] Unweighted fit.

[b] Weighted fit.

An alternate means of determining these coefficients is to perform a least-squares fit to the constraints. However, care must be taken to correctly weight the various constraints, else an erroneous solution will be found. In Table 11.6, we present results of fits to the constraints. Fit f1, an unweighted fit, combines constraints from Pioneer and the Titan, Maxwell, and 1.495 R_S ringlets. The fitted values of the gravitational harmonics are many formal errors different from solutions s1 or s2 (Table 11.5). If we look at the residuals from this fit for each of the constraints (Table 11.7) and compare it with the error in the constraint (given in the last row of this Table), we see that the fit favored the Maxwell and 1.495 R_S ringlet constraints by greatly lowering their residuals. This leaves the Pioneer constraint with a residual much larger than the constraint specifies. This points out the need for properly weighted the various constraints. Therefore, all further fits are weighted, by the reciprocal of the square of the constraint error (last row of Table 11.7). Fit f2 is weighted in such a manner, and the parameter values are much closer to solutions s1 and s2. Additionally, we see that the residuals from this fit are all comfortably within the constraint errors. The errors in the Maxwell and 1.495 R_S constraints are approximately of equal magnitude and opposite sign, indicating that these two constraints are played off against each other. There may be an error in one of the constraints, but without any additional information, we cannot tell which one. Therefore, fit f2 combines the constraints from both ringlets and, as expected, the parameter values thus found are intermediate between solutions s1 and s2, each of which use only one of the constraints.

Table 11.7. Residuals from Fits for Gravitational Harmonics

	$(O-C)\times10^6$ (deg day^{-1})				
Fit	Pioneer	Pioneer-2	Titan	Maxwell	1.495 R_S
f1	–53.0	—	0.2	–2.3	2.3
f2	–0.3	—	0.001	–613.8	609.5
f3	–0.2	-7.6	0.001	–622.3	603.7
f4	0.2	-12.9	0.02	–36.1	11.7
f5	–0.3	-7.9	–0.0004	–609.4	612.8
Errors in constraints	3	37	2.6	700	700

Table 11.8. Correlation Matrix for Fit f4

	J_2	J_4	J_6	J_8
J_2	1	0.40	0.31	0.28
J_4	0.40	1	1.00	0.99
J_6	0.31	1.00	1	1.00
J_8	0.28	0.99	1.00	1

Since we are fitting for the parameter values instead of solving simultaneous equations, there is no longer any reason to discard weak constraints. With our weighting scheme, a weak constraint will have less effect on the solution, but will still contribute to it. Therefore, we reintroduce the Pioneer-2 constraint. The results of a fit including this constraint are listed as Fit f3 in Table 11.6; the values are very close to those found in Fit f2, but the formal error has decreased slightly. Since we are now utilizing 5 constraints, it is conceivable that we will be able to fit for J_8 as well as J_2, J_4, and J_6. We attempt this in Fit f4. The parameter values found in this fit indicate that the constraints are not sufficient to determine the first 4 even harmonics. Although we did achieve a numerical result, the value for J_6 is negative while it should be positive. The J_6 parameter gives a measure of the second derivative of density with distance from the center of the planet, and is strongly correlated with J_4 (Hubbard 1974). Therefore, it is not strictly unphysical to have a negative value for this parameter, but the value is usually positive. The correlation matrix for this fit (Table 11.8) shows that the value of J_8 has a 1:1 correlation with the value of J_6, and an only slightly weaker correlation with J_4. To break this strong correlation, we try Fit f5 in which we fix the value of J6 at that obtained in Fit f3. The results of this fit differ very little from those of Fit f3. Because we had to fix the value of J_6 to get a meaningful fit for J_8, this is not a very useful fit and we find we are unable to fit for J_8. Therefore, we adopt the results of Fit f3 as our best solution for the gravitational harmonics. This fit incorporates 2 independent Pioneer constraints, as well as constraints from the Titan, Maxwell, and 1.495 R_S ringlets. The adopted values for gravitational harmonics are given in Table 11.9.

Table 11.9. Adopted Values of Gravitational Harmonics (R_S = 60330 km).

Parameter	Adopted Value $\times 10^6$	(Adopted Value - NP88 Value) $\times 10^6$
J_2	16301 ± 6	4 ± 19
J_4	-894 ± 9	12 ± 62
J_6	124 ± 5	10 ± 50
J_8	-10 (fixed)	—
J_{10}	2 (fixed)	—
J_{12}	-0.5 (fixed)	—
$J_{14}, J_{16}, J_{18}, \cdots$	0	—

We are unable to fit for the value of J_8 or higher-order harmonics at this time, as we do not possess constraints sensitive enough to these parameters. Because they are highly correlated with the lower-order harmonics, we investigate the dependence of J_2, J_4, and J_6 on changes in J_8, J_{10}, and J_{12}. These are presented in Table 11.10. They are found by changing the value of J_8, J_{10}, or J_{10} by 100%, and then fitting for a new solution. In most cases, changes in these parameters change the values of J_2, J_4, and J_6 by less than one formal error. However, J_6 is strongly correlated with J_8, and doubling the value of J_8 changes the value of J_6 by 3 formal errors. Therefore, the value of J_6 given above is dependent on the fixed value of J_8. It is desirable to break this dependence by including J_8 as a fitted parameter. However, in order to fit for J_8 or higher-order harmonics, we would need a constraint from smaller radii than we currently have. The best candidate for this at this time is feature 44, the inner edge of the C ring. The measured precession rate of this feature is many formal errors different from the predicted value, so we cannot use this feature until we understand this difference.

In Table 11.10, we also give the dependencies of J_2, J_4, and J_6 on the assumed ring surface density (used for calculation of the near-ring contribution to the precession rate) near the Titan, Maxwell, and 1.495 R_S ringlets (10 g cm^{-2} in all cases). A change of 100% in the surface density changes the values of J_2, J_4, and J_6 by about 1 formal error.

Table 11.10. Dependence of J_2, J_4, J_6 on $J_8, J_{10}, J_{12}, \sigma$

Parameter	δ parameter	$\delta J_2 \times 10^6$	$\delta J_4 \times 10^6$	$\delta J_6 \times 10^6$
J_8	10×10^{-6}	0.2	-7.5	16.1
J_{10}	2×10^{-6}	-0.5	-2.9	-3.9
J_{12}	0.5×10^{-6}	0.2	-0.8	1.0
σ	10 g cm^{-2}	3.5	13.2	9.7

Interior Models

To see how the measured values of these coefficients compare to those derived from interior models, we begin with a simplified case. In this method for determining J_2, we assume a polytrope of index 1. This takes too simple a view of the problem, but it provides a starting value. However, if we let this assumption hold, we can use a relation given by Hubbard (1984) which predicts a value for J_{2n} as a function of a dimensionless response coefficient, $\Lambda_{2n,l}$, and a dimensionless rotational distortion parameter, q:

$$J_{2n} = \sum_{l=0}^{\infty} \Lambda_{2n,l}\, q^{n+l} \tag{11.17}$$

The dimensionless response coefficient $\Lambda_{2n,l}$ is equal to 0.173 for a polytrope of index 1, with $n = 1$ and $l = 0$ (Hubbard 1984). The dimensionless distortion parameter q is equal to the ratio of the equatorial centrifugal acceleration to the zeroth-order term of the gravitational acceleration (Zharkov and Trubitsyn 1978):

$$q = \frac{\omega_{\mathrm{p}}^2 R_{\mathrm{p}}^3}{GM_{\mathrm{p}}} \tag{11.18}$$

where ω_{p} is the planet's rotation rate. Using the parameter values given in Table 6.1 and a value of 0.4440 days for period of Saturn's magnetic field rotation (Kaiser *et al.* 1984) we find a q for Saturn of 0.16 and therefore a value for J_2 of 0.027 or approximately 70% greater than the measured values given in Table 11.1. The response coefficient for Saturn calculated from the observed value of J_2 is 0.10, indicating that Saturn is more centrally condensed than is Jupiter, whose observed $\Lambda_{2,0}$ is 0.165 (Hubbard and Marley 1989). The smaller the response coefficient, the more centrally condensed is the planet.

Hubbard & Marley (1989) present a more physically realistic model of Saturn's interior, that is constrained by the NP88 values of J_2 and J_4, and that attempts to reproduce the observed helium depletion in the atmosphere (Hubbard and Stevenson 1984). Their model consists of a rocky core, that is relatively insensitive to the gravity harmonics; a metallic hydrogen envelope around this rock core, enriched in helium and/or other heavy materials; and a hydrogen atmosphere, depleted in helium compared with solar composition. They find that the model suggests that the entire hydrogen-helium atmosphere is not depleted in helium, that instead the model is consistent with a chemical gradient in this atmosphere that involves a species heavier than helium. Interestingly, the value of J_6 predicted by this model is significantly lower than our adopted value for this parameter, by ~8σ. They find values for J_6 of (72-74)$\times 10^{-6}$ (for R_S = 60330 km); J_6 was not an explicit constraint in their modeling as the formal error of the NP88 solution was too large. While the values predicted for J_6 by the Hubbard & Marley interior model are consistent with the value and error given by NP88, it did not satisfy a relation between J_4 and J_6 presented by NP88 (their Eq. 41). Nor is it consistent with our determination of the value for this parameter.

Hubbard & Marley suggest that the J_6 discrepancy with the NP88 constraint (and also with our value) may be resolved by altering the interior model to include cylinders in differential rotation (Hubbard 1982). When differential rotation is added, the absolute values of J_2, J_4, and J_6 increase by 0.5, 2.5, and 10%, respectively. This increase was shown to be fairly independent of the interior model used. While this change would bring the values of J_4 and J_6 predicted by the Hubbard & Marley models more in line with the values found here, it also increases the value of J_2 more than is possible for our solution. This suggests that models explicitly incorporating differential rotation should be attempted. The errors in these parameters are now small enough to be useful constraints in interior models.

12. B-RING FEATURES

Saturn's B Ring is its most optically thick ring. It has been difficult to measure features here, due to the low signal-to-noise ratio of the data in this region, and the common identification ambiguity among the many features here. Two recent occultations (GSC6323-10396 and 28 Sgr) changed things for B-Ring study by allowing relatively unambiguous feature identification throughout even the densest portions of the ring (28 Sgr much more so than GSC6323-01396). A series of features appearing at least semi-permanent was established (F93) and measured in the two data sets, as well as in the PPS data set when possible. In their analysis, F93 include several of these features in their fits as circular. We have avoided this, however, as we find high rms residuals for these features (usually several times that of circular features; see Table 12.1). There are several possible explanations for these high residuals: (i) the features are non circular, (ii) the features are evolving, changing in a manner not described by a non-circular model, or (iii) the features have been misidentified in one or more of the data sets. In this Section, we will investigate the characteristics of these B-Ring features.

Table 12.1. Circular Models for B-Ring Features

Feature	Semimajor Axis (km)	RMS (km)
83[a]	94438.85 ± 1.08	2.86
82[a]	95363.47 ± 1.77	4.33
81[a]	96895.94 ± 1.12	2.95
80	97209.81 ± 5.57	14.74
79	97594.37 ± 2.53	7.15
78[a]	98279.29 ± 1.61	3.95
77	100022.70 ± 0.47	1.14
76[a]	101003.15 ± 1.24	3.05
75[a]	101543.88 ± 1.18	2.90
74	101750.27 ± 4.24	11.98
73	103008.39 ± 2.21	6.25
72[a]	103658.79 ± 2.31	6.12
71[a]	104085.99 ± 1.66	4.07

[a] Features assumed circular by F93.

From Table 12.1, we see that most of the features in the B Ring have rms residuals per degree of freedom that are very large. Next we follow the procedure describes in Section 7 for performing partial fits to these data. We use the parameters of the adopted solution to calculate radii for the observed times of these features. We then fit a simple, freely precessing ellipse to the data. Of course, it is highly unlikely that any feature in the B Ring would be freely precessing, as nearby ring material would have a non-negligible component in the precession rate. However, we perform these simple fits first. The results of these fits are given in Table 12.2, which lists fitted precession rate as well as that predicted by the gravitational harmonics of NP88. For these features, we look for both a smaller rms from the eccentric fit than the circular fit, and a significant value of eccentricity ($e/\sigma_e > 2$) to indicate a non-circular ring. We find five features that satisfy these criteria: features 83, 79, 77, 74, and 72. A quick search through the Table 4.1 shows that there are no satellite resonances near these locations. We plot the models and data for these features in Fig 12.1. Note that for several features (79 and 77), the data are severely under-sampled in longitude. Therefore, while these features may be non-circular, there is not enough evidence at this time to confirm this. The remaining three features are candidates for new non-circular features. For three of these features (83, 74, 72), the measured precession rate does not differ from the predicted value by much, although in all cases the deviation is greater than one formal error.

Table 12.2. Simple Elliptical Models for B Ring Features

Feature	a (km)	$e \times 10^4$	ϖ_0 (deg)	$\dot{\varpi}$ (deg day^{-1})	$\dot{\varpi}$ (NP88)	RMS (km)
83[a]	94437.80 ± 0.50	1.02 ± 0.18	297.5 ± 13.9	11.0315 ± 0.0033	11.1295	1.10
82	95357.23 ± 23.24	7.17 ± 23.73	108.7 ± 11.0	10.7932 ± 0.0046	10.7455	2.54
81	96891.14 ± 2.91	3.54 ± 2.20	331.7 ± 10.4	6.7193 ± 0.0023	10.1421	2.50
80	97210.89 ± 6.65	3.51 ± 2.25	18.5 ± 44.9	10.1622 ± 0.0104	10.0219	14.82
79[a]	97577.53 ± 3.69	12.08 ± 2.56	340.8 ± 3.1	8.6003 ± 0.0007	9.8864	3.56
78	98273.26 ± 3.38	3.53 ± 2.42	317.9 ± 15.3	10.6600 ± 0.0039	9.6356	2.36
77[a]	100001.03 ± 6.86	21.86 ± 6.92	217.7 ± 0.3	8.4738 ± 0.0001	9.0478	0.72
76	101001.20 ± 17.82	0.69 ± 17.87	188.2 ±180.	8.7499 ± 1.8842	8.7282	1.88
75	101525.08 ± 25.64	18.27 ± 26.25	112.2 ± 2.9	9.8547 ± 0.0008	8.5668	2.72
74[a]	101742.85 ± 2.86	3.82 ± 0.81	319.6 ± 14.9	8.2190 ± 0.0035	8.5008	5.87
73	103011.85 ± 4.08	1.76 ± 1.95	203.4 ± 46.5	3.0742 ± 0.0091	8.1293	5.90
72[a]	103660.56 ± 1.70	3.26 ± 1.30	46.7 ± 15.3	7.9132 ± 0.0040	7.9474	1.47
71	104054.33 ± 46.52	32.63 ± 47.17	215.0 ± 2.6	8.4731 ± 0.0006	7.8396	4.84

[a] Features with significant eccentricities.

This is just the first step in the study of features in the B Ring. Clearly, any such study will include the effects of nearby ring material on the precession rate of the ring feature. We do not include that effect here, and therefore it is not prudent to continue any further in this analysis. To estimate the size of the contribution of nearby ring material on the precession rate, we follow the formalism presented in the Appendix of NP88. We scale the value given in their Table 3 (calculated using their Eq. 47), for the contribution from material near the Titan ringlet. For the scaling for a typical B-ring feature relative to the

Titan ringlet, we increase the surface density from 5 to 135 g cm^{-2}, and increase the radius from 77871 to 100000 km. Applying these changes, we find that the contribution to the precession rate from nearby ring material is 4.5 deg day^{-1}. This is the contribution expected from nearby ring material separated from the feature in question by a gap. Because this is not the case with the B Ring features we are studying, the interpretation is even more complex. Self-gravity of the ring particles probably plays a role in determining the precession rate. The B Ring is too complicated to attempt modeling its features with such a sparse collection of data.

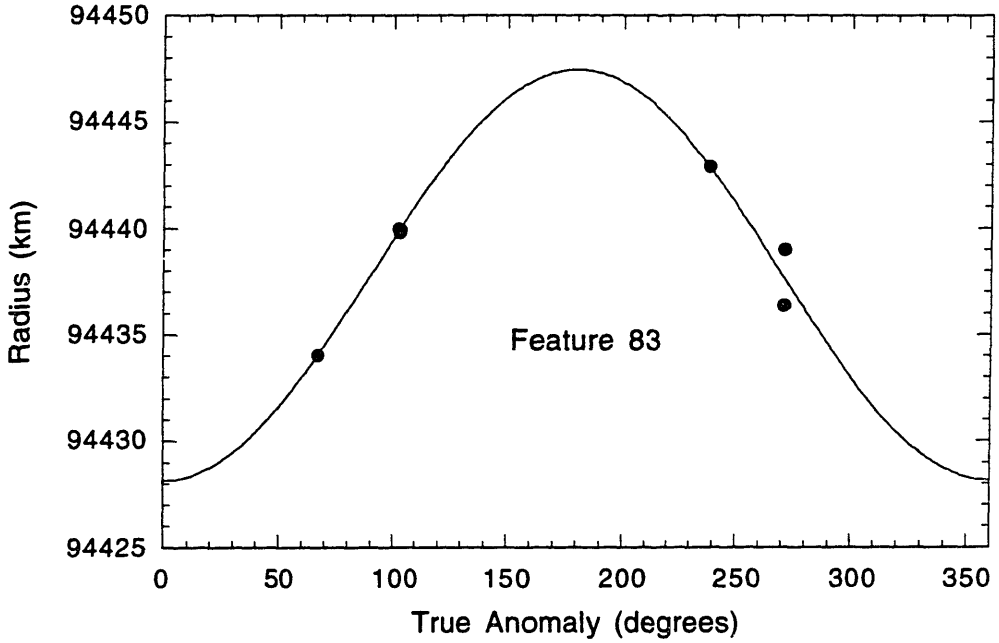

FIG 12.1. Data and models for suspected non-circular features in the B ring. (a) Feature 83.

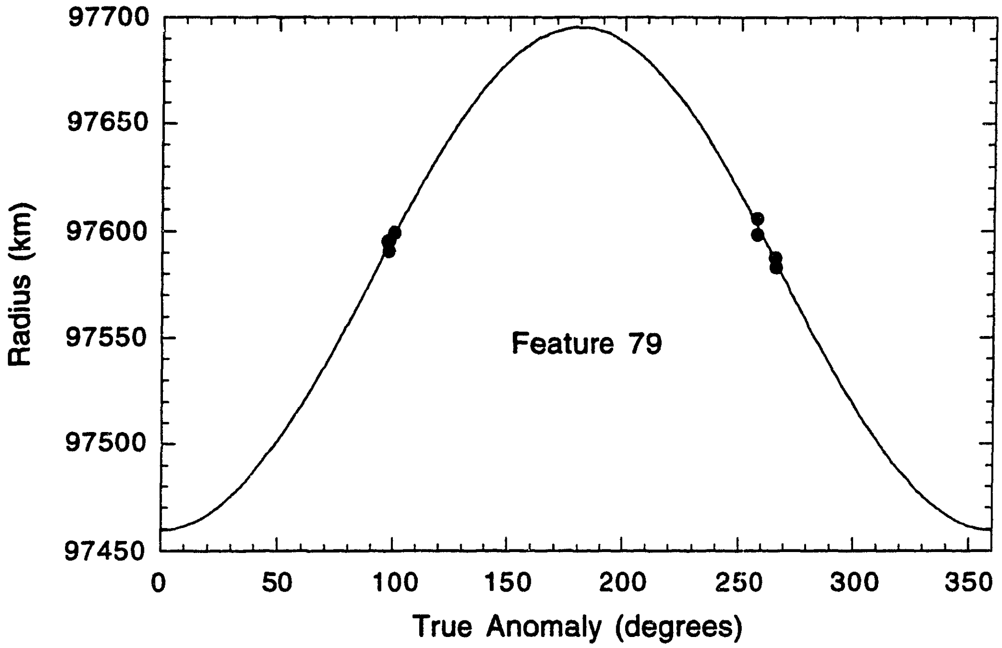

FIG 12.1. (b) Feature 79. Because there are only two distinct longitudes sampled by the data included here, this feature is more likely circular than elliptical with an amplitude of 112 km.

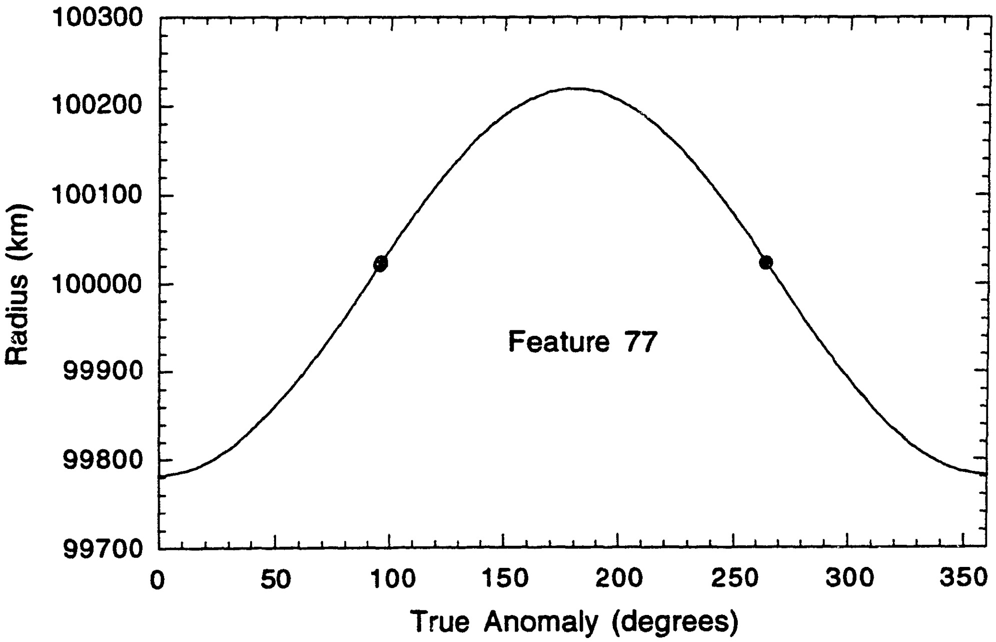

FIG 12.1. (c) Feature 77. Data for this feature exist at only 2 distinct longitudes, as with feature 79. There are more than 2 data points for this feature, but they are very closely spaced in radius and longitude to be seen on this plot, which is scaled to include the entire 220-km amplitude ellipse. The area including the data points is enlarged in Fig. 12.1 (d).

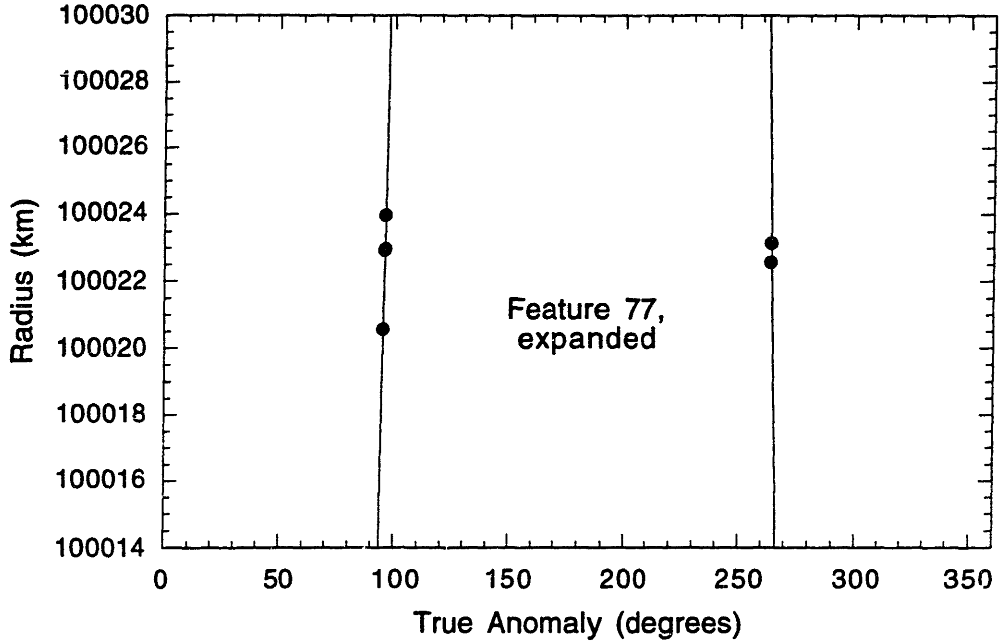

FIG 12.1. (d) Feature 77. Expanded view of Fig. 12.1 (c), showing the data points for this feature.

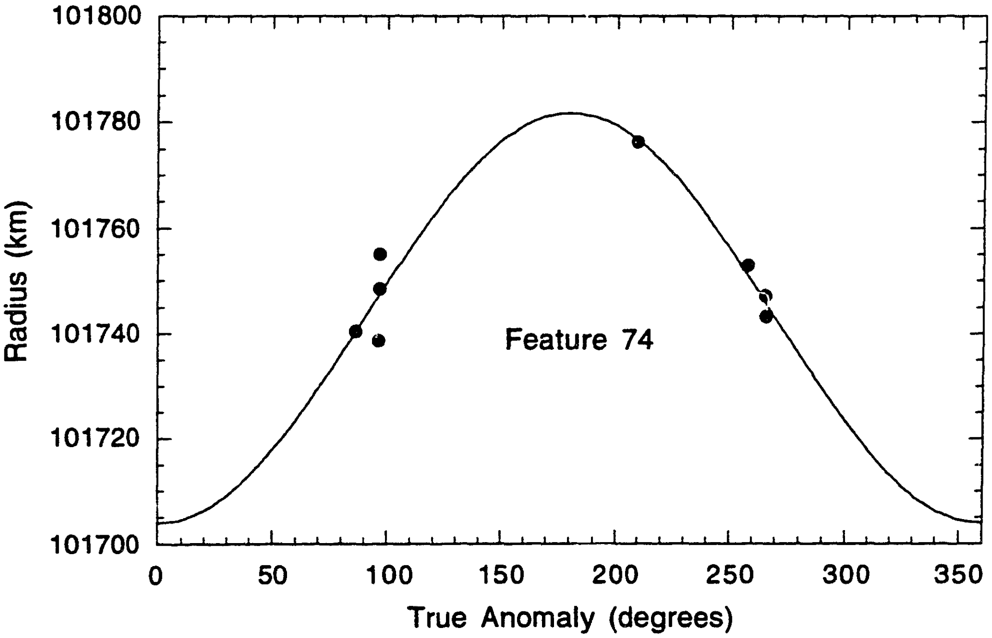

FIG 12.1. (e) Feature 74.

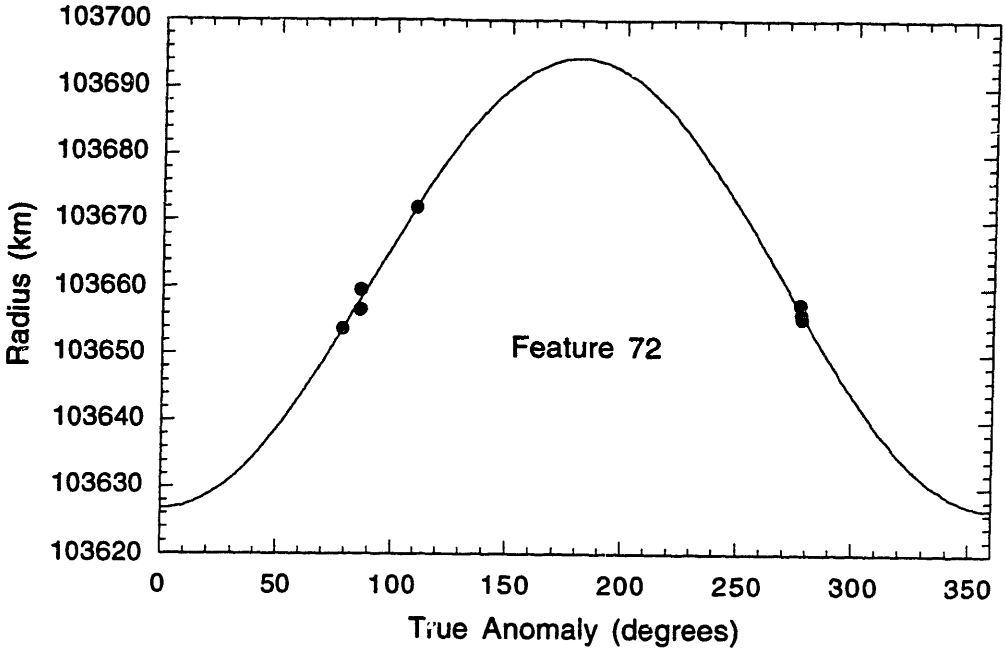

FIG 12.1. (f) Feature 72.

13. CONCLUSIONS

In this work we combine data from the HST, 28 Sgr, PPS, and RSS data sets to construct a geometric model for the ring-plane pole position and feature parameters (semimajor axis, eccentricity, longitude of periapse, precession rate or pattern speed, and azimuthal symmetry number). The geometric model, a solar-system barycentric vector formulation, was generalized to be able to handle inclined ring features, occultations of spacecraft signals, and occultations of stars observed by spacecraft. In this model, we included circular features only (not those in the B ring); the inclusion of non-circular features was attempted, but did not significantly reduce the fit rms. We searched for new non-circular features among those presumed to be circular, and found one candidate: the inner edge of the C ring, feature 44. We also investigated all features to find any that are inclined, but found none. Our final solution for pole position and radius scale is consistent with the results of E93, F93, and NCP. The solution is only slightly different from F93 because we added only one data set. The solution is still controlled by the 28 Sgr data set, because the many observations of that event from many stations effectively gave this data set a higher weight.

We attempted a solution without the 28 Sgr data set, and found very different (and implausible) results: feature radii increased by ~10 km. Rather than interpreting this as indicating a problem with the 28 Sgr data set, we noted that the three data sets included in this solution are not able to determine ring feature radii because they were all one-sided occultations. We added one 28 Sgr data set to the data pool to constrain feature radii, and the solution we found in this fit was very similar to our adopted solution ($< 1\sigma$ different). From this, we concluded that although the 28 Sgr data set may have undiscovered errors or internal inconsistencies, these do not affect the pole solution. Therefore, the weight of the 28 Sgr data set as a whole should not be reduced.

With the Voyager and 28 Sgr data sets, it had previously been shown that the measured rate of pole precession was consistent with the rate calculated by assuming the precession would be due to solar torques on Titan transferred to Saturn (F93). When adding the HST data, we found similar results: that the measured rate of pole precession is 1.3 ± 0.3 times the predicted rate. We attempted this same analysis without the 28 Sgr data set (except for data from one station to again constrain the feature radii), and we found a rate of 0.6 ± 0.3 times the predicted rate. This inconsistency is puzzling, and we concluded that the actual rate is near the calculated rate, but we do not know the exact value at this time. The additional time between the 28 Sgr and HST occultations should have resulted in a better determination of the rate of pole precession. In one case, it did, but only when 28 Sgr data was not included (except data from one station). To reduce the error to 10% of the calculated value of the precession rate, we would need an additional occultation observation in 2008 or later to gain enough time baseline, assuming the errors in pole position (currently ~2 arcsec) do not decrease. However, if we continue observations of occultations through the next decade, these pole errors should decrease, and we would need less time to improve the measurement of pole precession rate. It will be important to observe both immersion *and* emersion occultation events in the future, because these observations place a much stronger constraint on feature radii than do observations of only immersion or emersion.

There is an alternate method for improving the pole precession rate. In 1995 and 1996, the Earth will pass through Saturn's ring plane. The exact times of these three crossings vary by up to 1 hour depending on the rate of pole precession. By monitoring the photometric brightness of the rings, we should be able to determine the crossing time and therefore have an independent determination of the pole precession rate. The accuracy of this method depends on how well we will be able to model the photometric brightness of the rings as they reach minimum brightness.

Another major contribution of the HST data set was toward developing kinematic models for non-circular features. We obtained improved model parameters for several ringlets: (i) the Titan ringlet, in an apsidal resonance with Titan; (ii) the Maxwell ringlet, in free precession, and (iii) the Huygens ringlet, forced by the Mimas 2:1 Lindblad resonance but also with a freely precessing component. Other ringlets studied yielded interesting results. We found that the inner edge and centerline of the 1.470 R_S ringlet are circular, not freely precessing as previously reported (PN87). The outer edge of this ringlet is best described by an $m = 2$ body-centered ellipse forced by the Prometheus 2:1 Lindblad resonance. The outer edge of the 1.495 R_S ringlet, also previously reported as being freely precessing (PN87), now appears to be a superposition of freely precessing and Mimas 3:1 Lindblad resonance modes. The inner edge of the 1.990 R_S ringlet, despite its proximity to the Pandora 9:7 Lindblad resonance, is freely precessing. We also presented a kinematic model for the newly-discovered non-circular feature, the inner edge of the C ring (feature 44): there are no resonances nearby, and this feature fits a freely precessing model adequately. However its measured precession rate differs from the value calculated from gravitational harmonics by several formal errors. Because this feature is the closest non-circular feature to Saturn, it is diagnostic of Saturn's higher-order gravitational harmonics. Any inaccuracies in our assumed values of J_8 and higher could account for this discrepancy. We will need to pay special attention to this feature in future data sets.

Developing kinematic models for the outer edges of the B and A rings was more challenging. Both fit resonant models or superpositions of resonant with freely precessing models (Mimas 2:1 for the B ring, Janus 7:6 for the A ring), but the rms residuals were much larger than for other features. For the B ring outer edge, the effect of the massive B ring on the precession rate was included by approximating the B ring as a set of non-interacting, isolated ringlets. This is clearly not the case, and a better model for the precession induced by such nearby ring material should be formulated an applied to the B ring. For the A ring, we will need to include the effects of *both* co-orbital satellites (Epimetheus as well as Janus) on the ring kinematics.

A major problem for the further refinement of kinematic models for non-circular ringlets is the lack of adequate longitudinal coverage (in a frame rotating at the pattern speed of the ring feature). At present, we have data at only six distinct longitudes (one from HST, two from 28 Sgr, and 2 from the Voyager occultations); sometimes more, for a feature with fast pattern speed additional longitudes come from multiple 28 Sgr observing stations; sometimes less. Remedies for this are to incorporate Voyager imaging data (errors ~ few km) and Voyager occultation observations with the Ultraviolet Spectrometer (errors ~3 km), and to observe more stellar occultations by Saturn's rings. Because there were many more images taken during the two Voyager flybys than occultations were observed, there is a potential to greatly increase the longitudinal coverage of many ring features. Before the removal of the HSP, we obtained one additional light curve of the occultation of GSC5800-00460 by Saturn's rings. This occultation spanned the outer C ring and inner B ring only (see Fig. 13.1). We will be using the feature times from this data set in future kinematic models. With the removal of the HSP, we would need to use the Faint Object Spectrograph (FOS) (Paresce 1992) to observe future occultations from space. With its lower quantum efficiency and slower integration times, we would be limited to very bright and/or very slow occultations. Another option for observations of occultations by Saturn's rings is to observe them from the ground in the infrared. This technique was used for the 28 Sgr occultation, and resulted in high quality data because Saturn and its rings were dark (due to the 3μ water ice and methane absorption bands) thereby reducing noise over observations in the visible.

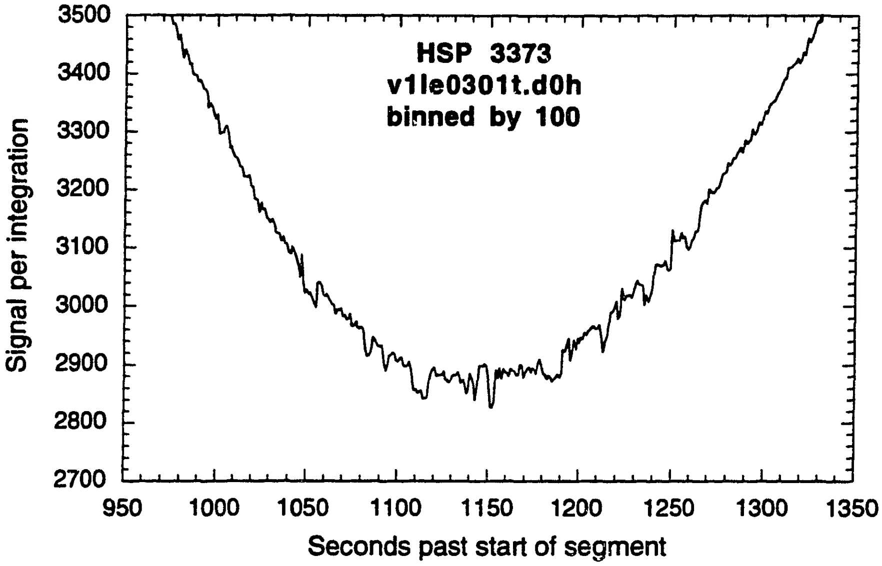

FIG. 13.1. Portion of occultation light curve of GSC5800-00460 in the outer C ring. Data are from the 7500 Å channel on the High Speed Photometer, and are binned by 100. Visible features include several C-ring plateaus, the Maxwell ringlet, and the 1.470 R_S and 1.495 R_S ringlets. The B ring is to the right (increasing time).

With the improved kinematic models for the Titan and Maxwell ringlets, we were able to determine the gravitational harmonics J_2, J_4, and J_6 to greater accuracy than was previously achieved (NP88). We combined constraints from Pioneer tracking, satellite precession rates, the location of the Titan ringlet, and non-circular ringlet precession rates (Maxwell and 1.495 R_S ringlets). Although our value for J_6 does not differ significantly from that of NP88, our formal error is much smaller. The uncertainty in this quantity is now small enough that we can say that the models of Hubbard and Marley (1989) do not produce a J_6 that is consistent with our value. A possible reason for this is that Saturn's interior may be rotating a different rates, essentially on concentric cylinders. Such a rotation state would effect the values of the gravitational harmonics determined through interior models enough to make them consistent with the values found here. With additional data sets and further improvement of kinematic models, we hope to be able to include more ringlets as constraints and to determine higher order gravitational harmonics.

There are several opportunities for continued studies of Saturn's rings in the coming years. The 1995-1996 ring-plane crossings may help determine the rate of pole precession, as well as allow study of the tenuous outer rings. And there are stellar occultations (Bosh and McDonald 1992) that should yield high quality data if observed from the ground in the infrared or from space. Several are listed in Table 13.1. The signal-to-noise ratio listed for these occultations is calculated for the HSP for a 1-second integration; signal-to-noise ratios for other instruments will have to be scaled down from these values.

Table 13.1. Saturn Occultation Candidates with S/N > 2, in 1994-1999.

Candidate GSC Number	Occultation Date (y m d)	Star B Mag.	Event Vel. (km s^{-1})	Predicted S/N per sec
5813-01022	1994 08 16	12.7	18.8	2.4
5815-01190	1994 09 18	11.7	18.7	6.1
5249-01240	1995 11 20	12.2	0.9	17.6
5250-00766	1995 12 10	9.8	9.6	49.1
0010-00284	1996 07 29	11.9	5.1	9.7

APPENDIX A: OCCULTATION OBSERVATIONS WITH THE HUBBLE SPACE TELESCOPE

The HSP Instrument Definition Team planned a suite of occultations by solar system bodies as part of its guaranteed observing time. Planning for specific occultations was difficult at first because the launch of the HST was delayed several times. After launch, orbital verification, and science verification, we had in place plans and instructions for the execution of 36 occultations. These are listed in Table A.1. There were 3 occultations by Jupiter and its ring, 1 by Mars, 9 by Saturn and its rings, 4 by Uranus and its rings, 3 by Neptune and its rings, 5 by Titan, 6 by Triton, and 5 by Pluto and/or Charon. Circumstances for all occultations listed in Table A.1 are given in several occultation prediction papers (Bosh and McDonald 1992; Dunham *et al.* 1991; Klemola and Mink 1991; McDonald and Elliot 1992; Sybert *et al.* 1992).

Observations of stellar occultations from the HST are beset with different complications than are faced by ground-based observers. Regardless of the observing platform, occultations are time-critical events: they occur at a specific time and a specific location. Ground-based observations are limited by the locations of the star and the occulting body at the time of the occultation. Are the objects at high enough altitude to observe? Is the sky dark at the chosen observing station at the time of the occultation? How long will the objects be visible (above a certain altitude)? Because the HST is an Earth-orbiting observatory, one would think that the above questions would be irrelevant for HST observations. However, the HST is in a low-Earth orbit, with an altitude of only 500 km (Bahcall and Spitzer 1982), and an orbital period of only 96 minutes. Therefore, the Earth is still a very large object in the sky for the HST. As a result, observers using the HST are limited by the same factors as ground-based observers, but on a different time scale. Objects "rise" and "set" as they do for ground-based observers, but for HST observers, the "day" is only 96 minutes long. So a long occultation (several hours) will be dotted with 45-60 minute gaps, when the objects are behind the Earth as viewed from the HST and are therefore unobservable. It is possible to observe an object uninterrupted for more than 96 minutes, but only when that object is in the Continuous Viewing Zone (CVZ). Objects in the CVZ are near the celestial poles; therefore, planets and satellites never enter this zone. Other factors that contribute to reducing the length of time that the object can be observed ("observing windows") are avoidance limits for the sun (±50°), moon (±15°), bright limb of the Earth (10°), dark limb of the Earth (5°), and the anti-solar direction (±3°). These limits occasionally increase in response to the current status of the HST. Another limit to the observing windows is the necessary shutdown of observations when the HST passes through the South Atlantic Anomaly (SAA). The size of the SAA avoidance zone varies by instrument and HST inclination; sometimes it can be ignored (although this leads to a degradation of the data quality). With all the avoidance zones present, the maximum observation length per orbit (for equatorial bodies) of ~50 minutes can be decreased to an actual observing time 0 minutes per orbit. This complicates the process of planning for observations with the HST, as we do not know the durations of the observing windows until ~2 months before the observation. A final obstacle to HST occultation observations is that the instrument used for these observations, the HSP, was removed in early December 1993 to make room for COSTAR, a set of optics that should compensate for the spherical aberration in the HST's primary mirror. Several occultations had to be canceled because they would occur after the HSP was removed.

The planned small-body occultations (Titan, Triton, Pluto/Charon) were serendipitous events; they depended on the occultation occurring at the location of the HST and on the HST being within the observing window. Of the 16 small-body occultations planned, 6 were attempted; the rest were canceled due to poorly-placed observing windows or the imminent removal of the HSP. Of the 6 attempted observations, 1 failed due to a target acquisition problem; the other 5 executed with no problems in the occultation observations. Of these 5, only 1 occultation (by Titan) probably occurred at the location of the HST. The rest of the observations were of appulses. The final statistics for small-body occultations was 1 successful out of 16 attempted, a 6% success rate.

Occultations by large solar system bodies are less likely to be canceled due to poorly-placed observing windows, and therefore we expected a higher success rate. This is because the bodies (including ring systems) are large so the time it takes for such a body to occult a star is longer. Of course, this depends on the velocity of the planet at the time. Mars and Jupiter are fast-moving bodies; even though they are large, occultations by these bodies may not last more than a few minutes. For Saturn, Uranus, and Neptune, this is rarely a problem. However, observing windows still can affect the achievable science negatively. For instance, it can happen that the only data recorded is during the uninteresting period when the star is entirely behind the planet.

There was only one large-body occultation canceled due to unfavorable observing windows. Of the 20 events attempted, 10 executed successfully, 1 failed execution due to a problem with target acquisition, and 9 were canceled for a variety of reasons (see Table A.1). Of the 10 events that were executed correctly, 5 produced usable scientific data. This is a success rate of 25%, a factor of 4 greater than for small-body occultations. Even though this value is greater, it is still discouragingly low. The overall success rate of the occultation program was 17%. Because large-body occultations are less susceptible to the placement of observing windows (which can reduce the observing time by 60-65% per orbit), our success rate for these occultations should have been much higher. Looking again at the canceled occultations, we decide it is not appropriate to include in the statistics those canceled because they were found to have insufficient signal-to-noise ratios (based on the quality of the GSC6323-01396 event), because the astrometry indicated the event would be an appulse instead of an occultation, or because the HSP will be removed. Removing these, we find a success rate of 36%. An additional 36% executed correctly, but were not scientifically useful. The remaining 29% (the percentages do no sum to 100% due to round-off error) were either executed incorrectly or were removed due to observing window or enlarged avoidance zone concerns. Our experience with occultation observations using the HST should provide a useful lesson for designers of future orbiting observatories.

Table A.1. Planned HSP Occultations

Occulting Body	Date (y m d)	Occulted Star	Successful Execution[a]?	Useful data[a]?
Mars	93 01 14	AGK+26D0765	no; TA	
Jupiter	92 07 08	AGK+08D1425	yes	yes
Jupiter	92 11 22	SAO138840	canceled; astrometry	
Jupiter	93 02 25	LS00305	canceled; windows	
Saturn	91 09 05	GSC6323-01466	yes	no; CT
Saturn	91 10 02	GSC6323-01396	yes	yes
Saturn	92 07 13	GSC6347-01433	yes	no; CT
Saturn	92 09 30	GSC6349-01499	yes	no; CT
Saturn	93 04 29	GSC5808-00138	canceled; S/N	
Saturn	93 08 25	GSC5808-00850	canceled; S/N	
Saturn	93 10 12	GSC5800-00460	yes	yes
Saturn	93 11 24	GSC5800-00595	canceled; S/N	
Saturn	93 12 07	GSC5801-00416	canceled; COSTAR	
Titan	92 10 07	GSC6349-01493	canceled; windows	
Titan	92 10 09	GSC6349-01493	yes	yes
Titan	93 07 05	GSC5809-00117	canceled; windows	
Titan	93 09 22	GSC5801-00585	canceled; windows	
Titan	94 06 06	GSC5813-00693	canceled; COSTAR	
Uranus	92 07 08	U102	yes	yes
Uranus	93 04 14	U111	yes	yes
Uranus	93 07 27	U115	canceled; SADE	
Uranus	94 03 15	U122	canceled; COSTAR	
Neptune	92 07 11	N61	yes	no; no arc
Neptune	92 11 18	N63	yes	no; no arc
Neptune	93 07 18	N66	canceled; SADE	
Triton	92 06 30	Tr18	canceled; windows	
Triton	92 07 21	Tr24	no; TA	
Triton	92 08 27	Tr30	yes	no; appulse
Triton	92 10 10	Tr32	yes	no; appulse
Triton	93 05 13	Tr46	canceled; windows	
Triton	93 07 10	Tr60	canceled; SADE	
Pluto/Charon	92 01 17	P14.C	canceled; windows	
Pluto/Charon	92 05 21	P17	yes	no; appulse
Pluto/Charon	92 09 13	P18	canceled; windows	
Pluto/Charon	93 02 01	P19.04	yes	no; appulse
Pluto/Charon	94 02 04	P20.03	canceled; COSTAR	

[a] Included in the last two columns are reasons for canceling a target, failed observations, and lack of scientifically useful data. These include: (TA) problem with target acquisition; (COSTAR) HSP will be replaced by COSTAR; (SADE) a March 1993 failure of the Solar Array Deployment Electronics resulted in wider solar and anti-solar avoidance limits than normal; (windows) observing windows were unfavorable; (astrometry) astrometry indicated the occultation would not occur; (CT) observations in coarse track instead of fine lock; lowers data quality; (S/N) inadequate signal-to-noise ratio in data; (no arc) the path of the occultation did not intersect a ring arc, and (appulse) the occultation did not occur at the location of the HST; instead it observed an appulse.

APPENDIX B: REPRINT OF ELLIOT *ET AL.* (1993).

Reprint of Elliot *et al.* (1993). An occultation by Saturn's rings on 1991 October 2-3 observed with the Hubble Space Telescope. *Astron. J.* **106**, 2544-2572.

THE ASTRONOMICAL JOURNAL VOLUME 106, NUMBER 6 DECEMBER 1993

AN OCCULTATION BY SATURN'S RINGS ON 1991 OCTOBER 2-3 OBSERVED WITH *THE HUBBLE SPACE TELESCOPE*[1]

J. L. ELLIOT
Department of Earth, Atmospheric, and Planetary Sciences,[2] Massachusetts Institute of Technology, Cambridge, Massachusetts 02139-4307 and Lowell Observatory, Flagstaff, Arizona 86001
Electronic mail: jim@astron.mit.edu

A. S. BOSH AND M. L. COOKE
Department of Earth, Atmospheric, and Planetary Sciences, Massachusetts Institute of Technology, Cambridge, Massachusetts 02139-4307
Electronic mail: amanda@lowell.edu, maren@mit.edu

R. C. BLESS,[3] M. J. NELSON, J. W. PERCIVAL, AND M. J. TAYLOR
Space Astronomy Laboratory, University of Wisconsin, Madison, Wisconsin 53706
Electronic mail: bless@larry.sal.wisc.edu, nelson@larry.sal.wisc.edu, jwp@larry.sal.wisc.edu, taylor@larry.sal.wisc.edu

J. F. DOLAN
Laboratory for Astronomy and Solar Physics, Goddard Space Flight Center, Greenbelt, Maryland 20771-6810
Electronic mail: tejfd@larry.sal.wisc.edu

E. L. ROBINSON
Department of Astronomy, University of Texas, Austin, Texas 78712-1083
Electronic mail: elr.aries.as.utexas.edu

G. W. VAN CITTERS
Division of Astronomical Sciences, National Science Foundation, Washington, DC 20550
and Department of Aerospace Engineering U. S. Naval Academy, Annapolis, Maryland 21402
Electronic mail: gvancitt@note1.nsf.gov

Received 1993 May 19

ABSTRACT

An occultation of the star GSC 6323-01396 ($V=11.9$) by Saturn's rings was observed with the High-Speed Photometer on the *Hubble Space Telescope* (*HST*) on 1991 October 2-3. This occultation occurred when Saturn was near a stationary point, so the apparent motion of Saturn relative to the star was dominated by the *HST* orbital motion (8 km s^{-1}). Data were recorded simultaneously at effective wavelengths of 3200 and 7500 Å, with an integration time of 0.15 s. Observations were interrupted by passages of the spacecraft behind the Earth and through the South Atlantic Anomaly. Fifteen segments of occultation data, totaling 6.8 h, were recorded in 13 successive orbits during the 20.0 h interval from UTC 1991 October 2, 19:35 until UTC 1991 October 3, 15:35. Occultations by 43 different features throughout the classical rings were unambiguously identified in the light curve, with a second occultation by 24 of them occurring due to spacecraft orbital parallax during this extremely slow event. Occultation times for features currently presumed circular were measured and employed in a geometrical model for the rings. This model, relating the observed occultation times to feature radii and longitudes, is presented here and is used in a least-squares fit for the pole direction and radius scale of Saturn's ring system. Combined fits with the *HST* occultation times and 28 Sgr occultation times [French *et al.*, Icarus, 103, 163 (1993) and Hubbard *et al.*, Icarus, 103, 215 (1993)] yield a ring-pole direction of $\alpha=40\overset{\circ}{.}5929\pm0\overset{\circ}{.}0151$ and $\delta=83\overset{\circ}{.}5348\pm0\overset{\circ}{.}0053$ (J2000.0, at the Voyager 1 epoch of UTC 1980 Nov. 12 23:46:32). This result, independent of Voyager data and its associated trajectory errors, is compared with other recent determinations of the pole and radius scale.

1. INTRODUCTION

Saturn's rings exhibit a wide variety of dynamical phenomena. From Earth-based observations prior to spacecraft flybys the overall structure of the A, B, and C rings had been identified, and the Cassini division separating the A and B rings had been associated with the 2:1 resonance with Mimas (Alexander 1962; Elliot & Kerr 1984). Also, a narrow division in the A ring (now called the Encke gap) had been observed as early as 1888 (Keeler 1889). As a result of the dramatic increase in spatial resolution available to the flyby spacecraft Voyagers 1 and 2, many new phenomena were discovered in Saturn's rings: gaps, moonlets, wakes, spiral density waves, bending waves, and narrow ringlets (Cuzzi *et al.* 1984). In addition to their in-

---

[1] Based on observations with the NASA/ESA *Hubble Space Telescope*, obtained at the Space Telescope Science Institute, which is operated by the Association of Universities for Research in Astronomy, Inc., under NASA Contract No. NAS5-26555.

[2] Also Department of Physics.

[3] Also Department of Astronomy.

2544 Astron. J. 106 (6), December 1993 0004-6256/93/106(6)/2544/29/$0.90 © Am. Astron. Soc. 2544

trinsic interest, precise modeling of these phenomena—especially their dynamical relationships and their interactions with Saturn's inner satellites—teaches us about fundamental processes that occur in particle disks. Furthermore, better understanding of these processes and how they affect ring evolution will be needed before we can reliably infer the age of Saturn's rings. The evidence now points to the conclusion that at least the A ring is young (Esposito 1986).

Further kinematic and dynamical studies of Saturn's rings require that we continually probe them with high spatial resolution. The only Earth-based method that allows us to achieve kilometer-scale spatial resolution is the stellar occultation technique (Elliot 1990). A notable achievement of this technique has been the development of a kinematic model for the Uranian rings over the decade between their discovery and the Voyager encounter in 1986 (Elliot *et al.* 1978; French *et al.* 1988). This development included the first examples of narrow rings (Elliot *et al.* 1977), eccentric rings (Nicholson *et al.* 1978), and inclined rings (French *et al.* 1982). Because the zones of occultation visibility on Earth are limited, mobile Earth-based observational platforms and fixed telescopes have been used to advantage for this work: for example, the Kuiper Airborne Observatory (Elliot *et al.* 1977; Dunham *et al.* 1982) and small, portable telescopes (Baron *et al.* 1983).

The goals of stellar occultation observers have been to learn more from new data sets by (i) acquiring occultation light curves with higher signal-to-noise ratio and greater spatial resolution, (ii) achieving greater spatial coverage by including more observing stations per event, (iii) obtaining light curves over a greater range of wavelengths, and (iv) increasing the time coverage of kinematic phenomena by observing more events. Toward these goals, the promise of the High Speed Photometer (HSP; Bless *et al.* 1993) on the *Hubble Space Telescope* (*HST*) was severalfold: there would be access to ultraviolet wavelengths, no clouds, no scintillation noise, and small focal-plane apertures that would admit lower levels of background light (and associated noise) into the occultation light curves.

The spherical aberration of the *HST* optics, however, has diminished the effectiveness of the *HST* for occultation observations in several ways: (i) due to the large point spread function (PSF; see Fig. 2 in Burrows *et al.* 1991), the signal level from a star within the focal plane aperture has been reduced by about 50%, (ii) the background level on the wings of the PSF from nearby bright objects (e.g., the occulting planets) has increased, and (iii) modulation of the large PSF by pointing jitter adds more noise to the data than had been anticipated. An additional diminution of occultation capability of the *HST* is that NASA's selected fix for the aberration problem—the installation of COSTAR—will require the removal of the HSP altogether near the end of 1993.

In spite of these difficulties, the *HST* now provides unique opportunities for occultation work, and in this paper we present the HSP observations of the occultation of the star GSC 6323-01396 by Saturn's rings that occurred in 1991 October (Bosh & McDonald 1992). A notable feature of this occultation is that it occurred near one end of Saturn's retrograde loop, so that the geocentric shadow velocity was 1-2 km s^{-1}, and ring egress lasted for 20 h. Since the orbital velocity of the *HST* is about 8 km s^{-1} and the orbit greater than one Earth diameter across, several regions of the rings were probed twice in spite of the unavoidable shutdown of data recording during Earth occultation and passages through the South Atlantic Anomaly (SAA). Hence this data set has some of the advantages of multiple station observations of a single event, such as the 28 Sgr occultation by Saturn that occurred in 1989 July (French *et al.* 1993; Hubbard *et al.* 1993; Harrington *et al.* 1993). These references will be referred to henceforth as F93, Hu93, and Ha93.

In this paper we present the light curves of the occultation, from which we measure occultation times for previously identified, circular features. These times are then used—in combination with the 28 Sgr data given in F93 and Hu93–in a least-squares solution for the radius scale and position of the ring-plane pole of Saturn.

2. PREPARATION FOR OBSERVATIONS

Preparation for occultation observations with the *HST* occurs in four stages: (i) selecting an event that will have sufficient signal to noise and observability to achieve the desired objectives; (ii) planning the sequence of exposures needed to acquire the occultation light curve and calibration data; (iii) updating the spacecraft observing plan ("proposal") as necessary (with improved star coordinates, etc.); and (iv) checking the derived spacecraft commands in order to increase the chances that the desired data will be recorded.

2.1 Occultation Signal to Noise and Observability

The occultation of GSC 6323-01396 was identified from a search of the *HST Guide Star Catalog* for Saturn occultation candidates by Bosh & McDonald (1992), and the colors of this star were measured by Sybert *et al.* (1992): $V=11.9$, $B-V=0.7$, $V-R=0.5$. For stars that do not have large UV fluxes (such as this one), our preferred mode of observation is the "SPLIT" mode of the HSP, which provides simultaneous data recording at 3200 and 7500 Å (Bless *et al.* 1992, also Table 1). In the presence of background light from the brightest parts of Saturn's rings, a total occultation of the star would be about 1% of the background, according to "HSPSIM," a program that calculates the expected throughput for any channel of the HSP from the magnitude and spectral type of the star (Percival 1993). Considering only photon noise from this background ring light, a total occultation of the star lasting 1.0 s would have a signal-to-noise ratio of 17 for the 7500 Å channel. This would be adequate to record most of the sharp-edged features in Saturn's rings with a spatial resolution of about a kilometer.

Another source of noise that must be considered for HSP occultation photometry is the modulation of the background and stellar signal due to jitter of the telescope

TABLE 1. HSP instrumental parameters relevant to occultations.

Parameter	"VIS" Channel	"PMT" Channel
Detector Type	image dissector	photomultiplier
Photocathode Type	bialkali	GaAs
Dark (s^{-1})	0.2	349
Signal for 1% Nonlinearity (s^{-1})	2.5×10^5	2.5×10^5
Central Wavelength (Å)	3200	7500
Bandpass (FWHM, Å)	100	1600
Aperture Diameter (arcsec)	1.0	1.0
Sky (s^{-1})	0.015	2.6
Source[a] for V=11.9[b] (s^{-1})	410	7000
Ring background at outer edge of A Ring (s^{-1})	2.7×10^4	3.7×10^5
Ring background in central B Ring (s^{-1})	5.0×10^4	1.3×10^6
S/N[c] at outer edge of A Ring	2.6	11.2
S/N[c] in the central B Ring	1.8	6.3

Notes to TABLE 1

[a] For the 60% of the total light admitted by the 1-arcsec aperture

[b] B–V=0.7, V–R=0.5

[c] Ratio of unocculted star signal to background noise for an integration time of 1.0 s calculated from rms variation of the background.

in "coarse track" guidance mode. An example of this from a Science Verification (SV) test for Saturn ring occultations (SV2771) is shown in Fig. 1, where the modulations have a peak amplitude equivalent to the flux from a star with $R=11.5$ and a period of 10–15 s (the period of the coarse track mechanism). These modulations are particularly severe when observing in a bright and varying background, but can be avoided if guide stars brighter than magnitude 13.0 are available and the "fine lock" tracking mode used. It has been our experience for occultation work that guide stars suitable for fine lock are available within the allowed ±30° roll for the spacecraft about 20% of the time. Fortunately, fine lock could be used for the observations of GSC 6323-01396.

A second consideration for selecting an occultation is the observability of the event with the *HST*. Generous avoidance zones for the Sun (50°), anti-Sun (7°), and Moon (14°) allow only about 63% of stellar occultations by solar system bodies to be safely observed. Also, because the *HST* is in a low-Earth orbit—in contrast with *IUE* (Boggess *et al.* 1978a; Boggess *et al.* 1978b)—the Earth causes significant interference. Specifically, an occultation is not observable due to limits imposed by the Earth if it occurs (i) during Earth occultation for the *HST*, (ii) within 10° of the bright Earth limb or within 5° of the dark limb, (iii) during *HST* passage over the SAA, or (iv) during the 5 minutes needed for reacquisition of the target by the *HST* after emerging from the Earth-limb avoidance limits. For short occultations (lasting a small fraction of an *HST* orbit), these factors reduce the fraction of observable events by another 67%—leaving only 21% of potential short occultations observable by the *HST*. For long occultations that are not prohibited because they are too close to the Sun or Moon—such as the present one—the avoidance factors associated with the Earth allow only about 33% of the data to be recorded. The exact value of this factor depends on the orientation of the *HST* orbit pole within its 2 month precession cycle and the declination of the object being observed.

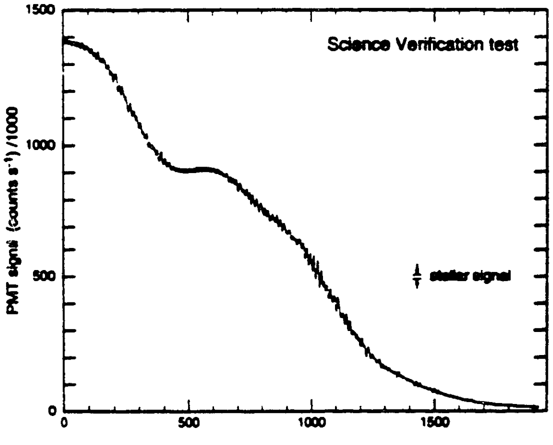

FIG. 1. SV 2771 light curve, illustrating the disastrous effects of jitter while in coarse track. The approximate stellar contribution to the total signal is indicated (for $V=13.0$, $B-V=0.8$; Sybert *et al.* 1992), and is only about half the maximum jitter amplitude.

Due to uncertainties in predicting the atmospheric drag on the *HST*, its orbital longitude cannot be known with certainty many months in advance. Hence in the early stages of planning occultation observations, one can know only the length of the data-recording window for an orbit. If this would be inadequate (no matter what the orbital phase of the *HST* might turn out to be) then the occultation can be rejected. More commonly the case, however, is that one must wait until about 60 days prior to the event (when the predicted orbital longitude has an error of about 25°) to learn enough about the time intervals when data can be recorded in order to decide whether observations should be attempted.

GSC 6323-01396 was occulted twice near one extremum of Saturn's retrograde loop. Each occultation lasted many hours, so that complete coverage of both occultations would have used almost all of our time available for occultation work. We decided that this would be too great a risk, because the execution of these observations occurred only 27 days after the SV test for occultations—an interval too short to allow changes of spacecraft commands for this observation in response to lessons learned from the SV test. Therefore we limited our observations to the first egress event (1991 October 2–3), since it would have the greatest radial resolution of the four events. We would acquire the star soon after planet egress, when it would be behind the D ring, and follow it past F ring egress.

2.2 Planning the Observations

For *HST* observations of stellar occultations, the planning stage is crucial because spacecraft instructions have to be finalized well in advance of the event. Although real-time control of observations is an option, this is impractical for stellar occultations because of the heavy constraints it places on the observing windows. In order to perform observations in real-time, a contact with the Tracking and Data Relay Satellite System (TDRSS) must be available throughout the observations. This adds considerably to scheduling difficulties, since the fraction of time that TDRSS is available to *HST* is limited to an average of 20%, and the times for TDRSS contacts are determined by priorities other than the needs of the *HST*. Therefore we chose to have no real-time components in our observations in order to increase the amount of data we could collect.

As discussed earlier, the "SPLIT" mode of the HSP would be the most suitable instrumental configuration for this occultation, since it would provide the greatest throughput of starlight and allow simultaneous light curves to be obtained at 3200 and 7500 Å (Bless *et al.* 1992, 1994). The detector in the 7500 Å channel is a photomultiplier tube (PMT) employing a GaAs photocathode for large throughput of red light. The optical path to the PMT contains a dichroic beamsplitter that routes the 3200 Å light to one of the image dissector tubes (the "VIS IDT," having a bialkali photocathode) for simultaneous data recording with both detectors. This mode is useful for removal of background light from the rings when they have a different relative flux from the occulted star in the two channels (Elliot *et al.* 1975). For stars that have adequate flux in the UV, these data can also be used to probe the composition of planetary atmospheres through the "spike-delay" technique (Elliot *et al.* 1974), or to probe the particle-size distribution of ring particles by studying differential extinction (Marouf *et al.* 1983).

The HSP can collect data in both digital and analog modes ("formats"). The digital format counts pulses but must be corrected for dead-time ($\tau \sim 40$ ns) count losses at high count rates (Bless *et al.* 1992). The analog format measures flux at a variable sample interval that is always shorter than 5 ms (Bless *et al.* 1992). Since the signal is sampled rather than integrated, however, it yields a much lower signal-to-noise ratio than the digital recording format. Hence we recorded data in both formats simultaneously, using the digital signal for analysis and the analog signal to calibrate the dead-time correction, if necessary.

The occultation exposures were set to record data for as long as possible (between SAA passages and Earth occultations), and the criterion for selecting the integration time was on the basis of radial resolution. The spatial resolution of occultation data is determined by the time resolution and signal-to-noise ratio of the data, the angular diameter that the occulted star subtends at the planet, and the Fresnel scale at the planet ($\sqrt{\lambda D/2}$, where λ is the wavelength of observation and D is the distance from the observer to the occulting body). The stellar size and the Fresnel scale depend on the particular occultation event, and ideally one would set the data integration time to oversample the resolution limit set by diffraction or stellar diameter by at least a factor of two. As estimated from its magnitude and colors (Sybert *et al.* 1992), the angular diameter of the star, projected at the distance of Saturn is 0.3 km—smaller than the Fresnel scale of 0.7 km (for the 7500 Å channel). Radial shadow velocities relevant to this event lie within the range 0–8 km s^{-1}. Hence, the minimum time for crossing 0.7 km would be 0.088 s, dictating an integration time of less than 0.044 s. Although instrumental restrictions (which have since been removed) for this data format in the SPLIT mode would allow an integration time as short as 0.06 s, we chose a somewhat longer time—0.15 s—in order to be well clear of the absolute limit. Even with this integration time, the spatial resolution was limited by the signal-to-noise ratio of the data, rather than by the integration time.

For the reduction of occultation data, knowledge of the absolute timing is critical. As data are sent from the spacecraft, time tags from the spacecraft clock are attached, and later converted to UTC. The calibration is specified to be correct to within 10 ms, and observations of the Crab pulsar show this to be the case (Percival *et al.* 1993). The calibration procedure for times reported by the *HST* clock has been described by Percival (1992).

When observing occultations by Saturn's rings at visible wavelengths, the accuracy of the derived optical depths of the rings is limited by the accuracy with which one can subtract the bright planet and ring background from the light curve. Previous Earth-based observations of Saturn ring occultations have either been in the infrared, where Saturn and its rings have several deep absorption bands, making them appear quite dark; or with imaging detectors such as CCDs, so that the ring background can later be removed through modeling (see F93, Ha93, Hu93, and references therein). With the *HST*, neither approach is possible: the Wide Field/Planetary Camera is not capable of reading out fast enough for occultation observations (MacKenty *et al.* 1992). The minimum time between integrations is 2 min, which translates into over a thousand Fresnel scales for this event. The Faint Object Camera is even slower, with 4–5 min between integrations (Paresce 1992), and there are no infrared detectors currently on the *HST*. The Faint Object Spectrograph (FOS) can be used for occultation observations, but it cannot record a continuous time series (Kinney 1993).

Our strategy for dealing with the background from the planet and rings involved mapping the background light. We performed 14 scans of Saturn and its rings, across a region that would include the apparent path of the star through the system (Fig. 2). The width of the smallest rectangle enclosing the stellar path is larger than the 1 arcsec aperture used (see Fig. 4); therefore, a single scan of the background following the middle of the path would not produce sufficient information about the background light entering the aperture during the occultation data collection. To overcome this, we planned a set of scans, offset from each other in the direction perpendicular to the apparent star path. In this manner we intended to map all parts of the rings that were included in the aperture during the occultation observations. We also collected 5 min of dark sky measurements in order to characterize the noise from the detector itself.

Finally, we consider the issue of acquiring the star near a large, bright object like Saturn. The most commonly used mode of target acquisition on the HSP is the onboard acquisition (Bless *et al.* 1992). In this mode, the 10 arcsec finding aperture is scanned on a 20×20 grid (the default setting). The center of the star is found from this raster scan, the process is repeated with the result of the first scan as the center of the second scan, and then the star is offset from the finding aperture to the 1 arcsec aperture. This mode fails in crowded fields or in fields with large background gradients. Because we were attempting to start the occultation observations while the star was behind the D Ring, we could not use the onboard acquisition method because the gradients produced by the bright ring and planet background would have been too large. Instead, we used the offset acquisition method. For this method, we perform an onboard acquisition on a nearby star, away from Saturn. We center on this star, and then perform a blind offset to the target star, GSC 6323-01396. The limitations imposed on this method are: (i) as the offset target, we must use a star close enough so that the error introduced by the blind offset under gyro control (~ 0.002 arcsec s^{-1}) will be small enough to keep the star well centered, (ii) the offset and target stars must be close enough that both can use the same guide stars, and (iii) the separation between the offset and target stars must be well known. The offset and target stars should be within 1.5 arcmin of each other. For the offset acquisitions, we chose GSC 6327-00161, a $V=15.5$ star that is 37.7 arcsec east and 87.4 arcsec south of the target star, GSC 6323-01396. These two stars are separated by 95.2 arcsec, just over the rough limit, but in this case neither guide stars nor gyro drift were a problem.

2.3 *Adapting the Plan to the HST Scheduling Cycle*

Even after planning all exposures for the observations, several tasks remain before the program is converted to instructions for the spacecraft. By 1991 Feb. 28 we had decided on GSC 6323-01396 as target for our first Guaranteed-Time Observer (GTO) occultation program, and we had updated the proposal except for the latest target position measurements. Astrometry of the two stars (GSC 6323-01396 and GSC 6327-00161) was performed at Wallace Astrophysical Observatory (Westford, MA), using the SNAPSHOT CCD in its strip-scanning mode (Dunham *et al.* 1985). For astrometric reference stars, we used the stars in the *HST Guide Star Catalog*, and reduced the data using the method described by Dunham *et al.* (1991). Because the acquisition planned was an offset acquisition, the important quantity was the *relative position* of the two stars. In order to assure accurate centering of the target star, its position relative to that of the offset star must be known to better than $0\overset{''}{.}1$. In order to achieve this, we measured the positions of both stars on four strips. These new position measurements were submitted on 1991 Sept. 5, 27 days before the observation (less than the 90 days currently required).

At about 4–6 weeks before an observation, the Science Planning Branch (SPB) generates the first spacecraft ephemeris that covers the observing time in question. Using these, the SPB predicts the approximate observing windows (the time that occultation data can be recorded, constrained by Earth occultation, Earth bright-limb avoidance, solar and lunar avoidance, SAA passage, and target reacquisition). The average shift in observing windows over 6 weeks is approximately 10–15 min. Predictions made 4 weeks before the observation are more accurate, with an average shift of 2–3 min, but shifts of more than 5 min at this time are not uncommon.

Armed with these predictive windows, the SPB worked to schedule the occultation to fit into the windows. The scheduling process is normally handled automatically with computer code. In order to collect the maximum amount of data before and after SAA passages, large parts of the schedule were done by hand. We credit the schedulers with achieving the longest exposures within the SAA constraints, allowing us to record significantly more data than would have been possible with the automatic scheduling program.

2.4 *Checking the Science Mission Schedule*

A Science Mission Schedule (SMS) was produced, containing one week's worth of instructions for the instruments onboard the *HST*. As a last check before the science program was executed, we inspected the SMS for any errors on 1991 Sept. 12. We found that a spatial scan over Saturn and its rings would not be executed correctly, due to moving target support limitations. Part of the set of scans was to be executed within a single exposure [start data collection at the beginning of the first line, ending at the end of the last line with no breaks in data collection between lines; see Downes (1992) for a more complete explanation], but that capability had not yet been incorporated into the Moving Object Support System (MOSS). Although the single-exposure configuration is not a necessary factor, neither we nor the planners knew about the MOSS limitation until it failed during our SV test. As a

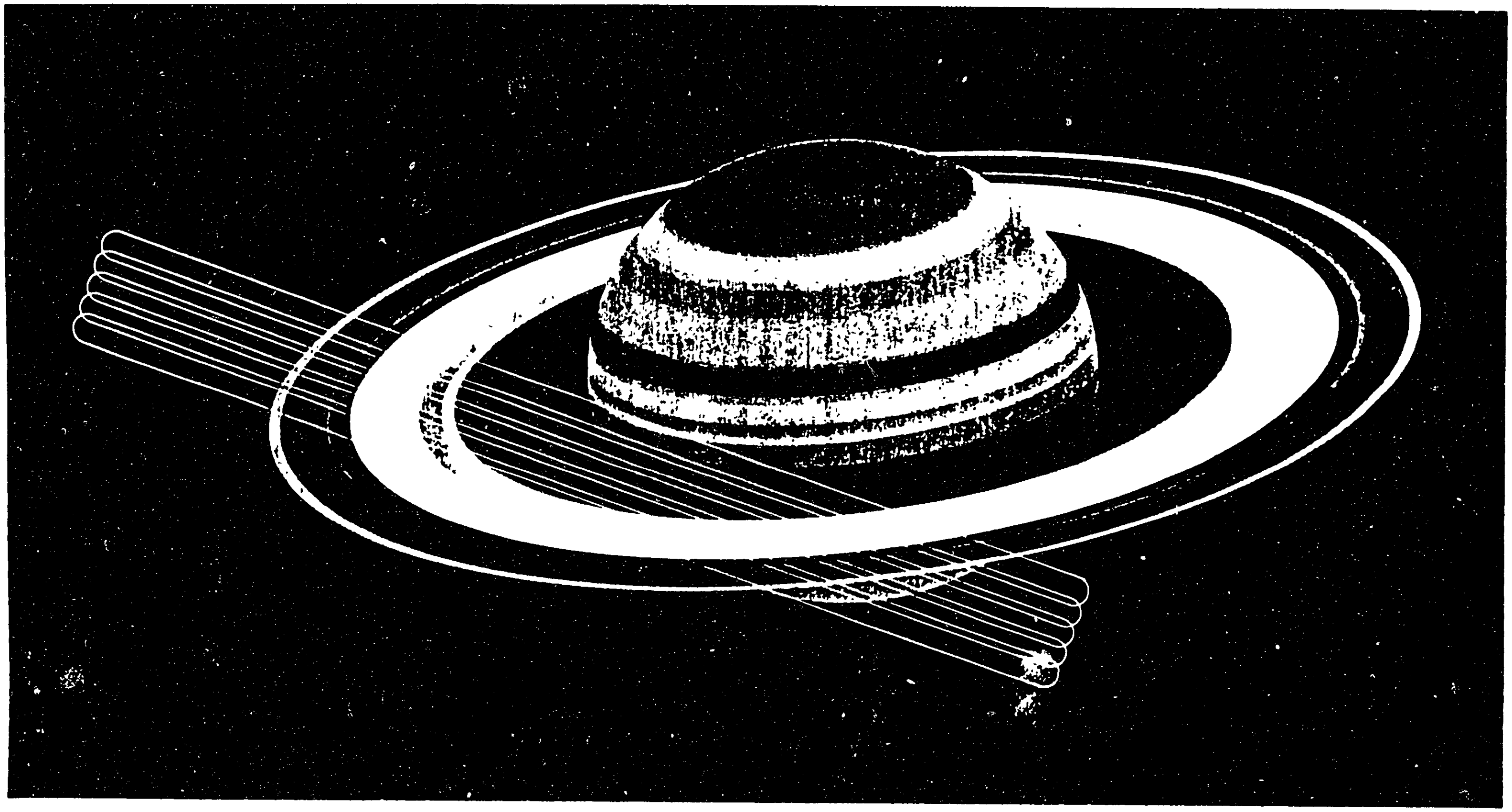

FIG. 2. Planned background scans, which encompass the overall track of GSC 6323-01396 relative to Saturn during the occultation. The stellar track is significantly distorted by spacecraft parallax (see Fig. 4), so a suite of overlapping background scans was planned to cover its entire path. Because of commanding difficulties, the multiple scan shown executed as a single pass, and an unanticipated time lag during telescope pointing led to incomplete and uncertain coverage of the length of the single track scanned.

TABLE 2. Exposure log.

Obs. ID[a]	Observation	Start Time (UTC)	Sample Time (s)	Exposure Time (s)
v0rr0101	Dark	1991 10 1 01 25 12.28[b]	0.15	288.0
v0rr0201	Back Scan	1991 10 1 19 40 43.29[b]	0.01	61.4
v0rr0202	Back Scan	1991 10 1 19 52 58.28[b]	0.15	777.6
v0rr0203	Back Scan	1991 10 1 21 00 57.29[b]	0.01	61.4
v0rr6301	Acquisition	1991 10 2 18 12 16.96[b]	0.30	120.0
v0rr6302	Acquisition	1991 10 2 18 18 10.96[b]	0.30	120.0
v0rr6401	Occ. Seg. 1	1991 10 2 19 35 10.5956	0.15	2419.2
v0rr6402	Occ. Seg. 2	1991 10 2 21 10 54.5955	0.15	518.4
v0rr6403	Occ. Seg. 3	1991 10 2 21 35 49.5955	0.15	979.2
v0rr6404	Occ. Seg. 4	1991 10 2 22 47 32.5957	0.15	633.6
v0rr6405	Occ. Seg. 5	1991 10 2 23 24 35.5948	0.15	199.5
v0rr6406	Occ. Seg. 6	1991 10 3 00 24 09.5956	0.15	777.6
v0rr6407	Occ. Seg. 7	1991 10 3 02 00 47.5957	0.15	1094.4
v0rr6408	Occ. Seg. 8	1991 10 3 03 37 24.5949	0.15	1468.8
v0rr6409	Occ. Seg. 9	1991 10 3 05 14 01.5958	0.15	1728.0
v0rr640a	Occ. Seg. 10	1991 10 3 06 50 39.5958	0.15	2188.8
v0rr640b	Occ. Seg. 11	1991 10 3 08 27 16.5959	0.15	2505.6
v0rr640c	Occ. Seg. 12	1991 10 3 10 03 54.5951	0.15	2505.6
v0rr640d	Occ. Seg. 13	1991 10 3 11 40 30.5949	0.15	2505.6
v0rr640e	Occ. Seg. 14	1991 10 3 13 17 08.5959	0.15	2505.6
v0rr640f	Occ. Seg. 15	1991 10 3 14 53 46.5969	0.15	2505.6
v0rr0501	Back Scan	1991 10 3 16 43 30.29[b]	0.01	61.4
v0rr0502	Back Scan	1991 10 3 16 55 45.28[b]	0.15	777.6
v0rr0503	Back Scan	1991 10 3 18 06 40.29[b]	0.01	61.4

Notes to TABLE 2

[a] Rootname of data set in HST Archive (Baum 1993).

[b] Indicated times do not include correction for spacecraft clock to UTC calibration, and are therefore approximate (by ~0.3 s).

result, the planned five-line scan would be executed as a single-line scan instead, scanning the middle of the apparent path only. This meant that we would lose valuable information about the ring background because we would not be scanning over the entire path followed by the star. However, we were not allowed to compensate for it by splitting the multiple-line scan into single-line scans because it was too close to the execution time. No other errors were detected in the SMS.

3. DATA

In contrast with ground-based and airborne occultation observations—where the most critical time for the observer is that just prior to and during the occultation—the observer has no duties during *HST* occultation observations: the die is cast with the final corrections to the SMS. By being present at the Observation Support System (OSS), we got a first look at the data coming in and noted the behavior of the spacecraft: the target acquisition was successful, and at times the guidance system suffered loss of lock (LOL). Although fine lock did not completely eliminate jitter, it vastly improved the quality of these data over those acquired in the SV test and enhanced the reliability of our feature measurements (described in Sec. 4). In this section we present the calibration and occultation data and discuss their properties.

3.1 Calibration Data

A list of all exposures for the data connected with this occultation is given in Table 2. The first exposures were "darks," for which the HSP aperture is trained on a dark region of sky and exposed for 5 min to ascertain the instrument noise level for both detectors (see Table 1). Although these exposures executed successfully, they identified a pre-existing limitation on data acquisition in our two-color mode which has since been rectified: although two separate detectors were used for our observations, their analog gains could not be set separately in star–sky mode of the HSP (Bless *et al.* 1993). Since the PMT and VIS detectors differ in sensitivity as well as wavelength, the relative signals received forced us to sacrifice potentially useful information from the analog format of the VIS detector in favor of the PMT.

As discussed above, our attempt to map the contribution of light from the rings to the total signal was thwarted by a previously unknown ground system restriction on single exposures in spatial scans. We had planned to scan back and forth across the planet and rings with the 1.0 arcsec aperture, with an offset of 0.75 arcsec between each

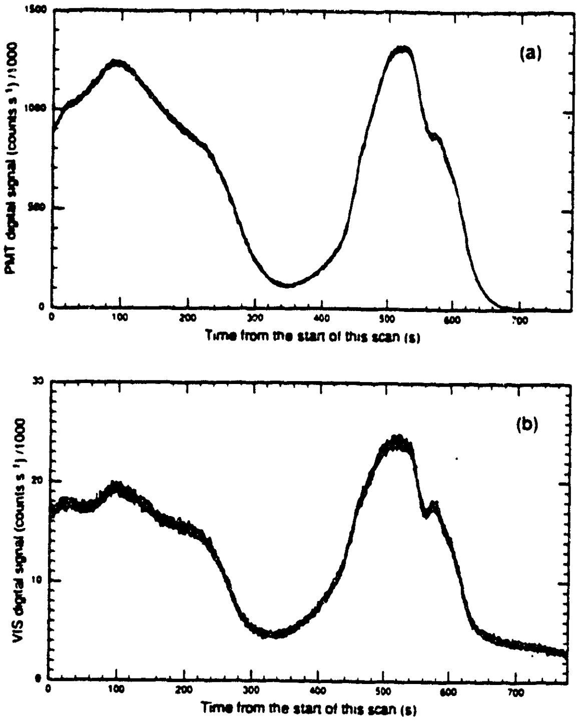

FIG. 3. A sample background scan from just southwest of the planet, across its bright face (interrupted by the rings and ring shadow), into the relatively empty (dark) space between planet and rings, and then outward through the ring system into dark sky, approximately along the path traced by the star as it was occulted by Saturn. Because of the uncertain timelag between the start of scanning and that of data collection, time is plotted relative to the start of this scan. Digital data are displayed from (a) photomultiplier tube (PMT, 7500 Å) and (b) image dissector tube (VIS, 3200 Å).

sweep (see Fig. 2). This restriction was discovered during the SV test, and thus the October observation was executed in the knowledge that the background would not be adequately mapped. An additional difficulty with background scans went unnoticed until data arrived. A timing problem that was masked by other problems in the SV test scans resulted in a significant uncertainty in the spatial coverage of the background scans. Commanding overhead delayed the onset of actual data collection within the scan intervals, thus both offsetting and reducing the scans' coverage of the Saturn-ring system. Since the background scans did not follow our planned raster, removal of the background from the occultation light curves will require considerable effort, and this task has not yet been attempted.

Figure 3 shows a sample background scan across the planet and rings, as recorded for each of the two photometric channels. The raw resolution of these background scans across Saturn and its rings is set by the smear of the HSP's 1.0 arcsec aperture (equivalent to 6000 km at the distance of Saturn). Although this is much larger than the few kilometer spatial resolution of the occultation data (see previous discussion, above) it can be improved through deconvolution.

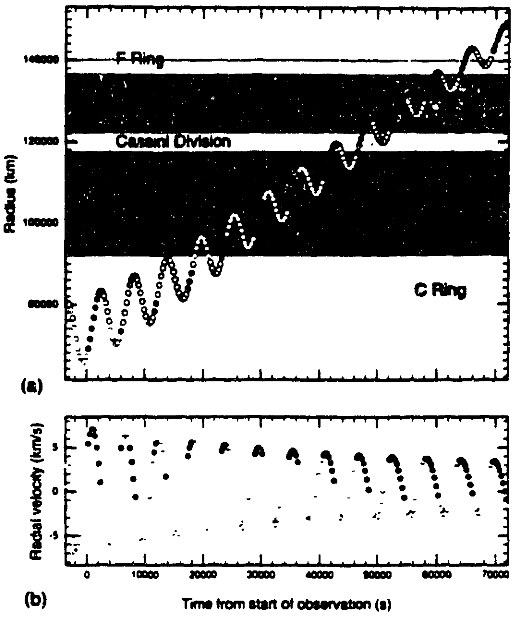

FIG. 5. (a) The variation of ring-plane radius with time, shown here with dots at 5 min intervals, is far from monotonic as the star moves generally outward in the rings. The portions of the track observed are indicated by the filled dots. (b) Variation of radial velocity (in the ring plane) with time during egress, at the same intervals as above. As the apparent stellar track nears its stationary point the radial velocity decreases to zero and then reverses sign as the *HST* rounds the limb of the Earth.

3.2 Occultation Data

The apparent path of GSC 6323-01396 through Saturn's rings as seen by the *HST* is shown in Fig. 4 (Plate 110) with dots at 5 min intervals. Saturn was traveling southwest on the sky, so the star appeared to travel northeast relative to the planet. Two motions determine what parts of Saturn's rings are sampled by the star: parallax due to the orbital motion of the *HST*, and the relative motions of Saturn and the Earth. The former causes the apparent position of Saturn to move in a small ellipse relative to the star, and the latter stretches these ellipses out into the loops portrayed in the figure. The dependence of ring-plane radius and radial velocity on time due to these motions is shown in Fig. 5.

Data collection was not continuous as the star traced out this path. The spacecraft moved behind the Earth as seen from Saturn (the equivalent of Saturn setting for ground-based observers) for almost half of each 96 min orbit. Also, observations were precluded when the *HST* passed south of the equator over the Atlantic Ocean, through the SAA. Observation time was further reduced by the necessity to reacquire the guide stars following each of these interruptions, a process that takes about 5 min. The windows of observability are indicated in green in Fig. 4 and by the filled circles in Fig. 5.

The combined stellar and planetary flux was sampled at 0.15 s intervals by the two detectors at 3200 and 7500 Å, with both analog and digital data being recorded. For our

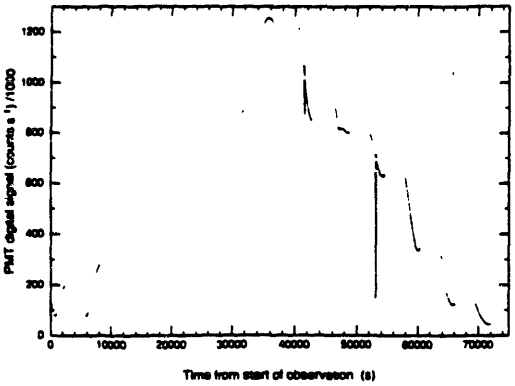

FIG. 6. Overview of the full occultation data set, fragmented by the visibility limitations discussed in the text (Earth occultations and SAA passages). The overall pattern is that of the bright Saturn-ring system convolved with the 1.0 arcsec aperture of the HSP, and the zigzag appearance is caused by parallax, the star moving in and out along its looping path relative to the varying ring background during each *HST* orbit. Most of the "glitches" on the smooth profile segments that can be seen at this scale are not ring features, rather they are episodes of loss of lock.

present goal of getting the most accurate times for ring-feature occultations, however, we treat only the digital signal from the photomultiplier tube (7500 Å), as it has a significantly higher signal-to-noise ratio (see Table 1). The 3200 Å digital data will not be used in this analysis.

An overview of the occultation light curve is shown in Fig. 6, fragmented by the visibility limitations imposed by Earth occultations and SAA passages. The overall pattern is that of the bright Saturn-ring system convolved with the 1.0 arcsec aperture of the HSP, and the zigzag appearance is caused by Saturn's parallax. The apparent position of the star moves along its helical path during each 96 min *HST* orbit; the apparent stellar path projected onto the ring plane traverses certain radial zones several times (see Fig. 5). A total of 6.8 h of occultation data were collected over a period of 20.0 h (covering 13 spacecraft orbits) during ring egress, for an "exposure efficiency" of 34 percent. The observation sequence spanned 65 h, including the acquisition of calibration and background data.

Most of the discontinuities on the smooth profile segments that can be seen at this scale are not ring features, but episodes of loss of lock (LOL). About 4 min after each day–night transition during the GSC 6323-01396 occultation observation, fine lock was sometimes seriously compromised or even lost. When lost, it was usually regained within a few minutes, as seen in Fig. 7. A LOL occurred, in fact, between the two onboard acquisitions of the offset star, but the second acquisition image was perfect nonetheless.

A typical case of pointing jitter and LOL incited just after day/night transition is shown in Fig. 7(a). Strong signal oscillations like those seen prior to total LOL can often be partially suppressed by smoothing the data [as in Fig. 7(c)] without seriously degrading the data content, but the star is well out of the aperture during LOL so the data are useless until fine lock is recovered. Complete LOL occurred only three times during our observations, but episodes of jitter affected most of the data segments at least briefly.

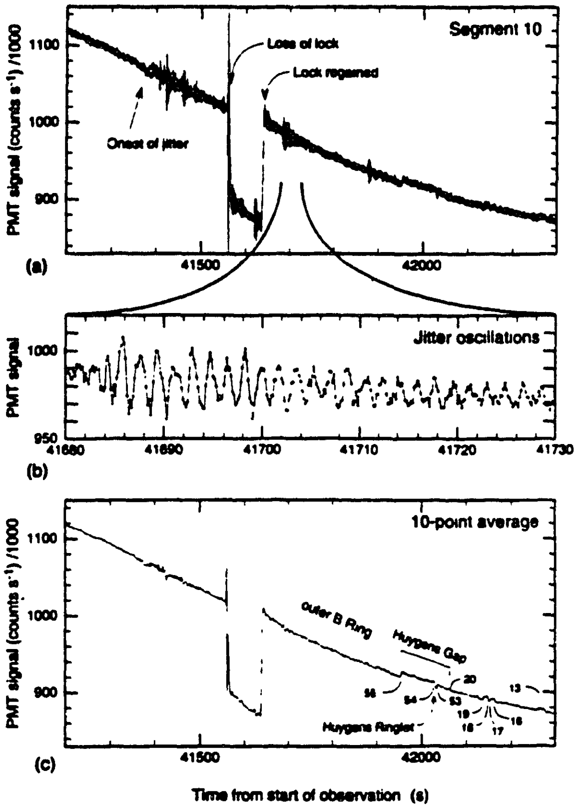

FIG. 7. PMT digital data for the tenth data segment, during which the telescope experienced jitter and loss of lock (LOL). (a) Full resolution, 0.15 s integrations. The star moving outward through the bright and optically thick outer B Ring at this time, so little if any of the fine-scale structure on the left of the plot is due to actual optical depth variations. On the right can be seen the outer edge of the B Ring, with the Huygens Gap and the inner Cassini Division. A few minutes after the *HST* passed into the Earth's shadow (orbital night), quasisinusoidal variations began in the received signal due to oscillations in telescope pointing across the strong background gradient. This effect can be seen expanded in (b), also at full resolution (open symbols mark each data point). Although the magnitude varies strongly, the frequency of the oscillation is fairly constant, about 0.7 Hz. Because of the jitter's regularity, much of its effect can be suppressed with moderate averaging. (c) A 10 point binned average of the light curve. Little of the jitter remains while the resulting 1.5 s resolution is adequate to unambiguously identify prominent ring features (labeled with feature number) once past the complete LOL.

The *HST* observation of this occultation began as the apparent position of the star was moving outward through the tenuous D ring, and continued as it traversed all of the classical C, B, and A rings and the F ring. The individual ring profile segments are shown in Fig. 8. In particular, several plateau regions in the C ring and the outer portion of the A ring (which contain the signatures of many satellite resonances) are each represented in two separate data segments at different azimuths.

Because of the orbital alignment of the *HST* at this time, all of the profile segments are approximately radial. In the later segments, the stellar track goes through a maximum in ring-plane radius just before data collection is interrupted for Earth occultation. The radial component of the relative stellar velocity varies by more than an order of magnitude along each observed segment, so the effective radial sampling rate and the apparent noise level vary strongly [see Fig. 5(b)].

Normalized data segments are plotted against radius (with the parameters from our adopted geometric solution, discussed in Sec. 7) in Fig. 8. In order to view the light

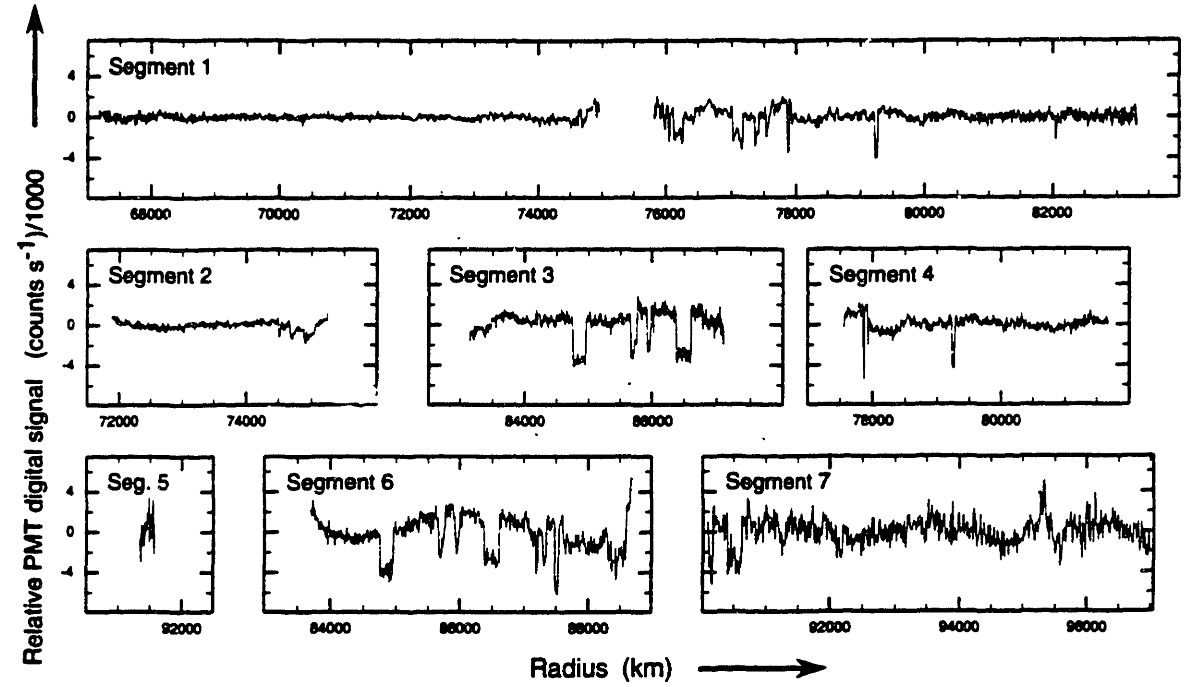

FIG. 8. The fifteen data segments of the occultation profile, shown at 1.5 s resolution (10 point binned averages) and plotted against radius in the ring plane. Although we have not been able to remove the true planetary background from the signal because of the commanding difficulties described in the text, in order to view the light curves on a reasonable scale we have filtered out the low frequency component of the profiles. Each segment has been detrended (subtracting a linear function in time so that both ends are at zero signal), and transformed into frequency space using an FFT algorithm. The lowest 1% of the frequencies were then transformed back into the time domain and subtracted from the detrended signal. Detrending of segments 11 and 14 was done with respect to the 100th point (rather than the first point) because of the strong increase in signal at the outer edges of the B and A rings, respectively. This process was performed in two parts for segments 1, 10, and 12, since LOL data were removed from these segments. Note also that because of SAA passages, the segments are not of uniform length. Many ring features are clearly discernible at this enhanced scale: (a) Segment 1: beginning interior to the main rings and moving outward through the variegated inner C Ring. Visible are features 44 (the inner edge of the C Ring), 40, 39, 63, and 62 (the Titan Ringlet), and 43 (the outer edge of the Titan Gap), 38, 37, 36. A mild episode of loss of lock (LOL) can be seen just before the ring edge crossing, but fortunately guidance had been recovered by the time the star passed behind the C Ring edge. (b) Segment 2: observation during this orbit was interrupted by an SAA passage, and with this segment the star just enters the innermost C Ring (crossing Feature 44 and its neighbors again). (c) Segment 3: the second observed portion of the same orbit as Segment 2 (after SAA passage), as the star moved from the middle into the outer C Ring. Features 35, 34, 33, 42, 31, 30, and 29 were traversed. (d) Segment 4: the first observed portion of the third orbit, covering the Titan Gap and Ringlet (features 63, 62, and 43) and the optical depth peak just outside it (edges 38 and 37). (e) Segment 5: a very short snippet at the other extreme of the third orbit, crossing no features. (f) Segment 6: although fairly brief, this segment spans the outer C Ring from the innermost plateau (features 35 and 34) out to the Maxwell Ringlet (61 and 60). (g) Segment 7: this segment runs from the outermost C Ring into the inner B Ring. (h) Segment 8: this segment covers many of the features in the B Ring (81 out through 71), though they can be difficult to identify and measure because of the high optical depth in the region and the possibility of noncircularity. (i) Segment 9: ring background brightness reaches a maximum during this segment, which contains probable identifications of features 72 and 71 in the middle B Ring. (j) Segment 10: the brightness of the aperture-smeared ring image decreased as the star moved outward in the B Ring; during this segment it crossed into the Cassini Division and features 55 (the outer edge of the B Ring), 54, 53, and 20 (the Huygens Ringlet and outer gap edge), and 19, 18, 17, 16, 13, and 15 are measured on this data segment. The prominent LOL (off-scale) is within the outer B Ring where there are no numbered features, so no measurements were compromised. (k) Segment 11: a second pass across the outer B Ring region, this time including the entire Cassini Division from feature 55 all the way out to feature 7. SAA passage is no longer interrupting observing time each orbit, so this and the remaining segments are the maximum length of almost 42 min, limited by Earth occultation and subsequent guide star reacquisition. These full-length segments (segments 11–15) also reach the extrema of the parallax-induced distortion, and the stellar track doubles back on itself. (l) Segment 12: spanned the inner and middle A Ring, where there are no distinct, numbered features. This episode of LOL (off-scale) thus had no serious effect on our feature measurements. (m) Segment 13: extends from the central A Ring out to the F Ring. Pointing jitter just outside the Encke Gap (features 4 and 3) is mostly suppressed by data averaging. (n) Segment 14: the Keeler Gap and the outer edge of the A Ring can be seen clearly near the left edge, but a probable F Ring feature detection is somewhat uncertain due to pointing jitter. (o) Segment 15: this entire segment is outside the main rings.

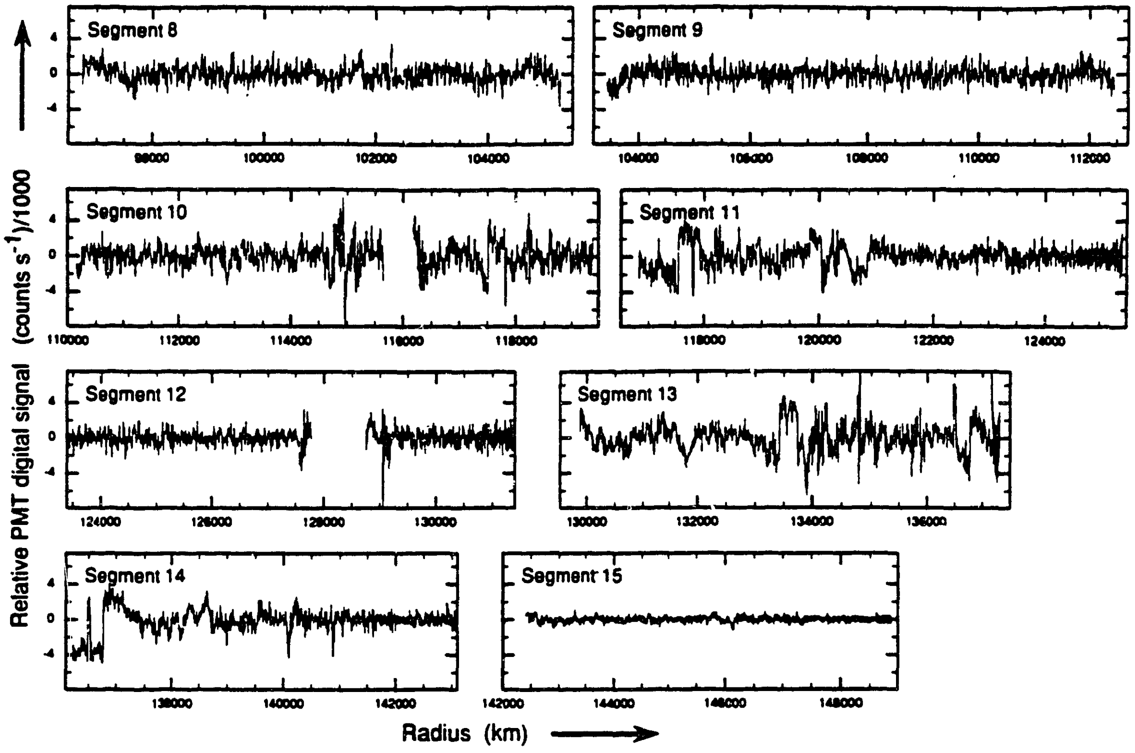

FIG. 8. (continued)

curves on a reasonable scale we have filtered out the low frequency component of the profiles. This filtering was done to remove the strong overall gradient in each segment, due to light from Saturn or its rings. We note that this filtering was performed only to aid in presentation; it is not a rigorous removal of background signal.

Some apparent azimuthal brightness variation is demonstrated by the relative background (ring) signal in multiple passages across the same radial regions as the telescope tracked the star (Fig. 9). This is likely due to a combination of foreshortening of the curved rings in the smeared image (which allows differing amounts of other regions to appear in the aperture) and the contribution of light reflected off the partially illuminated face of Saturn onto the rings: it highlights the necessity for detailed mapping of the background in future occultation observations. Another factor that may affect such differences between successive passages is the orbital variation in the system throughput that has become evident in other HSP observations (Bless *et al.* 1993).

3.3 Signal and Noise Levels

Because of the unfortunate lack of adequate background data, the best diagnostic within the data for determining the unocculted stellar signal received by our aperture is the light curve appearance near the Huygens Gap. This gap is basically empty, while the nearby B ring is almost opaque. The Titan, Maxwell, and Encke Gaps and the outer edge of the A ring provide similar stark transitions, but the ring optical depth is lower in those regions so appreciable stellar flux is transmitted outside the gaps. The stellar signal at the inner edge of the Huygens Gap is about 1050 detected photons per 0.15 s integration, or 7000 s^{-1} (about 0.5% of the full received signal in the B ring, and about 2% for the A ring; see Table 1). The measured rms noise is equivalent to 600 s^{-1} from the A ring for a 1.0 s integration, yielding a signal-to-noise ratio of 11 in 1.0 s. Although this signal-to-noise ratio is not as large as that for the best Earth-based observations of the 28 Sgr occultation (F93, Ha93, Hu93), it is entirely adequate for the purposes of measuring feature occultation times.

3.4 General Access to these Data

While these data are available in the *HST* Archives (Baum 1993), we intend to deposit them (along with ancillary information) in the Rings Node of the Planetary Data System (PDS), located at NASA Ames Research Center (M. R. Showalter, manager).

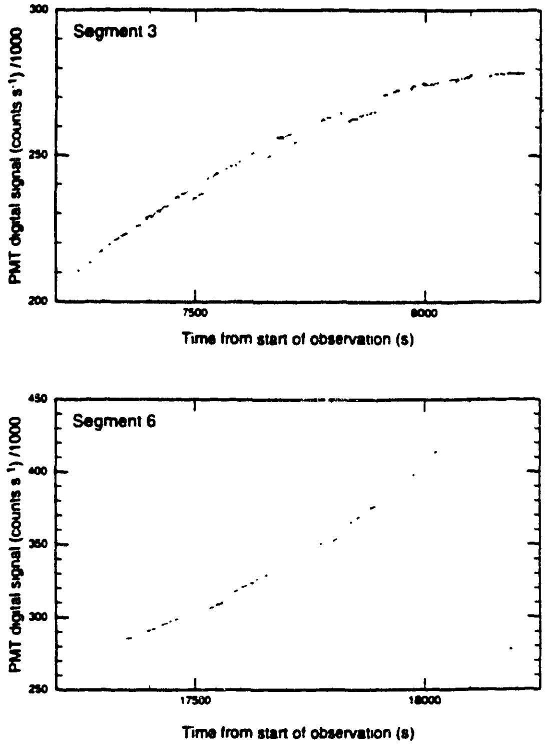

FIG. 9. Dual passages (during segments 3 and 6) of the star behind part of the outer C ring, a region characterized by sharp-edged, moderate optical depth ($0.3<\tau<0.5$) "plateaux" interspersed within a broad, low-optical depth "background." The strong overall gradients are the ring background; the differing curvature in the two profiles is due to the varying speed and curvature of the stellar track relative to the rings, as seen superposed on the synthetic ring "image" in Fig. 4, and is much reduced when a radial scale is applied. Note also the absolute difference in background signal between the two scans, despite similar radial coverage, indicating significant azimuthal brightness variation in the background, as discussed in the text.

4. FEATURE OCCULTATION TIMES

The signatures of many sharp optical-depth transitions in the rings are easily identified on the uncalibrated light curve, and several such features seen in two occultation segments are shown in Fig. 9. Ring features identified in the *HST* profile form a subset of those discussed by F93 and by Nicholson *et al.* (1990)—hereafter referred to as NCP. Not all of the features given in the catalog of F93 (see their Fig. 4) are included in our measurements, either because the feature was not covered by one of our light curve segments (we do not have a continuous radial profile), or because the optical depth change for the feature was not great enough to be apparent above the (radially variable) noise.

The first step in our analysis was to measure occultation times for the most prominent ring features in the uncalibrated profile. We used the "half-light" criterion employed by F93 for the definition of an edge. For a sharp edge, the "half-light" position for a monochromatic diffraction pattern would be shifted into the geometric shadow by 0.26 km for the 7500 Å channel. When the radial velocity is 8 km s^{-1}, however, the filtering imposed by the 0.15 s integration time reduces this shift to 0.15 km. Since "features" correspond to entering and exiting dense portions of ring material, this radial diffraction bias would tend to average out when these times are used in geometric models. Further evidence for the unimportance of diffraction effects in this data set relative to other data sets is that the signal to noise of these data is not sufficient to see diffraction fringes. For a radial velocity of 3 km s^{-1}, the main fringe for a sharp-edged opaque screen would have an amplitude of 1.28 if the phase of the integration bins relative to the edge crossing were optimized. Hence in the ideal case, detection of the main fringe would have an S/N of only 1.1; for the majority of real cases, however, the detectability would be less favorable.

The "half-light" times were incorporated into a first-generation geometrical model, and that solution was used to predict approximate event times for 104 possible crossings of features in the F93 catalog. The neighborhood of each of these predicted times was then examined, and times measured for those features that could be identified. This was done visually, since without accurate background calibration, the ring profile is superposed on a strongly varying baseline, which makes modeling difficult.

Of the 104 possible occultations (some multiple) by features in the F93 catalog, 18 fell just before or after the observed segment. About seven were probably traversed, but were either too difficult to detect in the data, or sufficiently noncircular that they fell outside the 30 s span of the search. Twelve features, mostly in the optically thick B ring or close to LOL jitter in the light curve, were identified as "probable." In some cases, intermediate refinements of the geometrical model using the full set of features enabled us to eliminate or improve ambiguous feature identifications (mostly in the B ring). This left 79 measured event times for feature crossings. These times are given in Table 3, along with an estimate of the certainty of identification. The estimated measurement uncertainties in the feature times range from 0.1 to 0.3 s (generally corresponding to less than 1 km radially), and these are also given in Table 3. Including only those features with confident identifications, we measure 67 event times. These correspond to 43 distinct features, with a second occultation by 24 of these.

Of our more confident identifications, many have been previously determined to be significantly noncircular (NCP,F93) and are thus not employed in our present model fits. Event times of the features that are currently presumed to be circular number 48 and are indicated in Table 4. Of these event times, 40 were identified with certainty, corresponding to 25 features presumed to be circular—15 features were occulted twice. These were the event times used in the geometric modeling.

5. MODEL FOR GEOMETRIC ANALYSIS

In order to interpret the occultation times for the features in Saturn's rings in terms of spatial coordinates

TABLE 3. Catalog of identified features.

Occ. Seg.	Feature ID[a]	Feature Radius[a]	Feature Time (after 1991 Oct. 2, 19:34:45.75 UTC)	Confidence Level[b]
1	44*	74490.76	968.52 ± 0.1	2
1	40*	76263.93	1165.72 ± 0.1	2
1	39*	77164.63	1269.13 ± 0.1	2
1	63	77854.9	1351.27 ± 0.1	2
1	62	77872.1	1353.01 ± 0.1	2
1	43	77918.0	1358.69 ± 0.1	2
1	38*	79220.31	1520.55 ± 0.1	2
1	37*	79265.28	1526.12 ± 0.1	2
1	36*	82040.58	1967.06 ± 0.1	2
2	44*	74490.76	6185.35 ± 0.1	2
3	35*	84749.44	7510.15 ± 0.1	2
3	34*	84949.38	7544.55 ± 0.1	2
3	33*	85660.65	7680.30 ± 0.1	2
3	42*	85758.59	7701.55 ± 0.2	2
3	31*	85921.38	7736.90 ± 0.2	2
3	30*	86370.61	7851.15 ± 0.2	2
3	29*	86601.11	7924.02 ± 0.1	2
4	63	77854.9	11625.75 ± 0.1	2
4	62	77872.1	11628.30 ± 0.1	2
4	43	77918.0	11638.15 ± 0.2	2
4	38*	79220.31	11852.05 ± 0.1	2
4	37*	79265.28	11858.35 ± 0.2	2
6	35*	84749.44	17555.95 ± 0.2	2
6	34*	84949.38	17588.50 ± 0.1	2
6	33*	85660.65	17702.05 ± 0.1	2
6	42*	85758.59	17716.45 ± 0.1	2
6	31*	85921.38	17742.05 ± 0.1	2
6	30*	86370.61	17809.45 ± 0.1	1
6	29*	86601.11	17843.55 ± 0.1	2
6	61	87486.3	17969.95 ± 0.1	2
6	60	87557.9	17977.75 ± 0.1	2
7	56	90197.3	23178.72 ± 0.1	2
7	24*	90404.08	23216.35 ± 0.1	2
7	23*	90614.87	23255.85 ± 0.2	2
7	83	94439.46	23867.55 ± 0.2	1
7	82	95358.3	24004.05 ± 0.1	2
7	81	96895.97	24235.50 ± 0.1	1
8	81	96895.97	28993.72 ± 0.1	1
8	80	97212.9	29053.85 ± 0.3	1
8	76	101002.53	29683.35 ± 0.2	1
8	74	101741.5	29811.79 ± 0.2	1
8	73	103009.2	30011.54 ± 0.3	1
9	72	103657.03	34797.05 ± 0.2	1
9	71	104087.19	34882.75 ± 0.2	1
10	55	117516.0	41981.10 ± 0.1	2
10	54	117814.4	42055.70 ± 0.1	2
10	53	117833.7	42059.95 ± 0.1	2
10	20*	117932.25	42089.10 ± 0.1	2
10	19	118183.2	42162.65 ± 0.1	2
10	18	118229.3	42173.65 ± 0.1	2
10	17	118256.5	42177.60 ± 0.1	2
10	16*	118283.29	42188.45 ± 0.1	2
10	13*	118628.11	42300.65 ± 0.1	2
10	15*	118965.69	42434.35 ± 0.1	2
11	55	117516.0	46502.50 ± 0.1	2
11	54	117814.4	46551.85 ± 0.1	2
11	53	117833.7	46555.75 ± 0.1	2
11	20*	117932.25	46578.35 ± 0.1	1
11	19	118183.2	46629.05 ± 0.1	2
11	18	118229.3	46636.25 ± 0.1	2
11	17	118256.5	46642.85 ± 0.1	2
11	16*	118283.29	46647.25 ± 0.1	2
11	13*	118628.11	46714.05 ± 0.2	2
11	15*	118965.69	46778.75 ± 0.2	2
11	14	120039.0	46983.35 ± 0.1	2
11	12*	120073.42	46988.85 ± 0.2	2
11	11*	120246.31	47023.05 ± 0.2	2
11	10	120305.7	47034.15 ± 0.1	2
11	9	120316.5	47036.60 ± 0.1	2
11	7*	122049.48	47383.30 ± 0.1	2
13	4*	133423.53	58701.69 ± 0.1	2
13	3*	133745.14	58773.32 ± 0.1	2
13	2	136488.2	59521.29 ± 0.2	2
13	1*	136522.28	59538.10 ± 0.1	2
13	52	136774.4	59650.97 ± 0.1	2
14	2	136488.2	63802.88 ± 0.1	2
14	1*	136522.28	63813.15 ± 0.1	2
14	52	136774.4	63867.42 ± 0.1	2
14	51	140461.0	64612.25 ± 0.3	1

Notes to TABLE 3

[a] Feature ID and feature radius are after adopted solution of F93. Those features that are presumed circular and were included in our fits are marked with an asterisk; the radius values for known non-circular features are from F93 Table II.

[b] A value of "2" indicates a certain detection of this feature, while a value of "1" indicates a probable detection.

within the system, one must first construct the geometrical relation between the star, observer, and occulting planet. Approaches to this analysis have been developed to accommodate lunar and stellar occultations observed from Earth (Smart 1977; Elliot *et al.* 1978)—as well as stellar, solar, and radio occultations involving spacecraft (French *et al.* 1988; Holberg *et al.* 1987; Rosen *et al.* 1991a,b; NCP). Recently F93 have compared these geometrical methods in the context of reducing stellar occultation data for 28 Sgr and Saturn's rings. Their work uncovered numerous subtleties that depend on the coordinate systems and approximations chosen for the analysis, as well as errors at the few kilometer level (when used for Saturn ring occultation reductions) in computer codes that had been in use for many years (French *et al.* 1988). This lesson has underscored the importance of fully describing geometric methods used for analysis of occultation data.

5.1 Our Approach

Our method for combining *HST* and Earth-based occultation data employs a solar system barycentric reference system. One advantage of this approach is that the direction of the occulted star remains constant—at least to the extent that its proper motion and stellar parallax can be neglected—so that one does not need to include differential stellar aberration. To simplify certain numerical calculations in our approach, however, we use a coordinate system centered on Saturn's shadow (cast in starlight) near the Earth and another centered on Saturn—a modification of the "sky-plane" method of Elliot *et al.* (1978).

Since our method does not include special relativistic effects, time and distance intervals will have inconsistencies that scale as $\sqrt{1-(v/c)^2}$, where v is the velocity of the planetary coordinate system relative to the solar system barycenter. For the velocity involved, this special relativity factor differs from unity by 5×10^{-9}. Hence the time interval between occultation and detection—about 10^4 s—would have inconsistencies at the 50 μs level (much smaller than our timing uncertainties for occultation features). The Earth–Saturn distance was about 1.5×10^9 km, so the distance inconsistencies would be about 8 km. Resultant errors in dimensions in the ring system, however, would be no more than 0.002 km (negligible for this work).

5.2 General Vector Equations

We begin the development of our method with vector equations describing the relationship between the positions of the occulting ring feature ("f"), planet center ("p"), barycenter of the planet-satellite system ("b"), Earth center ("e"), barycenter of the Earth-Moon system ("β"), and receiver ("r"). Some of these locations are illustrated by the vector diagram in Fig. 10. The main task of the geometric reduction is to derive the vector from the planet center to the occulting ring feature, $\mathbf{r}_{pf}$, that corresponds to the detection of the feature occultation at time t_r by the receiver (observer). This equals the difference between the vector from an arbitrary origin—in this case the solar system barycenter—to the ring feature, $\mathbf{r}_f$, and the vector from the same origin to the center of the planet, $\mathbf{r}_p$, at the time t_f when the feature occulted the star:

$$\mathbf{r}_{pf}(t_f)=\mathbf{r}_f(t_f)-\mathbf{r}_p(t_f). \tag{1}$$

Usually one must find the vector $\mathbf{r}_p(t)$ required by Eq. (1) from an ephemeris for the barycenter of the planet and its satellites, $\mathbf{r}_b(t)$. If $\mathcal{M}_p$ is the mass of the planet, $\mathcal{M}_j$ is the mass of the jth satellite, and $\mathbf{r}_{bj}(t)$ is the vector from the barycenter (of the planet and satellites) to the jth satellite, then we have

$$\mathbf{r}_p(t)=\mathbf{r}_b(t)-\sum_{j=1}^{\substack{\text{all}\\\text{satellites}}}\frac{\mathcal{M}_j}{\mathcal{M}_p}\mathbf{r}_{bj}(t). \tag{2}$$

The feature occultation time occurs prior to its detection time by an amount equal to the light travel time between the feature and the receiver:

$$t_f=t_r-\frac{|\mathbf{r}_f(t_f)-\mathbf{r}_r(t_r)|}{c}. \tag{3}$$

This vector to the receiver, $\mathbf{r}_r(t)$, is derived from several ephemerides. For observations carried out in the vicinity of the Earth, the position of the receiver is the sum of two vectors, one to the Earth's center, $\mathbf{r}_e(t)$, another from the Earth's center to the receiver, $\mathbf{r}_{er}(t)$:

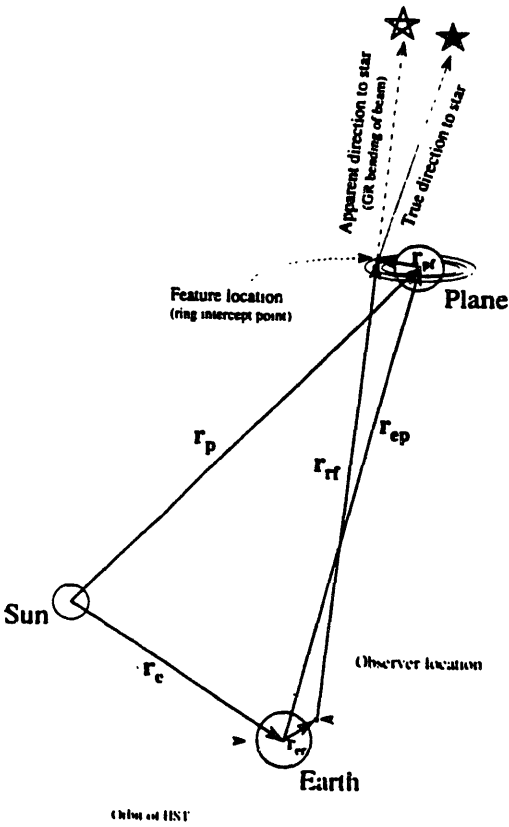

FIG. 10. Vectors used in our geometric model: $\mathbf{r}_e$ and $\mathbf{r}_p$, the geometric locations of Earth and the occulting planet from the solar-system barycenter (SSB); $\mathbf{r}_{er}$, the geocentric location of the observer (*HST*); $\mathbf{r}_{pf}$, the planetocentric location of an observed feature (such as a ring feature), and $\mathbf{r}_{rf}$, the vector from the observer to the feature as it is observed, i.e., along the apparent direction to the star, which differs from its real direction by a small angle due to gravitational bending of the beam by the occulting planet.

$$\mathbf{r}_r(t_r)=\mathbf{r}_e(t_r)+\mathbf{r}_{er}(t_r). \tag{4}$$

The vector to the Earth's center can be calculated from the vector to the Earth-Moon barycenter, $\mathbf{r}_\beta(t)$, the position of the Moon relative to the Earth, $\mathbf{r}_{em}(t)$, and the ratio of the mass of the Earth, $\mathcal{M}_e$, to the mass of the moon, $\mathcal{M}_m$:

$$\mathbf{r}_e(t_r)=\mathbf{r}_\beta(t_r)-\frac{1}{1+\mathcal{M}_e/\mathcal{M}_m}\mathbf{r}_{em}(t_r). \tag{5}$$

Having specified the positions of the planet and receiver, we proceed by adding and subtracting $\mathbf{r}_r(t_r)$ from the right-hand side of Eq. (1) and regrouping the terms for later convenience:

$$\mathbf{r}_{pf}(t_f)=\underbrace{[\mathbf{r}_f(t_f)-\mathbf{r}_r(t_r)]}_{\text{(i)}}-\underbrace{[\mathbf{r}_p(t_f)-\mathbf{r}_r(t_r)]}_{\text{(ii)}}. \tag{6}$$

5.3 Planet-Plane Equations in the Solar-System Barycentric System

Next we further expand the terms of Eq. (6) in a manner that will facilitate numerical evaluation in the solar-system barycentric system. We define two parallel planes, each perpendicular to the unit vector to the star. The first plane passes through the receiver at time t_r, and we shall refer to it as the *shadow plane*. The second plane passes through the center of the planet at time t_π [defined in terms of t_r by Eq. (9) below], and we shall call this the *planet plane* (denoted by "π"). Note that the planet plane differs from the *sky plane*, which is defined by Elliot *et al.* (1978) to be perpendicular to the line of centers between the Earth and planet and passing through the planet's center. Also, the *fundamental plane* of Smart (1977) differs from our shadow plane in that the fundamental plane passes through the center of the Earth and is perpendicular to the line of centers between the Earth and planet.

Next we solve for several quantities that specify the geometric relationship of the planet plane and the receiver. We shall need the vector between the planet and receiver that intersects the planet center at time t_π and the receiver at time t_r. We denote this special "nonsimultaneous" vector by $\mathbf{r}_{rp}(t_r,t_\pi)$, and it is defined by the equation

$$\mathbf{r}_{rp}(t_r,t_\pi)\equiv\mathbf{r}_p(t_\pi)-\mathbf{r}_r(t_r). \tag{7}$$

The perpendicular distance between the receiver and the planet plane, $d_{r\pi}(t_r,t_\pi)$, is given by the projection of this vector onto the direction to the star, $\hat{\mathbf{r}}_s$:

$$d_{r\pi}(t_r,t_\pi)=\mathbf{r}_{rp}(t_r,t_\pi)\cdot\hat{\mathbf{r}}_s. \tag{8}$$

Knowing this distance, we can compute the time t_π as the difference between the received time and the light-travel time between the planet plane and receiver:

$$t_\pi=t_r-\frac{d_{r\pi}(t_r,t_\pi)}{c}. \tag{9}$$

The relationship between these times is shown on the timeline of Fig. 11. To find $\mathbf{r}_{rp}(t_r,t_\pi)$, $d_{r\pi}(t_r,t_\pi)$, and t_π, we must perform an iterative, simultaneous solution of Eqs. (7), (8), and (9). This completes the specification of the planet plane in terms of the observed feature occultation time, t_r, and the geometric ephemerides for the planet and receiver.

5.4 Remaining Vector Equations for Feature Radii

Our approach will be to express occultation geometry in terms of solutions that would apply if the occulting feature were in the planet plane and then to correct for the position of the feature relative to this plane. First we expand term (i) of Eq. (6). This vector lies in the apparent direction of the star (as affected by the general relativistic bending of starlight) and has a length $d_{r\pi}(t_r,t_\pi)+d_{\pi f}(t_r)$, where $d_{\pi f}(t_r)$ is the perpendicular distance between the feature and the planet plane:

$$\mathbf{r}_{rf}(t_r,t_f)\equiv\mathbf{r}_f(t_f)-\mathbf{r}_r(t_r), \tag{10}$$

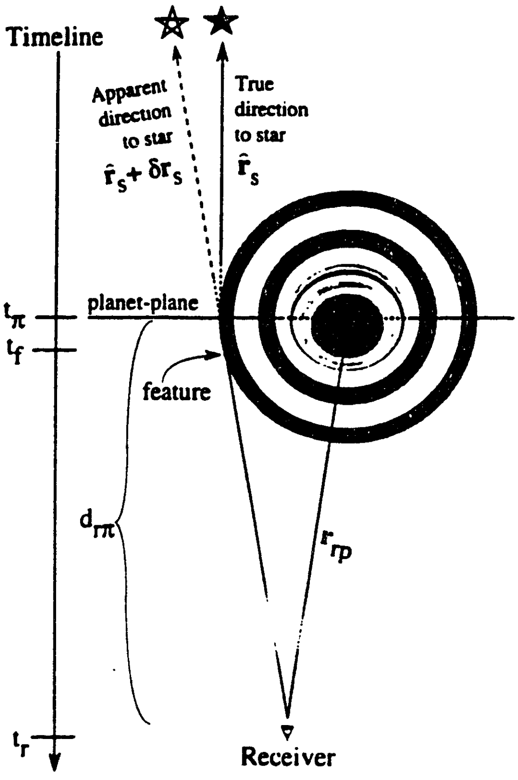

FIG. 11. Nonsimultaneous vector $\mathbf{r}_{rp}(t_r,t_\pi)$, illustrating the backdated times used in the geometric model. The planet position is calculated first at the time t_π, and this position is then corrected for the difference between t_π and t_f. The solar-system barycentric velocity of the planet is used in this calculation.

$$d_{\pi f}(t_r)=\mathbf{r}_{rf}(t_r,t_f)\cdot\hat{\mathbf{r}}_s-d_{r\pi}(t_r,t_\pi). \tag{11}$$

The direction to the star in the solar system barycentric frame is the sum of a unit vector, $\hat{\mathbf{r}}_s$, and a small correction term, $\delta\mathbf{r}_s$, due to the general relativistic bending of starlight by the gravitational field of the planet. The error introduced by approximating the bending effect of general relativity by an abrupt change of direction at the planet rather than the actual curved path is extremely small and therefore ignored. With these definitions, we write term (i) of Eq. (6) differently in two domains. The first domain applies when the feature is closer to the receiver than the planet plane, and the second applies when the feature is further. For $|\delta\mathbf{r}_s|<1$,

$$\mathbf{r}_f(t_f)-\mathbf{r}_r(t_r)$$
$$=\begin{cases}[d_{r\pi}(t_r,t_\pi)+d_{\pi f}(t_r)](\hat{\mathbf{r}}_s+\delta\mathbf{r}_s), & t_f>t_\pi,\\ [d_{r\pi}(t_r,t_\pi)+d_{\pi f}(t_r)]\hat{\mathbf{r}}_s+d_{r\pi}(t_r,t_\pi)\delta\mathbf{r}_s, & t_f<t_\pi.\end{cases} \tag{12}$$

The difference between these two cases, $d_{\pi f}(t_r)\delta\mathbf{r}_s$, amounts to less than 0.003 km for the present analysis—a small fraction of the 30 km deflection that would be experienced by a ray passing tangent to the limb of Saturn.

Since the second expression is more convenient algebraically, we shall always use it, independent of whether the feature is closer or further from the receiver than the planet plane.

In summary, we have made four approximations in our treatment of general relativity: (i) the bending occurs at a point, (ii) the second form of Eq. (12) is used even when $t_f > t_\pi$, (iii) $|\hat{\mathbf{r}}_s + \delta\mathbf{r}_s| \approx 1$, and (iv) $\mathbf{v}\cdot\hat{\mathbf{r}}_s \approx \mathbf{v}\cdot(\hat{\mathbf{r}}_s + \delta\mathbf{r}_s)$, where $\mathbf{v}$ is any vector. None of these approximations results in errors larger than a few meters for the present analysis.

Next we expand term (ii) of Eq. (6). We have previously defined t_π as the time that the occulted light arrives at the planet plane and, using our convention for "nonsimultaneous" vectors, we denote the difference in the vector $\mathbf{r}_{\mathrm{p}}$ between the times t_f and t_π by $\mathbf{r}_{\mathrm{pp}}$ (t_f, t_π), so that

$$\mathbf{r}_{\mathrm{pp}}(t_f,t_\pi) = \mathbf{r}_{\mathrm{p}}(t_\pi) - \mathbf{r}_{\mathrm{p}}(t_f). \tag{13}$$

We can now write term (ii) of Eq. (6) as

$$\begin{aligned}\mathbf{r}_{\mathrm{p}}(t_f) - \mathbf{r}_{\mathrm{r}}(t_r) &= \mathbf{r}_{\mathrm{p}}(t_\pi) - \mathbf{r}_{\mathrm{r}}(t_r) - \mathbf{r}_{\mathrm{pp}}(t_f,t_\pi),\\ &= \mathbf{r}_{\mathrm{rp}}(t_r,t_\pi) - \mathbf{r}_{\mathrm{pp}}(t_f,t_\pi).\end{aligned} \tag{14}$$

We substitute the expressions in Eqs. (12) and (14) for the corresponding terms in Eq. (6) and rearrange them into an order convenient for numerical evaluation. We find

$$\begin{aligned}\mathbf{r}_{\mathrm{pf}}(t_f) = &-\underbrace{\mathbf{r}_{\mathrm{rp}}(t_r,t_\pi)}_{\#1} + \underbrace{[d_{r\pi}(t_r,t_\pi) + d_{\pi f}(t_r)]\hat{\mathbf{r}}_s}_{\#2} + \underbrace{\mathbf{r}_{\mathrm{pp}}(t_f,t_\pi)}_{\#3}\\ &+ \underbrace{d_{r\pi}(t_r,t_\pi)\delta\mathbf{r}_s}_{\#4}.\end{aligned} \tag{15}$$

Our next task will be to convert each of the terms in Eq. (15) to an algebraic form that will be suitable for numerical evaluation with available ephemerides for the near-Earth receiver and the planet (*HST* and Saturn in this case). To do this, we must first define appropriate coordinate systems.

5.5 Coordinate Systems

We begin with the J2000.0 *XYZ* rectangular coordinate system (USNO 1992). In this system we specify the coordinates of a body at **r** either by its *X*, *Y*, and *Z* components, or by its distance from a specified origin (such as the center of the Earth) and its right ascension and declination, α and δ, respectively. The right ascension and declination are defined in terms of the projection of the unit vector $\hat{\mathbf{r}}$ to the body onto the unit vectors of the J2000.0 system, $\hat{\mathbf{X}}$, $\hat{\mathbf{Y}}$, and $\hat{\mathbf{Z}}$:

$$\begin{aligned}&\cos\alpha\cos\delta = \hat{\mathbf{r}}\cdot\hat{\mathbf{X}},\\ &\sin\alpha\cos\delta = \hat{\mathbf{r}}\cdot\hat{\mathbf{Y}},\\ &\sin\delta = \hat{\mathbf{r}}\cdot\hat{\mathbf{Z}}.\end{aligned} \tag{16}$$

Next we set up an *fgh* coordinate system in the shadow plane that originates at the center of the planet's shadow, with $\hat{\mathbf{f}}$ pointing in the direction of increasing right ascension. The axis $\hat{\mathbf{h}}$ lies in the direction of the star, $\hat{\mathbf{r}}_s$. Formally, the unit vectors of the *fgh* system are

$$\begin{aligned}&\hat{\mathbf{f}} = \frac{\hat{\mathbf{Z}}\times\hat{\mathbf{r}}_s}{|\hat{\mathbf{Z}}\times\hat{\mathbf{r}}_s|},\\ &\hat{\mathbf{g}} = \hat{\mathbf{r}}_s \times \frac{\hat{\mathbf{Z}}\times\hat{\mathbf{r}}_s}{|\hat{\mathbf{Z}}\times\hat{\mathbf{r}}_s|},\\ &\hat{\mathbf{h}} = \hat{\mathbf{r}}_s.\end{aligned} \tag{17}$$

We define another rectangular coordinate system—*uvw*—centered on the planet, with the *w* axis pointed in the direction of the star. The *u* axis is parallel to the major axes of apparent ring ellipses as seen from the geocenter, and the *v* axis is parallel to the minor axes of the apparent ring ellipses. The unit vectors of the *uvw* system are:

$$\begin{aligned}&\hat{\mathbf{u}} = \frac{\hat{\mathbf{r}}_n\times\hat{\mathbf{r}}_s}{|\hat{\mathbf{r}}_n\times\hat{\mathbf{r}}_s|},\\ &\hat{\mathbf{v}} = \hat{\mathbf{r}}_s \times \frac{\hat{\mathbf{r}}_n\times\hat{\mathbf{r}}_s}{|\hat{\mathbf{r}}_n\times\hat{\mathbf{r}}_s|},\\ &\hat{\mathbf{w}} = \hat{\mathbf{r}}_s.\end{aligned} \tag{18}$$

Finally we define an *xyz* coordinate system centered on the planet, with the *z* axis coincident with the north pole of the planet's ring plane, $\hat{\mathbf{r}}_n$. The *x* axis is the intersection of the planet's equatorial plane with the Earth's equatorial plane (J2000.0), with the positive portion at the ascending node for prograde revolution. The unit vectors defining the axes are:

$$\begin{aligned}&\hat{\mathbf{x}} = \frac{\hat{\mathbf{Z}}\times\hat{\mathbf{r}}_n}{|\hat{\mathbf{Z}}\times\hat{\mathbf{r}}_n|},\\ &\hat{\mathbf{y}} = \hat{\mathbf{r}}_n \times \frac{\hat{\mathbf{Z}}\times\hat{\mathbf{r}}_n}{|\hat{\mathbf{Z}}\times\hat{\mathbf{r}}_n|},\\ &\hat{\mathbf{z}} = \hat{\mathbf{r}}_n.\end{aligned} \tag{19}$$

In order to give the elements of the rotation matrices that are used to transform from one system to another, we define three auxiliary angles: B_s, the angle between the north pole of the planet and the *fg* plane $(-\pi/2 < B_s < \pi/2)$; P_s, the position angle of the projection of the north pole of the planet onto the *fg* plane, and U_s, the longitude of the projection of $\hat{\mathbf{h}}$ into the *xy* plane $(0 < P_s,\ U_s < 2\pi)$. We use the subscript "s" to remind us that these angles are defined in terms of the star position, rather than the usual definition in terms of the position of the planet. P_s is measured $\hat{\mathbf{g}}\rightarrow\hat{\mathbf{f}}$, and U_s is measured $\hat{\mathbf{x}}\rightarrow\hat{\mathbf{y}}$. These angles can be expressed in terms of the celestial coordinates of the star and north pole of the planet:

$$\begin{aligned}\sin B_s &= -\hat{\mathbf{h}}\cdot\hat{\mathbf{z}}\\ &= -\hat{\mathbf{r}}_n\cdot\hat{\mathbf{r}}_s = -\sin\delta_n\sin\delta_s\\ &\quad -\cos\delta_n\cos\delta_s\cos(\alpha_s-\alpha_n),\end{aligned} \tag{20}$$

$$
\begin{aligned}
\cos B_s \cos P_s &= \hat{\mathbf{g}} \cdot \mathbf{z} \\
&= \sin \delta_n \cos \delta_s \\
&\quad - \cos \delta_n \sin \delta_s \cos (\alpha_s - \alpha_n), \\
\cos B_s \sin P_s &= \hat{\mathbf{f}} \cdot \hat{\mathbf{z}} = -\cos \delta_n \sin (\alpha_s - \alpha_n),
\end{aligned} \tag{21}
$$

$$
\begin{aligned}
\cos B_s \cos U_s &= \hat{\mathbf{x}} \cdot \hat{\mathbf{w}} = \cos \delta_s \sin (\alpha_s - \alpha_n), \\
\cos B_s \sin U_s &= \hat{\mathbf{y}} \cdot \hat{\mathbf{w}} \\
&= \sin \delta_s \cos \delta_n - \cos \delta_s \sin \delta_n \cos (\alpha_s - \alpha_n).
\end{aligned} \tag{22}
$$

Next we write expressions for the rotation matrices needed to convert vectors between the *XYZ*, *fgh*, *uvw*, and *xyz* coordinate systems. If α_s and δ_s are the right ascension and declination of the star, defined by equations analogous to Eq. (16), then the rotation matrix for converting a vector to *fgh* from *XYZ*, J2000.0 is $\mathbf{R}_{XYZ-fgh}$ and is given by

$$
\mathbf{R}_1 \equiv \mathbf{R}_{XYZ-fgh}
$$

$$
= \begin{bmatrix} \hat{\mathbf{f}} \cdot \hat{\mathbf{X}} & \hat{\mathbf{f}} \cdot \hat{\mathbf{Y}} & \hat{\mathbf{f}} \cdot \hat{\mathbf{Z}} \\ \hat{\mathbf{g}} \cdot \hat{\mathbf{X}} & \hat{\mathbf{g}} \cdot \hat{\mathbf{Y}} & \hat{\mathbf{g}} \cdot \hat{\mathbf{Z}} \\ \hat{\mathbf{h}} \cdot \hat{\mathbf{X}} & \hat{\mathbf{h}} \cdot \hat{\mathbf{Y}} & \hat{\mathbf{h}} \cdot \hat{\mathbf{Z}} \end{bmatrix}
$$

$$
= \begin{bmatrix} -\sin \alpha_s & \cos \alpha_s & 0 \\ -\cos \alpha_s \sin \delta_s & -\sin \alpha_s \sin \delta_s & \cos \delta_s \\ \cos \alpha_s \cos \delta_s & \sin \alpha_s \cos \delta_s & \sin \delta_s \end{bmatrix}. \tag{23}
$$

The rotation matrix for converting the *f* and *g* components in the shadow plane to its *u* and *v* components in the planet plane is

$$
\mathbf{R}_2 \equiv \mathbf{R}_{fg-uv} = \begin{bmatrix} \hat{\mathbf{u}} \cdot \hat{\mathbf{f}} & \hat{\mathbf{u}} \cdot \hat{\mathbf{g}} \\ \hat{\mathbf{v}} \cdot \hat{\mathbf{f}} & \hat{\mathbf{v}} \cdot \hat{\mathbf{g}} \end{bmatrix} = \begin{bmatrix} \cos P_s & -\sin P_s \\ \sin P_s & \cos P_s \end{bmatrix}. \tag{24}
$$

We shall also use the inverse of $\mathbf{R}_2$, $\mathbf{R}_2^{-1}$, to convert from the planet plane to shadow plane.

The rotation matrix for conversion from *uvw* coordinates to the *xyz* system, $\mathbf{R}_{uvw-xyz}$, is given by

$$
\mathbf{R}_3 \equiv \mathbf{R}_{uvw-xyz}
$$

$$
= \begin{bmatrix} \hat{\mathbf{x}} \cdot \hat{\mathbf{u}} & \hat{\mathbf{x}} \cdot \hat{\mathbf{v}} & \hat{\mathbf{x}} \cdot \hat{\mathbf{w}} \\ \hat{\mathbf{y}} \cdot \hat{\mathbf{u}} & \hat{\mathbf{y}} \cdot \hat{\mathbf{v}} & \hat{\mathbf{y}} \cdot \hat{\mathbf{w}} \\ \hat{\mathbf{z}} \cdot \hat{\mathbf{u}} & \hat{\mathbf{z}} \cdot \hat{\mathbf{v}} & \hat{\mathbf{z}} \cdot \hat{\mathbf{w}} \end{bmatrix}
$$

$$
= \begin{bmatrix} -\sin U_s & \sin B_s \cos U_s & \cos B_s \cos U_s \\ \cos U_s & \sin B_s \sin U_s & \cos B_s \sin U_s \\ 0 & \cos B_s & -\sin B_s \end{bmatrix}. \tag{25}
$$

We conclude this section by noting that the direction to the ring-plane pole may vary with time, due to planetary precession. For the time scales of interest here, we can approximate this precession by its linear terms in right ascension and declination. If $\dot{\alpha}_n$ is the rate of polar motion in right ascension, $\dot{\delta}_n$ the rate of polar motion in declination, and t_n the reference epoch for the position of the pole, then we have

$$
\begin{aligned}
\alpha_n &= \alpha_n(t) = \alpha_n(t_n) + \dot{\alpha}_n(t - t_n), \\
\delta_n &= \delta_n(t) = \delta_n(t_n) + \dot{\delta}_n(t - t_n).
\end{aligned} \tag{26}
$$

Similarly, if the occulted star exhibits significant proper motion, we could introduce this in an analogous manner.

5.6 *Corrections to Time and Positions*

When evaluating the terms in Eq. (15) to find the feature radius, we find that all are not readily available, so we must write these terms as functions of the information we actually use to reduce the data. In this section we consider three correction terms that improve the connection of our model to the time and position measurements used for the data reduction. The effects included are: (i) a constant offset between the planetary ephemeris and the actual planetary position; (ii) a difference between the catalog star position and the actual star position; and (iii) a constant offset between the time scale used as the argument for the occultation light curve (e.g., *HST* clock) and UTC. An example of an effect not considered in our model is an error in the *HST* ephemeris. (To a great extent, however, an in-track error in the *HST* ephemeris would mimic an error in the *HST* clock.)

To evaluate the effect produced by a difference between the ephemeris position of the planet and its actual position, we define a vector $\mathbf{r}_{pp'}(t_f)$ that represents the difference between the ephemeris position and the planetary position

$$
\mathbf{r}_{pp'}(t_f) \equiv \mathbf{r}_{p'}(t_f) - \mathbf{r}_p(t_f). \tag{27}
$$

If we assume that this error is a constant offset, then

$$
\mathbf{r}_{pp'}(t_f)\,|_{fgh} \equiv \begin{bmatrix} f_0 \\ g_0 \\ h_0 \end{bmatrix} = \mathbf{R}_1 \mathbf{r}_{pp'}(t_f)\,|_{XYZ} = \mathbf{R}_1 \begin{bmatrix} X_{pp'} \\ Y_{pp'} \\ Z_{pp'} \end{bmatrix}. \tag{28}
$$

Analogously, we define $\hat{\mathbf{r}}_{ss'}$ as the difference between the catalog star position, $\hat{\mathbf{r}}_{s'}$, and actual star position, $\hat{\mathbf{r}}_s$. It will be convenient to express the difference as offsets in right ascension, α_0, and declination, δ_0:

$$
\begin{aligned}
\alpha_s &= \alpha_{s'} - \alpha_0, \\
\delta_s &= \delta_{s'} - \delta_0.
\end{aligned} \tag{29}
$$

Finally we allow the clock time used for the data recording, t_c, to have a constant offset, t_0, from the desired time in UTC, t:

$$
t = t_c - t_0. \tag{30}
$$

The implication of Eq. (30) is that all feature occultation times taken from the light curve are shifted by t_0.

5.7 *Evaluation of Sky-Plane Terms*

For the terms in Eq. (15), we know (or can calculate from known quantities) the planet-plane coordinates of the occulting ring feature, but not the coordinate perpendicular to this plane, $w_f(t_f)$. However, we shall be modeling the occulting features as circular rings, lying in the equatorial plane of the planet. This will allow us to determine $w_f(t_f)$ from planet-plane coordinates of the feature and the direction of the planet's ring-plane pole. So our plan for evaluation is as follows: (i) evaluate the fg components of the terms in Eq. (15), (ii) project the fg components from the shadow plane to the planet-plane to find the uv components of the occulting feature (this procedure involves only the correction for general relativity bending), (iii) assume the occulting feature lies in the equatorial plane of the planet, and find w from the planet-plane coordinates, and (iv) convert uvw to xyz from which we calculate the feature longitude and radius.

Except for term #1 given by Eq. (15), we require prior knowledge of $w_f(t_f)$ for evaluation, so we must resort to an iterative procedure in order to arrive at a solution. For our iteration procedure we begin with the loop index $i=1$, and for the ith iteration we denote the value of a quantity q by $q_{(i)}$. We begin with the prior value $w_{f(0)}=0$. Then we find the distance between the occulting feature and planet plane. Within our approximations for general relativity, this lies along the w axis:

$$d_{\pi f(i)}(t_r)=w_{f(i-1)}(t_f). \tag{31}$$

Knowing the light travel distance, we can now calculate the feature occultation time, $t_{f(i)}$:

$$t_{f(i)}=t_\pi-\frac{d_{\pi f(i)}(t_r)}{c}. \tag{32}$$

Now we can find the f and g components of term #3 of Eq. (15), the light travel correction from the feature to the planet center. We calculate these from the solar-system barycentric velocity of the planet (including effects of its satellite motions) $[\dot{X}_p(t_\pi)$, $\dot{Y}_p(t_\pi)$, and $\dot{Z}_p(t_\pi)]$, using a linear approximation

$$\mathbf{r}_{pp(i)}(t_f,t_\pi)\,|_{fgh}=\begin{bmatrix} f_{pp(i)}(t_f,t_\pi)\\ g_{pp(i)}(t_f,t_\pi)\\ h_{pp(i)}(t_f,t_\pi)\end{bmatrix}$$

$$=(t_\pi-t_{f(i)})\mathbf{R}_1\begin{bmatrix}\dot{X}_p(t_\pi)\\ \dot{Y}_p(t_\pi)\\ \dot{Z}_p(t_\pi)\end{bmatrix}. \tag{33}$$

We can now write complete equations for the f and g coordinates of the feature. The terms have been grouped in the equations below according to their parent terms in Eq. (15):

$$f_{pf(i)}(t_r)=\underbrace{-[f_{rp'}(t_r,t_\pi)-f_0]}_{\#1}+\underbrace{f_{pp(i)}(t_f,t_\pi)}_{\#3}+\underbrace{f_{s(i)}(t_\pi)}_{\#4}, \tag{34}$$

$$g_{pf(i)}(t_r)=\underbrace{-[g_{rp'}(t_r,t_\pi)-g_0]}_{\#1}+\underbrace{g_{pp(i)}(t_f,t_\pi)}_{\#3}+\underbrace{g_{s(i)}(t_\pi)}_{\#4}. \tag{35}$$

In order to evaluate Eqs. (34) and (35) we need an expression for the general relativity bending terms, $f_{s(i)}(t_\pi)$ and $g_{s(i)}(t_\pi)$. Finding these requires a second iterative loop, internal to the first. The general relativistic bending equations correct to second order are given by Hu93 [their Eqs. (13)–(14)]. First we define $r_{f,uv}$ as the radius of the occulting feature, projected into the planet plane:

$$r_{f,uv(i)}(t_f)=\sqrt{u^2_{f(i)}(t_f)+v^2_{f(i)}(t_f)}. \tag{36}$$

In the equations below, J_2 is the coefficient of the second-order gravitational harmonic and R_p is the equatorial radius of the planet. Using Eqs. (13) and (14) of Hu93, we write the equations for the general relativity bending in our notation:

$$\begin{bmatrix} f_{s(i)}(t_f)\\ g_{s(i)}(t_f)\end{bmatrix}=\frac{4G\mathscr{M}_p d_{r\pi}(t_r,t_\pi)}{c^2 r^2_{f,uv(i)}(t_f)}\mathbf{R}_2^{-1}\begin{bmatrix} u_{f(i)}(t_f)\left\{1-J_2R_p^2\cos^2 B_s\dfrac{3v^2_{f(i)}(t_f)-u^2_{f(i)}(t_f)}{r^4_{f,uv(i)}(t_f)}\right\}\\ v_{f(i)}(t_f)\left\{1+J_2R_p^2\cos^2 B_s\dfrac{3u^2_{f(i)}(t_f)-v^2_{f(i)}(t_f)}{r^4_{f,uv(i)}(t_f)}\right\}\end{bmatrix}, \tag{37}$$

$$\begin{bmatrix} u_{f(i)}(t_f)\\ v_{f(i)}(t_f)\end{bmatrix}=\mathbf{R}_2\begin{bmatrix} f_{pf(i)}(t_f)\\ g_{pf(i)}(t_f)\end{bmatrix}. \tag{38}$$

The second loop is an iterative procedure to find a self-consistent solution of Eqs. (34)–(38). Once this is complete, we proceed with the primary loop. The next step is to update the value of $w_{f(i)}(t_f)$. We calculate it by assuming that the occulting feature lies in the equatorial plane of the planet. Then:

$$w_{f(i)}(t_f)=v_{f(i)}(t_f)\cot B_s. \tag{39}$$

Finally we test for convergence of our primary loop. To do this, we calculate the change in planet-plane radius since the previous iteration:

$$\varepsilon_{(i)}=|r_{f,uv(i)}(t_f)-r_{f,uv(i-1)}(t_f)|. \tag{40}$$

If $\varepsilon_{(i)}$ is not smaller than a specified value, we return to Eq. (31) and repeat the loop. On the other hand if the convergence criterion is satisfied, we make the assignments $u_f(t_f)=u_{f(i)}(t_f)$, $v_f(t_f)=v_{f(i)}(t_f)$, $w_f(t_f)=w_{f(i)}(t_f)$ and exit the loop here.

5.8 Feature Radius and Longitude

To find the orbital longitude of the point where the occulted starlight intercepted the ring feature, we first calculate $x(t_f)$, $y(t_f)$, and $z(t_f)$ with Eq. (25):

$$\mathbf{r}_{pf}|_{xyz} = \mathbf{R}_3 \mathbf{r}_{pf}|_{uvw}. \tag{41}$$

Next we write an expression for the magnitude of the feature radius:

$$\begin{aligned} r_{pf}(t_f) &\equiv |\mathbf{r}_{pf}(t_f)| \\ &= \sqrt{x_f^2(t_f) + y_f^2(t_f) + z_f^2(t_f)}, \\ &= \sqrt{u_f^2(t_f) + v_f^2(t_f) + w_f^2(t_f)}. \end{aligned} \tag{42}$$

For the special case of rings that are not inclined relative to the planet's equatorial plane, this simplifies to

$$r_{pf}(t_f) = \sqrt{u_f^2(t_f) + v_f^2(t_f) \csc^2 B_s}. \tag{43}$$

The orbital longitude, $\theta(t_r)$, is the angle $x \rightarrow y$ in the equatorial plane of the planet. The zero point for orbital longitude is the ascending node of the intersection of the Earth's equatorial plane for J2000.0 with the planet's ring plane:

$$\begin{aligned} \sin \theta(t_f) &= y_f(t_f)/r_{pf}(t_f), \\ \cos \theta(t_f) &= x_f(t_f)/r_{pf}(t_f). \end{aligned} \tag{44}$$

The only approximations involved in deriving the final results expressed in Eqs. (42)–(44) are (i) omission of special relativity, (ii) our approximations for general relativistic bending, (iii) the linear approximation for the solar-system barycentric velocity of the planet, and (iv) the finite number of iterations used to calculate $u_f(t_f)$, $v_f(t_f)$, and $w_f(t_f)$.

5.9 Model Times and Radii

In order to fit feature times and radii to a model, we shall need a procedure for calculating a "model radius" and "model time" that corresponds to each observed feature radius, $r_{pf}(t_f)$, and feature occultation time, t_f. For circular features, the model radius, $r_m(t_f)$, is just the semimajor axis (radius) of the feature, a_f. The model time, however, is that time at which the star would have been occulted by a feature at the model radius, a_f, rather than the time t_f, when it was occulted by the "observed radius" of the feature, $r_{pf}(t_f)$. We represent the time derivative of the observed radius by $\dot{r}_{pf}(t_f)$. Then the model time, t_m, is given by the equation

$$t_m = t_f - \frac{r_{pf}(t_f) - a_f}{\dot{r}_{pf}(t_f)}. \tag{45}$$

6. NUMERICAL IMPLEMENTATION OF MODEL FITTING

Equally important with an explicit algebraic development of the ring-orbit geometry are specifications of the input parameters and the numerical procedures used to fit the model to the feature times. In this section we present the sources for the ephemerides and all other numerical input (summarized in Table 4); also we describe our numerical implementation of the algebra of the previous section into a least-squares fitting procedure. All the calculations to be described were implemented in *Mathematica* (Wolfram 1991). The "notebook" front end ran on various Macintosh computers, which were connected to a "kernel" on one of several UNIX workstations in order to increase the speed of computation. Although numerical calculations carried out with *Mathematica* are not as fast as the inherent speed of a given computer, its capability for symbolic manipulation and the extensive documentation provided by a notebook proved of great benefit in working with this complex model.

6.1 Calculating Model Times and Radii

For our *HST* ephemeris, we used the "definitive ephemerides" provided by the Flight Dynamics Facility at NASA's Goddard Space Flight Center; these are available through the *HST* Archives at Space Telescope Science Institute (Baum 1993). The ephemerides consist of binary files giving spacecraft coordinates (X_{er}, Y_{er}, Z_{er}) and velocity components in the J2000.0 frame. They are tabulated at approximate minute intervals.

In order to perform a joint fit of these data with those from the 28 Sgr event, we needed a method for including the coordinates of ground-based observers in our calculations. We converted observatory locations into geocentric "observer ephemerides," which is the form most easily used with the approach adopted here. We used the geodetic coordinates of each observatory provided in Table I of F93. These were converted to geocentric coordinates using the equatorial radius and flattening values for the Earth given in Table 4, then nutated and precessed to find J2000.0 coordinates versus time $[X_{er}(t), Y_{er}(t), Z_{er}(t)]$. The conversion used does not include geodetic datum offsets or altitude corrections because the values of these quantities were uncertain; nor does it include the small effects (up to 0.3 arcsec or 0.009 km at surface of Earth) of polar motion.

The Saturn and Earth ephemerides used in these analyses were generated for us by L. Wasserman from the JPL DE-130 (Standish 1990). They are solar-system barycentric, geometric ephemerides for the Saturn system barycenter and for the Earth center, which we converted from B1950.0 to J2000.0 with the matrix X(0) given by Eq. (5.711-4) in Standish *et al.* (1992). We chose this matrix from the various methods available in the literature for precession between these two epochs, because it reproduced the conversion of test points in the DE-130 ephemeris to the DE-202 ephemeris. The ephemerides, tabulated at 10 min intervals in TDB, supplied (X_b, Y_b, Z_b), (X_e, Y_e, Z_e) and their time derivatives. The ephemerides for eight Saturnian satellites (see Table 4) were supplied by the Navigation Ancillary Information Facility (NAIF) at the Jet Propulsion Laboratory (JPL) (Acton 1990).

The position of GSC 6323-01396 is given in Table 4 in FK4 J2000.0. For use in the geometric modeling, the star's position was converted from FK4 to FK5 (Green 1985).

TABLE 4. Parameters always fixed in model fits.

Parameter	Value	Reference
Physical Constants		
speed of light, c (km s^{-1})	299792.458	Seidelmann (1992)
Receiver Coordinates		
Ground-based observatories		Table I of F93
HST ephemeris	file "PBA20000R.ORX"	Space Telescope Science Institute
Earth and Moon		
Barycenter ephemeris	DE-130	Standish (1990)
Mass ratio, M_e/M_m	81.300587	DE-130 (Standish 1990)
Earth radius (km)	6378.137	MERIT 1983 (Archinal 1992)
Earth flattening	1/298.257	MERIT 1983 (Archinal 1992)
Saturn system		
Barycenter ephemeris	DE-130	Standish (1990)
Satellite ephemerides	file "SAT018H.BSP"	NAIF (Acton 1990)
$J_2R_p{}^2$ (km^2)	59316335.9433	Table VII of F93
$GM_{\rm system}$ (km^3 s^{-2})	37940626.075	(W. M. Owen, private communication)
$GM_{\rm p}$ (km^3 s^{-2})	37931246.375	derived from system and satellite masses
$GM_{\rm Mimas}$ (km^3 s^{-2})	2.5	(W. M. Owen, private communication)
$GM_{\rm Enceladus}$ (km^3 s^{-2})	5.6	(W. M. Owen, private communication)
$GM_{\rm Tethys}$ (km^3 s^{-2})	44.1	(W. M. Owen, private communication)
$GM_{\rm Dione}$ (km^3 s^{-2})	77.3	(W. M. Owen, private communication)
$GM_{\rm Rhea}$ (km^3 s^{-2})	154.1	(W. M. Owen, private communication)
$GM_{\rm Titan}$ (km^3 s^{-2})	8977.7	(W. M. Owen, private communication)
$GM_{\rm Hyperion}$ (km^3 s^{-2})	1.	(W. M. Owen, private communication)
$GM_{\rm Iapetus}$ (km^3 s^{-2})	117.4	(W. M. Owen, private communication)
Stars		
28 Sgr		
FK4/B1950.0	$\alpha_{s'} = 18^{h}\,43^{m}\,19^{s}.7946475$	F93
	$\delta_{s'} = -22^{\circ}\,26'\,46''.88424$	
FK5/J2000.0	$\alpha_{s'} = 18^{h}\,46^{m}\,20^{s}.5958671$	derived from the B1950.0 position
	$\delta_{s'} = -22^{\circ}\,23'\,32''.0525118$	
proper motion	0	approximation for this reduction
parallax	0	approximation for this reduction
GSC6323-01396		
FK4/J2000.0	$\alpha_{s'} = 20^{h}\,10^{m}\,30^{s}.35$	Bosh and McDonald (1992)
	$\delta_{s'} = -20^{\circ}\,36'\,47''.6$	
FK5/J2000.0	$\alpha_{s'} = 20^{h}\,10^{m}\,30^{s}.4275$	derived from the FK4 position
	$\delta_{s'} = -20^{\circ}\,36'\,47''.6$	
proper motion	0	assumption
parallax	0	assumption
Transformations		
B1950.0->J2000.0	rotation with X(0)	Eq. (5.711-4) of Standish *et al.* (1992)
TDB -> UTC	function library "SPICELIB"	Acton (1990)
SOGS seconds -> MJD	programs "orx2eph" and "preph"	(J. W. Percival, private communication)
Precession of receiver	procedure on p. B18	USNO (1992)
Nutation of receiver	procedure on p. B20	USNO (1992)
geodetic->geocentric	Eq. (4.22-7)	Archinal (1992)

The B1950.0 astrographic position of 28 Sgr is given in F93, and is reproduced in Table 4. In addition, the J2000.0 position of 28 Sgr is given.

We chose Modified Julian Date (MJD) as our reference time scale. In order to convert the times in the Saturn ephemeris from TDB to MJD, we first converted to UTC using a routine provided by the NAIF (Acton 1990). The time scale for the occultation light curve was derived from the spacecraft clock, described by keywords in the data file header. In the early stages of these analyses, we found that the data descriptor keywords were not accurate. The "EXPSTRT" keyword contained the value for the *predicted* start time, not the actual start time. In our case, these differed by about 24.5 s. In more recent data files, the keywords have been corrected, and the "EXPSTART" (note the addition of an "A") keyword value correctly describes the UTC as calculated using the database calibration for the spacecraft clock.

Another class of numerical input needed to calculate model times and radii consists of those parameters that we shall ultimately determine through least-squares fitting: ring-plane pole position, feature radii, clock offsets, star position offsets, and planet ephemeris offsets. The initial values of these quantities were generally taken from F93. Following the convention of F93, we use UTC 1980 November 12 23:46:32 (MJD 44555.99065) as the epoch for the pole position when considering pole precession, but we express the coordinates of the pole in the equator and equinox of J2000.0.

The final numerical ingredient in our model calculation is the set of feature occultation times. For this work, we used only those features with presumed-circular orbits

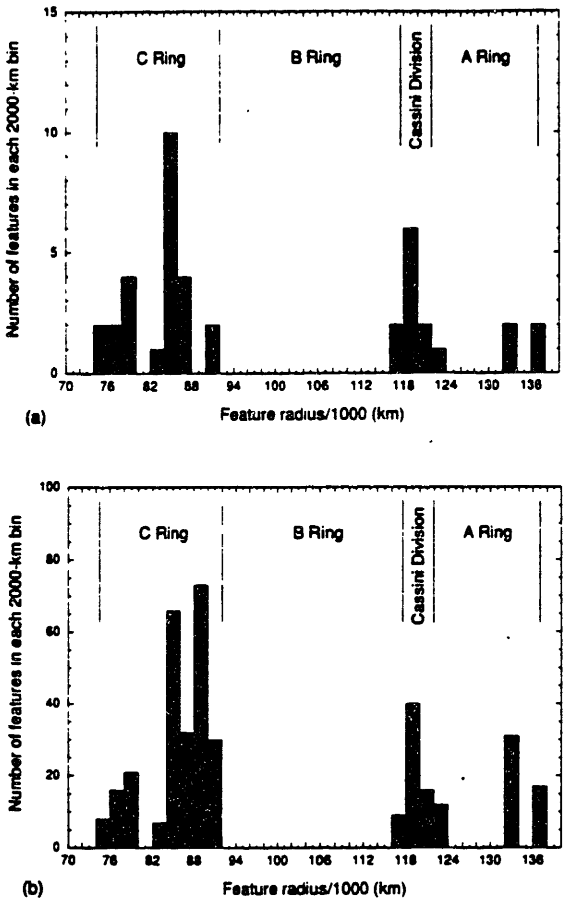

FIG. 12. Distribution of features with ring plane radius. Number of features in each 2000 km bin is plotted against feature radius for two analyses: (a) GSC 6323-01396 and (b) GSC 6323-01396 and 28 Sgr.

(F93), excluding B ring features as did F93. The measurements of the times for these features in the 28 Sgr data are described in F93 and Hu93. For the *HST* data, we measured the times of ring features in a manner consistent with the measurements of the Voyager and 28 Sgr data (see Sec. 4 above). This produced a total of 25 separate features measured in the *HST* data for use in the ring orbit fits. Fifteen of these occulted the star twice, for a total of 40 measurements of presumed-circular features. Five additional features are included in the 28 Sgr measurements, but were not crossed during the *HST* observations.

Figure 12 shows the distribution in ring-plane radius of the (a) GSC 6323-01396 features and (b) the combined GSC 6323-01396 and 28 Sgr features. These features span the area from the C ring to the outer A ring, with a gap in the B ring due to its high optical thickness. A total of 378 event-time measurements for 30 features were used in our geometric models that combined the 28 Sgr and *HST* data sets.

Since the speed of the model calculation proved to be an issue, the sky-plane calculation of feature radii is broken into two parts. In the first part, we calculate term #1 of Eq. (15), $\mathbf{r}_{rp}(t_f,t_\pi)$ for each observed feature time. Since this part of the calculation has to be done only once, the results are then stored to a file for later use in fitting the model. In the second step, we read in this file and perform the fit. Splitting the calculation in this way introduces a small approximation because the value of $\mathbf{r}_{rp}(t_f,t_\pi)$ depends on knowledge of the time t_π, which in turn depends on the star position. Therefore, if the star position is changed later in the calculation (when fitting for a star position offset), this previous determination of t_π is no longer exact.

Because the value of $\mathbf{r}_{rp}(t_f,t_\pi)$ is calculated at the specific time t_f, any change in this observed time when finding the model time requires a change in the value of the quantity. To calculate the values of time-variable quantities, we began by using a Taylor series to second order. We found no significant difference between second- and first-order series, so the first-order series was used thereafter.

As noted above, there are two iteration loops in the model: one for $w_{f(f)}(t_f)$, the component of the feature vector in the direction of the star, and one to determine the magnitude of bending due to general relativity. For both of these iteration loops, the convergence criterion was a change in the quantity of less than 0.25 km.

6.2 *Fitting the Model*

For modeling the geometry of this occultation, we used standard nonlinear least-squares fitting techniques (Press *et al.* 1988). Our procedure employs numerical derivatives, and model parameters can be free to vary or held fixed for a given fitting sequence. The model fits are iterated until the change in all fitted parameters is well below 0.001 of their formal error. Our code allows minimizing the sum of squared residuals either in time or radius. For the 28 Sgr data, it makes little difference whether the fit is done in time or radius, since the apparent stellar track through the ring system is nearly linear, so that most time and radius residuals are proportional to each other. However, for the looping path of the *HST* occultation (Fig. 4), time and radius residuals are not proportional for cases where the apparent path of the star approaches tangency to the features. Hence, fits in time and radius can produce significantly different fitted parameters.

If the errors in the feature times followed a Gaussian distribution, then minimizing the sum of squared time residuals would be the correct procedure. However, if the feature times have other types of errors (such as noncircular orbits for some features), then fitting in radius might be more appropriate. Hence we have tried both approaches. For the fits in radius, we calculate the "observed radius" from the feature time and all other input parameters, following the procedure described in Sec. 5 that culminates with Eq. (42). The model radius for circular features is just its semimajor axis, *a*, as described earlier. For fits in time, the observed time is t_f, and the model time is t_m, given by Eq. (45).

TABLE 5. Sample values of ephemerides.

TDB	Position (km)			Velocity (km s^{-1})		
Solar System Barycenter -> Earth Center						
	X_e	Y_e	Z_e	$\dot{X}_e$	$\dot{Y}_e$	$\dot{Z}_e$
1991 10 3 0 0 0	148008535.410	22715784.937	9836798.495	-5.339123	26.875007	11.653409
1991 10 3 5 0 0	147911481.540	23199394.582	10046498.750	-5.444636	26.859338	11.646592
1991 10 3 10 0 0	147812528.660	23682718.898	10256074.851	-5.550124	26.843303	11.639614
1991 10 3 15 0 0	147711677.251	24165751.301	10465523.891	-5.655583	26.826903	11.632474
Earth Center -> HST						
	X_{er}	Y_{er}	Z_{er}	$\dot{X}_{er}$	$\dot{Y}_{er}$	$\dot{Z}_{er}$
1991 10 3 0 0 0	-6050.361	2351.855	2543.274	-1.744000	-6.991000	2.314000
1991 10 3 5 0 0	-5770.992	-2077.364	3317.219	2.593195	-7.106929	0.068888
1991 10 3 10 0 0	-3127.246	-5657.543	2623.740	5.845894	-4.261192	-2.203911
1991 10 3 15 0 0	786.067	-6893.357	769.570	6.689000	0.366000	-3.502000
Solar System Barycenter -> Saturn System Barycenter						
	X_b	Y_b	Z_b	$\dot{X}_b$	$\dot{Y}_b$	$\dot{Z}_b$
1991 10 3 0 0 0	868965562.251	-1103544951.016	-493136507.485	7.319746	5.307125	1.877008
1991 10 3 5 0 0	869097312.007	-1103449415.572	-493102718.130	7.319116	5.307924	1.877365
1991 10 3 10 0 0	869229050.434	-1103353865.738	-493068922.346	7.318487	5.308724	1.877722
1991 10 3 15 0 0	869360777.533	-1103258301.517	-493035120.132	7.317857	5.309523	1.878079
Saturn System Barycenter -> Saturn Center						
	X_{bp}	Y_{bp}	Z_{bp}	$\dot{X}_{bp}$	$\dot{Y}_{bp}$	$\dot{Z}_{bp}$
1991 10 3 0 0 0	293.330	-72.329	-19.548	0.000327	0.001239	-0.000111
1991 10 3 5 0 0	298.348	-49.723	-21.482	0.000228	0.001272	-0.000104
1991 10 3 10 0 0	301.504	-26.601	-23.288	0.000121	0.001295	-0.000096
1991 10 3 15 0 0	302.669	-3.174	-24.943	0.000008	0.001305	-0.000087

6.3 Numerical Tests

We performed extensive numerical calculations to establish that our procedures yield the same numerical results as those used by F93. The first test was to check the numerical values of input ephemerides and to reproduce the numerical results described by F93, as in their Tables B-I and B-II. Since our respective calculations are carried out somewhat differently, some of the intermediate results could not be compared. We did compare ephemeris values (positions and velocities of Earth, Saturn barycenter, and barycenter offset due to satellites), observer positions, backdated time at feature crossing, magnitude of general relativity bending, ring radius and longitude. The agreement was usually within 0.003 km, with no discrepancies greater than 0.014 km. To facilitate tests of future analyses of these *HST* data, we have provided some check points for the *HST* and other ephemerides in Table 5 and a breakdown of our sky-plane calculations in Table 6.

The next numerical test was to fit the portion of the 28 Sgr data set used by F93. We fixed ring radii and clock offsets at the F93 values (note that our "offset time," t_0, to be subtracted from the recorded clock time, is the negative of the "station time offsets," to be added to the recorded clock time, used by F93). Then we fit for pole right ascension and declination and the ephemeris offsets. When we do this fit with B1950.0 ephemerides, our results agree with those of Fit 5 in Table VIII of F93 within 0″.0003 (0.006 of the formal error). We perform the same fit with J2000.0 ephemerides (Fit 1 in Table 7). Comparing this pole position with that obtained with the B1950.0 ephemerides and then converted to J2000.0 using the matrix procedure given in Table 4, we find agreement within 0″.0003 (0.007 of the formal error). Throughout our tests, we have found that the precession method we have adopted gives consistent results, independent of calculation epoch.

7. MODEL FITS TO THE OCCULTATION TIMES

Following the tests described in the previous section, we performed three types of fits: (i) fits to the 28 Sgr data, to determine the sensitivity of the solution to different assumptions than used by F93; (ii) fits with only the *HST* GSC 6323-01396 data set, to determine the overall usefulness of a single *HST* data set; and (iii) joint fits of the HST GSC 6323-01396 and the 28 Sgr data, to establish the pole position and radius scale for Saturn's rings independent from Voyager data. The fit results we present here were chosen to summarize what we learned from a much larger number of fits that were carried out.

7.1 A Further Test of the 28 Sgr Data

As noted by F93, model fits with only the 28 Sgr data yield a pole position that differs by several formal errors from the pole position determined by fits to both the 28 Sgr and Voyager data (see Fig. 13). Although the pole position adopted by F93 yields a feature radius scale that agrees with radii of bending waves determined from dynamical considerations, the failure of the 28 Sgr data set to stand on its own leads one to be suspicious of how this data set might be influencing the joint solution with Voyager. We note that the time residuals for their adopted solution given in Fig. 14 of F93 show a bimodal distribution for Palomar, systematically negative residuals for McDonald, and systematically positive residuals for the IRTF. This solution

TABLE 6. Numerical values for certain cases.

Quantity	Symbol	28 Sgr, MCD Test Case	GSC6323-01396, HST Test Case
Pole position[a], J2000 (deg)	α_n, δ_n	40.587582 83.534223	40.586206 83.534078
Star position, J2000 (deg)	$\alpha_{s'}, \delta_{s'}$	281.5858161129 -22.3922368088	302.6267812500 -20.6132222222
Planet ephemeris offset (km)	f_o, g_o	0.0 0.0	0.0 0.0
Star position offset (arcsec)	α_o, δ_o	0.164221 -0.125531	0.956999 -0.107345
Clock offset (s)	t_o	-0.077274	0.0
Feature name		38	23
Clock time (UTC)	t_c	1989 7 3 8 41 12.4041	1991 10 3 2 2 21.5950
Received time (UTC)	t_r	1989 7 3 8 41 12.4814	1991 10 3 2 2 21.5950
Earth center (km)	$\mathbf{r}_e(t_r)\|_{fgh}$	2135192.637357 -1477916.428756 151969338.341209	136973906.170086 30580115.083202 53116337.204003
Receiver relative to earth center (km)	$\mathbf{r}_{er}(t_r)\|_{fgh}$	2420.217832 4872.313198 3322.601021	-4422.527537 3504.074565 4106.602768
Time at planet plane (UTC)	t_π	1989 7 3 7 26 10.7821	1991 10 3 0 42 55.2547
Planet system barycenter (km)	$\mathbf{r}_b(t_\pi)\|_{fgh}$	2061844.80[illegible] -1475252.[illegible] 1501525132.69[illegible]	136880668.806791 30586930.561072 1482033121.315271
Planet center relative to system barycenter (km)	$\mathbf{r}_{bp}(t_\pi)\|_{fgh}$	-222.297581 -52.003695 -155.623141	210.465321 57.771464 209.921215
Velocity of planet center relative to solar system barycenter (km s^{-1})	$\dot{\mathbf{r}}_p(t_\pi)\|_{fgh}$	9.142927 0.345519 -0.085487	9.027025 1.572242 -1.151416
Planet center relative to receiver (km)	$\mathbf{r}_{rp}(t_r, t_\pi)\|_{fgh}$	-75990.345811 -2260.730651 1349552316.127516	-88604.370437 3369.174768 1428912887.429715
Time at feature (UTC)	t_f	1989 7 3 7 26 10.7081	1991 10 3 0 42 55.1927
Light travel correction, feature to planet plane (km)	$\mathbf{r}_{pp}(t_f, t_\pi)\|_{fgh}$	0.676636 0.025571 -0.006327	0.559325 0.097418 -0.071343
Feature coordinates in shadow plane (km)	$f_f(t_r), g_f(t_r)$	75991.022447 2260.756221	88604.929762 -3369.077350
Shadow plane radius (km)	$\sqrt{f_f^2 + g_f^2}$	76024.644105	88668.958832
Magnitude of GR bending (km)	$f_s(t_\pi), g_s(t_\pi)$	30.181259 0.966742	27.353449 -1.010997
Feature coordinates at planet plane (km)	$\mathbf{r}_{pf}(t_f)\|_{uvw}$	75321.383569 10536.981586 22186.586431	88397.968737 7268.992081 18575.480601
Planet plane radius (km)	$\sqrt{u_f^2 + v_f^2}$	76054.840764	88696.330942
Feature coordinates in ring plane (km)	$\mathbf{r}_{pf}(t_f)\|_{xyz}$	-55552.810853 -56484.233442 0.000000	-28317.191257 -86082.659587 0.000000
Ring plane radius (km)	$\|\mathbf{r}_{pf}(t_f)\|$	79224.891424	90620.569421
Feature longitude (deg)	$\theta_{pf}(t_f)$	225.476318830	251.791199062

Notes to TABLE 6

[a] The pole position is the adopted solution, Fit 11 of Table 7. The predicted amount of pole precession has been added to the adopted solution value to get the value listed here.

was generated under the assumption that the time offsets (t_o) are zero for Cerro Tololo, McDonald, Palomar, the IRTF, and UKIRT. As a test of this assumption we performed Fit 2, which is identical to Fit 1 except that the time offsets for all stations except for the IRTF were free parameters. We chose the IRTF as a time reference because we are most familiar with its calibration (Hx93).

The results show a similar pole position to that of Fit 1, but the fitted parameter errors are larger. As shown in Table 8, the time offsets for two of the stations that F93 fixed at zero, McDonald and UKIRT, differ from zero by several formal errors. Also, most of the time offsets are negative, which could mean that the IRTF time scale and/or position is in error. We conclude from this exercise that significant inconsistencies remain in the 28 Sgr data set—possibly in the time scales and/or observatory coordinates used by F93 and in this work. We believe that these lingering systematic errors cause the 28 Sgr data set, when

TABLE 7. Results of orbit model fits.

Fit Code[a]	Data Incl. HST	Data Incl. 28 Sgr	Coordinates of Pole (deg, J2000) α_n	Coordinates of Pole (deg, J2000) δ_n	Epoch of Pole[b]	Precession Rate Ratio[c]	Radius of Feature 23 (km)	t_0 (HST) (s)	RMS	Radii
28 Sgr Data										
1	–	y	40.4444 ± 0.0470	83.6140 ± 0.0236	28 Sgr	0	90557.255 ± 17.695	–	1.272 km	free
2	–	y	40.3686 ± 0.1051	83.6289 ± 0.0279	28 Sgr	0	90551.879 ± 18.101	–	1.189 km	free
GSC6323-01396 Data										
3	y	–	40.5954 ± 0.0222	83.5374 ± 0.0051	HST	0	90615.027	0.06 ± 0.25	0.423 s	fixed
4	y	–	40.5837 ± 0.0299	83.5390 ± 0.0064	HST	0	90615.027	0.11 ± 0.23	2.366 km	fixed
5	y	–	40.5838 ± 0.0296	83.5434 ± 0.0064	HST	0	90615.027	–0.08 ± 0.26	2.337 km	fixed
6	y	–	40.5870 ± 0.0286	83.5381 ± 0.0061	HST	0	90615.027	0	2.338 km	fixed
7	y	–	40.6260 ± 0.4780	83.5266 ± 0.0521	HST	0	90609.935 ± 566.176	0	1.682 km	free
8	y	–	40.5955	83.5381	Voyager 1	1.4 ± 1.3	90614.87	0	2.170 km	fixed
GSC6323-01396 and 28 Sgr Data										
9	y	y	40.5841 ± 0.0154	83.5373 ± 0.0021	28 Sgr–HST	0	90615.027	0	1.791 km	fixed
10	y	y	40.5854 ± 0.0151	83.5340 ± 0.0053	28 Sgr–HST	0	90619.038 ± 4.607	0	1.328 km	free
11[d]	**y**	**y**	**40.5929 ± 0.0151**	**83.5348 ± 0.0053**	**Voyager 1**	**1**	**90618.526 ± 4.606**	**0**	**1.328 km**	**free**
Robustness Tests of Adopted Solution (Fit 11)										
12	y	y	40.6086 ± 0.0051	83.5266 ± 0.0031	Voyager 1	1	90625.356 ± 3.060	0	0.099 s	free
13	y	y	40.5869 ± 0.0151	83.5344 ± 0.0053	Voyager 1	1	90619.653 ± 4.597	0	1.329 km	free
14	y	y	40.5974 ± 0.0154	83.5372 ± 0.0056	Voyager 1	1	90615.559 ± 5.043	–0.24 ± 0.17	1.326 km	free

Notes to TABLE 7

[a] Fits were performed either in radius or in time. To distinguish between the two types, see the "RMS" column. Fit in radius will list the RMS in kilometers, fits in time will list it in seconds. Only Fits #3 and #12 are performed in time.

[b] The epoch "28 Sgr" is defined as the mean epoch of the 28 Sgr occultation, approximately 1989 Jul. 3 8:0:0. The epoch "HST" is the mean epoch of the occultation of GSC6323-01396, approximately 1991 Oct. 3 7:0:0. An entry of "28 Sgr–HST" indicates a mean epoch between these two mean epochs. The epoch "Voyager 1" is defined as UTC 1980 Nov. 12 23:46:32.

[c] The precession rate ratio is defined as the ratio of fitted to predicted precession rates. The predicted precession rates are those given by F93.

[d] Adopted solution

used by itself, to yield a pole position inconsistent (within its formal errors) with that adopted by F93.

7.2 Models with only GSC 6323-01396 Data

The first fits performed with *HST* data alone had feature radii fixed at the revised Voyager values (from Fit 9, Table VIII of F93; radii supplied by R. French), but with the pole coordinates and a possible offset to the *HST* clock allowed to vary. The results are presented in Table 7, with Fit 3 carried out in time and Fit 4 in radius. The right ascensions of the pole agree within 0.5 formal errors, and the declinations agree within 0.3 formal errors, so the choice between fitting in radius and time is significant, but not critical. We note that the rms residual in the time fit, 0.423 s, is substantially larger than the errors that have been estimated for the feature times (<0.1 s for 28 Sgr data and <0.2 s for *HST* data). This indicates an inadequate model, possibly due to yet undetected noncircularities in some of the features (not surprising at this early stage for

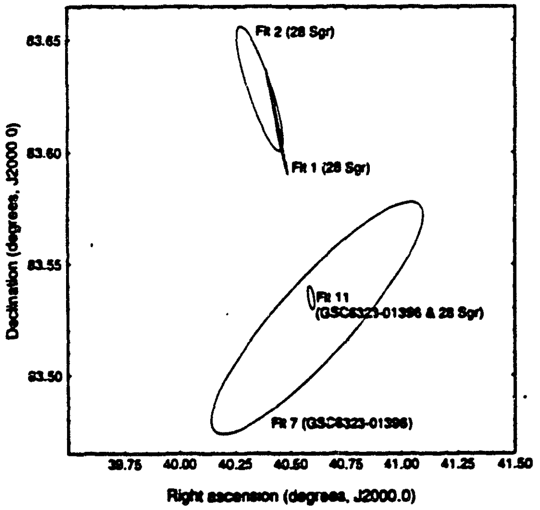

FIG. 13. Pole positions from fits using data from the occultation of 28 Sgr (Fits 1 and 2), data from the occultation of GSC 6323-01396 (Fit 7), and data from both occultations (Fit 11). All poles are plotted at the Voyager 1 epoch of 1980 November 12 23:46:32 UTC. Because Fits 1 and 2 were performed without pole precession and are therefore at the 28 Sgr epoch, the precession rate of F93 was added to the pole values for inclusion on this plot.

TABLE 8. Clock offsets for Fit 2 (28 Sgr).

Station Code[a]	Clock Offset, t_0 (s)	F93 Clock Offset[b], (s)
CAT	–0.064 ± 0.024	–0.030 ± 0.016
CTIO	–0.158 ± 0.158	0
ESO1	0.070 ± 0.155	0.219 ± 0.014
ESO2	0.053 ± 0.154	0.204 ± 0.015
IRTF	0	0
KPi	–0.103 ± 0.025	–0.064 ± 0.017
KPe	–0.079 ± 0.027	–0.059 ± 0.021
MCD	–0.067 ± 0.016	0
MMT	–0.096 ± 0.024	–0.068 ± 0.017
PAL	–0.016 ± 0.024	0
SPM	–0.005 ± 0.021	0.024 ± 0.011
UKIRT	–0.047 ± 0.016	0

Notes to TABLE 8

[a] Station naming conventions are after Table I of F93.

[b] F93 clock offset values have been reversed in sign to agree with our sign convention.

modeling Saturn ring orbits at this high precision). Hence we feel that the fits in radius would yield results closer to reality, so we shall carry out the remaining fits in radius.

Fit 5 of Table 7 is identical to Fit 4, except that the relative error between the planetary ephemeris and the star position has been expressed as an offset in km to the ephemeris (f_0 and g_0) rather than an offset in angle to the star position (α_0 and δ_0). Again, the differences between the right ascension and declination of the pole given by Fits 4 and 5 are not great. Faced with making the choice, however, we feel that the large offset of 1 arcsec would be more likely in the GSC position of the star, so we choose to relegate the offset to the star position in further fits.

Next we investigate the possibility of an offset to the *HST* clock. Since Fits 3–5 give clock offsets consistent with 0.0 s, we fix this parameter at 0.0 s for the remaining fits. Fit 6 shows that the result does not change significantly when the time is thus fixed.

In Fit 7, we allow all feature radii and pole coordinates to be free parameters. With this many free parameters, the formal errors are significantly larger, but we do get a result that agrees with previous work within the formal errors. The final fit presented with only *HST* data (Fit 8) is a fit in which the radii and pole parameters were fixed at F93 final values. The fit was then performed for the precession rate, expressed as a ratio of the fitted value to the value calculated by F93. Their calculation includes solar torque on Saturn, and the torque transmitted to Saturn through its satellites (principally Titan). For this fit, we find a ratio 1.4 ± 1.3, a value consistent with their calculated rate, but with an uncertainty too large to draw any conclusions about the precession of Saturn's ring-plane pole.

7.3 Models Combining GSC 6323-01396 and 28 Sgr Data

In Fits 9, 10, and 11 we used both the *HST* and 28 Sgr data sets. In Fit 9, ring radii were fixed at the revised Voyager values. In Fit 10, the radii were free parameters. The rms residual of the fit is substantially less, but the change in the pole position is well within the errors. Fit 11 includes all station time offsets (except *HST* and IRTF) as free parameters. Again the rms residual decreases, but the pole coordinates do not change. The results of these fits are listed in Table 7 and also plotted in Figs. 13 and 15. We determined that the 27 month time interval between the 28 Sgr and the GSC 6323-01396 occultations was not long enough to establish the precession rates from these data.

7.4 Adopted Solution

Fit 11 gleans the most information from the combination of the *HST* and 28 Sgr data sets without incorporating Voyager data, so we have adopted it as our best solution. The parameters and their formal errors for our adopted solution are given in Table 9. Radius residuals are shown in Fig. 14.

We now check the sensitivity of our adopted solution to those procedures that are a matter of judgment, as discussed above. We have performed fits that each have one of these procedures reversed from our adopted solution: Fit 12 has been done in time instead of radius, Fit 13 has f_0 and g_0 instead of α_0 and δ_0 as free parameters to describe the offset between the planet ephemeris and the star position, and Fit 14 allows the *HST* clock to have an offset. The coordinates for the pole in Fit 12 differ from that of our adopted solution by 1–1.5 formal errors of the adopted solution, but in other cases the differences are smaller. We note that for Fit 14, which has the time offset for the *HST* as a free parameter, the fitted *HST* time offset differs from zero by 1.4 formal errors. This could well have been forced by the remaining uncertainties in clock offsets and observatory coordinates for the 28 Sgr data set discussed above.

The reliability of our adopted solution depends not only on the formal errors and suitability of the procedures just discussed, but also on the accuracy of the assumptions on which our analysis has been based. Most of these potential systematic errors have been discussed by F93, and their conclusions concerning errors in observatory positions, ring plane distortions, and general relativity would apply here as well. They also bring up the issue of the direction to the occulted star changing during the occultation—due to the effects of proper motion and parallax—and they show that these effects can be neglected for 28 Sgr. Because the data-recording interval for the occultation of GSC 6323-01396 was about five times as long as that for 28 Sgr, however, we need to reexamine the parallax and proper motion issue. Since these quantities are not presently known for GSC 6323-01396, we cannot determine the changing direction explicitly. We do note that the star is about 6 mag fainter than 28 Sgr, meaning that it should be about ten times more distant, which would give it a parallax about ten times less. Furthermore, the length of the chord for the GSC 6323-01396 occultation is less than half that for 28 Sgr, and the former occultation occurred well away from opposition. Both of these effects would further reduce the change in the direction of the star due to parallax. Though we feel that it is unlikely that the effects of proper motion and parallax would be large enough to be

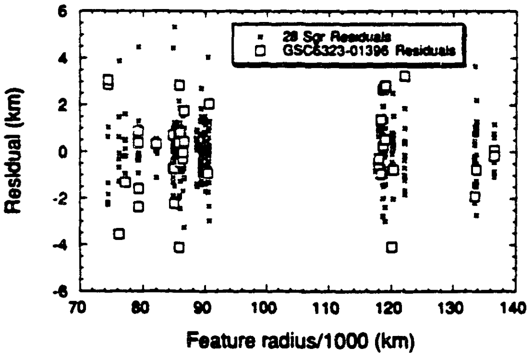

FIG. 14. Radius residuals for the adopted fit, Fit 11 in Table 7. Residuals for the GSC 6323-01396 data set are plotted as open squares, while those from the 28 Sgr data sets are plotted as crosses. All 28 Sgr data sets are included and have been plotted with the same symbol.

TABLE 9. Adopted solution.[a]

Saturn Pole, Voyager 1 epoch	Adopted Solution, present work	Difference[b]
α_n (deg, J2000.0)	40.5929 ± 0.0151	−0.0026
δ_n, (deg, J2000.0)	83.5348 ± 0.0053	−0.0036
$d\alpha_n/dt$ (deg yr^{-1}, J2000.0)	−0.00061172	0.000
$d\delta_n/dt$ (deg yr^{-1}, J2000.0)	−0.00006420	0.000

Stellar-position offsets	28 Sgr	GSC6323-01396
$\alpha_0 \cos \delta_s$ (arcsec)	0.1518 ± 0.0004	0.8957 ± 0.0005
δ_0 (arcsec)	−0.1255 ± 0.0005	−0.1073 ± 0.0006

Station Code[c]	Clock Offset, t_0 (s)	Difference[b] (s)	RMS (km)
HST	0.		1.85
CAT	−0.080 ± 0.019	−0.500	1.27
CTIO	−0.080 ± 0.035	−0.080	0.77
ESO1	0.146 ± 0.035	−0.073	1.23
ESO2	0.129 ± 0.035	−0.075	1.50
IRTF	0.	0.000	1.04
KPi	−0.119 ± 0.021	−0.055	1.50
KPe	−0.100 ± 0.023	−0.041	0.72
MCD	−0.077 ± 0.013	−0.077	0.83
MMT	−0.112 ± 0.020	−0.044	1.53
PAL	−0.038 ± 0.014	−0.038	0.95
SPM	−0.023 ± 0.015	−0.047	1.29
UKIRT	−0.037 ± 0.017	−0.037	1.84

Feature[c]	Semimajor Axis (km)	Difference[b] (km)	RMS (km)	Feature[c]	Semimajor Axis (km)	Difference[b] (km)	RMS (km)
44	74495.21 ± 4.17	4.45	2.06	41	89298.49 ± 4.57	3.43	1.11
40	76266.98 ± 4.17	3.05	2.01	26	89790.11 ± 4.59	3.31	0.73
39	77167.80 ± 4.20	3.17	0.85	25	89942.85 ± 4.59	3.57	0.86
38	79223.59 ± 4.24	3.28	0.82	24	90407.26 ± 4.60	3.18	1.55
37	79268.12 ± 4.25	2.84	1.78	23	90618.53 ± 4.61	3.66	1.25
36	82043.80 ± 4.32	3.22	0.51	20	117936.60 ± 5.71	4.35	0.66
35	84752.66 ± 4.38	3.22	1.36	16	118287.69 ± 5.72	4.40	0.80
34	84952.54 ± 4.39	3.16	1.64	13	118632.67 ± 5.73	4.56	1.40
33	85663.96 ± 4.40	3.31	0.67	15	118970.06 ± 5.75	4.37	1.46
42	85761.82 ± 4.41	3.23	1.67	12	120076.54 ± 5.81	3.12	1.75
31	85924.14 ± 4.41	2.76	1.30	11	120251.12 ± 5.82	4.81	1.02
30	86373.75 ± 4.43	3.14	0.73	7	122054.05 ± 5.89	4.57	1.43
29	86604.45 ± 4.44	3.34	1.07	4	133428.39 ± 6.37	4.86	1.38
28	88597.76 ± 4.55	3.47	0.88	3	133750.06 ± 6.39	4.92	1.28
27	89191.82 ± 4.57	3.22	0.74	1	136527.40 ± 6.52	5.12	0.53

Notes to TABLE 9

[a] Fit 11 of Table 7.

[b] Tabulated differences are values of this work minus those of F93.

[c] Station and feature naming conventions are after F93.

significant, we must await measurements of these quantities before we can be sure.

Errors in the *HST* ephemeris would directly propagate into our solution for the ring geometry, but one would expect that it would be easier to maintain an ephemeris for an Earth-orbiting spacecraft, rather than one so distant as Voyager during its Saturn encounter. The stated accuracy of the *HST* ephemeris is 0.2 km (Elkin 1990). Referred to an Earth-based observer, the *HST* ephemeris errors can be described by three components: "in-track" (along the instantaneous direction of motion, as seen by the observer), "range" (along the line of sight from the observer to the *HST*), and "cross-track" (orthogonal to the other two directions). Using plates taken at Anderson Mesa of the Lowell Observatory, Slivan (1991) found the cross-track position of the *HST* to be within 0.05 km of the definitive ephemeris values, but due to the difficulty in defining the time of the plate exposure to better than 1.0 s, the in-track uncertainty of the result was several kilometers. The range error was unobservable. Another check we have on the *HST* ephemeris is that an in-track error would appear as an error in the *HST* clock. When fit as a free parameter, the zero point moves to 0.1 ±0.2 s—equivalent to a 0.8 ± 1.6 km in-track error.

Another factor to consider is the weighting of the timings used for the fits. We have tried no schemes other than equal weighting. For light curves with ideal Gaussian noise, we should be weighting each feature time inversely proportionally to the square of its rms error. We have not attempted this because we do not believe that our light curves have only ideal Gaussian noise. One way to see what effect a different weighting scheme would have on the results is to compare our fits in time to those in radius (Fits 12 and 11). We prefer fitting in radius for the reasons discussed earlier, but fitting in time effectively gives a higher weight to measurements in those sections of the *HST* light curve for which the apparent radial velocity of the star is low. This different weighting alters the results, but not drastically.

7.5 Comparison with Other Solutions

Now we can compare the results of recent determinations of Saturn's ring-plane pole, based on models that include the feature radii as well as the pole coordinates as free parameters. These solutions are based on three data sets: Voyager (which includes both the PPS and RSS occultation data), 28 Sgr, and *HST*. Plots of the pole solutions from Earth-based data are shown in Fig. 13, where we see the results from four solutions, each having the pole and radii free: 28 Sgr alone (under two different assumptions about the observatory time offsets), *HST* alone, and our adopted solution for the combined *HST* and 28 Sgr data sets. In Figs. 15(a) and 15(b), which have greatly expanded scales compared with that of Fig. 13, we have plotted the poles and their error ellipses for various combinations of data from Voyager, 28 Sgr, and GSC 6323-01396. Figure 15(a) shows pole solutions with feature radii fixed, and Fig. 15(b) shows solutions with feature radii as free parameters. The solution using only Earth-based data is consistent with that for Voyager, although with larger formal uncertainties. The solutions involving Voyager data have smaller formal uncertainties than the Earth-based solution due to the different aspects probed by the two Voyager occultations. However, we emphasize that cross-track trajectory errors and pole precession were fixed parameters in both the NCP and F93 solutions, so the actual uncertainties in those pole positions may be somewhat larger.

Differences between our adopted solution and that adopted by F93 for all fitted parameters are given in Table 9. Our independent result confirms the general placement of the pole given by NCP and F93. Independent tests of the radius scale come from the density waves (Brophy & Rosen 1992) and Pan wakes (Showalter 1991), as discussed by F93.

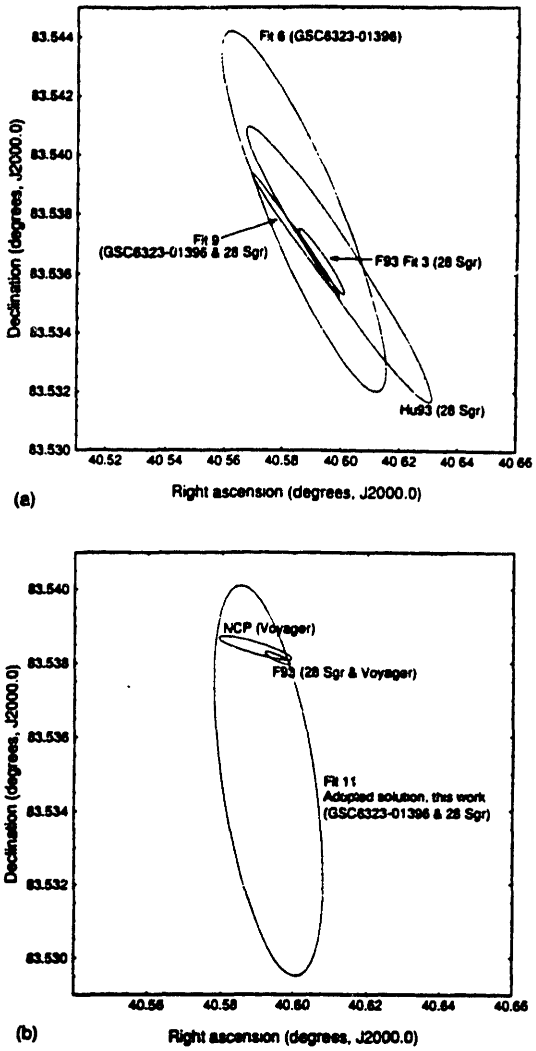

FIG. 15. Pole positions for fits described in text. (a) The pole positions from fits in which feature radii are fixed parameters. These include fits with data from only GSC 6323-01396 (Fit 6), data from GSC 6323-01396 combined with data from 28 Sgr (Fit 9), as well as a fit with 28 Sgr data from F93 (F93 Fit 3), and the final result from Hu93. Note that while Fits 6, 9, and F93 Fit 3 all held radii fixed at the revised NCP values (Fit 9 of Table VIII in F93), Hu93 fixed radii at the values originally published by NCP. See F93 and Hu93 for details. (b) The adopted solution from this work (Fit 11) is plotted with the solutions of NCP and F93, all of which allowed feature radii to be free parameters.

8. CONCLUSIONS

A significant result of this work is the demonstration that a single Earth-orbiting observatory can produce data that are calibrated well enough in space and time to allow a simultaneous solution for the radius scale and pole of Saturn's rings. Contrary to observations with multiple ground-based stations, these data were recorded relative to a single time base and observatory ephemeris. Data of this photometric quality for a star of this magnitude cannot be obtained from the ground with present techniques at optical or IR wavelengths.

Systematic errors still remain in the 28 Sgr data. From our tests it appears that these may result from errors in the observatory positions, which should be remeasured on a common system. Until these errors are corrected, we must remain cautious in estimating the true accuracy of models involving this data set.

This work, along with F93 and Hu93, begins the incorporation of Earth-based occultation data into a global kinematic model of Saturn's rings. The next step in this enterprise will be to improve upon current solutions by combining the *HST*, Voyager, and 28 Sgr data sets. The freely precessing, noncircular features can be added to the kinematic model, allowing Saturn's gravitational harmonics to be fitted as free parameters. In addition to possibly revealing new noncircular features, this work will improve the ring-system fiducial available for the Cassini mission. To measure the precession of the rings and the ring-plane pole, we shall need to continually acquire data. With the imminent demise of the HSP, the challenge will be to find occultation events that would yield adequate signal to noise with the FOS or with ground-based instruments (most likely in the IR).

We are encouraged about the potential of Earth-orbital observations of stellar occultations. The main improvement for a future spacecraft would be to minimize the restrictions on the times when data can be acquired. A higher orbit would allow more continuous data recording, with fewer interruptions (which prohibited recording of two-thirds of our potential light curve) for Earth occultation and SAA passages. Reductions in the solar and lunar avoidance zones would also increase the observational opportunities. Further advantage could be gained with extremely large orbits that would permit observation of occultations not visible from Earth. CCD's and IR array detectors would achieve greater signal to noise through their higher quantum efficiencies and their facility for more efficient background rejection.

Many people on the Space Telescope Project made essential contributions to the success of these observations. Specifically we thank P. Stanley for her heroic efforts in scheduling our SV test and these observations. A. Lubenow also had a critical role in scheduling this occultation. J. Younger implemented commanding changes shortly before the program was carried out, and R. White helped us to correct the offset acquisition commands. A. Storrs and P. Brodsky provided explanations of the management procedures used at the Space Telescope Science Institute for processing proposals and converting their instructions to spacecraft commands. S. McDonald measured the target positions; J. Kangas and S. Slivan wrote the software that we used to predict the occultation. We are grateful to R. French, P. Nicholson, W. Hubbard, and C. Porco for use of data in advance of publication. N. Donahue helped with the synthetic Saturn figures, and L. Young and C. Olkin critically reviewed a draft of Sec. 5. P. Nicholson and W. Hubbard (as referee) provided helpful comments on the manuscript. This work was supported, in part, by HSP GTO Grant No. NASG5-1613. A.S.B. is partially supported by the NASA Graduate Student Researcher Program, and M.L.C. is supported by a NASA Planetary Astronomy Postdoctoral Fellowship.

REFERENCES

Acton, Jr., C. H. 1990, in AIAA/NASA Second International Symposium on Space Information Systems, edited by L. A. Tavenner (AIAA, JPL, Pasadena, CA), Vol. 2, p. 1029

Alexander, A. F. O'D. 1962, Planet Saturn: A History of Observation, Theory, and Discovery (Macmillan, New York)

Archinal, B. A. 1992, in Explanatory Supplement to the Astronomical Almanac, edited by P K. Seidelmann (University Science Books, Mill Valley, CA), p. 199

Baron, R. L., Dunham, E. W., & Elliot, J. L. 1983, PASP, 95, 925

Baum, S. 1993, HST Archive Manual (St Sci)

Bless, R. C., *et al.* 1994, in preparation

Bless, R. C., Percival, J. W., Walter, L. E., & White, R. L. 1992, Hubble Space Telescope High Speed Photometer Instrument Handbook (St Sci)

Boggess, A., *et al.* 1978a, Nature, 275, 377

Boggess, A., *et al.* 1978b, Nature, 275, 372

Bosh, A. S., & McDonald, S. W. 1992, AJ, 103, 983

Brophy, T. G., & Rosen, P. A. 1992, Icarus, 99, 448

Burrows, C. J., Holtzman, J. A., Faber, S. M., Bely, P. Y., Hasan, H., Lynds, C. R., & Schroeder, D. 1991, ApJ, 369, L21

Cuzzi, J. N., Lissauer, J. J., Esposito, L. W., Holberg, J. B., Marouf, E. A., Tyler, G. L., & Boischot, A. 1984, in Planetary Rings, edited by R. Greenberg and A. Brahic (University of Arizona Press, Tucson), p. 73

Downes, R. 1992, Hubble Space Telescope Phase II Proposal Instructions (St Sci)

Dunham, E., Elliot, J. L., Mink, D. J., & Klemola, A. R. 1982, AJ, 87, 1423

Dunham, E. W., Baron, R. L., Elliott, J. L., Vallerga, J. V., Doty, J. P., Doty, & Ricker, G. R. 1985, PASP, 97, 1196

Dunham, E. W., McDonald, S. W., & Elliot, J. L. 1991, AJ, 102, 1464

Elkin, D. 1990, private communication

Elliot, J., & Kerr, R. 1984, Rings: Discoveries from Galileo to Voyager (MIT, Cambridge)

Elliot, J. L. 1990, in Asteroids to Quasars, edited by P. Lugger (Cambridge University Press, New York), p. 27

Elliot, J. L., Dunham, E., & Mink, D. 1977, Nature, 267, 328

Elliot, J. L., Dunham, E., Wasserman, L. H., Millis, R. L., & Churms, J. 1978, AJ 83, 980

Elliot, J. L., Wasserman, L. H., Veverka, J., Sagan, C., & Liller, W. 1974, ApJ, 719

Elliot, J. L., Wasserman, L. H., Veverka, J., Sagan, C., & Liller, W. 1975, AJ, 80, 323

Esposito, L. W. 1986, Icarus, 67, 345

French, R. G., Elliot, J. L., & Allen, D. A. 1982, Nature, 298, 827

French, R. G., *et al.* 1988, Icarus, 73, 349

French, R. G., *et al.* 1993, Icarus, 103, 163

Green, R. M. 1985, Spherical Astronomy (Cambridge University Press, Cambridge)

Harrington, J., Cooke, M. L., Forrest, W. J., Pipher, J. L., Dunham, E. W., & Elliot, J. L. 1993, Icarus, 103, 235

Holberg, J. B., Nicholson, P. D., French, R. G., & Elliot, J. L. (1987), AJ, 94, 178

Hubbard, W. B., *et al.* 1993, Icarus, 103, 215

Keeler, J. E. 1889, AJ, 8, 175

Kinney, A. L. 1993, Faint Object Spectrograph Instrument Handbook (St Sci)

MacKenty, J. W., *et al.* 1992, Hubble Space Telescope Wide Field-Planetary Camera Instrument Handbook (St Sci)

Marouf, E. A., Tyler, G. L., Zebker, H. A., Simpson, R. A., & Eshleman, V. R. 1983, Icarus, 54, 189

Nicholson, P., Cooke, M. L., & Pelton, E. 1990, AJ, 100, 1339 (NCP)

Nicholson, P. D., Persson, S. E., Matthews, K., Goldreich, P. D., & Neugebauer, G. 1978, AJ, 83, 1240

Paresce, F. 1992, Hubble Space Telescope Faint Object Camera Instrument Handbook (St Sci)

Percival, J. W. 1992, High Speed Photometer Pulse Timing and Light Curve Reduction (Space Astronomy Laboratory, University of Wisconsin)

Percival, J. W. 1993, PASP, 105, 551

Percival, J. W., *et al.* 1993, ApJ, 407, 276

Press, W. H., Flannery, B. P., Teukolsky, S. A., & Vetterling, W. T. 1988, Numerical Recipes in C (Cambridge University Press, Cambridge)

Rosen, P. A., Tyler, G. L., & Marouf, E. A. 1991a, Icarus, 93, 3

Rosen, P. A., Tyler, G. L., Marouf, E. A., & Lissauer, J. J. 1991b, Icarus, 93, 25

Seidelmann, P. K., Ed. 1992, Explanatory Supplement to the Astronomical Almanac (University Science Books, Mill Valley, CA)

Showalter, M. R. 1991, Nature 351, 709

Slivan, S. 1991, A Preliminary "Spot-Check" of HST Orbit Information (MIT, Cambridge)

Smart, W. M. 1977, Textbook on Spherical Astronomy, 6th ed. (Cambridge University Press, Cambridge)

Standish, E. M. 1990, A&A, 233, 252

Standish, E. M., Newhall, X. X., Williams, J. G., & Yeomans, D. K. 1992, in Explanatory Supplement to the Astronomical Almanac, edited by P. K. Seidelmann (University Science Books, Mill Valley, CA), p. 279

Sybert, C. B., Bosh, A. S., Sauter, L. M., Elliot, J. L., & Wasserman, L. H. 1992, AJ, 103, 1395

USNO 1992, The Astronomical Almanac for the Year 1992 (U.S. Government Printing Office, Washington)

Wolfram, S. 1991, Mathematica. 2nd ed. (Addison-Wesley, Redwood City, CA)

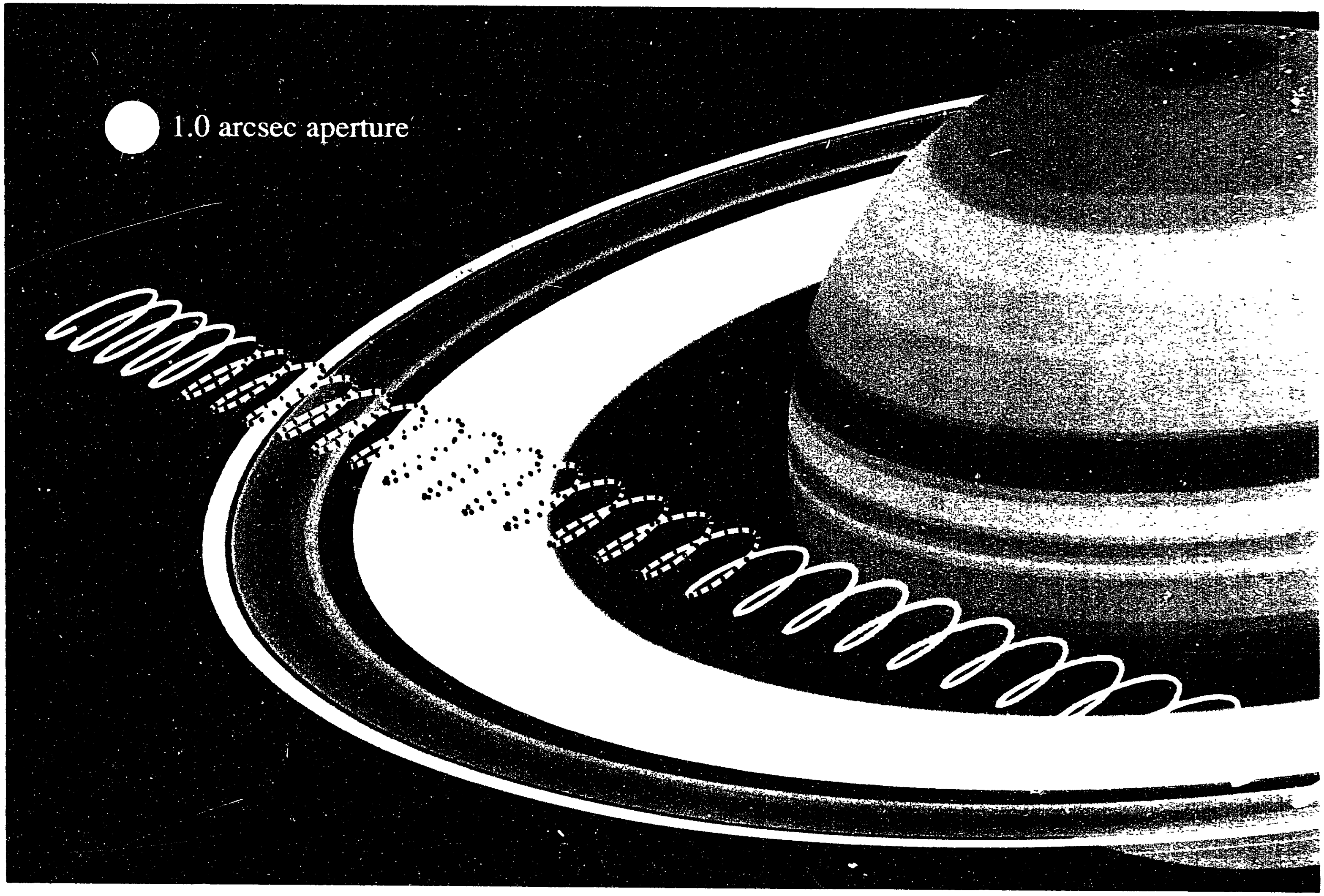

Fig. 4 The path of the star GSC 6323-01396 relative to Saturn's rings during the 1991 October 2–3 occultation, as distorted by spacecraft parallax. Dots are shown at 5 min intervals for the 20 h period of our observations. The spacecraft's motion around the Earth takes it behind our planet (as seen from Saturn) for almost half of each orbit; these Earth occultations are shown in blue. Red dots indicate SAA passages, also unobserved. The remaining stretches of the looping occultation track, shown in green, represent the windows of observability during which data were taken by the HSP's PMT and VIS detectors in "star-sky" mode.

Elliot *et al.* (see page 2551)

REFERENCES

Acton, C. H., Jr. 1990. *The SPICE concept: An approach to providing geometric and other ancillary information needed for interpretation of data returned from space science instruments.* AIAA/NASA Second International Symposium on Space Information Systems. JPL (Pasadena, CA).

Archinal, B. A. 1992. Terrestrial coordinates and the rotation of the Earth. In *Explanatory Supplement to the Astronomical Almanac* (P. K. Seidelmann, Ed.), pp. 199-277. University Science Books, Mill Valley, CA.

Bahcall, J. N., and L. Spitzer 1982. The Space Telescope. *Sci. Amer.* **247**, 40-51.

Bless, R. C., J. W. Percival, L. E. Walter, and R. L. White 1992. *Hubble Space Telescope High Speed Photometer Instrument Handbook.* Space Telescope Science Institute.

Borderies, N., P. Goldreich, and S. Tremaine 1983. The dynamics of elliptical rings. *Astron. J.* **88**, 1560-1568.

Borderies, N., P. Goldreich, and S. Tremaine 1984. Erratum: "The dynamics of elliptical rings" [Astron. J. **88**, 1560 (1983)]. *Astron. J.* **89**, 727.

Bosh, A. S. 1990. *An analysis of the Mimas 5:3 bending wave at 3.2 microns.* General Examination Paper. Massachusetts Institute of Technology.

Bosh, A. S., and S. W. McDonald 1992. Stellar occultation candidates from the Guide Star Catalog. I. Saturn, 1991-1999. *Astron. J.* **103**, 983-990.

Brophy, T. G., and P. A. Rosen 1992. Density waves in Saturn's rings probed by radio and optical occultation: observational tests of theory. *Icarus* **99**, 448-467.

Brouwer, D., and G. M. Clemence 1961. *Methods of Celestial Mechanics.* Academic Press, New York.

Brown, R. A., and H. C. Ford 1991. *Report of the HST Strategy Panel: A Strategy for Recovery.* Space Telescope Science Institute.

Campbell, J. K., and J. Anderson 1989. Gravity Field of the Saturnian System from Pioneer and Voyager tracking Data. *Astron. J.* **97**, 1485-1495.

Covault, C. E., I. S. Glass, R. G. French, and J. L. Elliot 1986. The 7 and 25 June 1985 Neptune occultations: Constraints on the putative Neptune "Arc". *Icarus* **67**, 126-133.

Cuzzi, J. N., and J. D. Scargle 1985. Wavy edges suggest moonlet in Encke's gap. *Astrophys J.* **292**, 276-290.

Dones, L. 1991. A recent cometary origin for Saturn's rings? *Icarus* **92**, 194-203.

Duncan, M., T. Quinn, and S. Tremaine 1988. The origin of short-period comets. *Astrophys. J. (Letters)* **328**, L69-L73.

Dunham, E. W., S. W. McDonald, and J. L. Elliot 1991. Pluto-Charon stellar occultation candidates: 1990-1995. *Astron. J.* **102**, 1464-1484.

Elliot, J. L., A. S. Bosh, M. L. Cooke, R. C. Bless, M. J. Nelson, J. W. Percival, M. J. Taylor, J. F. Dolan, E. L. Robinson, and G. W. van Citters 1993. An occultation by Saturn's rings on 1991 October 2-3 observed with the Hubble Space Telescope. *Astron. J.* **106**, 2544-2572.

Elliot, J. L., E. Dunham, and D. Mink 1977. The rings of Uranus. *Nature* **267**, 328-330.

Elliot, J. L., E. Dunham, L. H. Wasserman, R. L. Millis, and J. Churms 1978. The radii of Uranian rings α, β, γ, δ, ε, η, 4, 5, and 6 from their occultations of SAO 158687. *Astron. J.* **83**, 980-992.

Elliot, J. L., R. G. French, J. A. Frogel, J. H. Elias, D. J. Mink, and W. Liller 1981. Orbits of nine Uranian rings. *Astron. J.* **86**, 444-455.

French, R. G., J. L. Elliot, and S. Levine 1986. Structure of the Uranian rings. II. Ring orbits and widths. *Icarus* **67**, 134-163.

French, R. G., P. D. Nicholson, M. L. Cooke, J. L. Elliot, K. Matthews, O. Perkovic, E. Tollestrup, P. Harvey, N. J. Chanover, M. A. Clark, E. W. Dunham, W. Forrest, J. Harrington, J. Pipher, A. Barucci, A. Brahic, C. Ferrari, I. Grenier, F. Roques, B. Sicardy, and M. Arndt 1993. Geometry of the Saturn system from the 3 July 1989 occultation of 28 Sgr and Voyager observations. *Icarus* **103**, 163-214.

French, R. G., P. D. Nicholson, C. C. Porco, and E. A. Marouf 1991. Dynamics and structure of the Uranian rings. In *Uranus* (J. T. Bergstralh, E. D. Miner and M. S. Matthews, Ed.), pp. 327-409. University of Arizona Press, Tucson.

Goldreich, P., and S. Tremaine 1979. Towards a theory for the Uranian rings. *Nature* **277**, 97-99.

Goldreich, P., and S. Tremaine 1982. The dynamics of planetary rings. *Ann. Rev. Astron. Astrophys.* **20**, 249-283.

Gresh, D. L., P. A. Rosen, and G. L. Tyler 1986. An analysis of bending waves in Saturn's rings using Voyager radio occultation data. *Icarus* **68**, 481-502.

Harper, D., and D. B. Taylor 1993. The orbits of the major satellites of Saturn. *Astron. Astrophys.* **268**, 326-349.

Harrington, J., M. L. Cooke, W. J. Forrest, J. L. Pipher, E. W. Dunham, and J. L. Elliot 1993. IRTF observations of the occultation of 28 Sgr by Saturn. *Icarus* **103**, 235-252.

Harris, A. W. 1984. The origin and evolution of planetary rings. In *Planetary Rings* (R. Greenberg and A. Brahic, Ed.), pp. 641-659. University of Arizona Press, Tucson.

Holman, M. J., and J. Wisdom 1993. Dynamical stability in the outer solar system and the delivery of short period comets. *Astron. J.* **105**, 1987-1999.

Horanyi, M. 1993. New rings for Jupiter? *Bull. Amer. Astron. Soc.* **25**, 1044.

Hubbard, W. B. 1974. Inversion of gravity data for giant planets. *Icarus* **21**, 157-165.

Hubbard, W. B. 1982. Effects of differential rotation on the gravitational figures of Jupiter and Saturn. *Icarus* **52**, 509-515.

Hubbard, W. B. 1984. *Planetary Interiors.* van Nostrand Reinhold Co., New York.

Hubbard, W. B., A. Brahic, B. Sicardy, L.-R. Elicer, F. Roques, and F. Vilas 1986. Occultation detection of a neptunian ring-like arc. *Nature* **319**, 636-640.

Hubbard, W. B., and M. S. Marley 1989. Optimized Jupiter, Saturn, and Uranus interior models. *Icarus* **78**, 1041.

Hubbard, W. B., C. C. Porco, D. M. Hunten, G. H. Rieke, M. J. Rieke, D. W. McCarthy, V. Haemmerle, R. Clark, E. P. Turtle, J. Haller, B. McLeod, L. A. Lebofsky, R. Marcialis, J. B. Holberg, R. Landau, L. Carrasco, J. Elias, M. W. Buie, S. E. Persson, T. Boroson, S. West, and D. J. Mink 1993. The occultation of 28 Sgr by Saturn: Saturn pole position and astrometry. *Icarus* **103**, 215-234.

Hubbard, W. B., and D. J. Stevenson 1984. Interior structure of Saturn. In *Saturn* (T. Gehrels and M. S. Matthews, Ed.), pp. 47-87. University of Arizona Press, Tucson.

Jeffreys, H. 1954. Second order terms in the figure of Saturn. *Mon. Not. R. Astron. Soc.* **114**, 433-436.

Kaiser, M. L., M. D. Desch, W. S. Kurth, A. Lecacheux, F. Genova, B. M. Pedersen, and D. R. Evans 1984. Saturn as a radio source. In *Saturn* (T. Gehrels and M. S. Matthews, Ed.), pp. 378-415. University of Arizona Press, Tucson.

Klemola, A. R., and D. J. Mink 1991. Occultations by Uranus and Neptune: 1991-1999. *Astron. J.* **102**, 389-394.

Kozai, Y. 1957. On the astronomical constants of Saturnian satellite system. *Ann. Tokyo Astron. Obs.* **5**, 73-106.

Kozai, Y. 1976. Masses of satellites and oblateness parameters of Saturn. *Publ. Astron. Soc. Japan* **28**, 675-691.

Lane, A. L., R. A. West, C. W. Hord, R. M. Nelson, K. E. Simmons, W. R. Pryor, L. W. Esposito, L. J. Horn, B. D. Wallis, B. J. Buratti, T. G. Brophy, P. Yanamandra-Fisher, J. E. Colwell, D. A. Bliss, M. J. Mayo, W. D. Smythe, A. L. Graps, and W. R. Pryor 1989. Photometry from Voyager 2: Initial Results from the Neptunian Atmosphere, Satellites, and Rings. *Science* **246**, 1450-1454.

Lissauer, J. J. 1985. Bending waves and the structure of Saturn's rings. *Icarus* **62**, 433-447.

Lissauer, J. J., and J. N. Cuzzi 1982. Resonances in Saturn's rings. *Astron. J.* **87**, 1051-1058.

Lissauer, J. J., P. Goldreich, and S. Tremaine 1985. Evolution of the Janus-Epimetheus coorbital resonance due to torques from Saturn's rings. *Icarus* **64**, 425-434.

Luu, J., and D. Jewitt 1993. 1993 FW. IAU Circ. No. 5730.

Luu, J. X., and D. Jewitt 1992. 1992 QB1. IAU Circ. No. 5611.

McDonald, S. W., and J. L. Elliot 1992. Triton stellar occultation candidates: 1992-1994. *Astron. J.* **104**, 862-879.

Millis, R. L., L. H. Wasserman, and P. V. Birch 1977. Detection of rings around Uranus. *Nature* **267**, 330-331.

Nicholson, P., M. L. Cooke, and E. Pelton 1990. An absolute radius scale for Saturn's rings. *Astron. J.* **100**, 1339-1362.

Nicholson, P. D., and R. G. French 1993. The precession rate of Saturn's ring plane. *Bull. Amer. Astron. Soc.* **25**, 1108-1109.

Nicholson, P. D., and C. Porco 1988. A new constraint on Saturn's zonal gravity harmonics from Voyager observations of an eccentric ringlet. *J. Geophys. Res.* **93**, 10209-10224.

Null, G. W., E. L. Lau, E. D. Biller, and J. D. Anderson 1981. Saturn gravity results obtained from Pioneer II tracking data and earth-based Saturn satellite data. *Astron. J.* **86**, 456-468.

Owen, T., G. E. Danielson, A. F. Cook, C. Hansen, V. L. Hall, and T. C. Duxbury 1979. Jupiter's rings. *Nature* **281**, 442-446.

Paresce, F. 1992. *Hubble Space Telescope Faint Object Camera Instrument Handbook.* Space Telescope Science Institute.

Percival, J. W. 1992. *High Speed Photometer Pulsar Timing and Light Curve Reduction.* Space Astronomy Laboratory, University of Wisconsin.

Porco, C., P. D. Nicholson, N. Borderies, G. E. Danielson, P. Goldreich, J. B. Holberg, and A. L. Lane 1984. The eccentric Saturnian ringlets at 1.29Rs and 1.45Rs. *Icarus* **60**, 1-16.

Porco, C. C. 1983. *Voyager observations of Saturn's rings.* Ph. D. thesis, California Institute of Technology.

Porco, C. C., and P. D. Nicholson 1987. Eccentric features in Saturn's outer C ring. *Icarus* **72**, 437-467.

Rohde, J. R., and A. Sinclair 1992. Orbital ephemerides and rings of satellites. In *Explanatory Supplement to the Astronomical Almanac* (P. K. Seidelmann, Ed.), pp. 325-381. University Science Books, Mill Valley.

Rosen, P. A., G. L. Tyler, and E. A. Marouf 1991a. Resonance structures in Saturn's rings probed by radio occultation. I. Methods and examples. *Icarus* **93**, 3-24.

Rosen, P. A., G. L. Tyler, E. A. Marouf, and J. J. Lissauer 1991b. Resonance structures in Saturn's rings probed by radio occultation. II. Results and interpretation. *Icarus* **93**, 25-44.

Seidelmann, P. K. 1992. *Explanatory Supplement to the Astronomical Almanac.* University Science Books, Mill Valley, CA.

Shoemaker, E. M., C. S. Shoemaker, and D. H. Levy 1993. Collision of P/Shoemaker-Levy 9 with Jupiter. *Bull. Amer. Astron. Soc.* **25**, 1042.

Showalter, M. R. 1991. Visual detection of 1981S13, Saturn's eighteenth satellite, and its role in the Encke gap. *Nature* **351**, 709-713.

Showalter, M. R., J. N. Cuzzi, E. A. Marouf, and L. W. Esposito 1986. Satellite "wakes" and the orbit of the Encke Gap moonlet. *Icarus* **66**, 297-323.

Shu, F. H. 1984. Waves in planetary rings. In *Planetary Rings* (R. Greenberg and A. Brahic, Ed.), pp. 513-561. University of Arizona Press, Tucson.

Sicardy, B., F. Roques, and A. Brahic 1991. Neptune's rings, 1983-1989: Ground-based stellar occultation observations. *Icarus* **89**, 220-243.

Simpson, R. A., G. L. Tyler, and J. B. Holberg 1983. Saturn's pole: Geometric correction based on Voyager UVS and radio occultations. *Astron. J* **88**, 1531-1536.

Smith, B. A., L. A. Soderblom, D. Banfield, C. Barnet, A. T. Basilevksy, R. F. Beebe, K. Bollinger, J. M. Boyce, A. Brahic, G. A. Briggs, R. H. Brown, C. Chyba, S. A. Collins, T. Colvin, A. F. Cook II, D. Crisp, S. K. Croft, D. Cruikshank. J. N. Cuzzi, G. E. Danielson, M. E. Davies, E. De Jong, L. Dones, D. Godfrey, J. Goguen, I. Grenier, V. R. Haemmerle, H. Hammel, C. J. Hansen, C. P. Helfenstein, C. Howell, G. E. Hunt, A. P. Ingersoll, T. V. Johnson, J. Kargel, R. Kirk, D. I. Kuehn, S. Limaye, H. Masursky, A. McEwen, D. Morrison, T. Owen, W. Owen, J. B. Pollack, C. C. Porco, K. Rages, P. Rogers, D. Rudy, C. Sagan, J. Schwartz, E. M. Shoemaker, M. Showalter, B. Sicardy, D. Simonelli, J. Spencer, L. A. Sromovsky, C. Stoker, R. G. Strom, V. E. Suomi, S. P. Synott, R. J. Terrile, P. Thomas, W. R. Thompson, A. Verbiscer, and J. Veverka 1989. Voyager 2 at Neptune: Imaging science results. *Science* **246**, 1422-1449.

Standish, E. M. 1990. The observational basis for JPL's DE-200, the planetary ephemerides of the Astronomical Almanac. *Astronomy and Astrophysics* **233**, 252-271.

Standish, E. M., X. X. Newhall, J. G. Williams, and D. K. Yeomans 1992. Orbital ephemerides of the sun, moon, and planets. In *Explanatory Supplement to the Astronomical Almanac* (P. K. Seidelmann, Ed.), pp. 279-323. University Science Books, Mill Valley, CA.

STScI 1989. The Guide Star Catalog.

Sybert, C. B., A. S. Bosh, L. M. Sauter, J. L. Elliot, and L. H. Wasserman 1992. Magnitudes of selected stellar occultation candidates for Pluto and other planets, with new predictions for Mars and Jupiter. *Astron. J.* **103**, 1395-1398.

Turtle, E., C. Porco, W. Hubbard, V. Haemmerle, R. Clark, D. Hunten, G. Rieke, M. Rieke, J. Haller, J. Holberg, L. Lebofsky, R. Marcialis, D. McCarthy, B. McLeod, M. Buie, J. Elias, D. Jewitt, E. Persson, T. Boroson, S. West, R. Landau, and L. Carrasco 1990. The kinematics of Saturn's major narrow rings from combined Voyager and ground-based data. *Bull. Amer. Astron. Soc.* **22**, 1041.

Tyler, G. L., V. R. Eshleman, J. D. Anderson, G. S. Levy, G. F. Lindal, G. E. Wood, and T. A. Croft 1981. Radio science investigations of the Saturn system with Voyager 1: Preliminary results. *Science* **212**, 201-206.

USNO 1992. *The Astronomical Almanac for the Year 1992.* U. S. Government Printing Office, Washington.

Williams, I. P., A. Fitzsimmons, and D. O'Ceallaigh 1993. 1993 SB and 1993 SC. IAU Circ. No. 5869.

Wolfram, S. 1991. *Mathematica.* Addison-Wesley Publishing Co., Redwood City, CA.

Zebker, H. A., E. A. Marouf, and G. L. Tyler 1985. Saturn's rings: Particle size distributions for thin layer models. *Icarus* **64**, 531-548.

Zharkov, V. N., and V. P. Trubitsyn 1978. *Physics of Planetary Interiors.* Tucson.